

D4.3: Preliminary Report on the Unified Air Interface, User-Centric and Beamforming Solutions

Revision: V1.0

Work package	WP 4
Task	Task 4.1 and Task 4.2
Due date	31/04/2024
Submission date	3/05/2024
Deliverable lead	CNIT
Version	V1.0
Authors	Alessandro Guidotti, Tommaso Foggi, Amina Piemontese (CNIT) Marius Caus, Xavier Artiga, Musbah Shaat, Erislandy Mozo, Cristian J. Vaca-Rubio (CTTC) Nathan Borios (TASF)
Reviewers	Benjamin Barth (DLR), Stefano Cioni (ESA, External Expert Advisory Board)
Abstract	This document reports the initial outcomes of Tasks 4.1 “Flexible and unified Air Interface” and Task 4.2 “User-Centric and Digital Beamforming Solutions” related to the investigation of the NR-NTN standard, including the waveform, and user-centric beamforming technologies. In particular, the enhancements that are needed in the 3GPP NTN to support the architecture defined in WP3 are addressed. Building upon this air interface, user-centric beamforming designs and Radio Resource Management (RRM) solutions are conceived. The final outcomes on these activities will be reported in D4.6 in 2025.
Keywords	3GPP, NTN, 5G, 5G-Advanced, NTN procedures, Architecture, Waveform, OFDM, OTFS, User-centric beamforming, RRM

WWW.5G-STARDUST.EU

DOCUMENT REVISION HISTORY

Version	Date	Description of change	List of contributor(s)
V0.1	22/09/2023	Document creation	CTTC
V0.2	13/12/2023	Modifications to the ToC	CTTC
V0.3	6/02/2024	Finalisation of the ToC	CTTC, CNIT
V0.4	11/03/2024	Contributions to Section 3	CTTC
V0.5	12/03/2024	Contributions to Section 2	TASF
V0.6	2/04/2024	Contributions to Sections 2, 3, and 4	CNIT, CTTC, TASF
V0.7	18/04/2024	Contributions to Section 4 and 5	CNIT
V0.8	19/04/2024	Final contributions to Sections 2, 3, and 4.	CNIT, CTTC, TASF
V0.9	22/04/2024	First release for internal review	CNIT, CTTC, TASF
V1.0.D	3/05/2024	First release for submission to EC	CNIT, CTTC, TASF
V1.0.F	3/05/2024	Final approval for submission to EC	DLR

DISCLAIMER



Co-funded by
the European Union



5G-STAR DUST (*Satellite and Terrestrial Access for Distributed, Ubiquitous, and Smart Telecommunications*) project has received funding from the [Smart Networks and Services Joint Undertaking \(SNS JU\)](#) under the European Union's [Horizon Europe research and innovation programme](#) under Grant Agreement No 101096573.

Views and opinions expressed are however those of the author(s) only and do not necessarily reflect those of the European Union. Neither the European Union nor the granting authority can be held responsible for them.

COPYRIGHT NOTICE

© 2023 - 2025 5G-STAR DUST

Project co-funded by the European Commission in the Horizon Europe Programme	
Nature of the	R



Co-funded by
the European Union



deliverable:		
Dissemination Level		
PU	<i>Public, fully open, e.g. web (Deliverables flagged as public will be automatically published in CORDIS project's page)</i>	✓
SEN	<i>Sensitive, limited under the conditions of the Grant Agreement</i>	
Classified R-UE/ EU-R	<i>EU RESTRICTED under the Commission Decision No2015/ 444</i>	
Classified C-UE/ EU-C	<i>EU CONFIDENTIAL under the Commission Decision No2015/ 444</i>	
Classified S-UE/ EU-S	<i>EU SECRET under the Commission Decision No2015/ 444</i>	

* R: Document, report (excluding the periodic and final reports)

DEM: Demonstrator, pilot, prototype, plan designs

DEC: Websites, patents filing, press & media actions, videos, etc.

DATA: Data sets, microdata, etc.

DMP: Data management plan

ETHICS: Deliverables related to ethics issues.

SECURITY: Deliverables related to security issues

OTHER: Software, technical diagram, algorithms, models, etc.

EXECUTIVE SUMMARY

In this deliverable, 5G-STARBUST investigates aspects related to the 3GPP New Radio (NR) Air Interface for Non-Terrestrial Networks (NTN), including the waveform, and user-centric beamforming technologies as outcomes of Tasks 4.1 “Flexible and unified Air Interface” and Task 4.2 “User-Centric and Digital Beamforming Solutions,” respectively. In particular, the enhancements that are needed for the 3GPP NTN to support the architecture defined in WP3 are addressed. Building upon this air interface, user-centric beamforming designs and Radio Resource Management (RRM) solutions are conceived.

The first part of the document is devoted to defining a common framework that will be used across the activities of 5G-STARBUSTWP4 in different tasks, including: architecture, satellite and User Equipment (UE) specifications, antenna models, channel models, impairments, as well as system and orbit parameters.

In the above common framework, the elements of the air interface that are sensitive to be enhanced have then been identified, including the analysis of all the necessary steps to go from the IDLE to the CONNECTED state, *i.e.*, establish the connection from an NTN UE to an NTN gNB. Based on this analysis, two management steps have been differentiated:

- The transmission of broadcast beams to deliver system and control information that is common to all users.
- The transmission of data beams to satisfy the traffic demand.

Remarkably, to implement this approach, the 3GPP standard does not provide specific guidelines but leaves open some aspects to the manufacturers’ implementation, *i.e.*:

- Doppler compensation schemes;
- Mapping between cells and beams;
- Synchronisation Signal Block (SSB) multiplexing;
- System information scheduling;
- Polarization management;
- SSB detection;
- Physical layer Random Access Channel (PRACH) detection.

As a first iteration, two compensation schemes have been described. The first is referred to as UE compensation, which is the basic configuration described in 3GPP. In such a case, the UE is able to autonomously pre-compensate instantaneous delay and Doppler effects in the service link by exploiting the UE location and the satellite ephemeris. The coordinates can be obtained by means of Global Navigation Satellite System (GNSS) information or alternative positioning methods that exploit time difference and frequency difference of arrival measurements of SSB signals. An additional mechanism is to pre- and post-compensate at the satellite the Doppler on the downlink (DL) and uplink (UL) with respect to the beam centre. Then, the user will be only affected by the differential Doppler between the true coordinates and the centre of the beam reducing by an order of magnitude the frequency misalignment. The impact of these compensation mechanisms has been evaluated in DL and UL synchronization stages. The assessment reveals that for DL synchronization, the application of satellite compensation succeeds in reducing the frequency uncertainty. As for the UL, the mobility of the terminal is the most detrimental effect. To support the airway scenario in which

the terminal is mounted on a plane, the UE shall exploit the knowledge of the plane velocity to reduce the frequency offset. Alternatively, the Random Access Response (RAR), which comes into play in the second step of the Random Access (RA) procedure, shall provide Carrier Frequency Offset (CFO) corrections to reduce the frequency misalignment. The last observation is that the robustness of the preamble format needs to be enhanced to support GNSS-free operation during the network attachment.

Another important aspect that has been discussed is the beam footprint layout. In alignment with D3.2, [2], the preferred option in the project is to have a fixed grid on Earth. This allows to mimic terrestrial deployments to a high extent, which smooths the impact on the 5G 3GPP standard and reduces the number of handovers. Interestingly, the synthesis of Earth-fixed beams is advantageous from a system point of view, as a stationary user that is inside the Field of View (FoV) of the satellite will be served by the same beam in the visibility period. Based on the beam shapes and the grids, different options have been compared. The first one, is the scheme proposed by 3GPP, which consists of defining a hexagonal grid on the u-v plane. The main issue is that this solution does not produce a uniform grid on Earth. One possibility is to deploy a homogenous grid according to the footprint radius at Nadir. The consequence is that the FoV is divided into a large number of beams and, thus, large overlapping will be experienced at the edge due to the beam deformation. The alternative is to synthesize uniform beam shapes. This is achieved by taking as a reference the largest beam in the edge and widening the rest. Remarkably, in this case the number of beams in the FoV is substantially reduced. The most interesting conclusion from the investigations presented in the following of this document, is that a large number of beams preserves the Effective Isotropic Radiated Power (EIRP) but requires more resources in terms of time slots and hops, to sweep the coverage area. By deploying uniform beams, the resources needed to sweep the area are decreased. However, this comes at the cost of reducing the EIRP due to the widening. Essentially, the system is not using all the available power in all the amplifiers. An appealing solution is to bridge the gap between these two extreme cases, which would require to analyse in more detail the widening algorithm applied in the final version of this document, D4.6.

For what concerns the cell mapping, three options have been discussed:

- Number of cells higher than the number of beams. Initially this option is labelled as low priority as it entails discontinuous transmission, which is not supported by the standard.
- The second is the most direct implementation and consists in deploying as many cells as active beams. To control inter-cell interference some cooperation between cells is needed. The main drawback is that the Handover (HO) procedure may need to be executed in the FoV, due to the user mobility.
- The third option is to have a single cell. The main challenge is to have a single scheduler for the whole coverage area. It deserves to be mentioned that it has an impact on the standard, as only 64 beams can be managed during the initial cell search. According to the beam layout, the cell may include hundreds or even thousands of beams.

The initial assessment reveals that having a single cell offers more degrees of freedom to schedule the users. However, there are other implementation aspects that must be further analysed. The detailed comparison will be performed in D4.6.

With respect to user-centric beamforming, an extensive overview and discussion on the possible architectures to implement Multiple Input Multiple Output (MIMO) solutions is provided. The first step in this analysis is related to the identification of the protocol stack layers in which the requested operations are performed: i) scheduling and computation of the beamforming coefficients in the high Medium Access Control (MAC) layer; and ii) application of the beamforming coefficients in the low Physical layer (PHY). Based on these

considerations, the various functional split options provided by 3GPP are mapped onto three different beamforming management architectures:

- Distributed Beamforming Management (DBFM), in which all operations are implemented in the gNB Distributed Unit (gNB-DU).
- Centralised Beamforming Management (CBFM), in which the scheduling and the computation of the beamforming coefficients are implemented in the gNB Centralised Unit (gNB-CU) and the application of the coefficients is in the gNB-DU. In this case, depending on where the gNB-CU is implemented, two sub-architectures are identified: i) CBFM on-ground (CBFM-OG), where the gNB-CU is conceptually located at the gateway (GW); and ii) CBFM on-board (CBFM-OB), in which the gNB-CU is on-board a higher hierarchy NTN node in the constellation.

For all the architecture options introduced above, the various Network Elements (NE) are described in terms of the required operations and the high-level functional procedures are provided. These procedures provide a description of the process and flow of information to support user-centric beamforming techniques that are either based on Channel State Information (CSI) or on the location estimates provided by the UEs. This analysis pointed out two potential modifications required in the 3GPP specifications:

- CSI-based beamforming: in this case, the NE computing the scheduling and beamforming coefficients shall have the estimates of the channel coefficients between each visible user and each radiating element on-board. Current 3GPP specifications support the provision of quantised quantities, such as Channel Quality Indicator (CQI), Rank Indicator (RI), and Precoding Matrix Indicator (PMI) based on beam-level signalling. Thus, modifications are required to support the estimation of the non-quantised coefficients at radiating element level. One possibility is that of exploiting the available CSI Reference Signals (CSI-RS) operating at beam level to estimate the channel between the NTN node and the UE; then, the known antenna array configuration and radiation pattern can be exploited to complement this information and obtain the channel coefficients for each radiating element.
- Location-based: in this case, the UEs estimate their positions and report them to the network. However, this information is available in the 5G Core network (5GC) and not at Radio Access Network (RAN) level. The UEs' locations can be obtained by interacting with the Access and Mobility Management Function (AMF) and Location Management Function (LMF), but this would increase the impact of the information aging with a detrimental effect on the beamforming performance. Thus, an adaptation to the current standard would be required, in particular allowing the UEs' location to be available at RAN level without interacting with the 5GC.

The initial performance assessment is performed in clear-sky and Line-of-Sight (LOS) conditions with both CSI and location-based algorithms. The RRM is implemented assuming random scheduling, in order to first identify the major performance trends and trade-offs. The numerical assessment revealed that, over a very large service area (basically covering Europe) and with only 24 user-centric beams per time slot, the asymptotic capacity is in line with the expectations (600-800 Mbps), while the experienced capacity (*i.e.*, including the percentage of channel use per user) is particularly low. This is due to the very limited amount of time allocated to the transmission of each user (a few seconds in the best case). This analysis points out the direction for the next analyses to be performed in Task 4.2, *i.e.*, consider non-uniform users and traffic distributions. For these, various models and options are introduced in the document and will be discussed in the next steps. Scenarios with hot-spot areas where users are concentrated will allow to truly assess the benefit of user-centric

beamforming as: i) the users in the hot-spot areas will be served for larger periods of time, increasing the experienced capacity; and ii) increasing the co-channel interference will boost the performance benefit of algorithms based on Minimum Mean Square Error (MMSE) beamforming or its variants. In these scenarios, the importance of RRM algorithms will be central. Thus, non-random RRM solutions will be designed, starting from two solutions (Heuristic RRM, H-RRM, and Graph-based RRM, G-RRM) proposed in this document.

Finally, the main features of the Orthogonal Frequency Division Multiplexing (OFDM) and Orthogonal Time Frequency Space (OTFS) modulations are introduced. A performance assessment is performed for link-level user-centric beamforming technologies, with both waveforms. The mutual information of the virtual channel having at its input the constellation symbols and at its output the detector soft estimates of the symbols is used as main performance metric. Compared to the results obtained at system-level, a degradation in the performance is observed when taking into account modulated signals in the presence of Doppler shift and signalling overhead. The next steps for link-level evaluations will include the implementation of a software simulator that actually transmits and receives NR signals without resorting to the simplified assumptions based on Gaussian interference. In addition, also the inclusion of CQI reports will allow to implement Adaptive Coding and Modulation (ACM) schemes. Finally, the OTFS waveform will be considered.

TABLE OF CONTENTS

Document Revision History.....	2
Disclaimer.....	2
Copyright notice	2
1 INTRODUCTION.....	21
2 FRAMEWORK DEFINITION	22
2.1 System and orbit parameters.....	22
2.2 Satellite payload hardware impairments.....	23
2.2.1 Non-linear amplification.....	23
2.2.2 Phase noise.....	25
2.2.3 Gain flatness and group delay.....	26
2.3 Satellite and user terminal antenna patterns	28
2.3.1 Satellite antenna pattern	28
2.3.2 UE antenna pattern	29
2.4 Channel model	29
2.4.1 System-level.....	29
2.4.2 Link-level.....	33
3 NTN INITIAL ACCESS	40
3.1 Release 17 NTN initial access	40
3.1.1 Downlink synchronisation (Cell Search)	43
3.1.2 Random Access procedure	44
3.1.3 Doppler pre-compensation.....	45
3.1.4 Timing Advance	46
3.1.5 Summary.....	46
3.2 From standard to implementation	47
3.2.1 Management of satellite beams	47
3.2.2 Mapping satellite beams to 5G cells.....	56
3.2.3 Doppler Compensation Schemes	67
3.2.4 SSB detection	69
3.2.5 PRACH signal detection.....	72
4 USER-CENTRIC AND DIGITAL BEAMFORMING SOLUTIONS.....	79
4.1 Scientific review	79
4.1.1 Precoding and beamforming via satellite.....	79
4.1.2 Radio Resource Management for beamforming via satellite	83
4.2 System definition: standalone node.....	84
4.2.1 Network Elements and system procedures.....	84

4.2.2	Aging interval	94
4.2.3	User-centric beamforming.....	96
4.2.4	Random RRM algorithms.....	105
4.3	Performance assessment: standalone node	109
4.3.1	Simulation parameters.....	109
4.3.2	Numerical results.....	110
4.4	Overview of the next activities	118
4.4.1	Non-random RRM	118
4.4.2	User and traffic distribution	124
4.4.3	Users' movement.....	127
4.4.4	Non-ideal estimation of the ancillary information	128
5	FLEXIBLE AND UNIFIED AIR INTERFACE	130
5.1	Waveform design	130
5.1.1	OFDM-based.....	130
5.1.2	OTFS	131
5.1.3	Performance assessment	133
5.1.4	Doppler effects.....	134
5.1.5	Waveform and simulation parameters	134
5.1.6	Pragmatic capacity	135
5.2	Next developments	137
6	CONCLUSIONS.....	138
7	REFERENCES.....	140

LIST OF FIGURES

FIGURE 1: ILLUSTRATION OF THE KA-BAND AMPLIFIER CHARACTERISTICS..... 25

FIGURE 2: ILLUSTRATION OF FWD AND RTN CONSIDERED PHASE NOISE PROFILES... 26

FIGURE 3: AGGREGATED GAIN VARIATION..... 27

FIGURE 4: AGGREGATED GROUP DELAY..... 28

FIGURE 5: REFERENCE COORDINATE SYSTEM FOR THE LTV CHANNEL. 34

FIGURE 6: EQUIVALENT DESCRIPTIONS OF AN LTV CHANNEL. 36

FIGURE 7: NR UE STATES AND TRANSITIONS, [2]. 40

FIGURE 8: NR INITIAL ACCESS..... 41

FIGURE 9: TYPE OF NR SYSTEM INFORMATION BLOCKS AND RELATED CHANNELS ... 42

FIGURE 10: NR SSB STRUCTURE..... 43

FIGURE 11: FLOWCHART ILLUSTRATING THE ATTACHMENT PROCEDURE. 47

FIGURE 12: ONE SSB PER RANDOM ACCESS OCCASION..... 50

FIGURE 13: 2 SSBs PER RANDOM ACCESS OCCASION..... 51

FIGURE 14: ONE SSB IN 2 RANDOM ACCESS OCCASIONS 51

FIGURE 15: QUASI EARTH-FIXED BEAMS CONCEPT, WITH SATELLITE OVERALL FOOTPRINT MOVING OVER THE EARTH (THREE TIME INSTANTS SHOWN IN DIFFERENT COLOURS) ACCORDING TO THE SATELLITE PASS, BUT BEAM FOOTPRINT FIXED ON EARTH BY BEAM STEERING..... 51

FIGURE 16. 3GPP BEAM LAYOUT FOR LEO AT (0°,0°, 1300KM) WITH A HPBW 3.64°[4]... 52

FIGURE 17. LEFT: TARGET LAYOUT WITH UNIFORM FOOTPRINTS. RIGHT: DETAIL OF BEAM WIDENING OPERATION COMPARING TARGET FOOTPRINT (BLACK), REALISED FOOTPRINT (BLUE) AND NON-WIDENED FOOTPRINT (MAGENTA) 53

FIGURE 18. LEFT: BEAM FOOTPRINT LAYOUT SETTING A GRID ACCORDING TO THE BEAM RADIUS AT NADIR (MAXIMUM EIRP BEAMS). RIGHT: DETAIL OF BEAM WIDENING OPERATION FOR A COMPROMISE SOLUTION USING A MINIMUM BEAM RADIUS OF 64.6 KM. IT COMPARES THE TARGET FOOTPRINT (BLACK), REALISED FOOTPRINT (BLUE) AND NON-WIDENED FOOTPRINT (MAGENTA) 54

FIGURE 19: OBTAINED MEAN SNR AS A FUNCTION OF THE NUMBER OF SIMULTANEOUS BEAMS ILLUMINATED. 56

FIGURE 20: POLARIZATION MANAGEMENT: NON-OVERLAPPING CELLS..... 57

FIGURE 21: POLARIZATION MANAGEMENT: FULLY-OVERLAPPING CELLS. 58

FIGURE 22: POLARIZATION MANAGEMENT: DUAL -POLARIZED CELLS. 59

FIGURE 23: SSB MULTIPLEXING IN TIME DOMAIN. 59

FIGURE 24: BEAM SWEEPING BY SSB IN TERRESTRIAL DEPLOYMENTS..... 60

FIGURE 25: BEAM SWEEPING BY SSB IN NTN DEPLOYMENTS. 61

FIGURE 26: -3 DB BEAM CONTOURS WITH REDUCED GRID (BLUE); AND CIRCLE CORRESPONDING TO A MINIMUM ELEVATION ANGLE FOR USERS OF 30° (BLACK). 62

FIGURE 27: -3 DB BEAM CONTOURS OF BEAMS MAPPED TO SSB INDEX #0 FOR NINDEX=64 (LEFT) AND NINDEX=61 (RIGHT). 63

FIGURE 28: EXAMPLE OF INDEX MAPPING FOR NINDEX=61. 64

FIGURE 29: BEAM CENTERS MAPPED TO BLOCKS OF CONTIGUOUS SSB INDEXES FOR NINDEX=64 (LEFT) AND NINDEX=61 (RIGHT). 65

FIGURE 30: CDF OF THE SNR OBTAINED AT BEAM CENTERS FOR DIFFERENT BEAMFORMER STRATEGIES, WITH NINDEX=64..... 66

FIGURE 31: CDF OF THE SNR OBTAINED AT BEAM CENTERS FOR INDEPENDENT BEAMFORMERS EQUALIZING BEAM GAIN AND FOR DIFFERENT NINDEX VALUES FROM 32 TO 64..... 67

FIGURE 32: COMMON DELAY DETERMINATION AND BEAM SPECIFIC COMPENSATION.69

FIGURE 33: CONTOUR OF THE DIFFERENTIAL DOPPLER FREQUENCY SHIFT IN KHZ: A) ELEVATION ANGLE OF 30°, B) ELEVATION ANGLE OF 50°, C) ELEVATION ANGLE OF 70°, D) ELEVATION ANGLE OF 90°..... 71

FIGURE 34: PRE-COMPENSATION WITH AND WITHOUT MARGIN WHEN THE RTT IS OVERESTIMATED 75

FIGURE 35: THE DETECTION WINDOW FOR THE FRACTIONAL DELAY 75

FIGURE 36: THE DETECTION WINDOW FOR THE INTEGER DELAY. 77

FIGURE 37: MDP OVER SNR..... 78

FIGURE 38: FUNCTIONAL SPLIT OPTIONS AND BEAMFORMING ARCHITECTURE. 85

FIGURE 39: BEAMFORMING ARCHITECTURE WITH DBFM. 86

FIGURE 40: BEAMFORMING ARCHITECTURE WITH CBFM-OG (A) AND CBFM-OB (B). 86

FIGURE 41: HIGH-LEVEL RELATIONSHIP BETWEEN SCHEDULING AND REPORTING INTERVALS..... 88

FIGURE 42: UE POSITIONING ARCHITECTURE APPLICABLE TO NG-RAN, [96]. 89

FIGURE 43: LOCATION SERVICE SUPPORT IN 3GPP NR, [96]. 90

FIGURE 44: DBFM PROCEDURE - STEP 1..... 90

FIGURE 45: DBFM PROCEDURE - STEP 2..... 91

FIGURE 46: DBFM PROCEDURE - STEP 3..... 91

FIGURE 47: DBFM PROCEDURE - STEP 4..... 91

FIGURE 48: CBFM-OG PROCEDURE - STEP 1. 92

FIGURE 49: CBFM-OG PROCEDURE - STEP 2. 92

FIGURE 50: CBFM-OG PROCEDURE - STEP 3. 93

FIGURE 51: CBFM-OB PROCEDURE - STEP 1..... 93

FIGURE 52: CBFM-OB PROCEDURE - STEP 2..... 94

FIGURE 53: CBFM-OB PROCEDURE - STEP 3..... 94

FIGURE 54: AGING INTERVAL AND SATELLITE POSITION. 95

FIGURE 55: SERVICE AREA AND GROUND TRACK FOR USER-CENTRIC BEAMFORMING WITH LATS = 45°N, LONS = 5°E, ES = 30°, HSAT = 1000 KM..... 96

FIGURE 56: EXAMPLE OF VISIBLE USERS ACCORDING TO THE NTN NODE POSITION ON ITS ORBIT. 98

FIGURE 57: MINIMUM INTRA-SLOT DISTANCE WITH RS AND RS-MD, KDIST = 1, 2, ..., 7, RUV = 0.0316..... 108

FIGURE 58: RS-MD SCHEDULING EXAMPLE WITH DIFFERENT MINIMUM DISTANCE COEFFICIENTS..... 109

FIGURE 59: ASYMPTOTIC SPECTRAL EFFICIENCY AND CAPACITY WITH 10^{-3} UES/KM² IN CLEAR-SKY CONDITIONS. 111

FIGURE 60: ASYMPTOTIC SPECTRAL EFFICIENCY AND CAPACITY WITH $2 \cdot 10^{-3}$ UES/KM² IN CLEAR-SKY CONDITIONS..... 111

FIGURE 61: ASYMPTOTIC SPECTRAL EFFICIENCY AND CAPACITY WITH $4 \cdot 10^{-3}$ UES/KM² IN CLEAR-SKY CONDITIONS..... 112

FIGURE 62: AVERAGE EXPERIENCED CAPACITY IN CLEAR-SKY CONDITIONS..... 113

FIGURE 63: CDF OF THE NUMBER OF ALLOCATIONS PER USER, WITH 10^{-3} UES/KM² IN CLEAR-SKY CONDITIONS. 113

FIGURE 64: CDF OF THE NUMBER OF ALLOCATIONS PER USER, WITH $2 \cdot 10^{-3}$ UES/KM² IN CLEAR-SKY CONDITIONS. 114

FIGURE 65: CDF OF THE NUMBER OF ALLOCATIONS PER USER, WITH $4 \cdot 10^{-3}$ UES/KM² IN CLEAR-SKY CONDITIONS. 114

FIGURE 66: ASYMPTOTIC SPECTRAL EFFICIENCY AND CAPACITY WITH 10^{-3} UES/KM² IN LINE-OF-SIGHT SUB-URBAN CONDITIONS..... 115

FIGURE 67: ASYMPTOTIC SPECTRAL EFFICIENCY AND CAPACITY WITH $2 \cdot 10^{-3}$ UES/KM² IN LINE-OF-SIGHT SUB-URBAN CONDITIONS. 116

FIGURE 68: ASYMPTOTIC SPECTRAL EFFICIENCY AND CAPACITY WITH $4 \cdot 10^{-3}$ UES/KM² IN LINE-OF-SIGHT SUB-URBAN CONDITIONS. 116

FIGURE 69: AVERAGE EXPERIENCED CAPACITY IN LINE-OF-SIGHT SUB-URBAN CONDITIONS..... 117

FIGURE 70: LOSS IN THE ASYMPTOTIC CAPACITY IN LINE-OF-SIGHT SUB-URBAN COMPARED TO CLEAR-SKY. 118

FIGURE 71: EXAMPLE OF SEPARATE UNIFORM UES' DISTRIBUTIONS ON LAND AND SEA. 124

FIGURE 72: EXAMPLE OF POPULATION DATABASE FROM THE GHSL OF THE EC JRC, [98]. 125

FIGURE 73: EXAMPLE OF EXPONENTIALLY DECAYING TRAFFIC MODEL, $NHS = 5$, $C_{MIN} = 20$ MBPS, $C_{MAX} = 200$ MBPS, $\Delta C = 0.5$, 1 UE/KM²..... 126

FIGURE 74: EXAMPLE OF USERS' MOVEMENT OVER 2 MINUTES. 128

FIGURE 75: BLOCK DIAGRAM OF AN OTFS SYSTEM..... 132

FIGURE 76: EFFECT OF THE CHANNEL WITH $\Gamma(N,T) = A1\Delta(N - N1)\Delta(T - T1)$ ON THE GENERIC TRANSMITTED SYMBOL. THE ORIGINAL POSITION OF THE SYMBOL IS SHOWN ON THE LEFT. THE POSITION OF THE SAME SYMBOL AFTER THE CHANNEL IS SHOWN ON THE RIGHT. THE SHIFT HAS TO BE UNDERSTOOD AS A CIRCULAR SHIFT. 133

FIGURE 77: CDF OF EXPERIENCED DOPPLER SHIFTS. 134

FIGURE 78: OFDM TIME-FREQUENCY GRID. 135

FIGURE 79: CDF OF THE PRAGMATIC CAPACITY WITH USER-CENTRIC BEAMFORMING. 136

LIST OF TABLES

TABLE 1: 5G-STAR DUST SUB-CONSTELLATIONS AS DEFINED IN D3.2.....	22
TABLE 2: AM/AM AND AM/PM AMPLIFIER RESPONSE FOR A KA-BAND AMPLIFIER MODEL TYPE L-TWTA WITH ACTIVE ANTENNA [3].....	24
TABLE 3: SINGLE SIDEBAND AGGREGATED FWD PHASE NOISE PROFILE.....	25
TABLE 4: SINGLE SIDEBAND AGGREGATED RTN PHASE NOISE PROFILE.....	26
TABLE 5: GAIN FLATNESS AND GROUP DELAY PROFILES.	27
TABLE 6: LOS PROBABILITY AS A FUNCTION OF THE ELEVATION ANGLE, [5].....	29
TABLE 7: TROPOSPHERIC LOSSES AS PER TR 38.811, [5].	30
TABLE 8: SHADOWING STANDARD DEVIATION AND CLUTTER LOSS AS A FUNCTION OF THE ELEVATION ANGLE AND OPERATING BAND: DENSE URBAN SCENARIO, [5]. .	31
TABLE 9: SHADOWING STANDARD DEVIATION AND CLUTTER LOSS AS A FUNCTION OF THE ELEVATION ANGLE AND OPERATING BAND: URBAN SCENARIO, [5].....	31
TABLE 10: SHADOWING STANDARD DEVIATION AND CLUTTER LOSS AS A FUNCTION OF THE ELEVATION ANGLE AND OPERATING BAND: SUBURBAN/RURAL SCENARIO, [5].	32
TABLE 11: SUMMARY OF THE CONSIDERED CHANNEL MODELS.....	32
TABLE 12: SET OF PHYSICAL RESOURCES ASSIGNED TO CORESET#0.....	49
TABLE 13: SUMMARY OF BEAM DESIGN METHODS UNDER STUDY.....	54
TABLE 14: PARAMETERS FOR SNR CALCULATION.....	55
TABLE 15: PARAMETERS FOR SNR CALCULATION.....	66
TABLE 16: DOWNLINK CFO FOR LEO AT 1300 KM FOR DIFFERENT COMPENSATION SCHEMES IN KA-BAND.	70
TABLE 17: DIFFERENTIAL DOPPLER FREQUENCY SHIFT VALUES FOR DIFFERENT ELEVATION ANGLES.....	71
TABLE 18: UPLINK CFO FOR LEO 1300KM WITH PERFECT COMPENSATION IN KA-BAND.	73
TABLE 19: TOLERANCE TO TIME OFFSETS SUPPORTED BY PREAMBLE FORMATS B4 AND C2, [22]	74
TABLE 20: PRACH CONFIGURATION.	78
TABLE 21: SUMMARY OF BEAMFORMING ALGORITHMS WITH BFN ARCHITECTURE APPLICABILITY AND REQUIRED ANCILLARY INFORMATION.	81
TABLE 22: PROS AND CONS OF THE IDENTIFIED DBFN BEAMFORMING ALGORITHMS.	82
TABLE 23: AGING INTERVAL TERMS PER USER-CENTRIC BEAMFORMING ARCHITECTURE AND ALGORITHM.	95
TABLE 24: PARAMETERS FOR SYSTEM-LEVEL SIMULATIONS WITH A SINGLE NTN NODE.	110
TABLE 25: RECEIVER SPEED CHARACTERISTICS, [101].....	127
TABLE 26: PARAMETERS FOR LINK-LEVEL SIMULATIONS.....	134
TABLE 27: RESULTS OF LINK-LEVEL SIMULATIONS	137

ABBREVIATIONS

5GC	5G Core network
ABFN	Analog Beamforming Network
ACLR	Adjacent Channel Leakage Ratio
ACM	Adaptive Coding and Modulation
AF	Array Factor
AMF	Access and Mobility management Function
AoA	Angle of Arrival
AWGN	Additive White Gaussian Noise
BER	Bit Error Rate
BFN	Beamforming Network
BWP	Bandwidth Part
C-RNTI	Cell RNTI
CBF	Conventional Beamforming
CBFM	Centralised Beamforming Management
CBFM-OB	CBFM on-board
CBFM-OG	CBFM on-ground
CDF	Cumulative Distribution Function
CDL	Clustered Delay Line
CF-MIMO	Cell-Free MIMO
CFO	Carrier Frequency Offset
CFT	Continuous Fourier Transform
CI	Chebyshev Iteration
CIR	Carrier-to-Interference Ratio
CL	Clutter Loss
CoC	Channel coefficient of Correlation

CORESET	Control Resource SET
CP	Cyclic Prefix
CQI	Channel Quality Indicator
CRB	Cramer-Rao Bound
CSI	Channel State Information
CSI-RS	CSI Reference Signal
DA	Data Aided
DBFM	Distributed Beamforming Management
DBFN	Digital Beamforming Network
DCI	Downlink Control Information
DFT	Discrete Fourier Transform
DFT-s-OFDM	DFT spread OFDM
DL	Downlink
DM-RS	Demodulation Reference Signal
DPC	Dirty Paper Coding
DRA	Direct Radiating Array
DRX	Discontinuous Reception
EC	European Commission
ECB	Enhanced Normalized Conjugate
ECEF	Earth-Centered Earth-Fixed
EIRP	Effective Isotropically Radiated Power
ELSA	Enhanced Logarithmic Spiral Array
ESA	European Space Agency
FDD	Frequency Division Duplexing
FDOA	Frequency Difference of Arrival
FFR	Full Frequency Reuse
FoV	Field of View

FSL	Free Space Loss
FWD	Forward link
G-RRM	Graph-based RRM
GEO	Geostationary Earth Orbit
GHSL	Global Human Settlement Layer
GI	Guard Interval
GNSS	Global Navigation Satellite System
GSO	Geosynchronous Orbit
GW	Gateway
H-RRM	Heuristic RRM
HBFN	Hybrid Beamforming Network
HO	Handover
HPBW	Half Power Beam Width
HTS	High Throughput Satellite
IBO	Input Backoff
ICFT	Inverse CFT
INR	Interference-to-Noise Ratio
ISFFT	Inverse SFFT
ITU	International Telecommunication Union
ITU-R	ITU Radiocommunication sector
JRC	Joint Research Center
KPI	Key Performance Indicator
LB-MMSE	Location-Based MMSE
LCS	Location Service
LEO	Low Earth Orbit
LMF	Location Management Function
LOS	Line-of-Sight

LTV	Linear Time Variant
MAC	Medium Access Control
MADOC	Multiple Antenna Downlink Orthogonal Clustering
MB	Multi-Beam
MBS	Multicast Broadcast Service
MCS	Modulation and Coding Scheme
MDP	Missed Detection Probability
MF	Matched Filter
MIB	Master Information Block
MIMO	Multiple Input Multiple Output
MIQP	Mixed Integer Quadratic Programming
MMSE	Minimum Mean Square Error
ModCod	Modulation and Coding
MPC	Maximum Power Constraint
MU-MIMO	Multi-User MIMO
NE	Network Element
NGC	Next Generation Core
NI	Newton Iteration
NLOS	Non-LOS
NR	New Radio
NTN	Non-Terrestrial Network
O2I	Outdoor-to-Indoor
OBBF	On-Board Beamforming
OBBSC	On-Board Beamforming and Scheduling Computation
OFDM	Orthogonal Frequency Division Multiplexing
OGBF	On-Ground Beamforming
OGBSC	On-Ground Beamforming and Scheduling Computation

OSS	Operation Support Systems
OTFS	Orthogonal Time Frequency Space
PAC	Per Antenna Constraint
PAPR	Peak-to-Average Power Ratio
PBCH	Physical Broadcast Channel
PCI	Physical Cell ID
PDCCH	Physical Downlink Control Channel
PDSCH	Physical Downlink Shared Channel
PDU	Packet Data Unit
PER	Packet Error Rate
PHY	Physical Layer
PLMN	Public Land Mobile Network
PMI	Precoding Matrix Indicator
PRACH	Physical Random Access Channel
PRB	Physical Resource Block
PSD	Power Spectral Density
PSS	Primary Synchronisation Signal
PTRS	Phase Tracking Reference Signal
PUSCH	Physical Uplink Shared Channel
QoS	Quality of Service
RA	Random Access
RA-RNTI	RA RNTI
RAN	Radio Access Network
RAR	RA Response
RI	Rank Indicator
RNTI	Radio Network Temporary Identifier
RRC	Radio Resource Control

RRM	Radio Resource Management
RS	Random Scheduling
RS-MD	RS Minimum Distance
RSRP	Reference Signal Received Power
RTN	Return link
RTT	Round Trip Time
RZF	Regularised ZF
SatCom	Satellite Communications
SCS	Sub-Carrier Spacing
SDMA	Space Division Multiple Access
SF	Superframe
SFFT	Symplectic Finite Fourier Transform
SFN	System Frame Number
SI	System Information
SIB	System Information Block
SINR	Signal-to-Interference-plus-Noise Ratio
SLNR	Signal-to-Leakage-plus-Noise Ratio
SMUG	Sum Rate Maximization User Grouping
SNO	Satellite Network Operator
SNP	Sub-Node Point
SNR	Signal-to-Noise Ratio
SoA	State-of-the-Art
SPC	Sum Power Constraint
SRS	Sounding Reference Signal
SS-MMSE	Spatially Sampled MMSE
SSB	Synchronisation Signal Block
SSS	Secondary Synchronisation Signal

TA	Timing Advance
TAC	Tracking Area Code
TDD	Time Division Duplexing
TDL	Tapped Delay Line
TDMA	Time Division Multiple Access
TDOA	Time Difference of Arrival
TN	Terrestrial Network
TPE	Truncated Polynomial Expansion
TWTA	Travelling Wave Tube Amplifier
UE	User Equipment
UL	Uplink
UTSRP	Uplink Time Synchronisation Reference Point
VLEO	Very Low Earth Orbit
VSAT	Very Small Aperture Terminal
ZC	Zadoff-Chu
ZF	Zero Forcing

1 INTRODUCTION

This deliverable D4.3 reports the preliminary outcomes of Task 4.1 “Flexible and unified Air-Interface” and Task 4.2 “User-Centric and Digital Beamforming Solutions,”. Final results will be presented in a follow-up deliverable D4.6. This document is based on the inputs provided by WP3 and contained in deliverables D3.1, [1], and D3.2, [2]. More specifically, in this document, 5G-STARDUST investigates aspects related to the 3GPP NR Air Interface for NTN, including the waveform, and user-centric beamforming technologies. The enhancements that are needed in the 3GPP NTN to support the architecture defined in WP3 are addressed. Building upon this air interface, user-centric beamforming designs and Radio Resource Management (RRM) solutions are conceived. The potential modifications to be proposed for the 3GPP NTN standardisation are reported.

This document is organised as follows:

- Section 2 provides the general framework for the analyses discussed in this document, as well as those to be performed and reported in the final version, D4.6. In particular, also based on D3.1 and D3.2, the satellite orbit and parameters, the payload characteristics and hardware impairments, the satellite and user antenna models, and the channel models are extensively characterised.
- Section 3 focuses on the NTN initial access, *i.e.*, all the procedures that are needed to let a UE move from IDLE to CONNECTED state, and on the elements of the air interface that might need adaptations/enhancements. Two management steps have been addressed: i) the transmission of broadcast beams to deliver system and control information that is common to all users; and ii) the transmission of data beams to satisfy the traffic demand. The following standard topics are discussed: i) compensation schemes; ii) mapping between cells and beams; iii) SSB multiplexing and detection; iv) system information scheduling; v) polarization management; and vi) PRACH detection.
- Section 4 provides an extensive discussion on user-centric beamforming. Starting from the State-of-the-Art (SoA) of both beamforming and RRM algorithms, different architectures supporting beamforming are introduced, with the description of the role of each NE and the high-level functional procedures. The potential adaptations to the NTN specifications to support CSI or location-based beamforming are introduced. The initial numerical assessment provides interesting insights on the major performance trends and trade-offs, which allowed to define a clear path for the finalisation of the studies in D4.6.
- Section 5 provides an overview of the OFDM and OTFS waveforms and a link-level performance assessment of the user-centric beamforming solutions introduced in the previous section. The initial assessment already indicates performance results in line with those studied at system-level. The way forward will include
- Finally, Section 6 concludes this document.

2 FRAMEWORK DEFINITION

In this Section, we define the 5G-STAR DUST framework in which the activities related to waveform design (Task 4.1) and user-centric beamforming (Task 4.2) are performed. More specifically, based on the outcomes of WP3, we provide an overview of the most relevant system, orbit, and payload parameters, as well as the assumptions on the channel model and user antennas.

2.1 SYSTEM AND ORBIT PARAMETERS

The reference constellations derived in D3.2, [2], are assumed. The number of satellites is optimized to cover the target service areas. This led to following a typical design with 2 sub-constellations, tailored for the purpose of: i) ensuring worldwide coverage; and ii) satisfying higher demand over high user traffic density areas, typically between +/- 60° latitude.

In particular, unless otherwise stated, the evaluations will focus on the principal sub-constellation featuring 20 planes and 11 satellites per plane at 1300 km and an inclination of 50°. Moreover, it is assumed that each satellite covers a region corresponding to UEs seeing the satellite with a minimum elevation angle of 30°, which with the satellite at 1300 km translates to a FoV radius around 1500 km.

Table 1: 5G-STAR DUST sub-constellations as defined in D3.2.

Inclined orbit sub-constellation	Polar orbit sub-constellation
<ul style="list-style-type: none"> • Altitude: ~1300 km • Inclination: 50° • Number of planes: 20 • Number of satellites per plane: 11 	<ul style="list-style-type: none"> • Altitude: ~1000 km • Inclination: 99° • Number of planes: 6 • Number of satellites per plane: 13
	
<u>Inclined orbit - orbital view</u>	<u>Inclined orbit – orbital view</u>

2.2 SATELLITE PAYLOAD HARDWARE IMPAIRMENTS

The radio frequency block of the satellite payload generally degrades with increasing frequency. Particularly, the link performance at the Ka-band may be limited by some hardware impairments, such as the non-linear amplification and the phase noise.

2.2.1 Non-linear amplification

According to the satellite antenna model described in D3.2 [2], each radiating element has its own power amplifier. To compensate for the propagation losses and take maximum advantage of the amplifiers, it is desirable to operate as close as possible to their saturation point. However, the region that encloses the saturation point has a non-linear response. Hence, unless the input signal has a constant envelope, the output will be distorted. In such a case, especial attention must be paid to the out-of-band emission requirement, which is specified in terms of adjacent channel leakage ratio (ACLR). It is possible to avoid distortion and ease the fulfilment of the ACLR requirement by operating in the linear region of the amplifier. To do so, a large power input back off (IBO) may be needed to compensate the peak to average power ratio (PAPR) of the signal, but this could lead to a very significant power penalty. An alternative solution to large IBO insertion is the reduction of the signal PAPR. Another solution that is combined with the application of PAPR reduction techniques consists in implementing digital pre-distortion to linearize the response of the amplifier. The digital pre-distortion is a method that consists of modelling the behaviour of the power amplifier and then extracting its parameters to achieve a linear response. To be precise, upon applying digital pre-distortion, the power amplifier behaves like a peak limiter. In other words, signals below the saturation power pass unaffected. Otherwise, the peaks that exceed the saturation power are attenuated. Hence, the distortion that is inherent to the peak limiter cannot be removed with digital pre-distortion. Despite the interdependence between PAPR reduction and digital pre-distortion techniques, these two solutions are usually designed separately.

To study the non-linear amplification effects, it is necessary to characterize the amplitude-to-amplitude (AM/AM) and the amplitude-to-phase (AM/PM) distortions. In this regard, the signal at the output of the amplifier can be formulated as

$$y = F_a(u) e^{j(\arg(x) + F_p(u))} \quad (1)$$

where $x = u e^{j \arg(x)}$ is the input signal and $F_a(u)$ and $F_p(u)$, denote the AM/AM and the AM/PM functions, respectively. It is common to assume that the phase response can be pre-calculated and subtracted from the input signal, so that phase distortion is cancelled out. Although the phase distortion is usually negligible, the phase distortions will be addressed for completeness.

In general terms, the operating point of the amplifier is usually identified by the input and the output backoff:

$$P_{IBO} = 10 \log_{10} \frac{P_{0,IN}}{P_{IN}} \quad (2)$$

$$P_{OBO} = 10 \log_{10} \frac{P_{0,OUT}}{P_{OUT}} \quad (3)$$

Concerning the notation, P_{IN} is the mean power of the signal at the input of the amplifier, P_{OUT} is the mean power of the transmitted signal, $P_{0,OUT}$ is the maximum output power (saturation power), and $P_{0,IN}$ is the input power corresponding to the maximum output power.

In the following, the considered amplifier model is given in Table 2, [3]. Figure 1 illustrates the characteristics reported in this table.

Table 2: AM/AM and AM/PM amplifier response for a Ka-band amplifier model type L-TWTA with active antenna [3].

IBO (dB)	OBO dB	Phase [deg]
24,0000	19,4586	0,0000
23,0000	18,4133	0,0494
22,0000	17,4173	0,0472
21,0000	16,3591	0,0039
20,0000	15,3424	0,0360
19,0000	14,2954	0,1162
18,0000	13,2556	0,3809
17,0000	12,1685	0,6286
16,0000	11,0851	1,0183
15,0000	10,0238	1,7616
14,0000	8,9305	2,4184
13,0000	7,8286	3,0863
12,0000	6,7142	3,5320
11,0000	5,6247	3,9221
10,0000	4,5469	3,6716
9,0000	3,5644	3,3587
8,0000	2,6731	2,5310
7,0000	1,9102	1,2108
6,0000	1,2843	-0,2491
5,0000	0,7780	-1,7629
4,0000	0,4070	-3,3148
3,0000	0,1673	-5,0580
2,0000	0,0383	-6,3400
1,0000	-0,0060	-7,5836
0,0000	0,0000	-8,2804
-1,0000	0,0385	-8,7388
-2,0000	0,0874	-8,9858
-3,0000	0,1332	-9,0843
-4,0000	0,1723	-9,0998
-5,0000	0,2042	-9,1005
-6,0000	0,2292	-9,1417
-7,0000	0,2485	-9,2263
-8,0000	0,2636	-9,3428
-9,0000	0,2756	-9,4911
-10,0000	0,2854	-9,6615
-11,0000	0,2935	-9,7920
-12,0000	0,3002	-9,8313
-13,0000	0,3058	-9,8170
-14,0000	0,3101	-9,8128
-15,0000	0,3128	-9,8984
-16,0000	0,3135	-10,1349

Note:

- The amplifier saturation power is 70 W.
- The amplifier bandwidth is 2 GHz.

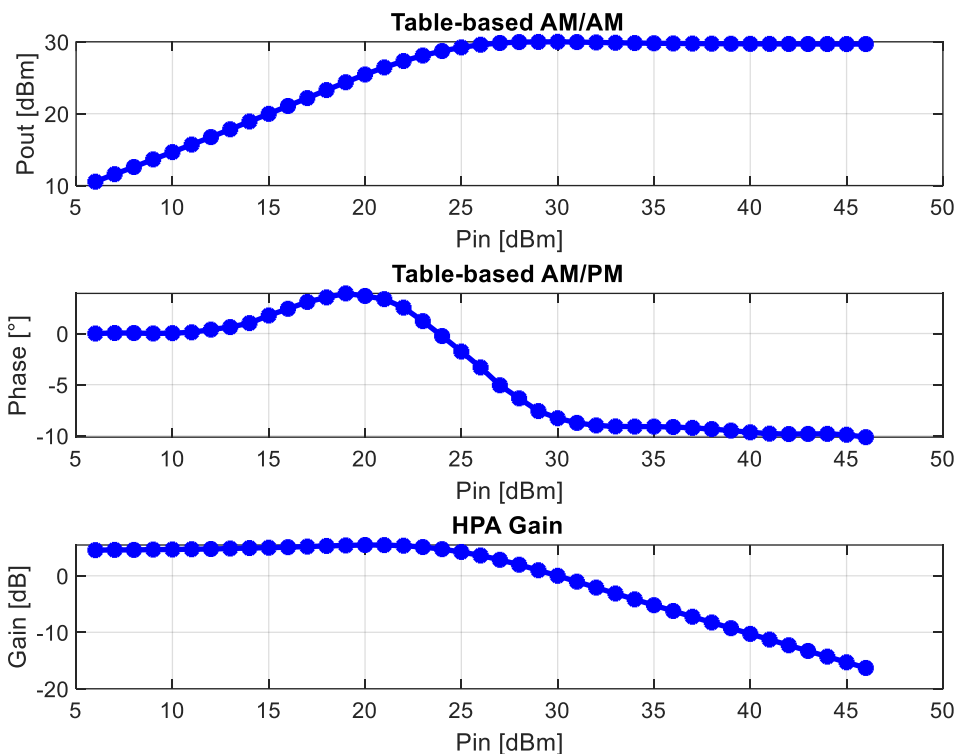


Figure 1: Illustration of the Ka-band amplifier characteristics.

2.2.2 Phase noise

The phase noise is a multiplicative phase term that is related to the instabilities of local oscillators, which are used as reference signals for time and frequency synchronizations. In the time domain, the phase noise is modelled like a phase fluctuation that varies over time. In the frequency domain, the phase noise is characterized by the power spectral density (PSD) of the phase fluctuation in dBc/Hz. Ideally, a local oscillator would produce a perfect sinusoidal signal, whose power spectrum is a delta function at the carrier frequency. However, in practical schemes, the power spreads around the desired frequency.

Adopting the profile proposed in [3], the PSD of the oscillator can be modelled as reported in Table 3 and Table 4, for the forward (FWD) and return (RTN) links, respectively. Figure 2 shows these profiles as a function of the frequency.

Table 3: Single sideband aggregated FWD phase noise profile.

Offset from Carrier Frequency	Forward link (dBc/Hz)
10 Hz	NA
100 Hz	[-25]
1 kHz	[-50]
10 kHz	[-73]
100 kHz	[-92]
1 MHz	[-102]
10 MHz	[-113]
100 MHz	[-116]

Table 4: Single sideband aggregated RTN phase noise profile.

Offset from Carrier Frequency	Return link (dBc/Hz)
10 Hz	[-36]
100 Hz	[-58]
1 kHz	[-69]
10 kHz	[-79]
100 kHz	[-87]
1 MHz	[-104]
10 MHz	[-109]
100 MHz	[-109]

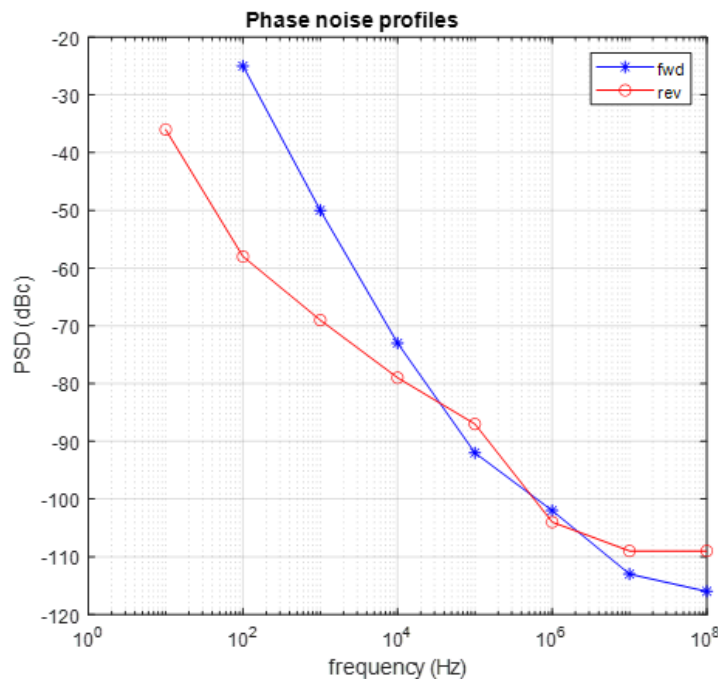


Figure 2: Illustration of FWD and RTN considered phase noise profiles.

2.2.3 Gain flatness and group delay

The channel filtering effects, introduced by several radio frequency and digital equipments through which the wanted signal passes, are modelled by a single equivalent filter which should be representative of the aggregated Gain Flatness and Group Delay (GF/GD) variations as seen by the receiver.

The considered end-to-end profile have been obtained from the aggregation of three type of profiles [1]: a slope, a parabola, and a ripple. These different types of profiles taking into account the contributions of the gateway, satellite payload and terminal are defined in Table 5.

The end-to-end gain response shall be derived as follows:

- A parabolic response, with minimum relative gain of -2.4dB at the edge of the channel.
- A sinusoidal ripple with 0.3 dB amplitude and 30 MHz period is added within 90% of the bandwidth.

- A smooth slope of -0.0085 dB/MHz within all the channel bandwidth.

The total response is the sum (in dB) of these contributions and displayed on Figure 3.

Table 5: Gain flatness and group delay profiles.

Profiles	Gain flatness profile	Group delay profile
Linear f_0 : channel center frequency	$GF = \frac{\Delta G}{\Delta F} * (f - f_0)$ [dB] $\frac{\Delta G}{\Delta F} = [0.25 \text{ dB/MHz}]$ (worst case local slope) $\frac{\Delta G}{\Delta F} = [-0.0085 \text{ dB/MHz}]$ (typical slope observed on channel bandwidth)	$GD = \frac{\Delta T}{\Delta F} * (f - f_0)$ [ns] $\frac{\Delta T}{\Delta F} = [2 \text{ ns/MHz}]$ (worst case local slope) $\frac{\Delta T}{\Delta F} = [0.0080 \text{ ns/MHz}]$ (typical slope observed on channel bandwidth)
Parabolic f_0 : channel center frequency B : channel bandwidth	$GF = 4\Delta G * (f - f_0)^2 / B^2$ [dB] $\Delta G = [2,4 \text{ dB}]$ for B=500 MHz	$GD = 4\Delta T * (f - f_0)^2 / B^2$ [ns] $\Delta T = [20 \text{ ns}]$ for B=500 MHz
Sinusoidal ripple Δf : ripple period f_0 : channel center frequency	$GF = \Delta G \cos(\frac{2\pi(f-f_0)}{\Delta f})$ [dB] within 90% of the band $\Delta G = [0.3 \text{ dB}]$ $\Delta f = 15 \text{ MHz}; 30 \text{ MHz}; 75 \text{ MHz}$	$GD = \Delta T \cos(\frac{2\pi(f-f_0)}{\Delta f})$ [ns] within 90% of the band $\Delta T = [1.5 \text{ ns}]$ $\Delta f = 15 \text{ MHz}; 30 \text{ MHz}; 75 \text{ MHz}$

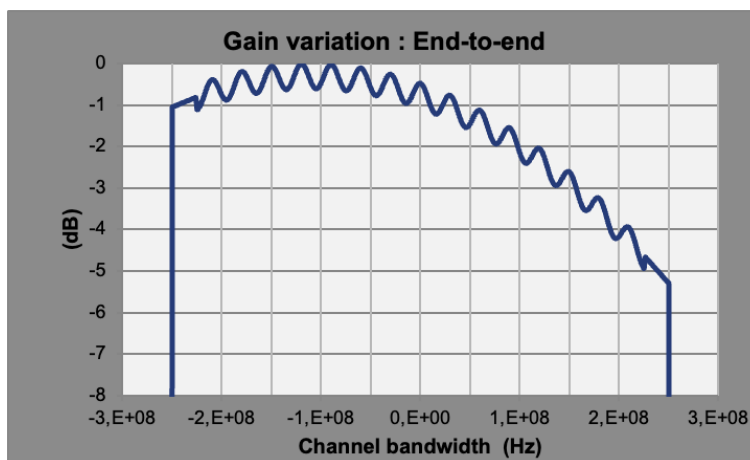


Figure 3: Aggregated gain variation.

The end-to-end group delay response is derived as follows:

- A parabolic response, with maximum value of 20 ns at the edge of the channel.
- A sinusoidal ripple with 1.5 ns amplitude and 30 MHz period is added within 90% of the bandwidth.
- A smooth slope of 0.0080 ns/MHz within all the channel bandwidth.

The total response is the addition (in ns) of these contributions and displayed on Figure 4.

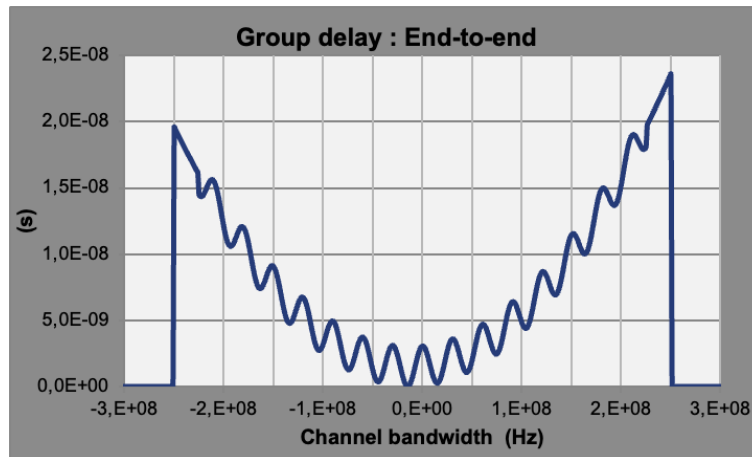


Figure 4: Aggregated group delay.

It has been assumed that these profiles can be considered representative for both FWD and RTN links. This is justified by the fact that the main GF/GD contributions are coming from the satellite payload.

2.3 SATELLITE AND USER TERMINAL ANTENNA PATTERNS

2.3.1 Satellite antenna pattern

This deliverable assumes the payload antenna model introduced in D3.2, featuring four apertures (TX-LHCP, TX-RHCP, RX-LHCP, RX-RHCP), each consisting of 512 radiating elements in an approximated circle shape with a Hexa-Deca structure, and inter-element spacing of 0.65λ . The resulting beam footprint at Nadir has a radius of approximately 41 km. The gain of each element is 4.7 dBi, their pattern can be modelled by a $\cos^2()$ function and each have an associated power amplifier of 65 mW. Moreover, we assume digital beamforming, so beamforming weights can be updated at OFDM symbol level. The resulting direct radiating array (DRA) has several degrees of freedom in the generation of beam layouts, so this functionality will be properly addressed in Section 3.2.1.

Provided that the bandwidth of the service link is divided into bandwidth parts (BWPs), each NTN beam can operate on a BWP. The bandwidth is not necessarily evenly split among beams. The settings can be adjusted according to the traffic demand. To efficiently serve on-ground users, the frequency is reused across the coverage area. The bandwidth allocation pattern is dictated by the frequency reuse scheme. By adopting a frequency reuse 3 or 4, a certain level of isolation is achieved between beams that share the same bandwidth part. Hence, inter-beam interference is usually treated as noise. In contrast in full frequency reuse schemes, all the NTN beams operate on the same frequency resources. Hence, the communication is interference-limited and the Signal-to-Interference-plus-Noise Ratio (SINR) regime of operation could be lower than 0 dB. Under these conditions, precoding schemes, beam hopping solutions or a combination of both need to be adopted to mitigate inter-beam interference. Owing to the satellite Effective Isotropic Radiated Power (EIRP) limitations, D3.2 estimated that only 24 simultaneous beams can be activated. If the hopping pattern is judiciously selected, full frequency reuse schemes can be adopted with negligible levels of co-channel interference. Section 3.2 will further discuss on these aspects but it is important to highlight that efficiently covering a region with 1500 km of radius with up to 24 beams having a beam footprint radius of just 41 km, represents one of the main challenges to be addressed.

2.3.2 UE antenna pattern

In FR2, as recommended by 3GPP for system level evaluations, [4]-[5], the normalized antenna pattern of a Very Small Aperture Terminal (VSAT) UE is:

$$G_{UE}(\theta) = \begin{cases} 4 \left| \frac{J_1(2\pi f_c d_A \sin\theta/c)}{2\pi f_c d_A \sin\theta/c} \right|^2 & \theta \neq 0 \\ 1 & \theta = 0 \end{cases} \quad (4)$$

where $J_1(\cdot)$ is the Bessel function of the first kind and first order with the argument, d_A is the antenna aperture radius, θ is the angle measured from the antenna boresight and c is the light propagation speed.

For handheld terminals, operating in FR1, an isotropic radiation pattern is considered.

2.4 CHANNEL MODEL

In this section, we describe the channel model that will be used for numerical evaluations. These will include both system-level (e.g., capacity and link budget) and link-level (e.g., Bit Error Rate (BER)) evaluations. As such, we describe the channel model for both of them.

2.4.1 System-level

2.4.1.1 3GPP NTN

The system-level channel model is largely inspired and aligned with the 3GPP specifications reported in TR 38.821, [4], and TR 38.811, [5]. In this model, different factors are taken into account depending on the elevation angle at which the UE sees the NTN node; in fact, as summarised in Table 6, a UE has a given probability of being in LOS conditions as a function of the elevation angle.

Table 6: LOS probability as a function of the elevation angle, [5].

Elevation [deg]	Dense urban	Urban	Suburban/rural
10°	28.2%	24.6%	78.2%
20°	33.1%	38.6%	86.9%
30°	39.8%	49.3%	91.9%
40°	46.8%	61.3%	92.9%
50°	53.7%	72.6%	93.5%
60°	61.2%	80.5%	94.0%
70°	73.8%	91.9%	94.9%
80°	82.0%	96.8%	95.2%
90°	98.1%	99.2%	99.8%

When the UE is in Non-LOS (NLOS) conditions, the overall path loss is computed as:

$$L = L^{(fs)} + L^{(sha)} + L^{(atm)} + L^{(sci)} + L^{(bui)} + L^{(cl)} \quad (5)$$

where the following terms are included:

- **Free Space Loss (FSL):**

$$L^{(fs)} = 32.45 + 20 \log_{10} f[\text{GHz}] + 20 \log_{10} d[\text{m}] \quad (6)$$

with $f[\text{GHz}]$ being the carrier frequency in [GHz] and $d[\text{m}]$ the slant range in [m]. The latter can be computed as a function of the elevation angle as:

$$d[\text{m}] = \sqrt{(h_{sat} + R_E)^2 - R_E^2 \cos^2 \varepsilon} - R_E \sin \varepsilon \quad (7)$$

In the above equation, $R_E = 6371$ km is the Earth's mean radius on the equatorial plane and ε the elevation angle.

- **Shadowing**, modelled as a log-normal random variable with zero mean and a variance denoted as σ_{sha}^2 , computed as a function of the elevation angle, propagation environment, and operating band (see Table 8-Table 10 below)

$$L^{(sha)}[\text{dB}] \sim \mathcal{N}(0, \sigma_{sha}^2) \quad (8)$$

- **Atmospheric losses** due to gaseous absorption, computed as per Annex 2 in ITU-R P.676, [6], assuming all UEs at ground level (for UEs above 10 km altitudes, it is neglected) and the mean annual global reference atmosphere as per ITU-R P.835, [7]. In particular, once the zenith atmospheric attenuation $A_{zenith}(f)$ has been computed for the considered frequency, the corresponding attenuation for the UE is given by:

$$L^{(atm)} = \frac{A_{zenith}(f)}{\sin \varepsilon} \quad (9)$$

- **Scintillation losses**, which can include either ionospheric or tropospheric effects depending on the carrier frequency. In particular:
 - In S-band, ionospheric scintillation is considered only for latitudes within $\pm 20^\circ$ and neglected in all other cases. When considered, it is fixed at $L^{(sci)} = 2.2$ dB.
 - In Ka-band, tropospheric losses are considered as a function of the elevation angle, as summarised in Table 7.

Table 7: Tropospheric losses as per TR 38.811, [5].

Elevation [deg]	Tropospheric loss [dB]
10°	1.08
20°	0.48
30°	0.30
40°	0.22
50°	0.17
60°	0.13
70°	0.12
80°	0.12
90°	0.12

- **Building entry loss** (or Outdoor-to-Indoor (O2I) loss): this term models the additional loss between the UE and the NTN node when the former is in indoor conditions. Considering the scope of the 5G-STAR DUST project and the use cases defined in WP2, this term is assumed to be zero, *i.e.*, outdoor conditions are always considered.
- **Clutter Loss** (CL), modelling the additional losses caused by obstructions on the propagation path. This term is only present in NLOS conditions and, as for the shadow fading, it is computed according to Table 8-Table 10.

Table 8: Shadowing standard deviation and clutter loss as a function of the elevation angle and operating band: Dense Urban scenario, [5].

Elevation [deg]	S-band			Ka-band		
	LOS	NLOS		LOS	NLOS	
	σ_{sha} [dB]	σ_{sha} [dB]	$L^{(cl)}$ [dB]	σ_{sha} [dB]	σ_{sha} [dB]	$L^{(cl)}$ [dB]
10°	3.5	15.5	34.3	2.9	17.1	44.3
20°	3.4	13.9	30.9	2.4	17.1	39.9
30°	2.9	12.4	29.0	2.7	15.6	37.5
40°	3.0	11.7	27.7	2.4	14.6	35.8
50°	3.1	10.6	26.8	2.4	14.2	34.6
60°	2.7	10.5	26.2	2.7	12.6	33.8
70°	2.5	10.1	25.8	2.6	12.1	33.3
80°	2.3	9.2	25.5	2.8	12.3	33.0
90°	1.2	9.2	25.5	0.6	12.3	32.9

Table 9: Shadowing standard deviation and clutter loss as a function of the elevation angle and operating band: Urban scenario, [5].

Elevation [deg]	S-band			Ka-band		
	LOS	NLOS		LOS	NLOS	
	σ_{sha} [dB]	σ_{sha} [dB]	$L^{(cl)}$ [dB]	σ_{sha} [dB]	σ_{sha} [dB]	$L^{(cl)}$ [dB]
10°	4	6	34.3	4	6	44.3
20°	4	6	30.9	4	6	39.9
30°	4	6	29.0	4	6	37.5
40°	4	6	27.7	4	6	35.8
50°	4	6	26.8	4	6	34.6
60°	4	6	26.2	4	6	33.8
70°	4	6	25.8	4	6	33.3
80°	4	6	25.5	4	6	33.0
90°	4	6	25.5	4	6	32.9

Table 10: Shadowing standard deviation and clutter loss as a function of the elevation angle and operating band: Suburban/Rural scenario, [5].

Elevation [deg]	S-band			Ka-band		
	LOS	NLOS		LOS	NLOS	
	σ_{sha} [dB]	σ_{sha} [dB]	$L^{(cl)}$ [dB]	σ_{sha} [dB]	σ_{sha} [dB]	$L^{(cl)}$ [dB]
10°	1.79	8.93	19.52	1.9	10.7	29.5
20°	1.14	9.08	18.17	1.6	10.0	24.6
30°	1.14	8.78	18.42	1.9	11.2	21.9
40°	0.92	10.25	18.28	2.3	11.6	20.0
50°	1.42	10.56	18.63	2.7	11.8	18.7
60°	1.56	10.74	17.68	3.1	10.8	17.8
70°	0.85	10.17	16.50	3.0	10.8	17.2
80°	0.72	11.52	16.30	3.6	10.8	16.9
90°	0.72	11.52	16.30	0.4	10.8	16.8

It is worthwhile mentioning that, in TR 38.811, a basic path loss term is defined, which includes the free space loss, shadowing, and clutter loss terms:

$$PL = L^{(fs)} + L^{(sha)} + L^{(cl)} \tag{10}$$

This term will be exploited in the next sections for the link-level models.

2.4.1.2 Channel types

In 3GPP NTN specifications, the channel model to be considered for system-level analyses and link budget calibration assumes UEs always in LOS conditions. The overall path loss is thus computed as in eq. (5), neglecting the clutter loss and building entry loss as explained in previous section.

Table 11: Summary of the considered channel models.

Channel	Equation	Additional losses				
		shadowing	atmospheric	scintillation	building entry	clutter loss
Clear-sky	$L^{(fs)}$					
LOS	$L^{(fs)} + L^{(sha)} + L^{(atm)} + L^{(sci)}$	X	X	X		
NLOS (low priority)	$L^{(fs)} + L^{(sha)} + L^{(atm)} + L^{(sci)} + L^{(cl)}$	X	X	X		X

In the 5G-STARUST project, the numerical evaluations will be performed under the same assumptions (in the following, we denote this channel as *LOS channel*). In addition, we will

also consider clear-sky conditions (denoted as *clear-sky channel*), in which the shadowing, atmospheric losses, and atmospheric losses are neglected. Numerical evaluations also taking into account UEs in NLOS conditions might be considered, but with a lower priority. In this case, the LOS or NLOS condition of a given UE is computed as per Table 6.

Table 11 summarises the system-level channel models and the corresponding terms considered hereafter.

2.4.1.3 Link budget computation

Once the channel model and the specific propagation environment have been defined, the link budget can be computed as:

$$CNR[\text{dB}] = EIRP[\text{dBW}] + \frac{G}{T}[\text{dB/K}] - \kappa \left[\frac{\text{dBW}}{\frac{\text{K}}{\text{Hz}}} \right] - L[\text{dB}] - L_{ad}[\text{dB}] + B[\text{dBHz}] \quad (11)$$

where: i) $EIRP[\text{dBW}]$ is the EIRP in [dBW] and $\frac{G}{T}$ is the receiver G/T in [dB/K]; ii) $\kappa = -228.6$ dBW/K/Hz is the Boltzmann's constant; iii) L is the path loss computed in eq. (5) according to Table 11; iv) L_{ad} models any additional loss that shall be taken into account; and v) B is the channel bandwidth in [dBHz].

2.4.1.4 Channel coefficients for system-level analysis

Based on the channel model described above, the channel coefficient between the generic n -th radiating element on-board and the generic i -th user on-ground can be written as:

$$h_{i,n} = \frac{g_{i,n}^{(tx)} g_{i,n}^{(rx)}}{\sqrt{L_{i,n}^{(lin)}} \sqrt{\kappa B_i T_i}} e^{-j\frac{2\pi}{\lambda} d_i} \quad (12)$$

where i) $g_{i,n}^{(tx)}$ and $g_{i,n}^{(rx)}$ represent the transmitting and receiving complex antenna patterns between the n -th element and the i -th UE, respectively, based on the models in Section 2.3; ii) $L_{i,n}^{(lin)}$ is the overall path loss computed as per eq. (5) and converted to linear scale; iii) $\kappa B_i T_i$ represents the thermal noise power, with B_i being the user bandwidth and T_i the equivalent noise temperature; and iv) $e^{-j\frac{2\pi}{\lambda} d_i}$ represents the phase shift due to the slant range d_i . It shall be noticed that, for the sake of clarity, the dependency of the above terms from time is not explicit included in the equation; however, all terms changing due to the users' or satellite's movement do depend on the time instant in which they are computed, *i.e.*, antenna patterns, path loss, and phase shift.

2.4.2 Link-level

This section describes the satellite channel model that is used for link-level simulations.

2.4.2.1 Linear time-variant model

We consider a linear time variant (LTV) channel, whose behaviour is fully described by its time-variant channel impulse response (CIR). The CIR depends on the environment, the deployment, the UE location and the position of the satellite. The local tangent plane with the origin in the UE position is used as a reference coordinate system. For the sake of the analytical tractability, it is assumed that the target UE is served by a single satellite. As Figure 5 shows,

the position of the serving satellite can be represented in spherical coordinates as $(r_{LOS}, \phi_{LOS}, \theta_{LOS})$.

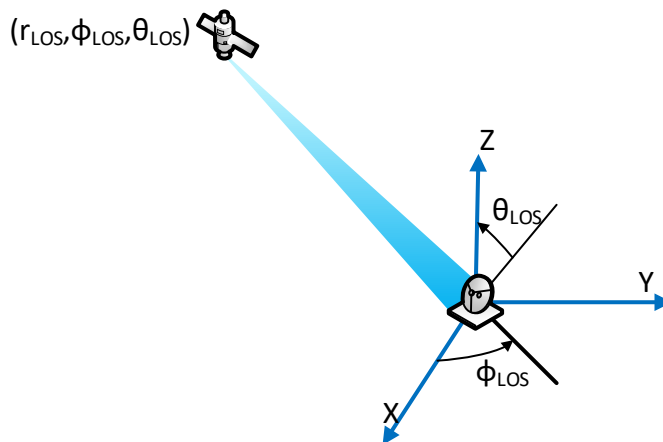


Figure 5: Reference coordinate system for the LTV channel.

At a given time instant, the received signal is represented by

$$y(t) = \int_{-\infty}^{\infty} h(t, \tau)x(t - \tau)\partial\tau + w(t) \quad (13)$$

where $w(t)$ denotes the noise that contaminates the reception and $x(t)$ the signal transmitted by the serving satellite. The CIR between the satellite and the UE is defined by $h(t, \tau)$. The discrete-time model can be expressed as

$$y[n] = \sum_m h[n, m]x[n - m] + w[n] \quad (14)$$

where $y[n], h[n, m], w[n]$ are respectively the sampled versions of $y(t), h(t, \tau), w(t)$.

Adopting the geometric-based stochastic model described in [8], the CIR can be formulated as

$$h(t, \tau) = \sum_{n=1}^N \sum_{m=1}^M a_{n,m} \delta(\tau - \tau_n) e^{j2\pi v_{n,m} t} \quad (15)$$

where N and M denote the number of clusters and the number of rays per cluster, respectively. Within the n -th cluster, $a_{n,m}$ is the complex amplitude and $v_{n,m}$ is the Carrier Frequency Offset (CFO) associated to the (n, m) -th path. The term τ_n corresponds to the n -th cluster delay. The channel model can be applied over time intervals where the scatters and the relative position of the UE and the satellite do not change significantly. The CFO is expressed as $v_{n,m} = v^{SAT} + v_{n,m}^{UE}$, where v^{SAT} and $v_{n,m}^{UE}$ denote respectively the Doppler frequency shifts due to the motion of the satellite and the UE. In alignment with satellite channels models available in the literature, the frequency shift due to the orbital motion is the same for all the paths [9]. An accurate Doppler model that is function of the orbital parameters can be found in [10].

To complete the model, the channel gain is formulated as:

$$a_{n,m} = \sqrt{\frac{G_T G_R(\phi_{n,m}, \theta_{n,m})}{PL K_B T B_W}} \rho_{n,m} \quad (16)$$

The channel depends on the complex-valued coefficient of the (n, m) -th path $\rho_{n,m}$, the satellite antenna gain measured from the bore sight of the antenna's serving beam G_T , the gain of the antenna terminal in the direction of the (n, m) -th path $G_R(\phi_{n,m}, \theta_{n,m})$, the basic path loss PL , the Boltzmann constant K_B , the bandwidth B_W and the system noise temperature T . The antenna patterns are provided in Section 2.3. All the paths are associated to the same satellite antenna gain G_T . The main reason lies in the fact that the angular spreads of departure are zero. The same assumption has been made in [5]. Since the differential slant range between paths is small, it follows that all the paths experience the same the path loss. The closed-form expression can be defined in dB as in equation (10).

When the satellite moves along the trajectory, the channel parameters $a_{n,m}, \nu_{n,m}, \tau_n$ vary over time. This effect can be taken into account by considering the following CIR:

$$h(t, \tau) = \sum_{n=1}^N \sum_{m=1}^M a_{n,m}(t) \delta(\tau - \tau_n(t)) e^{j2\pi \nu_{n,m}(t)t} \quad (17)$$

In the rest of this section, we will assume that the channel parameters vary slowly enough that they can be considered constant over the transmission time slot.

The CIR is not the only system function that fully describes the input-output behaviour of an LTV system. An equivalent description is provided by the so-called time-variant transfer function defined as:

$$H(t, f) = \text{CFT}_{\tau \rightarrow f}[h(t, \tau)] = \int_{-\infty}^{+\infty} h(t, \tau) e^{-j2\pi f \tau} d\tau \quad (18)$$

where $\text{CFT}_{\tau \rightarrow f}[\cdot]$ denotes the *continuous Fourier transform* (CFT) evaluated with respect to the variable τ and leading to an explicit dependence on the frequency variable f . From $H(t, f)$, $h(t, \tau)$ can be obtained through an *inverse continuous Fourier transform* (ICFT), i.e.,

$$h(t, \tau) = \text{ICFT}_{f \rightarrow \tau}[H(t, f)] \quad (19)$$

Other equivalent descriptions are the *delay-Doppler-spread function* $\gamma(\nu, \tau)$ and the *output Doppler-spread function* $\Gamma(\nu, f)$ defined as

$$\gamma(\nu, \tau) = \text{CFT}_{t \rightarrow \nu}[h(t, \tau)] \quad (20)$$

$$\Gamma(\nu, f) = \text{CFT}_{t \rightarrow \nu}[H(t, f)] \quad (21)$$

A pictorial representation of all these functions and their relationships is reported in Figure 6.

They can be used to grasp different physical characteristics of the channel. Let us consider for example the output Doppler-spread function $\Gamma(\nu, f)$. It can be easily shown that it allows to compute the Fourier transform $Y(f)$ of the output signal given the Fourier transform $X(f)$ of the input signal as:

$$Y(f) = \int_{-\infty}^{+\infty} X(\alpha) \Gamma(f - \alpha, \alpha) d\alpha \quad (22)$$

This equation can be used to illustrate the Doppler effect on the transmitted spectrum: when $X(f) = \delta(f - f_0)$, we obtain:

$$Y(f) = \Gamma(f - f_0, f_0) \tag{23}$$

By defining $\nu = f - f_0$, we have:

$$Y(f_0 + \nu) = \Gamma(\nu, f_0) \tag{24}$$

Thus, $\Gamma(\nu, f_0)$ fully expresses the spectral content of the output of an LTV system to a complex exponential with frequency f_0 . Unlike what happens in a Linear Time-Invariant (LTI) system, the output signal contains spectral components with $\nu \neq 0$. This means that there is a spread due to the Doppler effect.

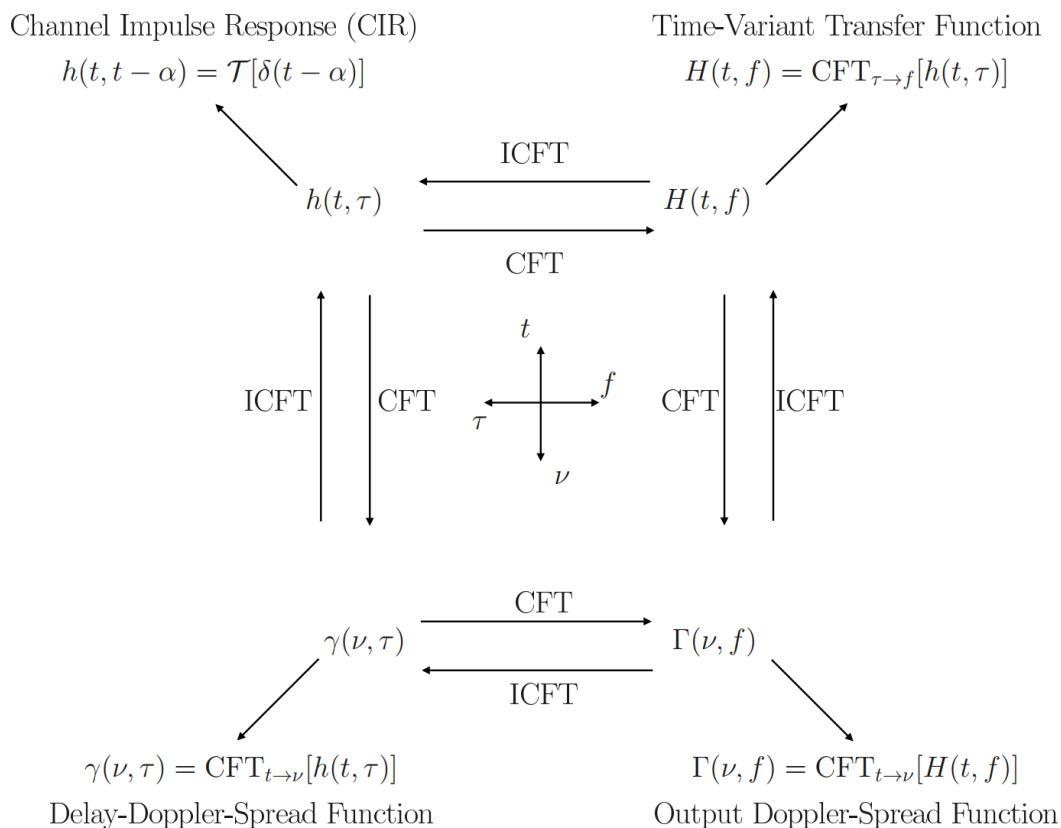


Figure 6: Equivalent descriptions of an LTV channel.

All these functions are defined over different two-dimensional domains. As an example, the domain of $H(t, f)$ is called *time-frequency* domain, whereas the domain of $\gamma(\nu, \tau)$ is called *Doppler-delay* domain. The OFDM modulation arranges the transmitted symbols on a rectangular grid in the time-frequency domain, with symbols associated to different equally spaced carriers (thus they are equally spaced in frequency) and multiple OFDM words transmitted over time.

By using an index p to identify the generic triplet, *i.e.*, by denoting $(a_p, \nu_p, \tau_p) = (a_{n,m}, \nu_{n,m}, \tau_n)$, we can write:

$$h(t, \tau) = \sum_{p=1}^P a_p \delta(\tau - \tau_p) e^{j2\pi v_p t} \quad (25)$$

$$H(t, f) = \sum_{p=1}^P a_p e^{j2\pi v_p t} e^{-j2\pi f \tau_p} \quad (26)$$

$$\gamma(v, \tau) = \sum_{p=1}^P a_p \delta(\tau - \tau_p) \delta(v - v_p) \quad (28)$$

$$\Gamma(v, f) = \sum_{p=1}^P a_p \delta(v - v_p) e^{-j2\pi f \tau_p} \quad (29)$$

Although these four descriptions of an LTV channel are equivalent from the mathematical point of view, they have a different impact, for example, from the channel estimation point of view. In addition, considering only one of the four domains (the time-delay domain, the time-frequency domain, the Doppler-delay domain, or the Doppler-frequency domain) can be convenient from the detection point of view. As an example, the estimation of the samples of the CIR can be very hard when the Doppler values are significant (and thus the channel varies in a fast way). On the other hand, working in the Doppler-delay domain can be very convenient since $\gamma(v, \tau)$ is the sparser representation of the channel and can be assumed to vary in a very slow way. In particular, in the Doppler-delay domain, in order to estimate the channel, we have to estimate P triplets (a_p, v_p, τ_p) and, considering that P is typically small, in the Doppler-delay domain the amount of interference is minimized. The multicarrier modulation format denoted as Orthogonal Time Frequency Space (OTFS) modulation is based on the idea to transmit the symbols in the Doppler-delay domain and will be described in Section 5.1.2.

2.4.2.2 3GPP technical multipath models

The 3GPP technical documentation, namely TR 38.811 and TR 38.821, specifies the NTN cluster-delay line (CDL) and tapped-delay line (TDL) models for link-level simulations and related calibration. The more general CDL model takes into account departure and arrival angles (azimuth and zenith, AOA, AOD, ZOA, ZOD, and related spreads) between transmitter and user, whereas the TDL model is tailored for isotropic antennas at 50° elevation angle.

Table 7: NTN-CLD-A.

Cluster #	Norm. delay	Power [dB]	AOD [°]	AOA [°]	ZOA [°]	ZOD [°]
2	1.0811	-4.675	0	-115.7	140	22.9
3	2.8416	-6.482	0	111.5	140	127.4
Per-cluster Parameters						
Parameter	C _{ASD} [°]	C _{ASA} [°]	C _{ZSD} [°]	C _{ZSA} [°]	XPR [dB]	
Value	0	15	0	7	10	

Table 8: NTN-CLD-B.

Cluster #	Norm. delay	Power [dB]	AOD [°]	AOA [°]	ZOA [°]	ZOD [°]
1	0	0	0	-174.6	140	42.2
2	0.7249	-1.973	0	144.9	140	63.4
3	0.7410	-4.332	0	-119.8	140	89.7
4	5.7392	-11.914	0	-88.8	140	174.1
Per-cluster Parameters						

Parameter	C _{ASD} [°]	C _{ASA} [°]	C _{ZSD} [°]	C _{ZSA} [°]	XPR [dB]
Value	0	15	0	7	10

For these models, tables are provided, where power, delays, angles, etc. are specified for four different kind of scenarios, namely for LOS, NLOS propagation conditions and S and Ka frequency bands (A, B, C, D). Doppler shift and rate should be added to these models according to the specific geometrical scenario, case by case.

Table 9: NTN-CLD-C.

Cluster #	Cluster PAS	Norm. delay	Power [dB]	AOD [°]	AOA [°]	ZOA [°]	ZOD [°]
1	LOS	0	-0.394	0	-180	140	40
	Laplacian	0	-10.618	0	-180	140	40
2	Laplacian	14.8124	-23.373	0	-75.9	140	87.1
	Per-cluster Parameters						
Parameter	C _{ASD} [°]	C _{ASA} [°]	C _{ZSD} [°]	C _{ZSA} [°]	XPR [dB]		
Value	0	11	0	7	16		

Table 10: NTN-CLD-D.

Cluster #	Cluster PAS	Norm. delay	Power [dB]	AOD [°]	AOA [°]	ZOA [°]	ZOD [°]
1	LOS	0	-0.284	0	-180	140	40
	Laplacian	0	-11.991	0	-180	140	40
2	Laplacian	0.5596	9.887	0	-135.4	140	146.2
3	Laplacian	7.3340	-16.771	0	-121.5	140	136.0
Per-cluster Parameters							
Parameter	C _{ASD} [°]	C _{ASA} [°]	C _{ZSD} [°]	C _{ZSA} [°]	XPR [dB]		
Value	0	11	0	7	6		

Table 11: NTN-TLD-A.

Tap #	Normalized delay	Power [dB]	Fading distr.
1	0	0	Rayleigh
2	1.0811	-4.675	Rayleigh
3	2.8416	-6.482	Rayleigh

Table 12: NTN-TLD-B.

Tap #	Normalized delay	Power [dB]	Fading distr.
1	0	0	Rayleigh
2	0.7249	-1.973	Rayleigh
3	0.7410	-4.332	Rayleigh
4	5.7392	-11.914	Rayleigh

Table 13: NTN-TLD-C.

Tap #	Normalized delay	Power [dB]	Fading distr.
1	0	-0.394	LOS
	0	-10.618	Rayleigh
2	14.8124	-23.373	Rayleigh
NOTE: first tap is Ricean with K-factor=10.224 dB and mean power 0			

Table 14: NTN-TLD-D.

Tap #	Normalized delay	Power [dB]	Fading distr.
1	0	-0.284	LOS
	0	-11.991	Rayleigh
2	0.5596	-9.887	Rayleigh
3	7.3340	-16.771	Rayleigh
NOTE: first tap is Ricean with K-factor=11.707 dB and mean power 0			

3 NTN INITIAL ACCESS

This section describes the NTN initial access procedure that is specified in Release 17. Interestingly, some decisions and configurations are left to the implementation, namely:

- Mapping between cells and beams;
- Synchronisation Signal Block (SSB) multiplexing;
- System information scheduling;
- Polarization management;
- SSB detection;
- PRACH detection.

This observation highlights that there is not a unified solution that works for all networks, but rather depends on the specific characteristics of the deployment. In this regard, the recommendations reported in [4] offer a wide range of possibilities. Some factors that come into play include the Doppler compensation scheme, the frequency reuse scheme, the beam layout, the beam illumination pattern, the system and the orbital parameters as well as the impairments of the satellite channel, to mention a few. Upon describing the PHY and MAC procedures that are involved in the standardized NTN initial access, this section tailors the practical implementation according to the framework definition outlined in Section 2.

3.1 RELEASE 17 NTN INITIAL ACCESS

Figure 7 shows the states in which a NR UE can be and the corresponding transitions. As reported in 3GPP TS 38.331, [11], a UE is either in RRC_CONNECTED or in RRC_INACTIVE state when a Radio Resource Control (RRC) connection has been established; if no RRC connection has been established, then the UE is in the RRC_IDLE state. For the scope of this document, we focus on the initial access procedure, *i.e.*, the procedure that moves the UE from the idle state to the connected state.

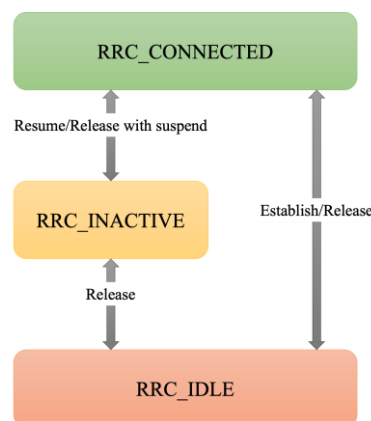


Figure 7: NR UE states and transitions, [2].

In general, in RRC_IDLE, the UE can monitor several paging channels, perform neighbouring cell measurements and cell (re-)selection, acquire system information and send information

requests, perform idle/inactive measurements, and acquire Multicast Broadcast Service (MBS) information (if configured for this type of service).

The initial access procedure with which the UE moves from RRC_IDLE to RRC_CONNECTED is depicted in Figure 8. To access an NR network, a UE needs to carry out initial access functionality which includes cell search and random access. To enable the UE to acquire DL time and frequency synchronization, an SS consisting of the primary SS (PSS) and the secondary SS (SSS) is periodically transmitted in the DL of each cell. After synchronization, the UE can decode the physical broadcast channel (PBCH) which carries the master information block (MIB) that the UE needs to decode in order to receive the remaining system information broadcast by the network. In NR, the PSS, SSS, and PBCH are jointly referred to as SS block (SSB) which occupies 20 resource blocks. It shall be noticed that, in this document, we focus on the operations performed between the UE and the gNB, while this procedure also requires interactions with some 5GC functions that are not discussed below.

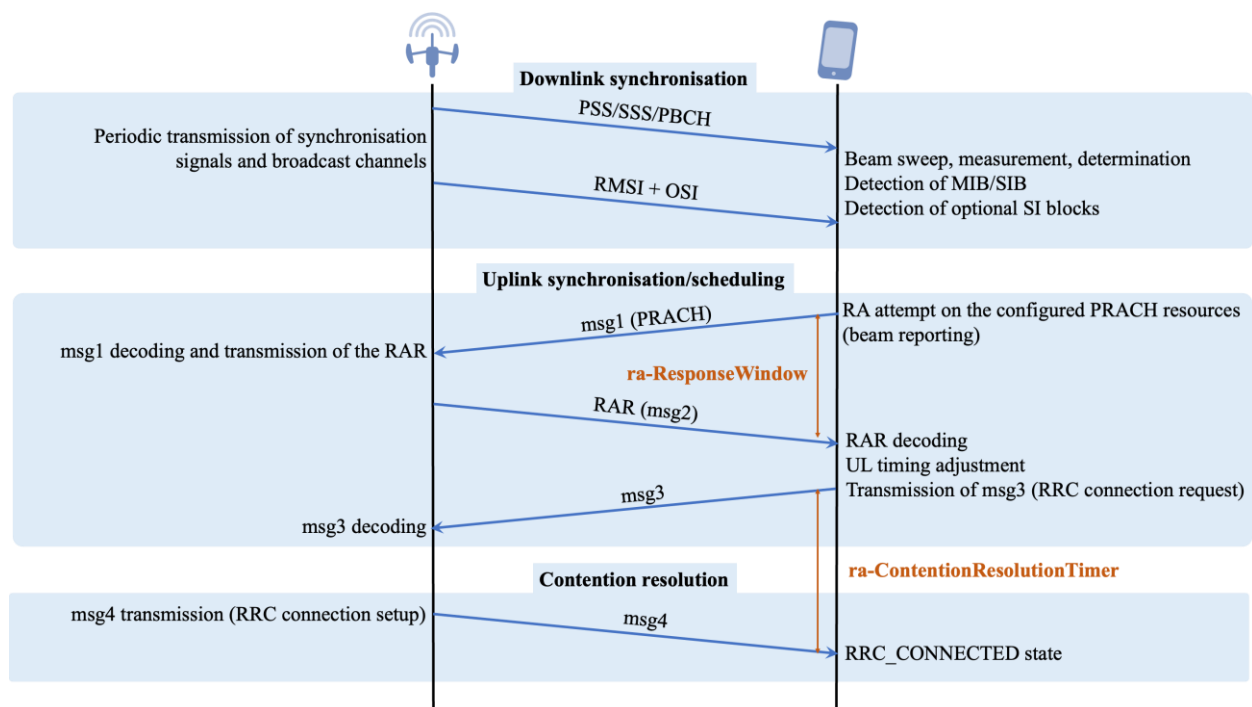


Figure 8: NR Initial Access.

The downlink synchronisation procedure (or Cell Search) is performed by the UE to acquire time and frequency downlink synchronisation within a cell and to detect the Physical Cell ID (PCI). To acquire such synchronisation, the UE exploits the System Information (SI) blocks (SIB) provided by the gNB that encompasses a set of synchronisation signals and broadcast channels. The different types of SIBs are depicted in Figure 9 together with the corresponding transmission channel, as defined in [12]-[13]:

The Master Information Block (MIB) and SIB1 are mandatory as they contain the required information to perform the initial access introduced above:

- the MIB is periodically (80 ms periodicity, with repetitions within such 80 ms as specified in TS 38.212, [14], scheduled according to the periodicity of the SSB broadcasted on the Physical Broadcast Channel (PBCH) and it provides the System Frame Number (SFN), Sub-Carrier Spacing (SCS), the resources on which SIB1 is transmitted, and cell-barred information (*i.e.*, if the cell is barred);

- after decoding the PBCH, the UE can move forward to decode the SIB1 which contains the system information that the UE needs to know before accessing the network. For example, SIB1 contains information about random access configuration that the UE needs in order to carry out random access procedure. Since the SSB has an associated SIB1 transmission, it is referred to as cell-defining SSB. The SIB1 is periodically (160 ms periodicity, with repetitions within such 160 ms with a default value of 20 ms as specified in TS 38.213, [15]¹) broadcasted on the Physical Downlink Shared Channel (PDSCH), on the resources indicated by the MIB. In addition, the SIB1 can also be sent on-demand to a specific UE (unicast transmission) on the PDSCH, but this is only applicable to a UE that is already in RRC_CONNECTED. SIB1 provides the scheduling of the other information blocks, cell selection information, the Public Land Mobile Network (PLMN) identity, the Tracking Area Code (TAC), PCI, RAN notification information, and serving cell information.

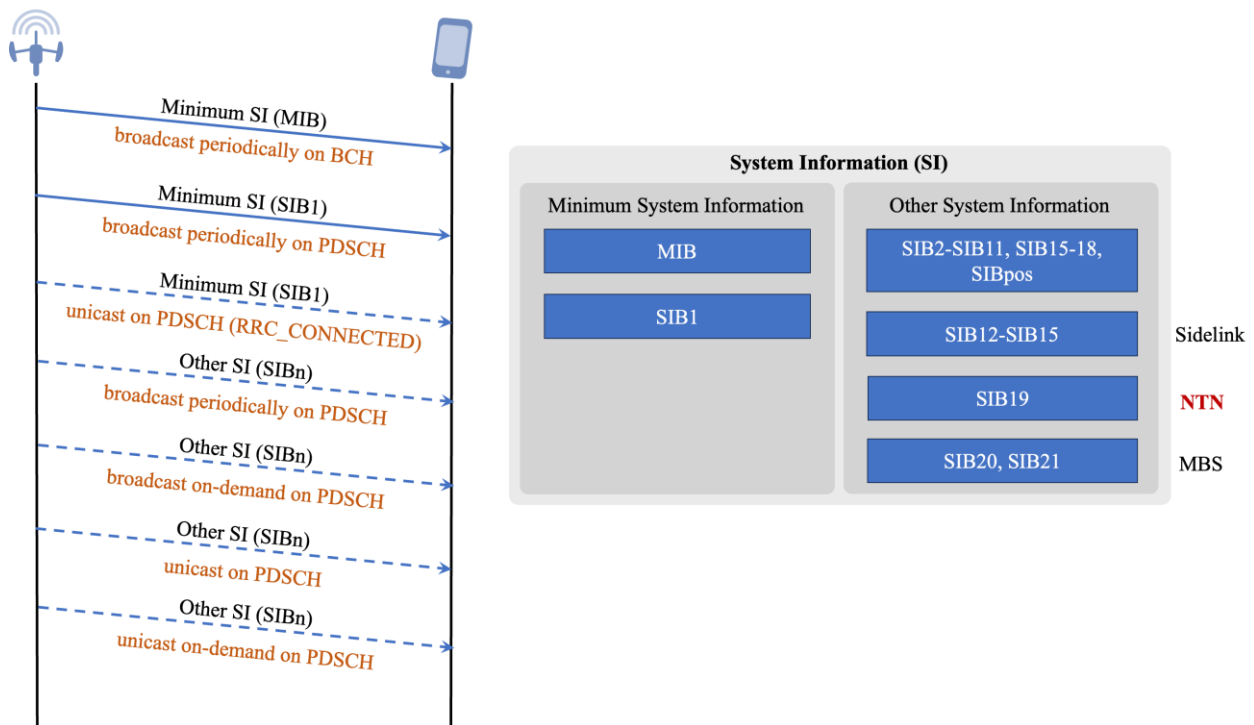


Figure 9: Type of NR System Information blocks and related channels

The other SI blocks can be broadcasted periodically or on demand, sent in unicast, or sent in unicast on-demand on the PDSCH. There are many SIB types in this category, but SIB19 has been specifically introduced in Rel. 17 for NTN and it provides, [11]:

- **distanceThresh**: distance from the serving cell reference location, used in location-based measurement initiation in RRC_IDLE and RRC_INACTIVE, as defined in TS 38.304, [16]. Each step in TS 38.331 represents 50 m and it can range from 0 to 65525 (*i.e.*, from 0 km to 3276.25 km);
- **ntn-Config**: parameters needed for the UE to access NR via NTN, such as ephemeris data, common Timing Advance parameters, *k_offset*, validity duration for UL synchronisation information and epoch;

¹ The actual transmission repetition periodicity is up to network implementation, [8].

- **referenceLocation**: reference location of the serving cell provided via NTN quasi-Earth fixed system, used in location-based measurement initiation in RRC_IDLE and RRC_INACTIVE, as defined in TS 38.304, [16];
- **t-Service**: time information on when a cell provided via NTN quasi-Earth fixed system is going to stop serving the area that it is currently covering. The field indicates a time in multiples of 10 ms after 00:00:00 on Gregorian calendar date 1 January, 1900 (midnight between Sunday, December 31, 1899 and Monday, January 1, 1900). The exact stop time is between the time indicated by the value of this field minus 1 and the time indicated by the value of this field. The maximum value of this field is 549755813887;
- **ntn-NeighCellConfigList**, **ntn-NeighCellConfigListExt**: list of NTN neighbouring cells including their **ntn-Config**, carrier frequency and PCI.

All SIBs, except SIB1 and SIBpos, are associated to a given SI window and the SI windows of different SI messages do not overlap. As such, within a given SI window, only the corresponding SI message can be transmitted and in such window the specific SI message can be repeated multiple times. The mapping of SIBs to SI messages is defined in TS 38.331 with the parameters **schedulingInfoList** and **schedulingInfoList2**.

3.1.1 Downlink synchronisation (Cell Search)

The Cell Search procedure is used by the UE to acquire the time and frequency synchronisation in the cell and to detect the PCI. To this aim, the SSB is exploited (Figure 10):

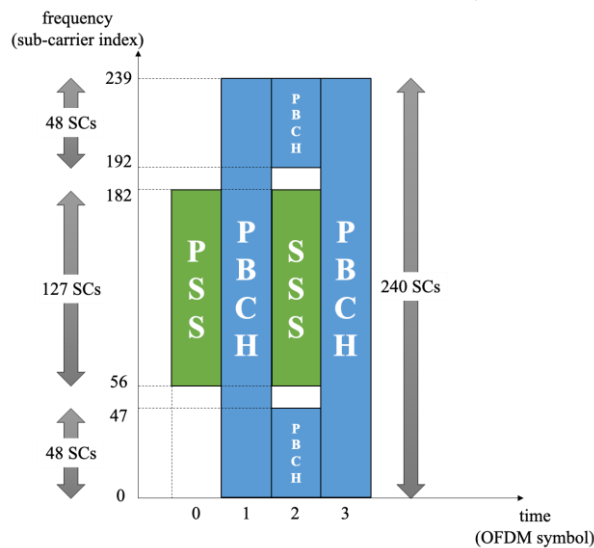


Figure 10: NR SSB structure

- **Primary Synchronisation Signal (PSS)**: used for the detection of the initial symbol boundary, Cyclic Prefix (CP), sub-frame boundary, and initial frequency synchronisation to the cell; it consists of one out of 3 possible known m-sequences BPSK modulated.
- **Secondary Synchronisation Signal (SSS)**: used for the identification of the radio frame boundary and of the PCI; it is one out of 336 sequences (together with the PSS, there are thus $3 \cdot 336 = 1008$ PCIs), obtained as the combination of two BSPK modulated m-sequences.

- Physical Broadcast Channel (PBCH): it contains the MIB, which provides also information on how to detect the SIB1, as previously mentioned. To decode the MIB, the Demodulation Reference Signal (DM-RS) is decoded, based on the PCI detected from the combination of PSS and SSS; this allows the UE to estimate the channel coefficients and exploit such information for the decoding of the MIB. Once the MIB is decoded, information on where the SIB1 is transmitted (and how to decode it) is available at the UE. The SIB1 provides the final information on the cell and where to find other SIs in case they are needed (such as SIB19 for NTN). Once the SIB1 and the SIB19 have been successfully decoded, the cell search procedure can be considered as concluded.

It shall be noticed that each SSB corresponds to a specific beam (this is how the UE performs the initial beam sweep), beamformed in a different direction. A group of SSBs forms a SS burst that always spans 5 ms; depending on the numerology of the transmission scheme, *i.e.*, the SCS value, a different duration of the OFDM symbols is possible, leading to a maximum number of beams that can be managed:

- FR1 up to 3 GHz: 4 SSBs per burst;
- FR1 between 3 and 7.125 GHz: 8 SSBs per burst;
- FR2: 64 SSBs per burst.

It shall also be mentioned that, as an outcome of the NTN study phase, 3GPP concluded that no enhancements were needed for the SSB to support its detection in NTN scenarios. During the NTN normative phase, it was agreed that: i) DL frequency compensation on the service link is not performed at the gNB, while it is left for implementation at the UE; and ii) any frequency compensation on the feeder link or management of transponder frequency errors is operated at the gateway, thus left for system implementation.

3.1.2 Random Access procedure

Once the UE has decoded all the SI messages, it can initiate the RA procedure, which begins with the acquisition of the uplink synchronisation, [17]-[18]. The RA procedure can be:

- triggered for initial access to move from RRC_IDLE to RRC_CONNECTED (contention-based RA);
- triggered by other events, *e.g.*, handover or beam failure recovery (contention-free RA).

In the following, we focus on the more general case of contention-based RA (which is shown in Figure 8).

From the completion of the Cell Search procedure, the UE can obtain the RA parameters, including the RA format type and time/frequency resources of the RA occasions. The RA procedure is initiated with the transmission of a RA preamble denoted as msg1, consisting of a Zadoff-Chu (ZC) sequence, on the PRACH. The RA preamble is associated with a RA Radio Network Temporary Identifier (RA-RNTI) computed based on the time/frequency location of the transmitted msg1 [15].

Once the msg1 has been transmitted, the UE starts monitoring the PDCCH for the RA Response (RAR, or msg2), *i.e.*, for the response of the gNB to its initial request to be recognised based on the RA-RNTI (the RAR carries Downlink Control Information, DCI, scrambled with the RA-RNTI). This time window is controlled by the higher layer parameter **ra-ResponseWindow**, which starts at a predefined time interval after the transmission of msg1 [15]. In case no RAR is received by the UE within the RAR window, it is assumed that the RA

procedure failed and a new attempt can be made (if possible based on the maximum number of RA attempts that can be performed). The RAR window is one of the timing parameters that required adaptations in NTN compared to Terrestrial Networks (TNs), due to the larger propagation delay. In particular, the start of the **ra-ResponseWindow** in NTN is delayed by an additional offset corresponding to the estimated UE-gNB Round Trip Time (RTT); the estimated RTT is computed as $T_{TA} + k_{mac}$, where T_{TA} is the Timing Advance (TA) applied by the UE and k_{mac} is defined in the **ntn-Config** field of SIB19 (in case it is not provided, it is set to 0). It shall be mentioned that the transmission of msg1 implicitly informs the gNB on the beam selected by the UE (beam determination and reporting); as previously mentioned, the identification of the best serving beam is based on the Reference Signal Received Power (RSRP) of the PSS and SSS for RRC_IDLE terminals. For RRC_CONNECTED terminals, the identification of the best serving beam is based on the CSI-RS on the downlink and on the Sounding Reference Signal (SRS) on the uplink.

Decoding the RAR (msg2) allows the UE to define the resources to be used for msg3 on the Physical Uplink Shared Channel (PUSCH), whether it shall use transform precoding for msg3 or not, and the TA command for timing adjustment.

Using the PUSCH resources indicated in the RAR, the UE sends a msg3 to the gNB. Prior to Rel. 17, assuming that msg2 was received ending in slot n , the PUSCH slot for msg3 was defined as $n + k_2 + \Delta$, with k_2 being a number of slots defined in the DCI based on the PUSCH numerology and Δ defined in TS 38.214, [18], e.g., 2 slots for 15 kHz SCS and 3 slots for 30 kHz SCS. For NTN access, to accommodate the larger propagation delays, the start slot for msg3 is computed as $+k_2 + \Delta + 2^\mu K_{cell,offset}$, where μ is the SCS numerology and $K_{cell,offset}$ is provided by the parameter **cellSpecificKoffset** within the **ntn-Config** field of SIB19 (maximum 1023 slots).

Once msg3 has been transmitted, the UE starts another timer, denoted as **ra-ContentionResolutionTimer**, and start monitoring the PDSCH for msg4. The maximum value of **ra-ContentionResolutionTimer** defined for TNs is sufficient to accommodate the large RTT over NTN channels; however, in order to reduce the power consumption of the UE, the behaviour of the contention resolution timer has been modified in Rel. 17 NTN so as to start with a delay equal to $T_{TA} + k_{mac}$.

After processing msg3, the gNB sends msg4 to the UE, finalising the contention resolution step. This message contains the UE's identity, confirming that the gNB has correctly identified the UE, and that potential contentions have been resolved. At this step, the network assigns to the UE a Cell RNTI (C-RNTI).

3.1.3 Doppler pre-compensation

As mentioned above, during the NTN normative phase it was agreed to not pre-compensate for the service link Doppler shift at the gNB, but rather to have such operation in the UE. More specifically, Rel. 17 specifies that before any uplink transmission in RRC_IDLE or RRC_INACTIVE, i.e., before the RA procedure, the Doppler on the service link shall be pre-compensated.

The pre-compensation is performed by exploiting the UE location information, obtained from the equipped GNSS, and the satellite velocity provided obtained from the ephemeris information in SIB19. It shall be mentioned that NTN compliant UEs must support uplink time/frequency pre-compensation and the enhanced timing relationships (such as those for the RA procedure); such support shall be indicated in the **uplinkPreCompensation-r17** as part of the UE capabilities.

3.1.4 Timing Advance

To perform the uplink timing pre-compensation, the UE is again assisted by GNSS capabilities, which is the baseline assumption for 5G NTN terminals. The TA value that shall be applied for the transmission of msg1 is given by:

$$T_{TA} = T_C (N_{TA} + N_{TA,offset} + N_{TA,adj}^{common} + N_{TA,adj}^{UE}) \quad (30)$$

where:

- N_{TA} and $N_{TA,offset}$ are the parameters defined for TNs in TS 38.213 and TS 38.211;
- $N_{TA,adj}^{common}$ is a parameter controlled by the network, which includes any timing offset that is considered to be relevant for pre-compensation (e.g. feeder link delay). It is derived from the higher layer parameters **ta-Common**, **ta-CommonDrift**, and **ta-CommonDriftVariation** in TS 38.331 and, in case they are not specified, it is set to 0. A scenario in which it is set to 0 is that of a regenerative payload, with the Uplink Time Synchronisation Reference Point (UTSRP) located on-board, as it does not require any feeder link compensation;
- $N_{TA,adj}^{UE}$ is a parameter estimated by the UE to pre-compensate the delay on the service link, computed by exploiting the GNSS acquired location and the satellite ephemeris provided in SIB19;
- $T_C = 1/(480000 \cdot 4096)$ s is the basic time unit in the specifications.

The value of N_{TA} is updated in a closed-loop approach through msg2 or MAC TA commands, while $N_{TA,adj}^{common}$ and $N_{TA,adj}^{UE}$ are updated by the UE via open-loop control as specified in TS 38.213.

3.1.5 Summary

As a summary, the compounding steps that are required to complete the initial access are briefly described in the following:

1. Broadcast transmission: gNB periodically transmits SSBs and SI signals on the initial BWP with a predefined pattern across time, frequency and space dimensions;
2. Beam sweeping: UE searches the SSB of the serving beam, with respect to azimuth, elevation, frequency and time, on the initial BWP;
3. Beam determination: The transmit and receive beam pairs where the SSB has been detected are stored. The UE estimates the angle of arrival (AoA) as well as the serving beam by selecting the best beam pair based on the RSRP measurement. The selected beam pair is associated to an SSB index;
4. Mapping: The UE determines the PCID and generates a mapping between the detected SSB and the satellite communication parameters. These parameters include the common subcarrier spacing and the resources of the COntrol REsource SET 0 (CORESET#0), which allows the UE to demodulate the frame containing the detected SSB;
5. Preparation to access the system: UE reads SIB1, which carries important information to perform the random access procedure;

6. Pre-compensation: UE reads the SIB19, which is used together with the GNSS information to pre-compensate the RTT and the Doppler frequency shift of the satellite service link;
7. Preamble transmission: UE transmits the PRACH signal in the direction of the serving beam in the random access occasion associated to the detected SSB;
8. Random access response: the gNB generates the RAR that is intended to each detected user. The RAR conveys the identity of the detected preamble, a (TA value, an initial uplink resource grant for transmission of the step 3 message, and an assignment of a temporary identifier;
9. Connection request: the UE monitors the PDCCH to detect the corresponding RA-RNTI while the random access response window is running. If the RA-RNTI matches with the identifier carried out by the RAR, the UE performs an uplink timing adjustment and sends a connection request in the PUSCH;
10. Contention resolution: every correctly decoded connection request is acknowledged by the gNB in the connection setup message.

The flowchart of the procedure described in this section is depicted in Figure 11.

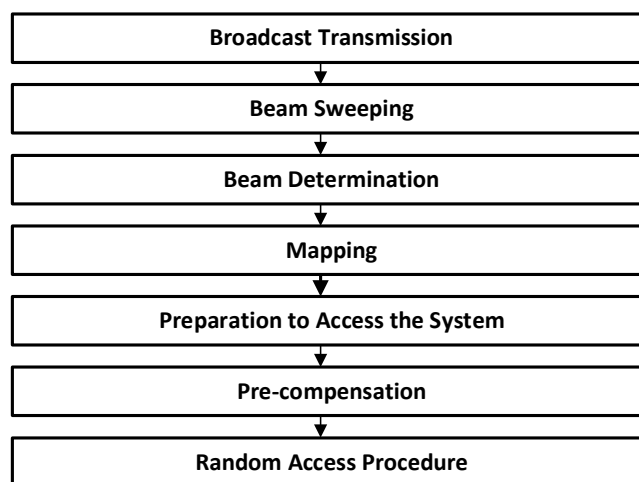


Figure 11: Flowchart illustrating the attachment procedure.

3.2 FROM STANDARD TO IMPLEMENTATION

All the aspects that are left to the implementation but have an impact on the attachment procedure in NTN are hereinafter analysed.

3.2.1 Management of satellite beams

Beam management is the term used by 3GPP to define the procedures that permit aligning transmit and receive antenna beams when directional antennas are used. In NTN, beam management at the UE side translates to traditional satellite acquisition and tracking operations. At the satellite side, beam management procedures go far beyond identifying the beam in which a given user is located. It should address the mapping of satellite beams, frequencies, and polarizations to 5G cells for an efficient use of resources. These topics have been discussed in Release 17, but no agreement was reached, so they were left open for implementations of each manufacturer/operator. Therefore, the efficient management of

satellite beams is still an open problem, which becomes fundamental in an EIRP limited system like the one targeted by 5G-STAR DUST, where each satellite covers a large region on Earth with a radius on the order of 1500 km (*i.e.*, user elevation angle above 30° from a satellite at 1300 km of altitude), with a very limited number of beams (*i.e.*, 24) with a beam footprint radius at Nadir of only 41 km. This section addresses this topic, analysing different alternatives and describing their corresponding trade-off.

Let us remark that 5G-STAR DUST targets user centric beamforming solutions for data transmission. As a consequence, two different beam management stages are envisaged:

- The transmission of broadcast beams to deliver system and control information that is common to all users.
- The transmission of data beams based on user centric solutions for dedicated data and control information.

Data transmission will be discussed in more detail in Section 4 and 5. For broadcast signalling, the figure of merit is to minimize the number of broadcast beams, *i.e.*, the number of time/frequency resources required to cover the whole coverage area of a single satellite. This section focuses on this area of research, starting with an overview description broadcast signalling and multiple access.

3.2.1.1 Broadcast signalling

In the downlink, the need to cover the satellite FoV applies to: SSB, SIB1, other SIBs, paging and msg2/msg4 during the random access procedure.

SSB

The SSB is used by the UE to acquire the downlink synchronisation and to detect the PCI. The SSB is confined within a 5 ms window and the default periodicity is 20 ms. The SSB frequency position depends on the operating band, which is specified in [15]. A more thorough SSB description has been provided in Section 3.1.1.

SIB1

The SIB1 is the first broadcast message, which transmits cell-specific information. Hence, the SIB1 is essential for proper network operation. The SIB1 is mapped into a PDCCH and is transmitted in the time and frequency resources specified by the CORESET#0. Upon decoding the MIB, the UE can use the tables predefined in [15] to determine:

- The number of RBs and OFDM symbols that are assigned to CORESET#0;
- PDCCH common search space, meaning the system frame number and slot index that the UE needs to monitor.

Table 12 provides some configurations for different SSB and PDCCH subcarrier spacing.

The transmission repetition periodicity of SIB1 is up to network implementation. The minimum value is 20ms, which coincides with the SSB period. Another important configuration parameter that is worth analysing is the multiplexing pattern, which specifies the location of the CORESET#0 with respect to the SSB. The pattern 1 refers to time domain multiplexing. As a consequence, the SIB1 and the SSB could be transmitted in different time slots. To reduce the number of broadcast beams it is mandatory to allocate the SSB and the SIB1 in the same time slot. This is allowed by patterns 2 and 3.

Table 12: Set of physical resources assigned to CORESET#0.

SSB SCS (KHz)	PDCCH SCS (KHz)	(Multiplexing pattern, number of RBs, Number of symbols)
240	120	(1,48,1), (1,48,2), (2,24,1), (2,48,1)
240	60	(1,96,1), (1,96,2)
120	120	(1,24,2), (1,48,1), (1,48,2), (3,24,2), (3,48,2)
120	60	(1,48,1), (1,48,2), (1,48,3), (1,96,1), (1,96,2), (2,48,1), (2,96,1)

OTHER SIBS

The information regarding the availability, the scheduling, and the search space of other SIBs, *i.e.*, SIB2 and beyond, is conveyed by SIB1. Other SIBs can be periodically broadcasted or transmitted on on-demand.

PAGING

The paging messages are sent from the gNB to the UE in idle mode in order to initiate UE terminated calls. In idle mode, the gNB does not know the exact position/beam in which the user is located so paging messages are transmitted in a tracking area basis, to ensure they reach the target user. From SIB1 the UE will extract the search space, which determines the physical resources that shall be monitored for incoming paging messages.

MSG2 AND MSG4

Upon detecting msg1 in the selected time-frequency resources, the gNB generates a response called msg2. At this stage, all UEs requesting access shall monitor the PDCCH to receive the corresponding response message. If UE successfully decodes the PDCCH, it gets the random access response data, which carries critical information such as the time advance command for timing adjustment and an initial uplink grant for the UE. The gNB also assigns a temporary identifier, the RA-RNTI, to the UE.

Using the initial uplink grant provided in msg2, the UE transmits msg3 on the PUSCH to request connection. After processing msg3, the gNB sends msg4 to the UE. msg4 is the contention resolution message that contains the UE's identity, confirming that the gNB has correctly identified the UE. At this step, the network provides the UE with a C-RNTI.

The search space that is dedicated to transmitting msg2 and msg4 during the random access procedure is explicitly configured by SIB1.

Impact on the standard: In idle mode the user typically performs discontinuous reception (DRX) to receive both SSB and paging messages. For this the UE must monitor the PDCCH during paging occasions, which are linked to a specific search space. In this sense, it is convenient to consider that this search space is the same as the one for SIB 1, and to consider also a co-scheduling of SSB blocks and paging messages. This is advantageous to reduce the number of broadcast beams, so that more resources are available for data beams. Furthermore, in the same slot, the UE is able to perform SSB measurements for cell reselection

or reception of system information and check for incoming paging messages. This is enabled by the multiplexing patterns 2 and 3. However, it is worth highlighting these patterns are only specified for SSB signals that are generated with a subcarrier spacing of 120 KHz. To increase the resilience of the initial cell search procedure to Doppler effects, which are prominent in LEO satellite systems, one option is to increase the subcarrier spacing to 240 KHz. To this end, additional configurations for patterns 2 and 3 supporting SSB subcarrier spacings of 240 KHz shall be added to [15].

3.2.1.2 Multiple access

In the uplink, the need to cover the FoV applies to the multiple access mode. More precisely, for reception of msg1 during the random access procedure.

MSG1

The msg1 is transmitted in the initial access of the random access procedure to access the network. To this end, the UE uses a set of configured random access resources. This information is conveyed in SIB1. The configuration of RACH transmission parameters are described in [15], which include the preamble format and the time and frequency resources of random access occasions. A specific mapping between the SSB and the random occasion is specified in the standard so that the network can figure out which SSB beam is selected by the UE, [15]. The mapping indicates:

- How many RA occasions are allocated in frequency domain at the same time location.
- How many SSBs can be mapped into one random access occasion and how many preamble index can be mapped to single SSB.

The standard supports one-to-one, one-to-many and many-to-one association between the SSB and the random access occasion. Some examples are depicted in Figure 12, Figure 13 and Figure 14.

Recommendation: When multiple SSBs are mapped into one random access occasion, as in Figure 13, the preamble sets associated to different SSB index could be reused. In such a case, if the bundle of SSBs that share the random access occasion are transmitted with a sufficient angle separation, then it follows that the serving beam for each detected UE can be unambiguously determined. The mapping rule that is implemented shall enable the reuse of preamble sets among SSBs.

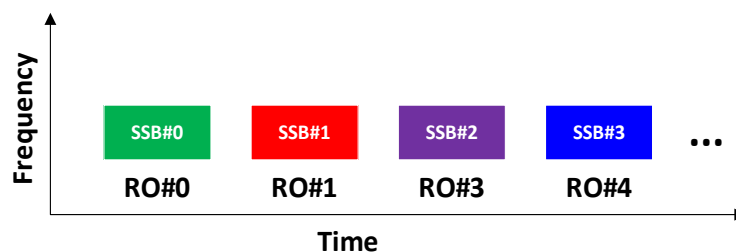


Figure 12: One SSB per random access occasion.

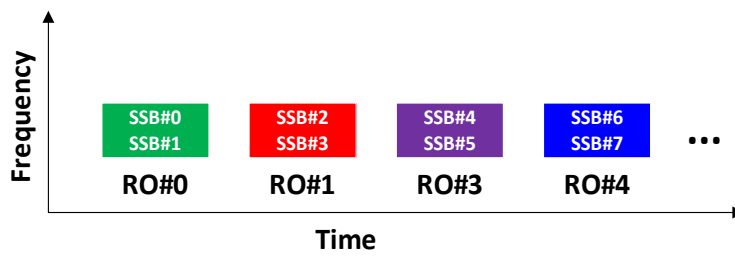


Figure 13: 2 SSBs per random access occasion.

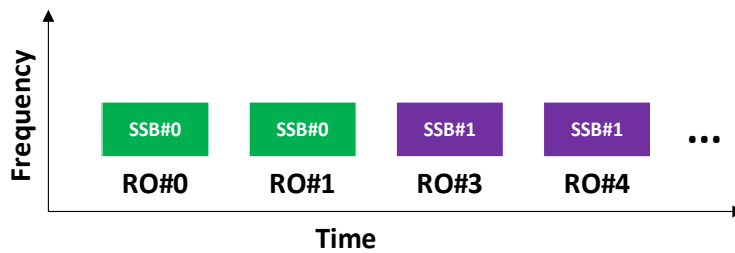


Figure 14: One SSB in 2 random access occasions

3.2.1.3 Quasi Earth-fixed beams

3GPP considers two types of satellite beams for LEO constellations. Earth-moving beams are fixed on the satellite and move over the Earth surface as the satellite passes above. They require frequent beam switching, every few seconds, and frequent intra-satellite hand-overs in the case of having multiple cells mapped in the satellite field of view (even for static users, due to the satellite/beam movement). To solve this issue and resemble terrestrial cells, in which handover/beam switching is only triggered by moving users, 3GPP considered Quasi Earth-fixed beams. In this case, the beams are static on ground for a given period of time, enabled by the use of steerable antennas at the satellites. This is the preferred choice of 5G-STARDUST, as specified in deliverable D3.2. A concrete implementation has been not defined in 3GPP, different alternatives are discussed in the following.

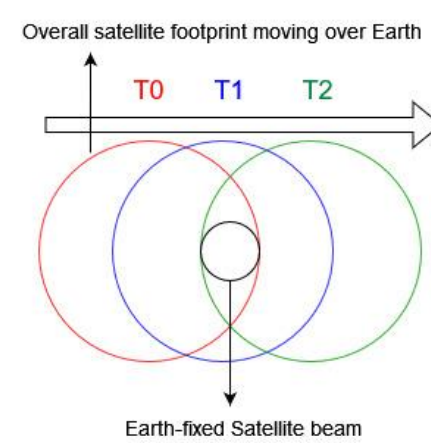


Figure 15: Quasi Earth-fixed beams concept, with satellite overall footprint moving over the Earth (three time instants shown in different colours) according to the satellite pass, but beam footprint fixed on Earth by beam steering.

First, it is important to highlight that, for Quasi Earth-fixed beams, it is considered that the overall satellite footprint moves over the Earth as in the case of Earth-moving beams, but once a region equivalent to a beam footprint enters in the satellite FoV, it is served by the same satellite beam until it leaves the FoV on the other end [19], as sketched in Figure 15. In this way, a fixed user is served by the same satellite beam/cell across the whole satellite pass.

From a system level point of view, it is preferred to have a single global grid of beam footprints fixed on Earth (and covering the whole Earth) and shared among all satellites. In this way, the satellites start serving a given position on the grid as soon as it enters on the satellite FoV, keeps serving it with the same satellite beam during the satellite pass and stops serving it as soon as it falls outside the FoV. Moreover, sharing the grid between all satellites facilitates satellite coordination when the FoV of more than one satellite overlap, since the interference can be easily predicted if the satellites point to known grid positions. The challenge here is how to create the grid of footprints given that the footprints at FoV edge are widely expanded with respect to those close to Nadir, due to the large FoV and the Earth curvature. This is shown in Figure 16, which depicts the beam layout (beam contours at -3dB) suggested by the 3GPP [4] for a satellite at $(0^\circ, 0^\circ, 1300\text{Km})$, considering a minimum user elevation angle of 30° (black circle) and the 5G-STAR DUST downlink antenna, which provides a mean half power beam width (HPBW) of 3.64° . The mean value is used since due to the slightly cross shape, [2], the antenna provides slightly different HPBW in different azimuth angles. Note that the 3GPP beam layout considers a hexagonal grid in the u-v plane with spacing between beams of $ABS = \sqrt{3} \sin(\text{HPBW}/2)$.

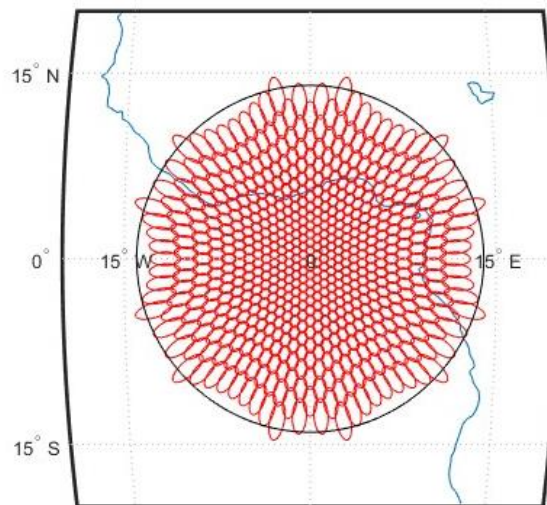


Figure 16. 3GPP beam layout for LEO at $(0^\circ, 0^\circ, 1300\text{Km})$ with a HPBW 3.64° [4]

The resulting beam layout in Figure 16 cannot be directly used for Earth-fixed operation since it does not provide a uniform beam grid on Earth. Indeed, the resulting grid depends on the satellite position, with a denser beam distribution at positions closer to satellite Nadir. Therefore, we next propose three alternatives to synthesize a uniform grid of beams on Earth.

UNIFORM BEAMS

From the system level point of view, it would be desirable to have uniform footprint shapes within the whole coverage area, so that beam footprints and inter-beam interferences can be predicted regardless of the satellite position. The only way to achieve this is to take as a reference the largest semi-axis of the ellipsoidal footprint at coverage edges and widen each beam to realise a circular footprint with that reference diameter. In Figure 17 on the left the

resulting beam footprint layout is depicted, featuring 169 beams with a radius of 129 km. Figure 17 the right shows an example of the beam widening operation for the beams at azimuth=0°. Let us remark that beams at cell edge still need to be widened in the tangential dimension whereas the rest of beams need to be widened in both dimensions (*i.e.* radial and tangential)

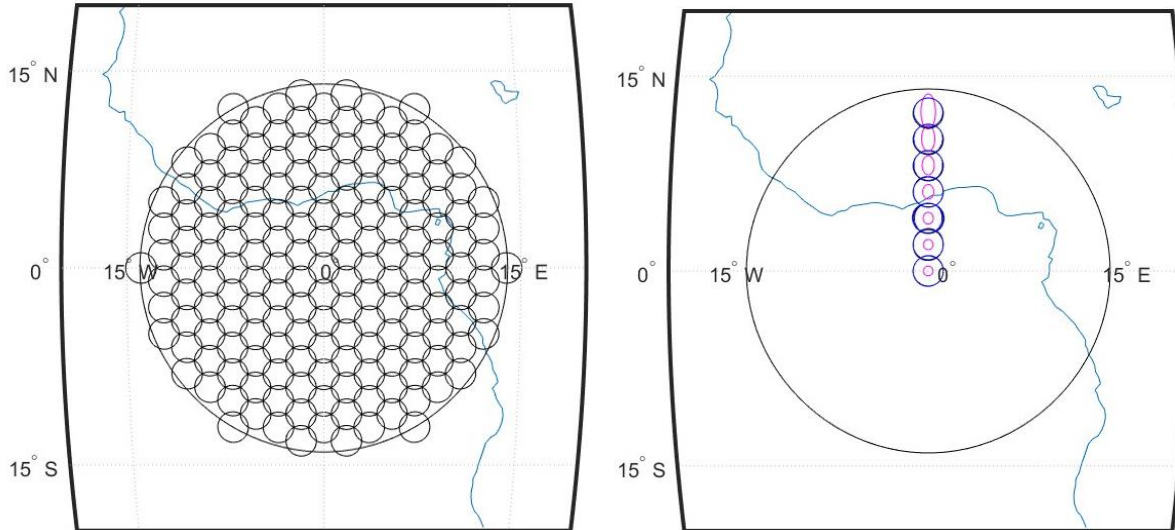


Figure 17. Left: target layout with uniform footprints. Right: detail of beam widening operation comparing target footprint (black), realised footprint (blue) and non-widened footprint (magenta)

Beam widening has been well studied in the literature (*e.g.*, [20]-[21]). There are three main solutions: aperture truncation (*i.e.* switching off some elements making the resulting antenna aperture smaller), amplitude tapering and phase tapering. Aperture truncation and amplitude tapering cause EIRP reduction since not all amplifiers are used at their maximum power. In contrast to this, phase tapering keeps EIRP values constant but at the price of increased gain ripples. Phase or amplitude/phase tapering optimization trading off EIRP reduction and gain ripples are out of the scope of this. For the sake of comparing different alternatives, we will consider an upper bound of beam widening process, consisting of applying aperture truncation but keeping the transmit power unaltered, so only taking in account the directivity reduction.

MAXIMUM EIRP BEAMS (BEAM OVERLAPPING)

The alternative to beam widening for preserving EIRP is to create a grid of beams according to the beam footprint radius at Nadir, which implies increasing significantly the number of beams and having large beam overlapping as we move towards coverage edge. Figure 18 on the left depicts the resulting beam layout, featuring 1723 beams with a minimum radius (at Nadir) of 41.3 km.

COMPROMISE SOLUTION

Any point between the two already discussed alternatives (*i.e.* applying certain level of beam widening but not fully compensating the beam spread at coverage edges) represents a solution trading off EIRP reduction, beam overlapping and total number of beams. Basically, the beam grid is set according to a beam radius which is smaller than the radius at cell edge but bigger than the one at Nadir. As a result, beams near Nadir are widened whereas beams at cell edge are not widened but present high overlapping. This solution is exemplified in Figure 18 on the right which depicts the beam widening process at azimuth=0° when the grid is set according to a beam footprint radius of 64.6 km, so half of that used for uniform beams, producing a layout with 703 beams.

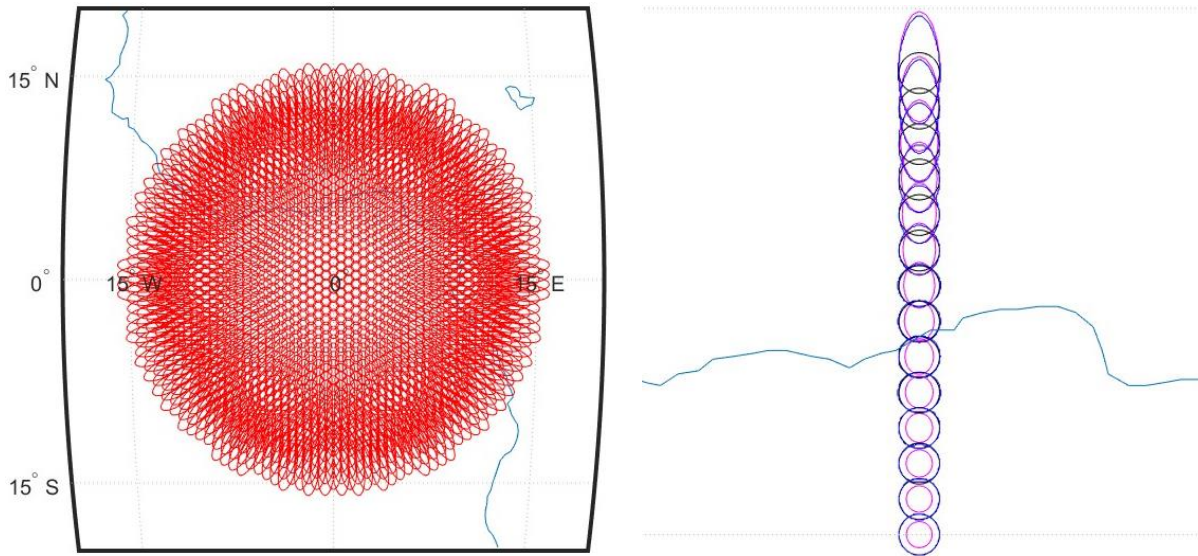


Figure 18. Left: Beam footprint layout setting a grid according to the beam radius at Nadir (Maximum EIRP beams). Right: detail of beam widening operation for a compromise solution using a minimum beam radius of 64.6 km. It compares the target footprint (black), realised footprint (blue) and non-widened footprint (magenta)

Table 13: Summary of beam design methods under study.

Solution	Minimum beam radius (km)	Minimum Beam Gain (dBi)	Number of beams	Simultaneous illuminated beams for reference SNR=3.3dB	Required resources for broadcast
3GPP reference	41.3	28.9	595	24	-
Maximum EIRP beams	41.3	28.9	1723	24	108 (72)
Compromise solution	64.6	28.2	703	12	59
Uniform beams	129	22.1	169	4	43

Table 13 compares the three alternatives described so far (uniform beam, beams keeping maximum EIRP and compromise solution) with the reference layout considered by 3GPP (see Figure 15) that does not produce a uniform grid on Earth. The first three columns summarize the achieved minimum beam footprint radius, minimum beam gain and the total number of beams required to cover the full satellite FoV. Let us remark that the minimum beam gains are observed at Nadir for uniform beams and the compromise solution and at coverage edge for Maximum EIRP beams and the 3GPP reference.

The last two columns of Table 13 show the performance comparison of the three proposed methods derived through numerical simulations. As stated before, the considered payload is EIRP limited, so it cannot illuminate all beams simultaneously with sufficient power. Therefore, for broadcast signalling transmissions, the relevant figure of merit is the number of resources required to perform a single beam sweep across the whole FoV, which corresponds to

$$required\ resources = \frac{total\ number\ of\ beams}{number\ of\ simultaneous\ beams} \quad (31)$$

and it is included in the last column of Table 13. The number of simultaneous illuminated beams depends on the target Signal-to-Noise Ratio (SNR) that a user should perceive, on which beams are co-scheduled in the same time/frequency resources and on how we distribute the available power across them (typically it differs to equalize the path loss differences). The latter is application dependant, so for a more generic analysis we consider a mean SNR value, calculated as the mean of the SNRs obtained by users located at the centre of each beam, for beams at azimuth=0° and tilt angle going from Nadir to coverage edge. For instance, the beams plotted on the left side of Figure 17 and Figure 18. Figure 19 left presents the numerical evaluation of the mean SNR obtained by the three presented solutions as the number of simultaneous illuminated beams increases. The SNR values have been calculated assuming the parameters of Table 14, which consider the downlink transmission to mobile users that was found to be the worst-case scenario of the link budgets provided in D3.2. Figure 19 left includes also the mean SNR for the reference 3GPP beam layout, that was indeed the baseline used in D3.2. Furthermore, D3.2 stated that the maximum number of simultaneous beam supported was 24. Since in Figure 19 left, 24 simultaneous beams corresponds to a SNR of 3.3 dB for the reference 3GPP beam layout, we assume this value as the target SNR level to calculate the number of supported simultaneous beam sin by each method, as indicated in the fourth column of Table 13. It can be observed that to achieve and SNR close to 3.3 dB, the 24 beams illuminated in the 3GPP reference beams case need to be reduced to 16 for maximum EIRP beams, to 11 for the compromise solution and to 4 for the uniform beams case. In addition, Figure 19 right compares the corresponding SNR obtained at the centre of each of the beams at azimuth=0° and satellite antenna tilt going from Nadir to coverage edge, when 24, 16, 11, and 4 beams are simultaneously illuminated for the 3GPP reference, maximum EIRP, compromise and uniform beam cases, correspondingly.

Having derived the number of simultaneous beams, we can now analyse the figure of merit of Resources required for broadcast using (31). The most efficient scheme is uniform beams that need 43 resources, whereas the compromise solution requires 59 and for the maximum EIRP beams they increase up to 108.

Table 14: Parameters for SNR calculation.

Parameter	Value	Comments
Frequency	20 GHz	
Bandwidth	236 MHz	
Available power	15.2 dBW	512 antennas each with a PA of 65 mW
Power per beam	$\frac{\text{Available power}}{\text{number of beams}}$	
Channel	LOS	
Atmospheric loss	0.5dB @elev=90°, 0.71dB @elev=45°, 1.1dB @elev=30°	Linear interpolation used for angles in between
Shadow fading	Not considered	
Receiver G/T	11dB @elev=90°, 10dB @elev=45°, 8dB @elev=30°	Linear interpolation used for angles in between
Implementation loss	2 dB	

Let us remark that this analysis is sensitive to the way the mean SNR value is calculated. Indeed, both the reference 3GPP beams and the maximum EIRP beams solutions use in fact the same beams with the full antenna at full power. The differences in mean SNR come then from the fact that the maximum EIRP beams use a denser grid that have much more points close to the edge, reducing the effective mean value. However, even considering the mean SNR value of the 3GPP reference curve, the Maximum EIRP beam solutions keep being the less effective requiring up to 72 resources. A deeper analysis would require evaluating the

SNR taking into account the specific beams illuminated in each time instant and a given power equalization strategy.

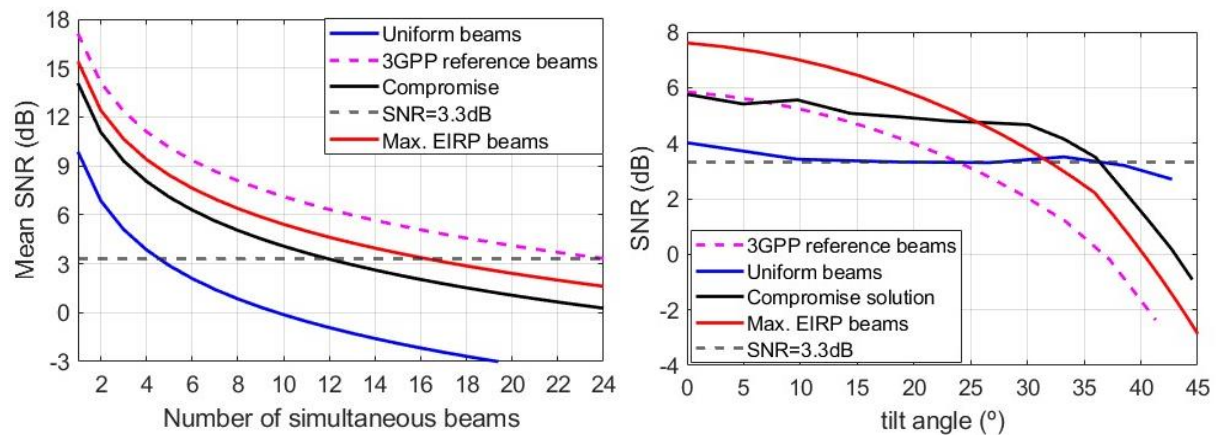


Figure 19: Obtained mean SNR as a function of the number of simultaneous beams illuminated.

3.2.2 Mapping satellite beams to 5G cells

In terrestrial systems, the number and size of cells follow the capacity-mobility management trade off. Denser grid of smaller cells provide larger capacities at the expense of increased mobility management requirements. In theory, considering power unlimited NTN systems, a one-to-one mapping between beam and cells would allow increasing the capacity since each beam can handle independent time/frequency resource grids. However,

in the system under discussion with EIRP limited quasi-Earth-fixed beams, the capacity is limited by the number of simultaneous beams that can be activated, regardless of the beams to cell mapping. Besides, the larger fixed beam footprints on Earth reduce the complexity of mobility management. Only UEs at high-speed, like those on airplanes, would require constant beam switching/cell handovers. In these conditions three alternatives can be evaluated:

- **Number of cells greater than the number of simultaneous illuminated beams:** At the boundary this solution converges to mapping each satellite beam (considering here the total number of beams in the grid) to a single 5G cell. Since in certain instants there is no active beam for given cells, the cell operations need to be turned on and off at beam illumination rates, what can be understood as a beam hopping operation that is not included in the standard. Indeed, the study on beam hopping operation has been recently included in Release 19 topics. A potential solution would be to ensure that during periods in which a beam is not illuminated no data transmissions are scheduled to any user. This would add additional complexity and not bring any capacity benefits, as discussed before. Finally, having multiple cells implies cell handovers due to user movement.
- **Number of cells equal to the number of simultaneous illuminated beams:** This is the first intuitive solution but presents two challenges. First, the cells cannot operate independently. Indeed, they need to ensure that broadcast transmission of different cells do not overlap (at least in case highly overlapped beams like maximum EIRP beams in Section 3.2.1), and a scheduler needs to handle users across the whole coverage area, not only in a cell level basis. The second challenge is that it has limited payload flexibility and provides uniform capacity over the coverage area unless a scheduler across the whole FoV and beam hopping operation is implemented. This last option would permit scheduling multiple users in one cell and left other cells without serving any user. Finally, having multiple cells implies cell handovers due to user movement.

- Number of cells lower than the number of simultaneous beams:** Considering the challenges of the previous cases, a straightforward option is to consider a single cell with a single scheduler managing the whole coverage area. In this case, the main limitation is that Release 17 only considers 64 blocks per SSB burst, so efficient SSB multiplexing schemes need to be evaluated. Solutions with a number of cells between one and the number of active beams represent compromise options reducing the requirements on SSB multiplexing. SSB multiplexing is addressed in section 3.2.2.2.

3.2.2.1 Polarization management

5G-STAR DUST considers satellite payloads with dual-polarization capabilities for the service link. Indeed, as specified in deliverable D3.2, the payload antenna will consist of four apertures: Tx-LHCP, Tx-RHCP, Rx-LHCP and Rx-RHCP. The mapping scheme shall be conceived to make an efficient use of the degrees of freedom provided by the dual-polarization capability. Let us first review the polarization use in current Ka band HTS and terrestrial 5G systems.

Commercial High Throughput Satellite (HTS) missions often rely on fixed multibeam schemes with 4 colours frequency reuse, which can be implemented using two frequency bands and two orthogonal polarizations, typically circular for Ka band. In this way, inter-beam interference is minimized since adjacent beams operate in orthogonal polarizations or different frequency bands. In 5G-STAR DUST, a more flexible use of radio resources is envisaged for data transmissions, with full-frequency reuse and user centric beamforming as a baseline. In this sense, the operation is closer to terrestrial 5G systems at mm-waves, with the main exception of the polarization. Typically, those systems operate in dual-linear polarization and could experience low cross-polarization discrimination in NLOS channels or when the number of multipath components increases. It must be noted that NTN broadcast signalling still requires full coverage of the satellite (FoV), which in this case must include the efficient use of the dual-polarization. Three alternatives are discussed in the following.

NON-OVERLAPPING CELLS

This option considers mapping the two polarizations to different 5G cell groups each of them covering half of the satellite field of view, as sketched in Figure 20. In this way, considering quasi-Earth fixed beams, a given geographic area is only illuminated with a given polarization, allowing the deployment of low-end single-polarized fixed terminals. Indeed, only moving terminals will require performing polarization switch when going from one cell to the other. The current polarization indication in SIB 19 considered in Release 17 will be sufficient to indicate the operation of the serving and neighbour cells. In addition, independent schedulers for each polarization (*i.e.*, half satellite FoV) can be used.

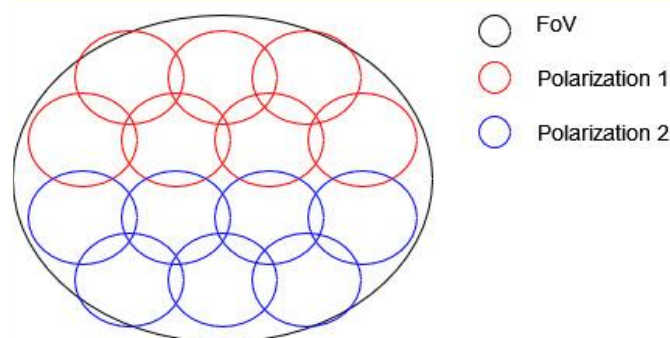


Figure 20: Polarization management: non-overlapping cells.

The drawbacks of this solution are the need to perform an intra-gNB handover when crossing from one cell to another within the satellite FoV, and a 50% reduction of the “spot beam capacity”. Theoretically, the capacity of this scheme is half of the full frequency reuse with the use of the two polarizations within the whole satellite FoV. But in practice, the capacity is already limited by the number of simultaneous active beams as already discussed. However, the proposed non-overlapping scheme does not permit serving to closely located users with orthogonal polarizations, thus resulting in the 50% capacity reduction in a given spot.

FULLY-OVERLAPPING CELLS

This option considers serving each region with two independent cells working in two different polarizations. There is a full overlap between the cells and the use of orthogonal polarizations minimizes inter-cell interferences, as depicted in Figure 21. It keeps the maximum capacity per spot. In addition, this scheme also provides connectivity to single-polarized terminals, whichever the circular polarization they support, and permits polarization switch for capacity maximization or for efficient use of resources.

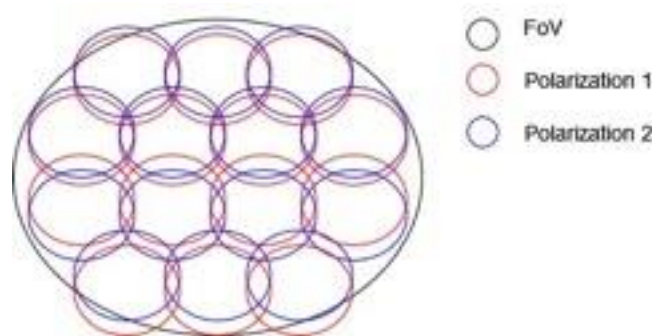


Figure 21: Polarization management: fully-overlapping cells.

The drawbacks of this solution are that, for broadcasting signals, each satellite needs to sweep the whole FoV with half of the available resources, *i.e.*, with just the available beams in one polarization, not in both polarizations as in the previous alternative. Moreover, UE capable of simultaneously receiving both polarizations need to resort to multi-connectivity schemes since the two polarizations correspond to different cells. Finally, the SSB beam sweeping design must ensure that same signals are not transmitted at the same time to the same geographic spots from both polarizations in order to prevent from depolarization (*i.e.*, converting the two orthogonal circular polarizations to a single linear one).

DUAL-POLARIZATION CELLS

In this option, each cell is served using both polarizations, as shown in Figure 22. Therefore, the satellite can use all beams available (*i.e.*, in both polarizations) to efficiently cover the FoV in a given instant, for broadcast signalling. This provides the maximum flexibility and allows rank 2 data transmissions from the same cell using both polarizations.

However, this option presents a set of open questions if both polarizations are used to transmit SSB burst. First, SIB 19 cannot indicate the polarization since it is different for different beams. Second, a user performing initial access should try to receive the SSB transmissions with both polarizations, or the satellite should illuminate the same geographical spot with different polarizations in different time instances. Third, a user may need to switch polarization within a given SSB burst to be able to measure the RSRP of the serving and neighbouring beams. All these issues are solved by just transmitting SSB in one polarization, but then the drawback of

covering the whole FoV with half of the number of beams available (*i.e.*, one polarization) arises as in the previous alternative.

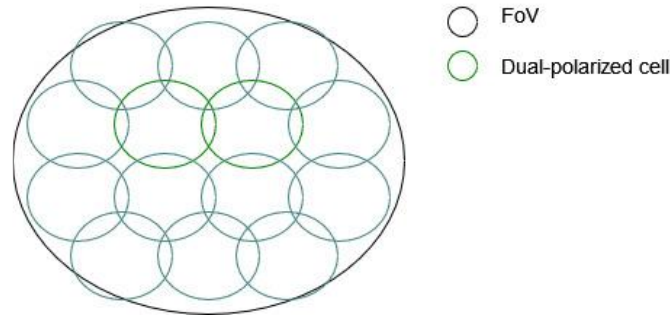


Figure 22: Polarization management: dual -polarized cells.

3.2.2.2 SSB multiplexing

The key aspect of the SSB multiplexing is to reach all the spots of the coverage area spending the minimum time, frequency and space resources. Hence, it can be determined that the SSB multiplexing scheme has an impact on the broadcast transmission.

To make beam determination agile, the serving satellite shall ensure that the SSB is received in a given time window, regardless of the location. Owing to EIRP limitations, the satellite cannot simultaneously illuminate the whole coverage area. As it is specified in Table 13, only a subset of N_A beams, out of N_B , can be simultaneously illuminated. The number of active beams N_A essentially depends on the bandwidth and the beam footprint layout. In its basic configuration, the satellite can simultaneously maintain N_A beams of 200 MHz bandwidth. The number of beams can be increased at the expenses of reducing the bandwidth with the same factor. Otherwise, the link budget will be significantly reduced, which means that the system needs flexibility to sweep through the coverage area to distribute SIB everywhere. A fundamental question in this case is how to make the efficiently use satellite resources to deliver the SSB across the coverage area. The starting point is the SSB configuration described in 38.211 [22]. As Figure 10 shows the SSB allocates the PSS, the SSS and the PBCH in 4 OFDM symbols and occupies 240 consecutive subcarriers in the frequency domain (20 Physical Resource Blocks, PRBs). Figure 4 shows the SSB allocates the PSS, the SSS and the PBCH in 4 OFDM symbols and occupies 240 consecutive subcarriers in the frequency domain (20PRBs).

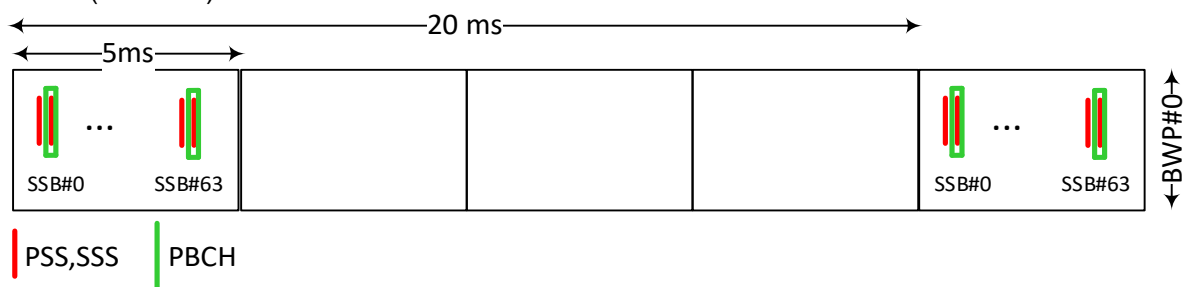


Figure 23: SSB multiplexing in time domain.

In FR2, the SSB subcarrier spacing can be up to 240 KHz. Therefore, the SSB could span 57.6 MHz. The default SSB periodicity is 20 ms, which can be extended to 40ms, 80ms or 160ms. However, shorter periodicities are preferred to enable fast synchronization. In FR2, up to 64 SSBs can be multiplexed in the time domain within a 5 ms window. The set of SSBs within a beam-sweep is referred to as SS burst set. The specific time location of the SSBs in

the time domain is specified in 38.213. The SSB pattern is illustrated in Figure 23. It is considered that the SS burst set is transmitted in the initial bandwidth part, which is referred to as BWP#0. Each SSB is assigned a unique index starting from zero. The indexes are reset after a period of 20 ms.

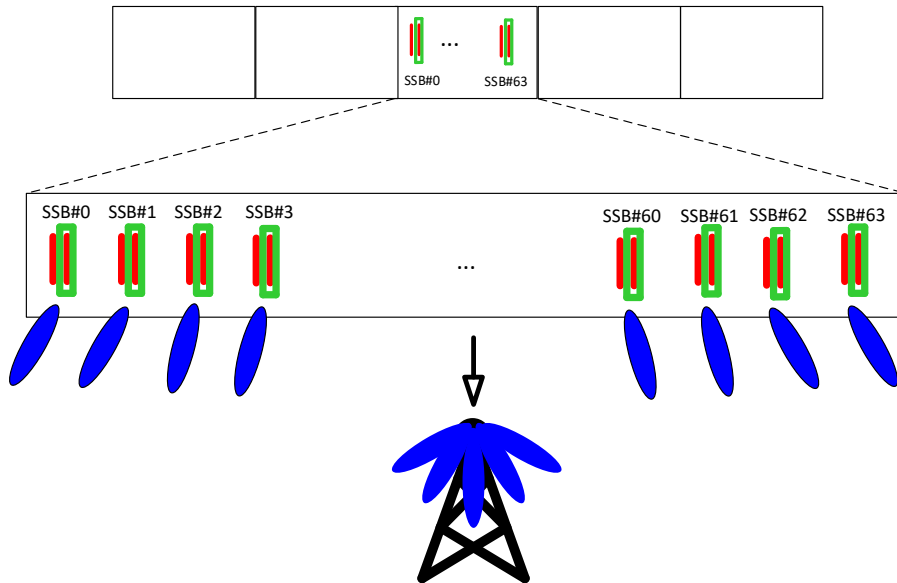


Figure 24: Beam sweeping by SSB in terrestrial deployments

In terrestrial deployments, there is a one-to-one correspondence between the SSB index and the beam index. Only a single SSB is transmitted at a time. The idea is illustrated in Figure 24. If the cell contains 64 or fewer NTN beams, then it follows the SSB multiplexing scheme and beam management procedure adopted in terrestrial deployments can be also applied in NTN. The application of the conventional mapping is not efficient when the cell contains more than 64 NTN beams. In such a case, it would not be possible to cover 64 NTN beams in 20 ms. A larger period than 20 ms would be required, which would slow down the DL synchronization. More efficient SSB multiplexing schemes are required therefore.

The proposed enhancement for NTN consists in multiplexing the SSBs in time and space dimensions. The concept is shown in Figure 25. To be didactic, in the proposed deployment the cell is divided into 64 NTN beams. In such a case, the solution adopted in NR to broadcast the SSBs is based on illuminating a single NTN beam at each time slot. To sweep the area, 64 SSB time indexes are needed. The proposed solution illuminates two spot beams of different colour at a time. The main difference with respect to the standardized procedure is that each SSB can be fed into a group of two NTN beams simultaneously. This means that the area can be swept with 32 SSB time indexes. Remarkably, the scheme can be easily extended to associate a higher number of beams per SSB time index. It becomes evident that if the mapping is judiciously devised, the beams that carry the same SSB time index are sufficiently separated so that they virtually do not overlap. The immediate consequence is that adjacent beams are active in different time slots. This can be verified in the scheme depicted in Figure 25. It is worthwhile mentioning that the mapping scheme other schemes can also be considered. Based on the mapping criteria to avoid interference between beams carrying the same SSB time index, it follows that UEs will not experience any ambiguity, i.e. each UE will be able to relate the SSB time index with a single NTN beam, as the replica is fed into an NTN beam that is received with a very low power.

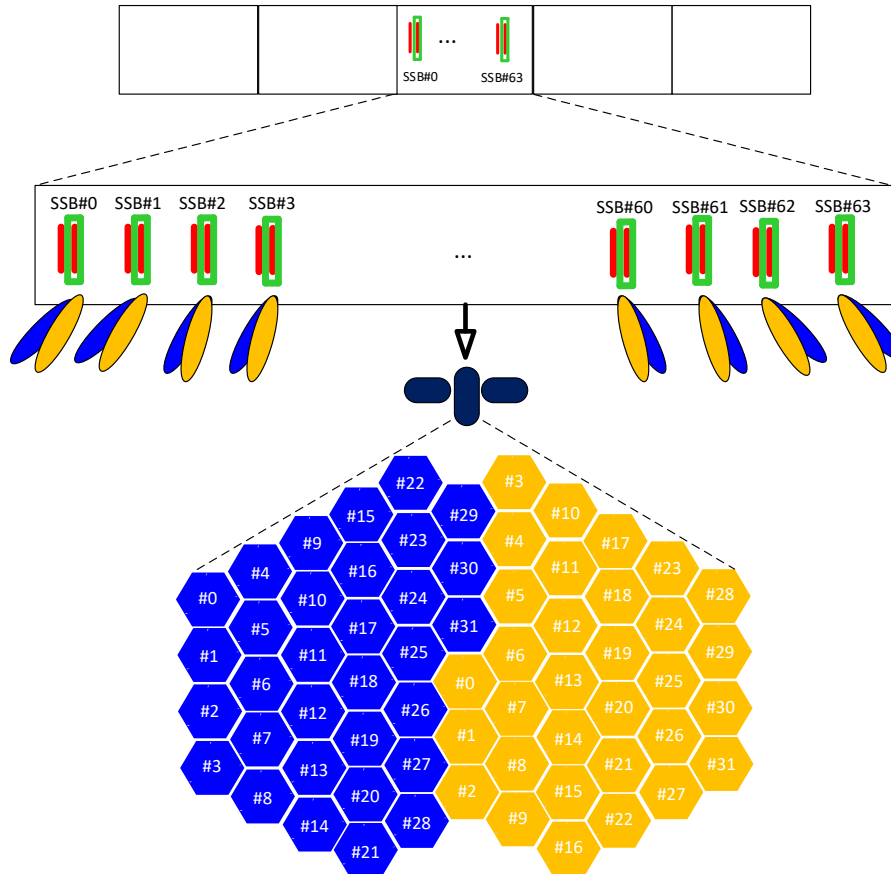


Figure 25: Beam sweeping by SSB in NTN deployments.

Alternatively, the SSBs could be multiplexed in the frequency domain. This approach may entail additional complexity with respect to the time multiplexing counterpart. The main reason lies in the fact that the frequency resources that shall be monitored to search the SSB are extended. This complicates the cell search procedure, as the SSB could be located in multiple frequencies. Hence, the grid search is substantially increased.

Impact on standardization: as specified in 38.211, [22], the SSB is transmitted using the antenna port 4000. To transmit the SSB in multiple directions, the SSB shall be fed into multiple beams. For simultaneous multi-beam transmission, a plurality of antenna ports is needed. To discriminate multiple directions, the standard should allow the transmission of the SSB through multiple antenna ports with the respective beamforming vectors.

The proposed SSB multiplexing scheme offers flexibility to sweep the coverage area. Although different configurations are possible, the two extreme cases are described in the following.

- SSB multiplexing scheme 1: This solution is using the maximum number of SSB indexes. Then, at each slot, the maximum number of NTN beams that broadcast the same SSB is $\lceil M/64 \rceil$.
- SSB multiplexing scheme 2: This solution is using the minimum number of SSB indexes. Then, at each slot, the maximum number of NTN beams that broadcast the same SSB is N_B .

In the following we numerically evaluate the two schemes. It has been assumed that the cell contains M NTN beams and that the satellite is able to simultaneously illuminate N_B NTN

beams. In both multiplexing schemes, special attention must be drawn to the inter-beam interference. The active beams in each slot shall be sufficiently separated, so that the interference that comes from the interfering beams is negligible.

As baseline we are using the dense beam grid called Maximum EIRP beams in Section 3.2.1. It is chosen here because it presents that highest challenge on SSB multiplexing due to the large number of beams (*i.e.*, 1723). We first reduced the number of beams to 1365 by discarding those providing most of their coverage outside the circle corresponding to a minimum elevation angle seen by the user of 30°. Note that, due to the large overlapping, those beams do not contribute much to provide coverage but they increase the complexity of multiplexing solutions. Figure 26 depicts the contour of beams at -3 dB from their corresponding centre.

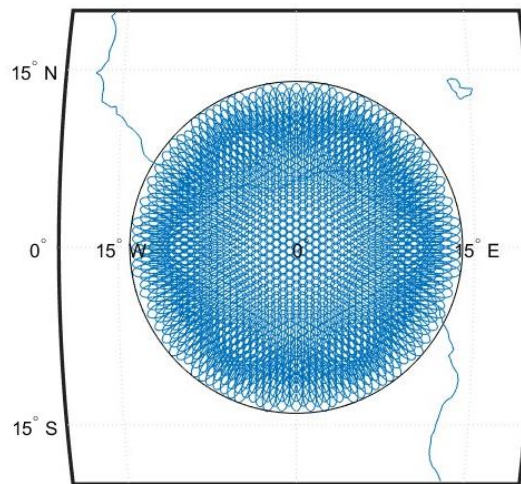


Figure 26: -3 dB beam contours with reduced grid (blue); and circle corresponding to a minimum elevation angle for users of 30° (black).

There are a lot of degrees of freedom in the operation of mapping up to 64 SSB indexes to 1365 beams. Here we propose a regular predetermined mapping over the fixed grid on Earth, to guarantee that beams using the same beam do not overlap, that beams with contiguous indexes are close to each other so they can be directly grouped in cells, and to avoid complex mapping calculations as the satellites moves over the Earth grid. Being $nIndex$, the total number of SSB index to be mapped, we consider that consecutive indexes are mapped to rectangular blocks with number of columns ($nCols$) and the number of rows ($nRows$) equal to

$$nCols = \text{ceil}(\sqrt{nIndex}) \quad (32)$$

$$nRows = \text{ceil}\left(\frac{nIndex}{nCols}\right) \quad (33)$$

For instance, for $nIndex=64$, blocks of 8x8 are formed, meaning that each SSB index is repeated every 9 beams in both latitude and longitude dimensions. For $nIndex=56$, the blocks would be 8x7. Between 56 and 64, blocks of 8x8 are used but we cannot fill it with unique SSB indexes caused by the limitation of the standard. For the first block we reuse the indexes starting from 0. Then next block starts with the last index used in the previous one, and we repeat this operation until a block is completed and the last index is $nIndex - 1$. For instance, for $nIndex=61$, we would need 8 blocks of 8x8. The resulting 64x8 block is then regularly repeated along the Earth grid.

Figure 27 compares the beams mapped to SSB index #0 when $nIndex$ is 64 and 61. It can be observed that $nIndex=64$ produces a regular lattice whereas for $nIndex=61$, it is not as regular but still provides the required beam isolation. Figure 28 exemplifies the index mapping procedure for $nIndex=61$.

This SSB mapping solution can be used for different beam to 5G cell mappings as long as the blocks with contiguous beam indexes (*i.e.*, from 0 to $nIndex$) are allocated to the same cell. Each block or group of blocks can be mapped to a different cell. Figure 29 shows the beam centers corresponding to these blocks, a different colour and marker shape is used for each block containing SSB indexes from 0 to 61/64. Regular square blocks are observed for $nIndex=64$ whereas not so regular square blocks result for $nIndex=61$. It must be noted that at FoV edges blocks of SSB indexes, and so corresponding cells, are not complete, so the number of beams per cell changes with the satellite movement.

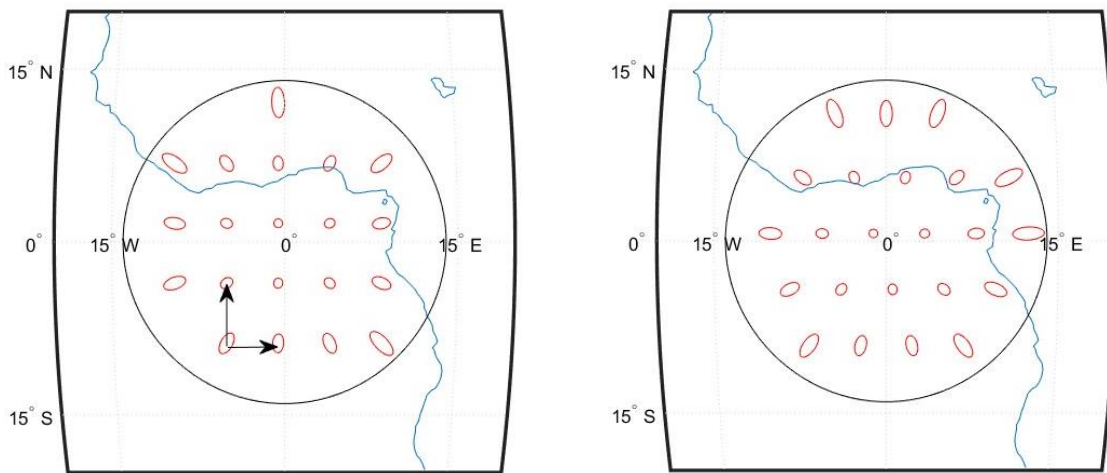


Figure 27: -3 dB beam contours of beams mapped to SSB index #0 for $nIndex=64$ (left) and $nIndex=61$ (right).

0	1	2	3	4	5	6	7	0	1	2	3	4	5	6	7
8	9	10	11	12	13	14	15	8	9	10	11	12	13	14	15
16	17	18	19	20	21	22	23	16	17	18	19	20	21	22	23
24	25	26	27	28	29	30	31	24	25	26	27	28	29	30	31
32	33	34	35	36	37	38	39	32	33	34	35	36	37	38	39
40	41	42	43	44	45	46	47	40	41	42	43	44	45	46	47
48	49	50	51	52	53	54	55	48	49	50	51	52	53	54	55
56	57	58	59	60	0	1	2	56	57	58	59	60	0	1	2
3	4	5	6	7	8	9	10	3	4	5	6	7	8	9	10
11	12	13	14	15	16	17	18	11	12	13	14	15	16	17	18
19	20	21	22	23	24	25	26	19	20	21	22	23	24	25	26
27	28	29	30	31	32	33	34	27	28	29	30	31	32	33	34
35	36	37	38	39	40	41	42	35	36	37	38	39	40	41	42
43	44	45	46	47	48	49	50	43	44	45	46	47	48	49	50
51	52	53	54	55	56	57	58	51	52	53	54	55	56	57	58
59	60	0	1	2	3	4	5	59	60	0	1	2	3	4	5
6	7	8	9	10	11	12	13	6	7	8	9	10	11	12	13
14	15	16	17	18	19	20	21	14	15	16	17	18	19	20	21
22	23	24	25	26	27	28	29	22	23	24	25	26	27	28	29
30	31	32	33	34	35	36	37	30	31	32	33	34	35	36	37
38	39	40	41	42	43	44	45	38	39	40	41	42	43	44	45
46	47	48	49	50	51	52	53	46	47	48	49	50	51	52	53
54	55	56	57	58	59	60	0	54	55	56	57	58	59	60	0
1	2	3	4	5	6	7	8	1	2	3	4	5	6	7	8
9	10	11	12	13	14	15	16	9	10	11	12	13	14	15	16
17	18	19	20	21	22	23	24	17	18	19	20	21	22	23	24
25	26	27	28	29	30	31	32	25	26	27	28	29	30	31	32
33	34	35	36	37	38	39	40	33	34	35	36	37	38	39	40
41	42	43	44	45	46	47	48	41	42	43	44	45	46	47	48
49	50	51	52	53	54	55	56	49	50	51	52	53	54	55	56
57	58	59	60	0	1	2	3	57	58	59	60	0	1	2	3
4	5	6	7	8	9	10	11	4	5	6	7	8	9	10	11
12	13	14	15	16	17	18	19	12	13	14	15	16	17	18	19
20	21	22	23	24	25	26	27	20	21	22	23	24	25	26	27
28	29	30	31	32	33	34	35	28	29	30	31	32	33	34	35
36	37	38	39	40	41	42	43	36	37	38	39	40	41	42	43
44	45	46	47	48	49	50	51	44	45	46	47	48	49	50	51
52	53	54	55	56	57	58	59	52	53	54	55	56	57	58	59
60	0	1	2	3	4	5	6	60	0	1	2	3	4	5	6
7	8	9	10	11	12	13	14	7	8	9	10	11	12	13	14
15	16	17	18	19	20	21	22	15	16	17	18	19	20	21	22
23	24	25	26	27	28	29	30	23	24	25	26	27	28	29	30
31	32	33	34	35	36	37	38	31	32	33	34	35	36	37	38
39	40	41	42	43	44	45	46	39	40	41	42	43	44	45	46
47	48	49	50	51	52	53	54	47	48	49	50	51	52	53	54
55	56	57	58	59	60	0	1	55	56	57	58	59	60	0	1
2	3	4	5	6	7	8	9	2	3	4	5	6	7	8	9
10	11	12	13	14	15	16	17	10	11	12	13	14	15	16	17
18	19	20	21	22	23	24	25	18	19	20	21	22	23	24	25
26	27	28	29	30	31	32	33	26	27	28	29	30	31	32	33
34	35	36	37	38	39	40	41	34	35	36	37	38	39	40	41
42	43	44	45	46	47	48	49	42	43	44	45	46	47	48	49
50	51	52	53	54	55	56	57	50	51	52	53	54	55	56	57
58	59	60	0	1	2	3	4	58	59	60	0	1	2	3	4
5	6	7	8	9	10	11	12	5	6	7	8	9	10	11	12
13	14	15	16	17	18	19	20	13	14	15	16	17	18	19	20
21	22	23	24	25	26	27	28	21	22	23	24	25	26	27	28
29	30	31	32	33	34	35	36	29	30	31	32	33	34	35	36
37	38	39	40	41	42	43	44	37	38	39	40	41	42	43	44
45	46	47	48	49	50	51	52	45	46	47	48	49	50	51	52
53	54	55	56	57	58	59	60	53	54	55	56	57	58	59	60

Figure 28: Example of index mapping for nIndex=61.

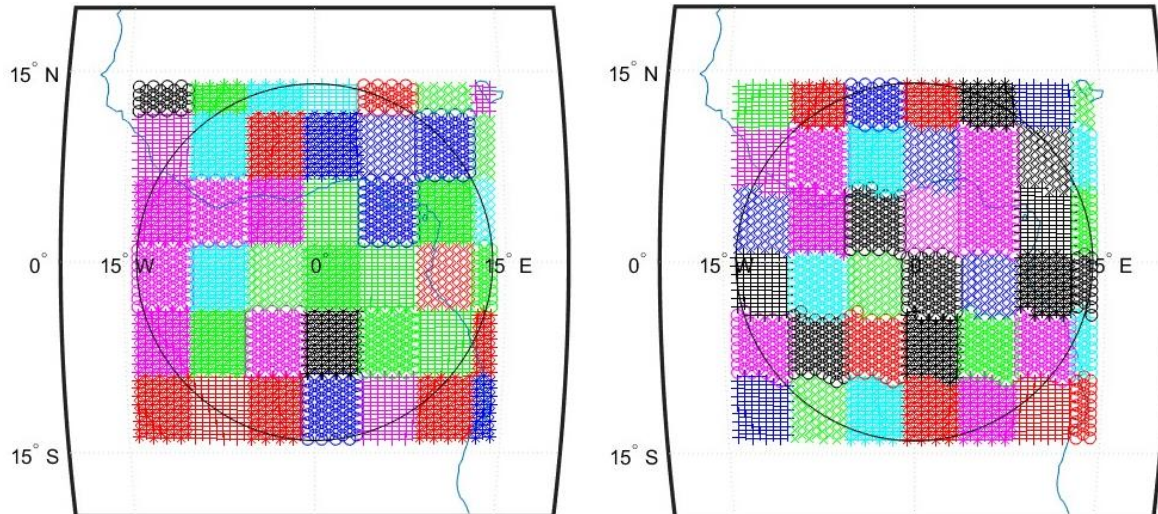


Figure 29: Beam centers mapped to blocks of contiguous SSB indexes for $nIndex=64$ (left) and $nIndex=61$ (right).

In this discussion, we assume that even if multiple cells are mapped within the FoV, all are perfectly synchronized so all beams mapped to the same SSB index are transmitted simultaneously, independently to the cell they belong to. If a single cell for the whole FoV is used, exactly the same signals will be transmitted by each beam associated to the same SSB index. From a transmission point of view, this translates to a single beamformer generating multiple beams, which can be calculated as the superposition of the beamformers pointing to each of the beam centres associated with the same SSB index. Although each individual beamformer use same amplitude coefficients for all antennas, it is well known that their superposition provides amplitude variations due to constructive and destructive additions. Consequently, the overall transmit power needs to be reduced in order to fulfil the power constraint in the antenna experiencing maximum constructive additions. Forcing constant amplitude beamformer and keeping the phase from the superposition still provides a multibeam pattern, but with differences in the gain of the different beams and with larger sidelobe levels. To recover a clean multibeam pattern, phase only synthesis methods such as alternating projection method or Particle Swarm optimizations should be used [23]. Mapping the different SSB blocks to different cells does not really solve this issue since the signals transmitted by the same SSB on different cell cannot be assumed to be statistically independent since the alphabet of PSS and PSS is limited.

In Figure 30 a numerical evaluation is presented of this issue. It depicts the CDF of the SNR obtained at the beam centers for different multi-beam beamformer assumptions. An $nIndex=64$ is assumed and the CDF considers the multibeam transmission of all SSB indexes. The parameters for SNR calculations are summarised in Table 15. The beamforming assumptions are:

- **Statistically independent symbols for each beam:** In this case we do not consider a single beamformer but a number of independent beamformers equal to the number of beams mapped to the same SSB index. It is provided as a reference and as an upper bound of what can be achieved with phase only optimization solutions.
- **Statistically independent symbols for each beam and beam gain equalization:** Same assumption as in the previous case, but adding a per beam power control such as all beams mapped with the same SSB index experience the same SNR.

- **Single stream transmission through superposition beamforming:** Same symbols transmitted in each beam, so a single multibeam beamformer with amplitude variations in its coefficients.
- **Single stream transmission through superposition beamforming forcing equal amplitude to all beamforming coefficients, so phase only solution:** same as previous case but equalling the amplitude of all beamforming coefficients.

Table 15: Parameters for SNR calculation.

Parameter	Value	Comments
Frequency	20 GHz	
Bandwidth	200 MHz	
Available power	15.2dBW	512 antennas each with a PA of 65mW
Channel	clear sky LoS	
Receiver G/T	11dB @elev=90°, 10dB @elev=45°, 8dB @elev=30°	Linear interpolation used for angles in between

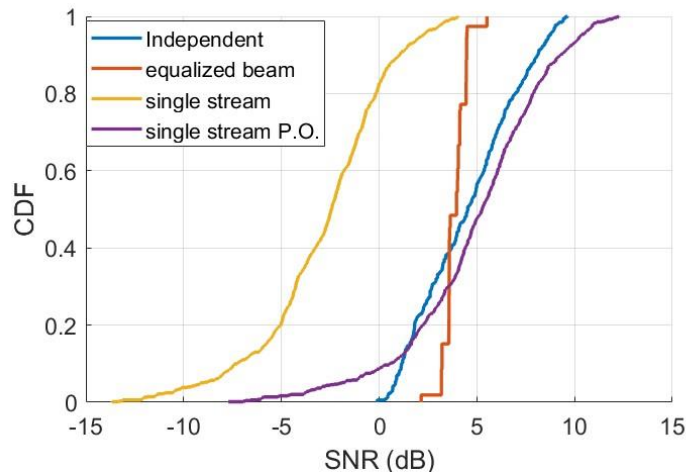


Figure 30: CDF of the SNR obtained at beam centers for different beamformer strategies, with $nIndex=64$.

Applying superposition with a single stream transmission, results in lower SNR since power need to be reduced to meet per antenna power constraints. Forcing equal amplitude coefficients, permits recovering a mean SNR close to that obtained with the reference of independent beamformers, but with a larger excursion of the CDF curve due to the already mentioned not so clean multibeam pattern. Therefore, phase only optimization methods are key here to perform closer to this reference.

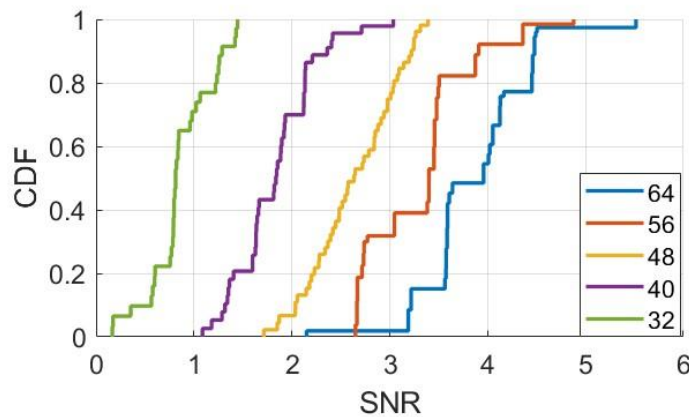


Figure 31: CDF of the SNR obtained at beam centers for independent beamformers equalizing beam gain and for different n Index values from 32 to 64.

Taking equalized independent transmissions as a reference, Figure 31 shows the evolution of the received SNR as the number of SSB indexes used is reduced from 64 to 32, so the number of beams transmitted simultaneously increases from around 21 to around 43. Considering that these SNR are already calculated at beam centers, so at beam edges a reduction of 3 dB could be envisaged, it seems that using 64 SSB index is already almost at the limit to provide enough link margin.

Figure 31 considered that the full channel bandwidth of 200MHz was used. However, broadcast signalling may not require the full bandwidth. Indeed, considering a subcarrier spacing of 120 kHz; a multiplexing pattern 3 so SSB and CORESET#0 are scheduled simultaneously in contiguous resource blocks, as explained in Section 3.2.1; and a CORESET#0 of 48 resource blocks, the occupied bandwidth would be 97.92 MHz, so half of the available one. Two alternatives are envisaged to make use of the remaining bandwidth. Beams designed for SSB transmission may use the full bandwidth of 200 MHz conveying SSB, CORESET#0 and data in the remaining 100 MHz. Note however that these data transmissions are forced to use the SSB beams so cannot benefit from user centric beamforming. Alternatively, beams designed for SSB transmission may only use 97.92 MHz conveying SSB and CORESET#0. Keeping bandwidth transmissions to roughly 100 MHz permit either:

- Increasing SNR perceived by users in 3 dB with respect to those in Figure 31, which can be interesting in locations with larger link margin needs.
- Keeping SNRs but doubling the number of beams transmitted per SSB index, so reducing in a 50% the number of used SSB indexes, which implies a better use of resources.
- Keeping SNR and used SSB indexes but dedicating half of the available transmission power to data transmission through user centric beamforming.

If link margin permits it, it seems that the most interesting solution is the second alternative, so to increase the number of SSB releasing resource blocks for data transmission. In this way, data and SSB transmission are not simultaneous, so the scheduler only needs to consider data transmission but not the position of SSB transmission beams.

3.2.3 Doppler Compensation Schemes

This section introduces different Doppler compensation schemes, namely, UE compensation and satellite compensation. Remarkably, the UE compensation is the mechanism specified by the standard to compensate the Doppler. With the aim of going beyond the standard, the

satellite compensation is introduced, so that users only have to cope with residual Doppler values.

UE compensation: This mechanism relies on a UE that can autonomously compensate the instantaneous Doppler effects and the RTT of the service link. To carry out this fundamental operation, the UE must acquire its location and the satellite ephemeris. To this end, the basic configuration specified by 3GPP assumes that the UE is equipped with a GNSS receiver and that the gNB broadcasts the common delay and the satellite ephemeris in SIB19. Upon successfully completing the downlink synchronization process, the SIB19 is parsed into the satellite ephemeris.

Satellite compensation: This compensation mechanism is conceived to mitigate the impact of the Doppler effects on the attachment procedure. In regenerative architectures, the gNB is located on-board the satellites. Hence, in this mode of operation, in the downlink and the uplink, the satellite pre- and post-compensates, respectively, the Doppler frequency shift at a given reference point (e.g., the beam centre). It is important to highlight that in such a case, users will experience residual time and frequency errors, which correspond to the differential values with respect to the reference point. It is worth mentioning that the residual errors may be an order of magnitude lower than those experienced before the compensation mechanism. In practice, the frequency misalignment observed by the UE will be significantly reduced, which facilitates the downlink synchronization.

In NTN deployments, it is possible to combine the compensation schemes. The challenges of different variants are analysed hereinafter.

UE compensation with no satellite compensation: When the GNSS is available, same assumptions made in Rel. 17 can be adopted. In scenarios where GNSS is unavailable, the UE resorts to alternative methods for Doppler compensation. These methods typically involve leveraging the synchronization signals broadcasted by the gNB. With the absence of satellite compensation, the UE relies solely on its internal mechanisms to estimate and compensate for Doppler effects. This process entails employing techniques to estimate the position using time difference of arrival (TDOA) and frequency difference of arrival (FDOA) measurements on the SSB signals and compensate for Doppler shifts accordingly, [24]-[25]. While this approach may not achieve the same level of accuracy as GNSS-based compensation, it provides a feasible solution for scenarios where GNSS signals are inaccessible.

UE compensation with satellite compensation: When satellite compensation is employed in conjunction with UE-based compensation methods, the overall accuracy and reliability of Doppler compensation are significantly enhanced. In this configuration, the satellite broadcasts information regarding the frequency shifts applied during compensation processes and includes the common delay as part of the system information broadcasted to the UE where the common delay refers to the minimum RTT between the satellite and the closest point on earth in the satellite's beam coverage as indicated in Figure 32.

This information related to the common delay and the satellite compensation is crucial for UEs to synchronize with the compensated signals accurately. By integrating satellite compensation data into the synchronization process, UEs can refine their Doppler compensation algorithms and ensure precise alignment with the transmitted signals. The compensation algorithms at the UE only need to deal with the residual Doppler effect that need to be estimated and compensated. The combined approach can result in improved overall system performance and enhanced user experience, particularly in challenging propagation environments such as LEO communication systems.

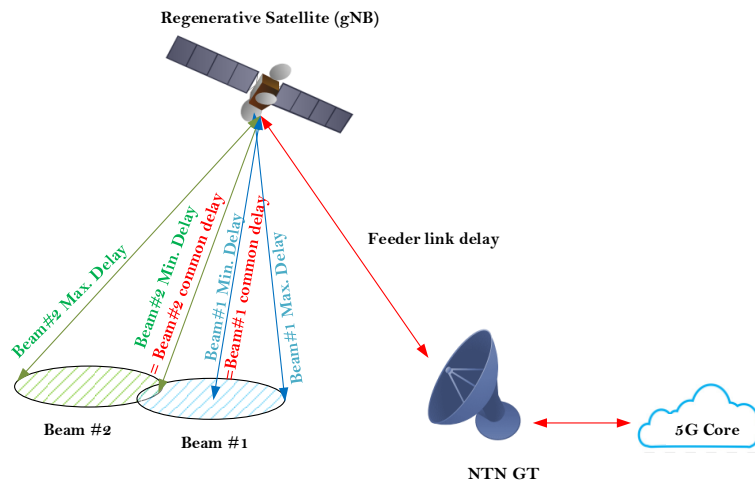


Figure 32: Common delay determination and beam specific compensation.

3.2.4 SSB detection

In FR2, to compensate for the propagation losses, the UE must establish directional links that accurately point towards the serving beam. For users that are not connected, this can be accomplished by provisioning the UE with the AoA. This option is suitable for satellite systems where the AoA does not significantly vary over time, which is the case of GEO satellites. In LEO satellite systems, the UE needs to track the source satellite and prepare frequent satellite handover. Hence, the AoA is constantly changing. In such a case, the steering vectors are available through an estimate. In direct satellite access schemes, the 5G NR waveform is transmitted over the satellite links. This opens the door to use the SSB as reference signal for beam selection and downlink synchronization. The phase uncertainty that stems from the CFO becomes the main impairment to locate the SSB in the downlink frame. The effects that contribute to the downlink CFO are divided into:

- UE oscillator offset (f_{UE}).
- Satellite oscillator offset (f_{SAT}).
- Doppler frequency shift due to satellite movement (DS_{SAT}).
- Doppler frequency shift due to UE movement (DS_{UE}).

In the worst-case scenario, all the effects are added. Provided that the resulting magnitude is lower than the subcarrier spacing of the SSB, the synchronization can be performed with the same algorithm used in terrestrial deployments. In this case, it is common to leverage on the redundancy symbols transmitted in the form of a CP to perform an initial coarse synchronization. After that, a more accurate synchronization is performed by detecting the SSB. However, by adopting this approach, the CFO cannot exceed one half of the subcarrier spacing [26]. Otherwise, the synchronization fails. If the CFO is larger than half the subcarrier spacing, additional complexity is needed at the UE receiver to achieve initial downlink synchronization. Different solutions are available in the literature.

Multiple hypothesis testing. The framework that is proposed in [27] increases the robustness to the CFO by resorting to parallel correlations. The idea is to perform a 2D search in time and frequency dimensions. To this end, the local sequence used in each correlator is matched to a different CFO candidate. The larger the CFO range, the more parallel correlators are needed.

By selecting the branch that exhibits the highest correlation peak, the uncertainty range is reduced and the probability of detection is improved.

Two-step estimation: The approach described in [28] involves two estimation steps. In the first step, the fractional frequency offset is obtained by exploiting the circular structure of OFDM. Next, the carrier is adjusted, so that the receiver is aware of the fractional frequency offset. Finally, the integer part of the CFO is estimated by performing a grid search in a reduced set. That is, only a few CFO values are tested, making the algorithm feasible in practical application.

Existing works such as [27]-[28] show that time and frequency synchronization can be accurately estimated for $SNR > -4 \text{ dB}$ in presence of large CFO values that exceed the subcarrier spacing. The maximum CFO values that can be encountered in NTN have been computed with and without satellite compensation in Table 16. The downlink CFO without compensation is given by:

$$CFO_{DL} = (f_{UE} + f_{SAT} + DS_{SAT} + DS_{UE}) \times 10^{-6} \times f_c^{DL} \quad (34)$$

where f_c^{DL} denotes the downlink carrier frequency. The rest of parameters are introduced at the beginning of the section. It is noteworthy to mention that all the offsets are expressed in ppm. When the satellite compensation comes into play, the expression becomes:

$$\begin{aligned} CFO_{DL} &= (1 + (f_{UE} + f_{SAT} + DS_{SAT} + DS_{UE}) \times 10^{-6}) \times (1 - DS_0 \times 10^{-6}) \times f_c^{DL} - f_c^{DL} \\ &\approx (f_{UE} + f_{SAT} + DS_{SAT} + DS_{UE} - DS_0) \times 10^{-6} \times f_c^{DL} \end{aligned} \quad (35)$$

The offset is mitigated because the satellite shifts the carrier frequency by $-DS_0$, which is the Doppler frequency shift observed in the reference point. The approximation is obtained by neglecting the terms that barely contribute to the error.

Table 16: Downlink CFO for LEO at 1300 km for different compensation schemes in Ka-band.

Compensation scheme	No compensation				Satellite compensation			
Beam diameter (km)	130		40		130		40	
Scenario	Airway	Stationary	Airway	Stationary	Airway	Stationary	Airway	Stationary
CFO (KHz)	626	610	626	610	249	233	233	217

Table 16 shows the CFO for several scenarios. It is considered that the service link operates in the Ka band. For LEO constellations, the orbital height is 1300 km and the inclination is assumed to be 50° . Two beam sizes have been analysed:

- Beam diameter 40 km: This value corresponds to the finest spatial resolution that is offered by the LEO satellite antenna towards the Nadir direction.
- Beam diameter 130 km: This is the reference value for the LEO satellite antenna to deploy a homogeneous fixed grid of beams.

For f_{UE} and f_{SAT} the values provided in TR 38.821 have been considered: $f_{SAT} = 0.5 \text{ ppm}$ and $f_{UE} = 10 \text{ ppm}$. With regards to the user mobility, two scenarios have been considered:

- Airway scenario: it is assumed that NTN could provision service to airplanes. In this case, when the travel speed is 1000 km/h and the minimum elevation angle is 30° , the Doppler frequency shift that corresponds to the terminal movement could be up to $DS_{UE} = 0.8 \text{ ppm}$.
- Stationary scenario: in this case, users are stationary and thus, $DS_{UE} = 0 \text{ ppm}$.

In LEO satellite systems, when the satellite does not apply any compensation scheme, the maximum Doppler frequency shift is $DS_{SAT} = 20$ ppm.

Table 17: Differential Doppler frequency shift values for different elevation angles

Beam diameter and elevation	130 km	40 km
$DS_{SAT} - DS_0$ at 30°	0.672 ppm	0.206 ppm
$DS_{SAT} - DS_0$ at 50°	0.920 ppm	0.281 ppm
$DS_{SAT} - DS_0$ at 70°	1.08 ppm	0.333 ppm
$DS_{SAT} - DS_0$ at 90°	1.14 ppm	0.351 ppm

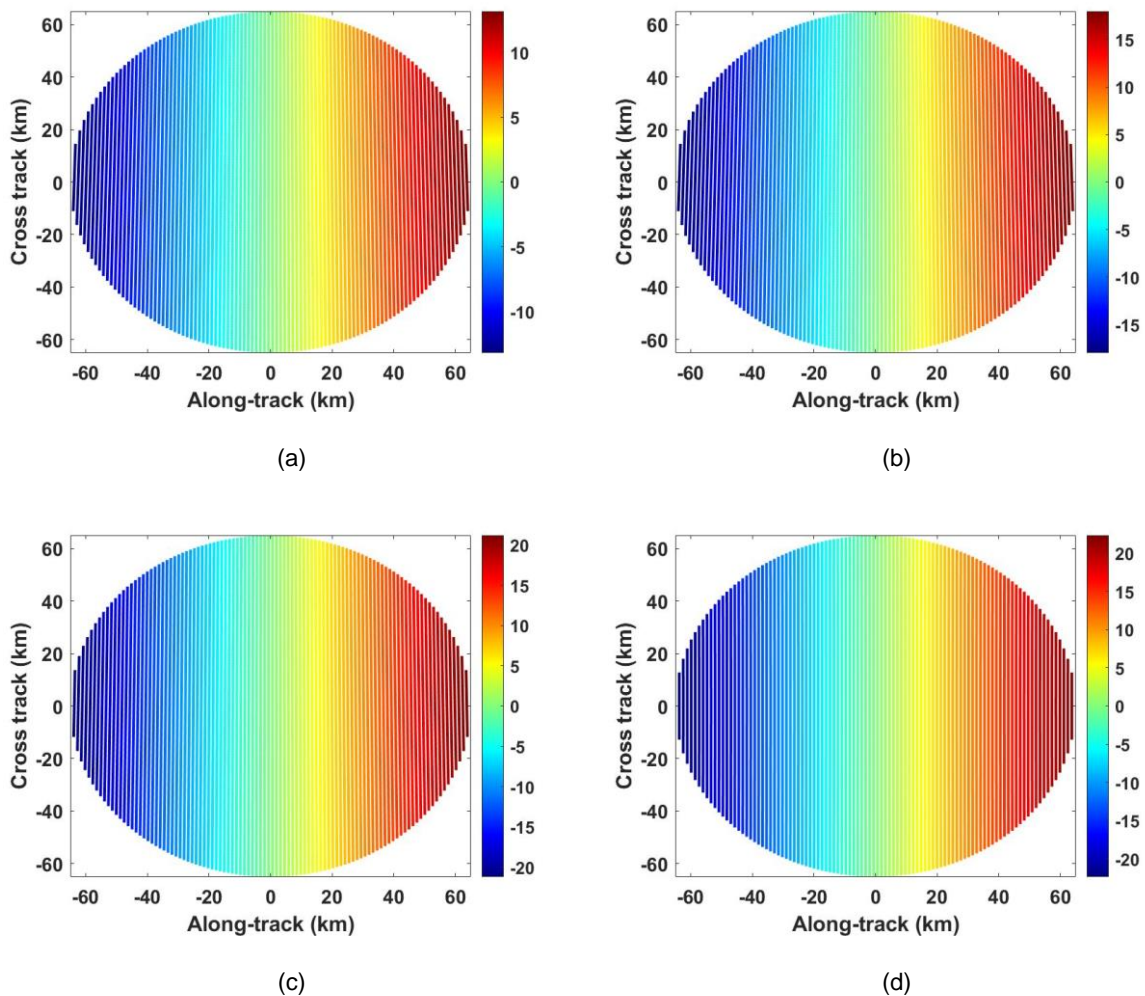


Figure 33: Contour of the differential Doppler frequency shift in KHz: a) elevation angle of 30° , b) elevation angle of 50° , c) elevation angle of 70° , d) elevation angle of 90° .

Table 17 presents $DS_{SAT} - DS_0$ corresponding to the LEO satellite deployment and for different elevation angles. In this case, the carrier frequency is adjusted so that at the centre of the beam, the received signal is synchronized in frequency. The highest frequency misalignment is observed at high elevation angles and at the edges of the beam, where the differential

Doppler frequency shift reaches the maximum. To compute the downlink CFO, the highest frequency misalignment is considered. The contour of the differential Doppler frequency shift is shown in Figure 33. Remarkably, in the cross track direction, (*i.e.*, perpendicular to the trajectory of the satellite), the differential Doppler is almost constant. The variation is more prominent in the along-track direction (*i.e.*, parallel to the trajectory of the satellite).

For Rel. 18, NTN deployments on the Ka band consider 60 kHz and 120 kHz subcarrier spacing for SSB.

Proposal: Based on the flexibility offered by the standard and the values provided in Table 16 and Table 17, the most suitable configuration is to consider 240 KHz of subcarrier spacing for SSB. This value offers the highest level of resilience against the CFO. As the UE is not provisioned with satellite ephemeris for initial downlink synchronization, typical synchronization algorithms implemented in terrestrial deployments will probably fail. To achieve downlink synchronization, the satellite shall pre-compensate the Doppler frequency shift at a given reference point, so that the UE is able to handle the residual Doppler frequency. Alternatively, when the satellite does not compensate the Doppler frequency shift, more advanced synchronization algorithms are required, such as those reported in [27]-[28].

3.2.5 PRACH signal detection

Upon performing the downlink synchronization, the random access procedure is executed to ensure that UEs and the gNB share a common time reference. Thanks to the random access procedure the communication can occur on scheduled channels. The procedure, which involves 4 steps, is summarized in Section 3.1.2. The time and the carrier frequency offsets are the main impairments that affect the first step of the procedure in NTN, *i.e.*, the PRACH signal detection. The magnitude of the offsets is dependent on the compensation mechanism and the information that is broadcasted by the gNB. The detrimental effects that shall be overcome for successful PRACH signal detection are examined in this section.

3.2.5.1 Carrier frequency offset

With regard the frequency misalignment, the main issue stems from the fact that the uplink signals are transmitted at frequencies shifted by the downlink Doppler and received at frequencies further shifted by the uplink Doppler.

UE compensation with and without satellite compensation: The Doppler frequency shift associated to the orbital motion is estimated and compensated in both uplink and downlink. When the satellite applies the compensation mechanism, the UE just needs to correct the differential Doppler frequency shift with respect to the beam reference point. Regardless of the compensation scheme that is applied at the satellite, the maximum CFO in the uplink can be expressed as

$$CFO_{UL} = (DS_{UE} \times 10^{-6} + 1) \times (DS_{UE} \times 10^{-6} + 1) \times (f_{RO} \times 10^{-6} + 1) \times f_c^{UL} - f_c^{UL} \quad (36)$$

where f_c^{UL} is the carrier frequency in the uplink and f_{RO} denotes the residual frequency offset after the downlink synchronization in ppm. As it is specified in [29], the UE modulated carrier frequency should be accurate to within +/-0.1ppm. Accordingly, $f_{RO} = 0.1$ ppm.

In practice, the UE may not adjust perfectly the carrier frequency to counteract the Doppler effects. Then, the carrier frequency offset becomes:

$$CFO_{UL} = (DS_{RO} \times 10^{-6} + DS_{UE} \times 10^{-6} + 1) \times (DS_{RO} \times 10^{-6} + DS_{UE} \times 10^{-6} + 1) \times (f_{RO} \times 10^{-6} + 1) \times f_c^{UL} - f_c^{UL} \quad (37)$$

The parameter DS_{RO} denotes the residual Doppler frequency shift owing to the imperfect compensation. The sources of error include:

- Inaccuracies in the satellite position
- Inaccuracies in the UE position.

From Table 18, it can be inferred that the beam radius does not come into play when the UE is aware of the exact Doppler frequency shift. The uplink CFO increases significantly in aeronautical communications. In this regard, the highest mismatch of the uplink frequency corresponds to the scenario where the satellite has to absorb the Doppler introduced by the terminal mobility.

Table 18: Uplink CFO for LEO 1300km with perfect compensation in Ka-band.

Compensation scheme	UE compensation			
Scenario	Airway	Stationary	Airway	Stationary
Beam diameter (km)	130	130	40	40
CFO (KHz)	51	3	51	3

Impact on standardization: To support the airway use case, the requirements for the standard are speeds up to 1000 km/h. This leads to a Doppler frequency shift of 0.8 ppm when the minimum elevation angle is 30°. The 3GPP has studied the high-speed train use case to support maximum speed with 350 km/h in FR2 [30]. In this case, the Doppler frequency shift corresponds to 0.324 ppm. To ensure connectivity with more severe Doppler effects, such as the airway scenario, several procedures need to be enhanced. Concerning the random access procedure, the enhancements that are needed to support terminals mounted on planes, can follow two different approaches:

- Exploit plane velocity and position information together with the satellite ephemeris, in order to compensate in the first phase of the random access procedure the Doppler effects induced by both the motion of satellite and the plane.
- Modify the random access response that is transmitted in the second step of the random access procedure so that it conveys a frequency offset correction command in addition to the time advance. The preamble detector shall be modified to estimate the delay and the carrier frequency offset that is associated to each user that initiates the attachment to the network. The resolution of the estimated frequency values shall ensure that the residual frequency misalignment will be lower than that encountered in the high speed train use case. The target could be to have a similar error as vehicle mounted relays.

3.2.5.2 Time offset

The delay that experiences PRACH signal is essentially the service link RTT, which is twice the slant range between the satellite and the user divided by the speed of light.

UE compensation with and without satellite compensation. In this mode of operation, the time misalignment introduced by the propagation delay can be virtually corrected by the UE. In such a case, only small offsets corresponding to the channel delay spread shall be present.

Impact on the standard: The estimated RTT delay may be subject to errors given by satellite and UE position inaccuracies. Under these conditions, the CP of the PRACH signal could be extended to absorb the resulting time offset.

3.2.5.3 Analysis of 5G NR preamble formats

The objective of this section is to analyse the robustness of the preamble formats specified in [22] to deal with time and frequency offsets. The most suitable designs for NTN correspond to the formats B4 and C2. The rationale is as follows. The repetition scheme that is used to generate the format B4 allows detecting the preamble in low SNR conditions. The CP transmitted by the format C2 is useful to support large time offsets. The rest of formats either transmit a shorter CP or less repetitions. Hence, they are more vulnerable to time offsets and more sensitive to noise and interference than the formats C2 and B4, respectively.

Preamble format B4: The preamble signal is generated by concatenating 12 Zadoff-Chu sequences. The CP duration is given by $T_{CP} = 30.47 \times 2^{-\mu}$ [us].

Preamble format C2: The preamble signal is generated by concatenating 4 ZC sequences. The CP duration is given by $T_{CP} = 66.66 \times 2^{-\mu}$ [us].

Note that the variable μ controls the subcarrier spacing as $\Delta_f = 15 \times 2^\mu$ kHz. On the one hand, increasing the subcarrier spacing is beneficial to increase robustness against the CFO. On the other hand, the higher the subcarrier spacing, the shorter the CP and thus, the system becomes more sensitive to time misalignments. To investigate this trade-off, Table 19 presents the time offset that is tolerated by the preamble formats B4 and C2, for different subcarrier spacings. The general rule to ensure successful preamble detection depends on the fulfilment of two conditions, namely:

- The time offset shall be lower than the CP duration
- The frequency offset shall not exceed half the subcarrier spacing.

If these conditions are not met, it is not possible to separate the two effects, *i.e.*, delay and frequency shifts, leading to timing ambiguities.

Table 19: Tolerance to time offsets supported by preamble formats B4 and C2, [22]

Preamble formats	B4				C2			
Subcarrier spacing (KHz)	15	30	60	120	15	30	60	120
Time offset (us)	30.47	15.23	7.61	3.80	66.67	33.34	16.67	8.33

3.2.5.4 Design guidelines for a robust PRACH format

According [11], the satellite ephemeris and the common time advance parameters can be used for uplink synchronization upon acquiring the SIB19. This information is valid during a period (from epoch time) that is also signalled in SIB19. As specified in [11], the highest update rate for satellite ephemeris is every 5 seconds.

In presence of UE and satellite position inaccuracies, the pre-compensated Doppler frequency and RTT delay will be subject to errors. The magnitude of the errors depends on the UE and satellite position updated frequency. Imperfect tracking of the UE antenna leads to either underestimated or overestimated RTT. Consequently, the PRACH signal could be delayed or received in advance with respect to the random access occasion. This is shown in Figure 34. The time misalignment may lead to interference to already synchronized signals. The delays can potentially be absorbed by the guard interval (GI). However, when the PRACH signal reception is affected by negative offsets, previous slots cannot be protected.

To overcome the effects from overestimating the RTT, the transmission timing of the PRACH signal has to be delayed according to the maximum estimation error made by the UE. Then, the TA that shall be applied for the transmission of msg1 is given by:

$$T_{TA} = T_C (N_{TA} + N_{TA,offset} + N_{TA,adj}^{common} + N_{TA,adj}^{UE} - N_{TA,margin}) \quad (38)$$

where $N_{TA,margin}$ is a new configurable parameter used as a margin to handle the UE's estimation uncertainty. The rest of the parameters are described in Section 3.1.4. As the uncertainty is unlikely to be known, the proposed approach is to set the pre-compensation margin $N_{TA,margin}$ such that the PRACH is delayed by half the CP period T_{CP} . With this solution, if the uncertainty error is within $[-T_{CP}/2, T_{CP}/2]$, then it follows that the network can handle overestimated RTT with unipolar TA commands. The concept is illustrated in Figure 34.

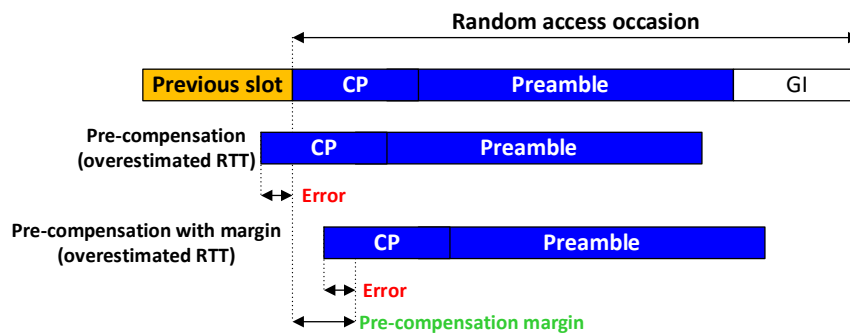


Figure 34: Pre-compensation with and without margin when the RTT is overestimated

The PRACH configuration can be changed to increase the robustness to time offsets. To this end, the legacy FR2-TDD configuration [22] will be used as baseline. Accordingly, in TDD mode, some PRACH signals do not start at symbol zero. The resulting margin is placed to mitigate the impact of TDD DL-UL scheduling. In FDD, the non-zero starting symbol is not necessary. This opens the door to use the remaining resources within the subframe to extend the CP and the GI, so that higher uncertainty errors can be corrected, and gives possibilities new PRACH configurations.

To generate the PRACH signal, first the preamble is obtained by concatenating N identical Zadoff-Chu (ZC) sequences, where N depends on the format. Then, the CP is appended. Analogously to the preamble, the CP can encompass multiple ZC sequences as well. Remarkably, this format is currently not supported by the standard. The resulting signal is fed into the multicarrier modulator, which implements the discrete Fourier transform spread OFDM (DFT-s-OFDM) waveform. At reception, the PRACH signal is delayed, due to the imperfect compensation.

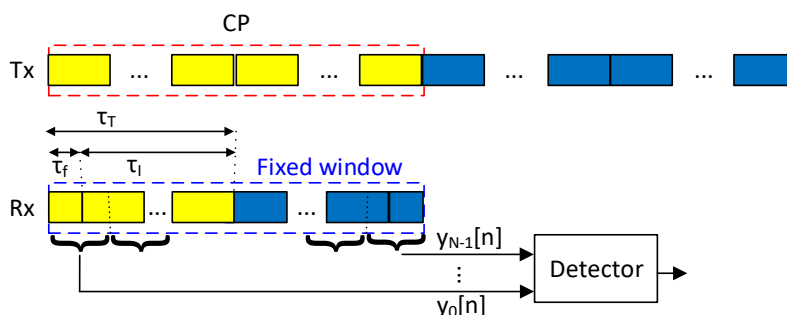


Figure 35: The detection window for the fractional delay

As Figure 35 shows, the delay can be expressed in samples as $\tau_T = \tau_f + \tau_I$. The fractional and the integer delays and are expressed as

$$\tau_f = \text{mod}(\tau_T, N_{ZC}) \quad (39)$$

$$\tau_I = T_{SEQ} \left\lfloor \frac{\tau_T}{N_{ZC}} \right\rfloor \quad (40)$$

where N_{ZC} is the duration of one ZC sequence. Next, upon discarding the CP, the gNB uses a fixed detection window to capture the samples of the preamble. Then, the samples are divided into N sequences that are processed by the OFDM demodulator. The j -th demodulated sequence is represented by $y_j[n]$, for $j = 0, \dots, N - 1$. Due to the CP transmission, the received sequence exhibits circularity. To find the signature of the received preambles and to estimate the delay, the detector first computes the correlation as

$$\rho_{jm} = \left| \sum_n y_j[n] y_{u,v}^*[n] e^{\frac{j2\pi}{N_{FFT}} mn} \right|^2, \quad 0 \leq m \leq N_{FFT} - 1 \quad (41)$$

where

$$y_{u,v}[n] = \frac{1}{\sqrt{N_{ZC}}} \sum_{m=0}^{N_{ZC}-1} x_{u,v}[m] e^{-\frac{j2\pi}{N_{ZC}} mn} \quad (42)$$

The signal $y_{u,v}[n]$ is the frequency domain representation of the preamble $x_{u,v}[m]$, which is generated according to

$$x_{u,v}[n] = x_u(\text{mod}(n + C_v, N_{ZC})) \quad (43)$$

$$x_u(i) = e^{-\frac{j\pi u i(i+1)}{N_{ZC}}}, \quad 0 \leq i \leq N_{ZC} - 1 \quad (44)$$

where u represents the root index of ZC sequence, and C_v represents cyclic shift of the preamble. The variable N_{FFT} denotes the size of the DFT and controls the resolution of the estimated delays. To enhance the detection, the decision variable is computed by performing a non-coherent accumulation, namely:

$$\rho_m = \sum_{j=0}^{N-1} \rho_{jm} \quad (45)$$

If the candidate preamble $x_{u,v}[n]$, which is locally generated, coincides with the transmitted preamble, then ρ_m will exhibit a correlation peak at $m = \left\lfloor \frac{N_{FFT}}{N_{ZC}} \tau_f \right\rfloor$. It is worth emphasizing that only the correlation values that exceed a predefined threshold are classified as peak values. The peak search is executed in the subset that satisfies $\rho_m \geq r_{th}$. The threshold is fully characterized by the chi-square distribution with N degrees of freedom and the target false alarm probability, [31]-[32]. From the peak position, it is straightforward to estimating the fractional delay. However, the detector is not able to find the boundaries between the CP and the preamble signal, leading to estimation errors. This observation highlights that new detection strategies shall be devised to estimate the integer part of the delay. Some insights are provided in the following.

Once the fractional part of differential delay is obtained, the received PRACH signal can be shifted back τ_f samples, so that the symbol boundaries are aligned with the reference of the PRACH slot. The estimation of the index that is related to the integer component is equivalent to determining the beginning of the PRACH signal. Without loss of generality, it is assumed that the CP and the GI encompass N_{CP} and N_{GI} symbols, respectively. Hence, the PRACH slot is formed by $N + N_{CP} + N_{GI}$ symbols. As Figure 36 highlights, the idea is to remove the symbols that have been used to detect the fractional delay and then, find the boundaries of the received burst from the demodulated sequences $\{z_0[n], \dots, z_{N_{CP}+N_{GI}-1}[n]\}$. This can be accomplished by computing the cross-correlation measurement

$$S_j = \left| \sum_n z_j[n] y_{u,v}^*[n] \right|^2 \quad (46)$$

The sequences $\{z_j[n]\}$ either integrate a complete ZC sequence or just contain noise and interference. This observation highlights that the estimation of the integer delay could be governed by $\{S_j\}$. Upon identifying the N_{CP} highest measurements, the ambiguity can be resolved and thus, the integer delay can be estimated.

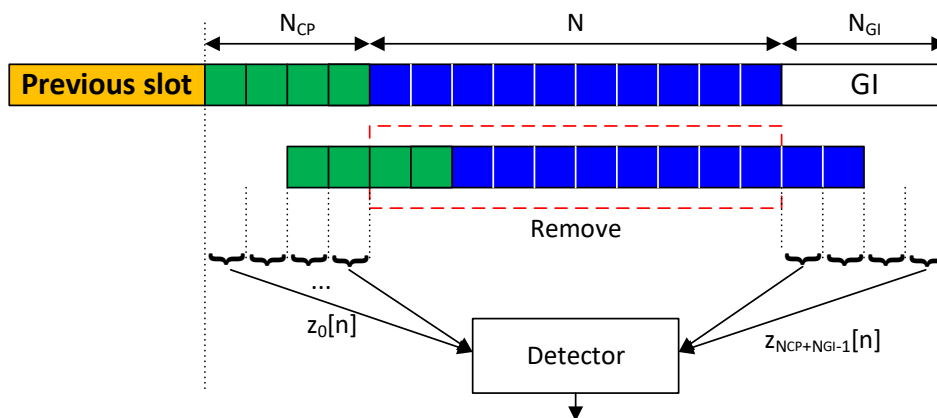


Figure 36: The detection window for the integer delay.

NUMERICAL RESULTS

The performance of the proposed design is evaluated using the orbit and the system parameters described in section 2. Concerning the channel model, LOS conditions have been assumed. The PRACH configuration is provided in Table 20. The modified preamble is implemented with $\Delta_f = 60\text{KHz}$, $N_{ZC} = 139$ and $N_{GI} = N = N_{CP} = 4$. This configuration is able to handle the TO and the CFO that come from the positioning errors at the Ka band. More precisely, the detector is able to estimate delays up to four times the maximum value supported by the standard in FR2.

In Figure 37, the missed detection probability (MDP) is illustrated for a UE positioning error uniformly distributed inside a circular uncertainty region of a 5km radius. As a benchmark, the standardized preamble format C2 ($N_{ZC} = N_{GI} = 1, N = 4$) is simulated in a terrestrial deployment, where the delay does not exceed the duration of one ZC sequence and the CFO is zero. The error cases resulting in incorrect detection encompass several possibilities: 1) detecting a preamble different from the one transmitted, 2) failing to detect any preamble at all, and 3) correctly detecting the preamble but with an erroneous timing estimation. Specifically, a timing estimation error is declared if the magnitude of the error exceeds $1/(N_{ZC} \times \Delta_f)$. The number of simultaneous users is denoted as N_U and the elevation angle as

θ . The threshold that is used to classify the correlation values as peaks is computed to ensure a false alarm probability of $P_{FA} = 10^{-3}$.

Table 20: PRACH configuration.

PRACH bandwidth	$B_{PRACH} = 8.34\text{MHz}$
PRACH subcarrier spacing	$\Delta_f = 60\text{ KHz}$
Size of the ZC sequence	$N_{ZC} = 139$
FFT size of the detector	$N_{FFT} = 256$
Length of the preamble	$N = 4\text{ symbols}$
Length of the CP	$N_{CP} = 4\text{ symbols}$
Length of the GI	$N_{ZC} = 4\text{ symbols}$

The simulation verifies that the proposed design for NTN is able to estimate higher delays than the standardized random access procedure in TN without significant performance degradation. Interestingly, similar performance is observed at low and high elevation angles. As expected, by increasing the number of users, the performance of the detector degrades.

Future work may consider developing more efficient detection algorithms and investigating other preamble formats than those based on repeating ZC sequences.

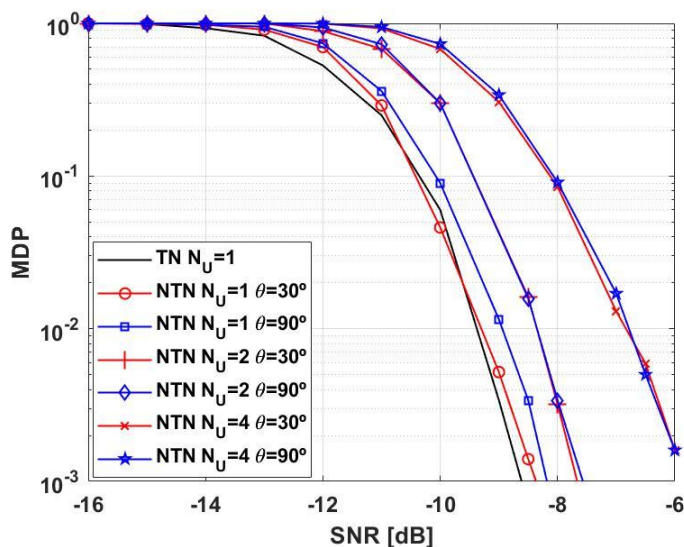


Figure 37: MDP over SNR.

4 USER-CENTRIC AND DIGITAL BEAMFORMING SOLUTIONS

This section aims at setting the scene for user-centric beamforming solutions in 5G-Advanced systems, to be then completed in D4.6 with the finalisation of Task 4.2. More specifically, this section provides the following contributions:

- A scientific review of the State-of-the-Art (SoA) related to user-centric beamforming algorithms. Solutions based on both the CSI and location estimates provided by the UE are considered.
- A scientific review of the SoA related to RRM algorithms supporting the implementation of beamforming/precoding via NTN.
- The system functional procedures for CSI-/location-based user-centric beamforming considering a single NTN node, highlighting the role of each network element and the required adaptations compared to the current NR-NTN specifications.
- The performance assessment of the considered CSI-/location-based algorithms with a single transmitting NTN node. This evaluation is based on a full buffer assumption and a random RRM scheduling. In this version, the CSI/location estimates are ideal and non-instantaneous, *i.e.*, ancillary information aging is taken into account. Both clear-sky and LOS channels are considered, as introduced in Section 2.4.1.
- The design and performance evaluation of a random RRM algorithm with a minimum distance requirement among the users scheduled in the same time slot, aimed at improving the beamforming performance
- The description of candidate models for non-uniform user and traffic distributions, users' movement, non-uniform RRM algorithms, and non-ideal CSI/location estimates, which will be evaluated during the prosecution of Task 4.2.

It shall be noticed that in the following the outcomes of the initial activities of Task 4.2 are presented. As such, its objectives are : i) defining the high-level procedures and information flows for the possible system architectures that support CSI-/location-based user-centric beamforming; ii) providing an initial performance assessment in a standalone NTN node scenario to identify the most significant performance trade-offs and system parameters; and iii) defining the activities to be performed to finalise the study in the final issue of this deliverable.

4.1 SCIENTIFIC REVIEW

4.1.1 Precoding and beamforming via satellite

4.1.1.1 Overview

Notably, legacy Satellite Communication (SatCom) systems are typically based on frequency reuse schemes, for instance 3 or 4 colours, in which the available bandwidth is split into multiple non-overlapping channels differentiated in the frequency and polarisation domains. Then, these channels are assigned to the on-ground coverage on a geographic basis to limit interference, by mapping them to specific beams of the desired beam lattice. Targeting higher capacities allowing to cope with the ever-increasing requirements for 5G, and now 6G, services, system design approaches have been directed, among the others, to a better exploitation of the available spectrum. This can be achieved by means of advanced spectrum

usage paradigms, such as Cognitive Radios, [33]-[34], or Dynamic Spectrum Access, [35], or by aggressively allocating the resources through full frequency reuse (FFR) schemes, in which the frequency reuse factor is decreased to 1. Focusing on the latter approach, effective interference management techniques are required to cope with the massive co-channel interference, such as precoding and beamforming.

The research surrounding the integration of the MIMO technology, through precoding and digital beamforming solutions, into NTN systems is quite comprehensive. Initial studies on Multi-User MIMO (MU-MIMO) via satellite primarily examined the use of Zero Forcing (ZF) and MMSE approaches, revealing potential throughput improvements of up to 80% for both the forward and the return links, [36]. Then, a thorough survey has been conducted in [37] on employing MIMO over satellite channels, covering both stationary and mobile satellite communication and identifying key challenges in particular related to the satellite channel. In [38], discussions have emerged on the critical issue of having only partial CSI at the transmitter in satellite MIMO systems, proposing a new strategy to enhance both the sum-rate and the availability. Additionally, European Space Agency (ESA)-funded initiatives have explored the incorporation of precoding into systems implementing DVB-S2X, tackling various practical MIMO challenges in HTS systems, [39]. These challenges include frame synchronization, inaccurate phase estimates, imperfect CSI due to user terminal estimation errors, and the effects of utilizing multiple gateways. Recent studies have reviewed precoding approaches for multi-beam satellite systems, considering precoder design optimization under linear and non-linear power constraints, [40]-[42]. Furthermore, discussions on linear precoding's efficiency, considering traffic demand and integrating generic linear constraints into the transmit covariance matrix, have shown significant gains over traditional frequency reuse methods, [43]. Issues and solutions regarding On-board Beamforming (OBBF) for MIMO in multi-gateway contexts, as well as system design considerations for MMSE precoding with adaptive antennas, have been explored, [44]-[45]. Other research has focused on traffic-driven beam design and user scheduling for precoding in Geostationary Earth Orbit (GEO) systems, alongside unsupervised machine learning techniques for scheduling and location-based beamforming algorithms, [46]-[48].

More recent discussions have delved into distributed antenna array implementations in Satellite Communications, evaluating array configurations to address grating lobes and presenting an Enhanced Logarithmic Spiral Array (ELSA) design, [49]-[51]. Studies on satellite swarms have concentrated on network and link level handovers, cross-layer design for power allocation and handover management, and AI-enhanced solutions. Additionally, the examination of distributed MIMO effectiveness on the uplink and a hybrid architecture merging Cell Free-MIMO (CF-MIMO) in terrestrial segments with a non-terrestrial layer for aiding users in challenging channel conditions have been introduced, [52]-[53].

Additionally, CNIT (through the RU of the University of Bologna) has been addressing user-centric beamforming and CF-MIMO via NTN in the last few years, as reported in [48], [54]. The activities of Task 4.2 reported in this deliverable build on such baseline.

4.1.1.2 Beamforming algorithms

As already highlighted above, the massive research interest in beamforming led to a vast literature and, thus, to many different algorithms. These algorithms can be broadly classified taking into account two factors: the on-board Beamforming Network (BFN) and the type of ancillary information that is needed at the transmitter to compute the beamforming coefficients.

The different available BFN solutions have been detailed in D3.2 Section 3.2.4, and summarised in the previous sections of this deliverable: i) Analog BFN (ABFN), which is relatively simple compared to other architectures but it provides a limited flexibility for generating/re-directing the beams; ii) Digital BFN (DBFN), in the time domain or in the

frequency domain, providing the most flexibility in resource allocation at the expense of an increased complexity; and iii) Hybrid BFN (HBFN), which mixed ABFN and DBFN aiming at reducing the energy consumption and complexity.

With respect to the ancillary information, two categories of beamforming algorithms can be identified: i) CSI-based, in which each user shall estimate the channel coefficient with respect to each transmitting equivalent antenna (precoding) or radiating element (beamforming); and ii) location-based, in which the CSI vector of each user is inferred through its location estimate and the knowledge, at the transmitter, of the current satellite position. Both approaches will be evaluated in the 5G-STARUST project and more details are discussed in the next sections.

Table 21 provides a summary of the beamforming algorithms available in the literature. For each algorithm, we provide its applicability to the ABFN, DBFN, HBFN architectures and the type of ancillary information required at the transmitter to compute the beamforming matrix.

Table 21: Summary of beamforming algorithms with BFN architecture applicability and required ancillary information.

Beamforming (BF) technique	Architecture applicability	Ancillary information	References	Notes
Minimum Mean Square Error (MMSE)	DBFN	CSI	[48], [53]-[57]	
Location-Based MMSE (LB-MMSE)	DBFN	Location	[48], [54]	
Signal-to-Leakage-plus-Noise Ratio (SLNR)	DBFN	CSI	[9], [56], [58], [59]	
Zero Forcing (ZF)	DBFN	CSI	[55], [56]	
Spatially Sampled MMSE (SS-MMSE)	DBFN	Location	[48], [54]	
Generalized Multicast Multibeam precoding	DBFN	CSI	[60]	
Block Singular Value Decomposition	DBFN	CSI	[61]	
Matched Filter (MF) or Conjugate BF	DBFN	CSI	[57], [62]	
Enhanced Normalized Conjugate BF (ECB)	DBFN	CSI	[62]	
Truncated Polynomial Expansion (TPE) Newton Iteration (NI) Chebyshev Iteration (CI)	DBFN	CSI	[63]	Those algorithms are examples of advanced precoders/beamformers with approximate/avoid matrix inversion methods
Dirty-Paper Coding (DPC)	DBFN	CSI	[63]	Example of non-linear algorithm
Conventional BF (beam steering)	ABFN	Location	[56], [64]	Conventional BF, i.e., applying a pure Analog BF based on the beam steering towards the intended user
Multi-Beam (MB)	ABFN	Location	[48], [56], [57]	
ZF + Conventional BF	HBFN	CSI	[65]	
Conjugate BF + Conventional BF	HBFN	CSI	[65]	
DFT beam space codebook	HBFN	Location	[66]	DFT-based grid of beams as in Type I and Type II 5G New Radio CSI codebooks

In line with the payload assumptions reported in the previous sections and in D3.2, unless otherwise specified, we focus on DBFN architectures in the frequency domain, which provide

the best flexibility in allocating the resources at sub-carrier level (frequency) and OFDM symbol level (time). In this context, Table 22 provides an overview of the advantages and disadvantages of the DBFN algorithms reported above.

Table 22: Pros and cons of the identified DBFN beamforming algorithms.

Beamforming (BF) technique		Pros	Cons
MMSE		<ul style="list-style-type: none"> • Good performance in both low and high SNR regime 	<ul style="list-style-type: none"> • Requires CSI estimation. • High complexity: requires matrix inversion
LB-MMSE		<ul style="list-style-type: none"> • Good performance in both low and high SNR regime • Requires only users' locations 	<ul style="list-style-type: none"> • High complexity: requires matrix inversion
SLNR		<ul style="list-style-type: none"> • Good performance in both low and high SNR regime • Uses a customized regularization factor for each user 	<ul style="list-style-type: none"> • Requires CSI estimation • High complexity: requires matrix inversion for each user
ZF		<ul style="list-style-type: none"> • Good performance in high SNR regime. 	<ul style="list-style-type: none"> • Noise enhancement in low SNR regime • Requires CSI estimation
CBF		<ul style="list-style-type: none"> • Requires only users' locations • Low complexity • Analog BF (low cost) 	<ul style="list-style-type: none"> • Poor interference rejection capability
MB		<ul style="list-style-type: none"> • Requires only users' locations • Very low complexity, it uses a predefined codebook 	<ul style="list-style-type: none"> • Approximated location scheme • Poor performance with a small number of beams
SS-MMSE		<ul style="list-style-type: none"> • Requires only users' locations 	<ul style="list-style-type: none"> • Approximated location scheme • High complexity: requires matrix inversion
MF		<ul style="list-style-type: none"> • Low complexity 	<ul style="list-style-type: none"> • Poor interference rejection capability.
ECB		<ul style="list-style-type: none"> • Improves the channel hardening and reduces channel fluctuations • Enhanced DL spectral efficiency 	<ul style="list-style-type: none"> • Requiring accurate CSI estimation • Minor variation of the Conjugate BF scheme
MMSE based on Matrix Inversion Approximation	TPE	<ul style="list-style-type: none"> • Similar performance of MMSE • Has an optimized coefficient to speed up the convergence rate 	<ul style="list-style-type: none"> • The determination of the optimized coefficient is complicated and must be updated in each iteration (costly and with relatively high complexity).
	NI	<ul style="list-style-type: none"> • The matrix inversion is easy to be implemented • Fast convergence rate in the later stage of iterations 	<ul style="list-style-type: none"> • Its initial value calculation is very complicated
	CI	<ul style="list-style-type: none"> • Fast convergence rate during the whole algorithm (faster than NI with only few iterations) • The same achievable rate of MMSE only after 2 iterations 	<ul style="list-style-type: none"> • It has higher complexity than NI
DPC		<ul style="list-style-type: none"> • High performance and capability to reduce the interference compared to linear algorithms 	<ul style="list-style-type: none"> • High computational complexity especially in massive MIMO
DFT beam space codebook		<ul style="list-style-type: none"> • Does not require CSI estimation • Compatibility with antenna array structures 	<ul style="list-style-type: none"> • Limited adaptability to dynamic channel conditions and changing users' locations due to the predefined structure of the codebook

Among these algorithms, in the following we consider MMSE (CSI-based) and LB-MMSE (location-based), as they provide the optimal performance as extensively demonstrated in the literature. In addition, conventional beamforming (CBF) is considered to have a performance benchmark with a low-complexity technique, which can be implemented also in ABFN architectures. As highlighted in the above table, CBF has a poor interference rejection capability; this behaviour will be useful to highlight some interesting performance trends with respect to the overall system dimensioning in the next sections.

While the performance evaluation in the following is based on MMSE, LB-MMSE, and CBF, it shall be noticed that future releases of this document might also consider other digital beamforming algorithms. Such possibility will be explored during the upcoming activities of Task 4.2, based on the continuation of the performance assessment. For instance, beam-based solutions, such as SS-MMSE and MB will be implemented to have a comparison of user-centric solutions with respect to more traditional beam-based approaches.

4.1.2 Radio Resource Management for beamforming via satellite

The necessity to efficiently allocate the resources to provide broadband access via SatCom has always been one of the key aspects for a proper system design. During the last years, the evolution of advanced technologies that exploit the flexibility of satellite payloads in time, frequency, and power is leading to interesting opportunities to optimise the resource allocation, in particular to cope with non-uniform traffic conditions. This is even more fundamental when taking into account the implementation of precoding and beamforming algorithms, the performance of which is notably impacted by the selection of the co-channel users. In the following, *precoding* denotes a system in which an on-ground beam lattice is pre-determined to serve the desired area and in which, to support FFR solutions, MIMO algorithms are implemented. With *beamforming*, we denote the generation of beams in desired directions. *User-centric beamforming* denotes beamforming algorithms that generate spot beams in the users', not the pre-determined beam centers', directions. It shall be mentioned that the vast majority of past studies related to RRM, with or without precoding, in multi-beam SatCom considers stationary Geosynchronous Orbit (GSO) systems, [67]-[87] and references therein. When considering LEO/VLEO deployments, the design of RRM algorithms is even more challenging, due to the high mobility characterising LEO constellations leading to limited visibility periods of the flying platform (down to a few minutes) and a potentially large number of available serving satellites per user. For the sake of completeness, it is worthwhile highlighting the work in [81], which provides an interesting and exhaustive overview of RRM algorithms in terrestrial networks implementing MU-MIMO solutions.

Within the existing literature, RRM algorithms can be broadly classified as SINR-based or non-SINR based scheduling. The former approach typically involves the initial computation of the achievable SINR for each user; this information is then exploited to allocate the user to a scheduling slot such as to optimise the performance (e.g., to limit the SINR degradation of the other co-channel users). This is an effective approach, but it rapidly becomes unfeasible when managing a large number of users due to the processing latency and computational complexity. Non-SINR based solutions do not rely on SINR estimates/pre-computations, but on other supporting information, e.g., channel matrix or users' locations. In both cases, the user scheduling problem can be framed as a grouping problem, i.e., the identification of the best possible grouping of the users based on a set of specific performance requirements, with each group associated to a transmission time interval. Such grouping problem is an NP-complete problem, typically solved through exhaustive search approaches.

In [88], an algorithm denoted as Sum Rate Maximization User Grouping (SMUG) is introduced. This algorithm divides users into multiple groups, with the users within each group simultaneously via Space Division Multiple Access (SDMA) and different groups served

through Time Division Multiple Access (TDMA); the proposed algorithm shows a competitive performance when the overall number of users in the system is relatively small. The work in [89] delves into designing user scheduling metrics for MU-MIMO systems and two hybrid user scheduling algorithms are proposed to balance the fairness among users, while maximising overall capacity with a greedy approach. Based on this work, the authors in [90] presented a novel computationally efficient algorithm, Multiple Antenna Downlink Orthogonal Clustering (MADOC), which considers both minimizing the number of groups and ensuring fairness among users; this work is an extension of [91]. In [92]-[93] the authors proposed a greedy iterative user scheduling based on the maximum clique algorithm for standalone LEO satellites implementing MU-MIMO; the results are compared to a location-assisted random RRM approach. The proposed RRM provides a good performance in terms of the per-user capacity. To further improve the experienced capacity per user, a possible approach is that of minimising the number of time slots (or scheduling groups), as this ultimately increases the percentage of time in which the users are served. To this aim, the same authors proposed an improved Maximum Clique Scheduler with constant graph density, [94]. Finally, in [57], the authors propose an interesting SINR-based RRM algorithm that takes into account massive MIMO scenarios for a GEO system. This algorithm is based on a dense beam lattice deployment, acting as a spatial sampling of the service area with more beams than antenna elements; the RRM algorithm exploits the expected SINR in order to iteratively define the user scheduling, by selecting the users so as to limit the increase in the interference of the potential co-channel users. The algorithm was also tested under non-uniform traffic distributions.

4.2 SYSTEM DEFINITION: STANDALONE NODE

4.2.1 Network Elements and system procedures

Two main NTN architecture design choices directly impact the implementation of beamforming solutions, [54]. First, the type of NTN payload, *i.e.*, transparent or regenerative, defines if functional split can be implemented. In the latter case, part or all the network elements providing beamforming-specific operations can be deployed on-board. In fact, the identification of a functional split option directly defines the layers of the NR protocol stack implemented in the gNB-DU and those implemented in the gNB-CU. Once the functional split option is defined, we can identify the Network Elements (NEs) in charge of the various beamforming operations:

- **Scheduling the users** to be served for a given period of time, *i.e.*, the NE implementing the desired RRM algorithm (see Section 4.2.4). In 3GPP NR specifications, the scheduler is located within the (high) MAC layer and it oversees the following operations, [13]:
 - assigning the resources to the UEs taking into account the buffer status and the Quality of Service (QoS) requirements of each UE and the associated radio bearers;
 - assigning resources taking account the radio conditions at the UE identified through measurements made at the gNB and/or reported by the UE.

In the downlink, which is our focus for user-centric beamforming, the gNB can dynamically allocate the resources to the UEs signalling them on the Physical Downlink Control Channel (PDCCH), which is continuously monitored by the UEs to find possible assignments when their downlink reception is enabled.

- **Computing the beamforming coefficients** based on the selected beamforming algorithm (see Section 4.2.3), power distribution, and required ancillary information (CSI or location). Notably, at each modification of one scheduled user, all user-centric beamforming coefficients shall be updated. This computation is co-located with the

scheduler, *i.e.*, in the high MAC layer. In fact, with beam-based techniques (*e.g.*, precoding, Beam Hopping), the scheduler selects the beams to be illuminated in a given time slot according to the selected RRM algorithm and this information is sufficient to obtain the pre-computed beamforming coefficients; with user-centric solutions, this approach is not applicable and the scheduler shall directly compute the beamforming coefficients, as there is no beam lattice to which a beam-based illumination plan is applicable. Then, depending on the type of required ancillary information, different interactions between the MAC layer and other NEs might be needed: i) for CSI-based algorithms, from the above discussion on the scheduler, no other element is required as the CSI elaboration can be co-located with the scheduler; ii) for location-based algorithms, the MAC layer shall obtain information on the UEs' locations, which requires interactions with the 5GC.. More specifically, location information can be provided by the Location Management Function (LMF) through a location service request; once such information is obtained, it can be assumed that all the operations required for location-based algorithms to define the beamforming coefficients are, again, co-located with the scheduler. Aspects related to the LMF and, more in general, ancillary information signalling are discussed in Section 4.2.1.2.

- **Applying the beamforming coefficients** to the signals to be transmitted (low PHY). In legacy SatCom systems, this led to the definition of On-Ground Beamforming (OGBF), when the coefficients are applied at the GW/gNB, or On-Board Beamforming (OBBF), when they are applied on-board. As in 5G-STARUST we focus on regenerative payloads, in the following we assume to always apply the beamforming coefficients on-board the NTN platform.

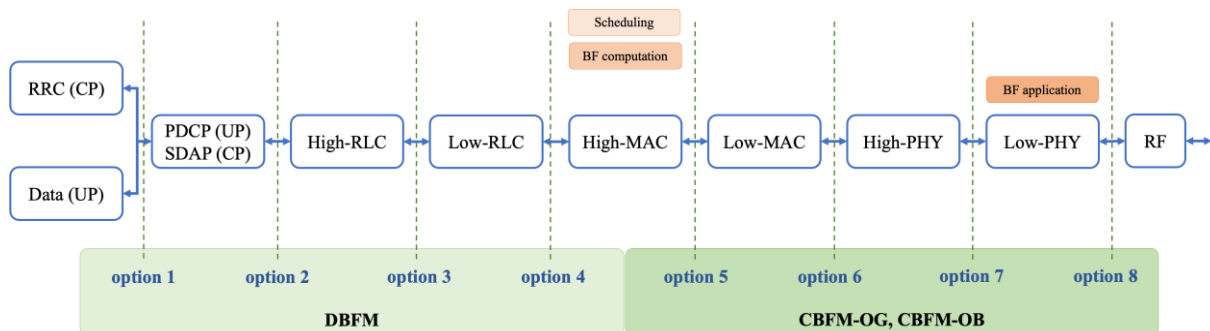


Figure 38: Functional split options and beamforming architecture.

Figure 38 shows the functional split options defined by 3GPP and the location of the operations listed above for the beamforming implementation. In particular, we can notice that:

- The application of the beamforming coefficients is always located in the low PHY. Thus, only with Option 8 it is located in the gNB-CU, while for all other options the application of the coefficients is located in the gNB-DU. Option 8 is not considered in the following, as it is out of scope of the 5G-STARUST project; thus, the beamforming coefficients are always applied to the transmitted signals in the gNB-DU.
- The computation of the beamforming coefficients and the users' scheduling are located in the high MAC. Thus, for options 4 (included) and below it is located in the gNB-DU, while with options 5 (included) and above they are located in the gNB-CU. In [3], these two cases are labelled On-Ground Beamforming and Scheduling Computation (OGBSC) and On-Board Beamforming and Scheduling Computation (OBBSC), respectively. It shall be noticed that this nomenclature assumes that, with split option 5 or above, the gNB-CU is located on-ground. However, there might be scenarios, in particular looking at 6G NTN

systems, in which the gNB-CU is located on-board another NTN platform, which then manages a set of gNB-DUs on-board “lower hierarchy” nodes in a multi-orbit multi-layer 3D network. In such scenario, the OGBSC definition would clearly not apply. Thus, we introduce the following extended definitions:

- **Distributed Beamforming Management (DBFM)**, which encompasses options 4 and below, *i.e.*, systems in which the scheduling and the beamforming computation and application are all implemented in the on-board gNB-DU.
- **Centralised Beamforming Management (CBFM)**, including options 5 and above, in which scheduling and beamforming coefficients computation are in the gNB-CU. As discussed above, the gNB-CU can be either on-ground or on-board a higher hierarchy NTN node; thus, the CBFM scenario can be further split in: i) **CBFM on-ground (CBFM-OG)**, when the gNB-CU is implemented on-ground; and ii) **CBFM on-board (CBFM-OB)**, when the gNB-CU is on-board another higher hierarchy NTN node in the global architecture.

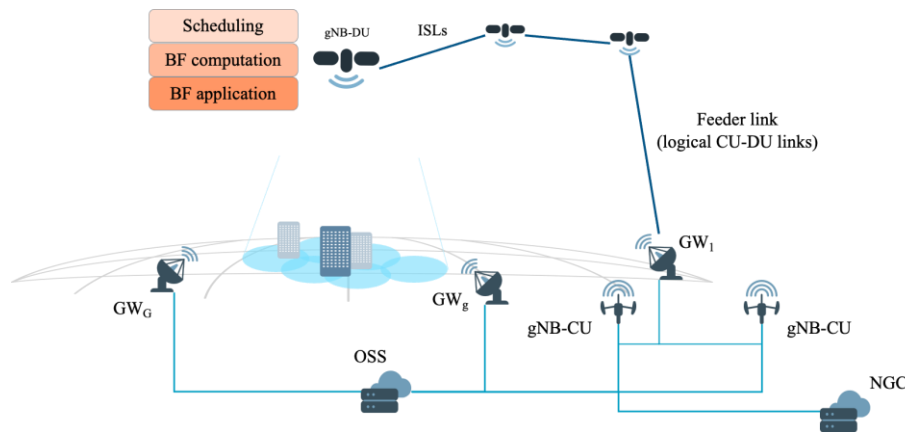


Figure 39: Beamforming architecture with DBFM.

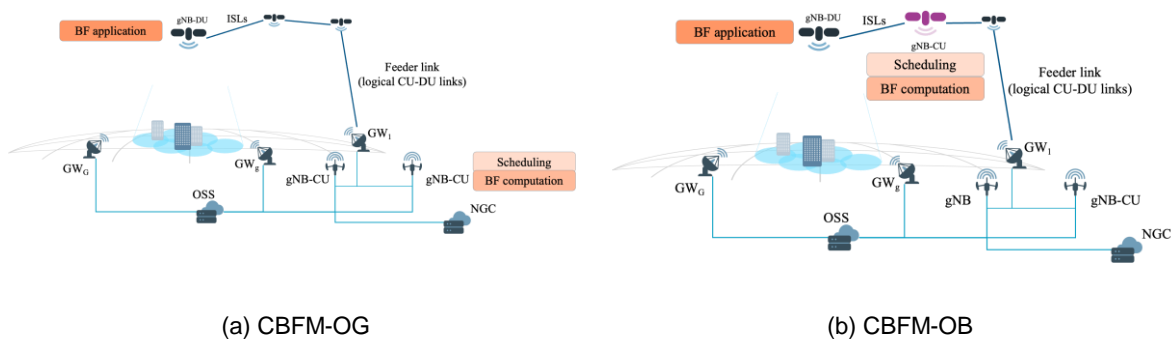


Figure 40: Beamforming architecture with CBFM-OG (a) and CBFM-OB (b).

Based on the above considerations, Figure 39 and Figure 40 show the high-level system architecture with DBFM and CBFM, respectively. The following segments can be identified:

- The ground segment includes G GWs providing NTN access to the terrestrial infrastructure, *i.e.*, among the NTN NGSO nodes equipped with gNB-DUs, the gNB-CUs and the 5GC. The ground segment also includes the Operation Support Systems (OSS), in charge of the overall satellite system management.

- The NT access segment, which includes the NGSO NTN nodes in the constellation equipped with gNB-DUs and, for future 5G-Advanced and 6G systems, also nodes embarking gNB-CUs. These nodes can provide either Earth-fixed or Earth-moving coverage, in 3GPP terminology. It shall be noticed that, in the DBFM and CBFM-OG solutions, the serving gNB-DU might be in direct visibility of the GW/gNB-CU; in this case, no ISLs is required. However, as soon as the satellite goes beyond the visibility of any GW, ISLs are required. In the CBFM-OB solution, ISLs are always required to guarantee the connectivity between the DU and CU, both on-board NTN platforms. Moreover, in the CBFM-OB solution, the ground segment clearly includes other gNBs or gNB-CUs, but the on-board gNB-CU directly connects to the NGC and OSS. Clearly, it might still interact with on-ground gNBs/gNB-CUs for network coordination purposes, but its operations in the user-centric beamforming framework do not require such connection.
- The on-ground user segment, in which a potentially massive number of UEs, either fixed or moving, is distributed and is served through the NTN infrastructure.

In both CBFM and DBFM scenarios, the NE in charge of computing the scheduling and beamforming coefficients shall provide the following functions:

- Implementing the RRM algorithm based on the UEs' traffic types and requests. The users' scheduling is usually performed over longer periods compared to the time frame/slot duration, e.g., between a few seconds and a few minutes. We denote the periodicity of the scheduling update as T_{sched} and as N_{sched} their number during the period in which the NTN node is serving the desired area, T_{serv} .
- Computing the beamforming coefficients for each time slot/frame, depending on the RRM resolution in the time domain. We denote this resolution as transmission slot, T_{slot} . For each transmission slot, the scheduler computes a complex beamforming matrix \mathbf{B} with size $N_B \times N_R$, where N_B denotes the number of separate user-centric beams per transmission slot and N_R the number of radiating elements in the on-board DRA antenna.
- The computation of the beamforming coefficients and the RRM algorithm are based on either the estimated CSI or the estimated location per visible user. In the former case, we can assume that the UEs directly provide their CSI reports to this NE; in the latter, this NE shall interact with the NGC to obtain the location of each visible UE. The location information, as discussed in Section 4.2.3, is exploited to extrapolate all non-stochastic terms in the channel coefficients, leaving all stochastic terms out of the estimated CSI (e.g., atmospheric loss and shadowing). We denote the periodicity of the reporting of ancillary information from the UEs to this NE as T_{rep} . It shall be mentioned that, usually, $T_{rep} \ll T_{sched}$ (e.g., $T_{rep} = 80$ ms and $T_{sched} = 2$ s, as in the initial performance assessment reported in this document); thus, the beamforming coefficients can be computed based on the scheduling defined previously, but exploiting updated CSI/location information.

The reports provided by the users shall include the following information: i) the requested traffic type and request; ii) the CSI estimates or their location; and iii) the terminal type/class, to derive information to estimate the noise power at the receiving equipment (required for the beamforming algorithms). The latter might be classified by the terminal manufacturers; in such cases, estimates shall be exploited. Figure 41 shows a representation of the relationship between the scheduling and reporting intervals, compared to transmission slots.

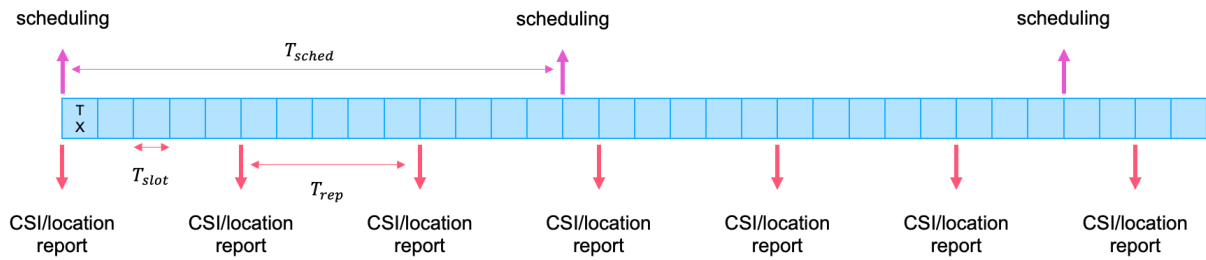


Figure 41: High-level relationship between scheduling and reporting intervals.

- Exploit the estimated or extrapolated CSI vectors to compute with good approximation the expected Signal-to-Noise-plus-Interference Ratio (SINR) for each user and select the best Modulation and Coding Scheme (MCS) for the expected channel conditions. This approach is a closed-loop solution, as it exploits the reports provided by the UEs. Also, open-loop solutions can be implemented using channel simulations; in fact, the main input data for the simulator are well known (e.g., total available power, number of antenna feeds, etc.) and they can be updated during the satellite lifetime (antenna feed patterns, users' positions, satellite power gains and losses, receiving antenna gain) or be measured (e.g., fading due to rain attenuation, shadowing, etc.). This solution would provide SINR estimates more in line with the current channel conditions, as it is not affected by the aging of the ancillary information. However, it also requires to implement a channel simulator on-board, which might significantly increase the payload complexity and energy consumption. In the following, we assume that the SINR estimates for the MCS selection are available.

Once the scheduling and the corresponding beamforming coefficients have been computed, these shall be provided to the NE applying the coefficients to the transmitted signals. As mentioned above, the coefficients can be updated for each transmission slot based on the latest CSI/location report, which means that $N_B \times N_R$ complex coefficients shall be transmitted with periodicity T_{slot} .

4.2.1.1 CSI report and required adaptations

In 3GPP specifications, the CSI-RS are used for: i) the downlink CSI acquisition (CSI report); ii) the downlink beam management procedure (beam reporting, measurements); and iii) the downlink mobility (e.g., handovers). In the standard, the CSI-RS can be periodic (continuous periodic transmission), aperiodic (single transmission), and semi-persistent (periodic transmission until de-activated).

Considering the importance of the ancillary information for user-centric beamforming, we consider periodic CSI-RS configurations. In this case, the period is defined in the RRC signalling and it can be set to 4, 5, 8, 10, 16, 20, 32, 40, 64, 80, 160, 320, or 640 slots. As we are assuming FR2 operation, the Sub-Carrier Spacing is either 120 kHz or 240 kHz, which correspond to time slots with duration 0.125 ms and 0.0625 ms, respectively. Thus, the largest periodicity that can be configured for the CSI-RS is 80 ms, obtained with 120 kHz SCS. This leads to the worst-case scenario in terms of CSI information aging and, thus, to a worst-case performance assessment in terms of ancillary information availability.

There are two aspects that shall be considered for the adoption of user-centric beamforming in NR-NTN. First, in 3GPP specifications, the CSI-RS signals are exploited to measure quantities such as the CQI, the PMI (i.e., an indicator of the pre-computed precoding codebook), or the Rank Indicator (RI). These measures provide quantised quality indications of the channel conditions, to be exploited to select the best precoding codebook at the

transmitter side. Second, the CSI-RS are designed and based on a beam-basis, *i.e.*, they would allow to estimate the channel between the UE and a beam, not between the UE and the radiating element. Thus, two modifications are needed from the point of view of 3GPP specifications: i) **the actual channel coefficients shall be estimated**, not quality indicators; and ii) **the channel coefficients must be estimated at radiating element level**, not beam level.

4.2.1.2 Positioning and required adaptations

The architecture supporting the UE positioning is defined in 3GPP TS 38.305, [96], and it is shown in Figure 42. The highlighted part of this architecture is the one we can consider in the following for user-centric beamforming in 5G-Advanced systems via NTN.

In general, the AMF receives a request for location services associated with a target UE from another network entity (such as the NE in charge of computing the scheduling and beamforming coefficients) or the AMF directly decides to initiate a location service on behalf of a target UE (*e.g.*, for emergency calls). The location service request is sent to the LMF, a new entity introduced in Rel. 16 that is central in the 5G positioning services. This network function processes the location service request and returns its answer to the AMF (*e.g.*, the estimated location of the UE). In case the service location was requested by another NE, as in our scenario, the AMF forwards such information to it.

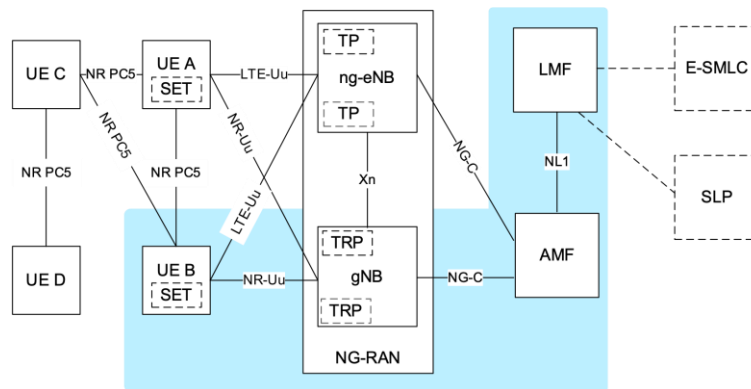


Figure 42: UE positioning architecture applicable to NG-RAN, [96].

Figure 43 shows the flow of the location service procedure for a UE in connected state, which can be assumed for the purpose of user-centric beamforming analyses:

- Step 1: a location service is requested by either a 5GC LoCation Service (LCS) entity (1a), or the AMF (1b), or the UE (1c).
- Step 2: the AMF transfers the location service request to the LMF.
- Step 3: the LMF triggers location procedures within the service (and, if possible, neighbouring) gNBs in the NG-RAN (3a) as well as in the UE (3b), for instance to obtain positioning measurements.
- Step 4: the LMF provides the location service response to the AMF with the required results, such as a location estimate for the UE.
- Step 5: depending on the NE requesting the location service, the response is forwarded by the AMF to the 5GC (5a) or the UE (5c), or it is directly used by the AMF (5b).

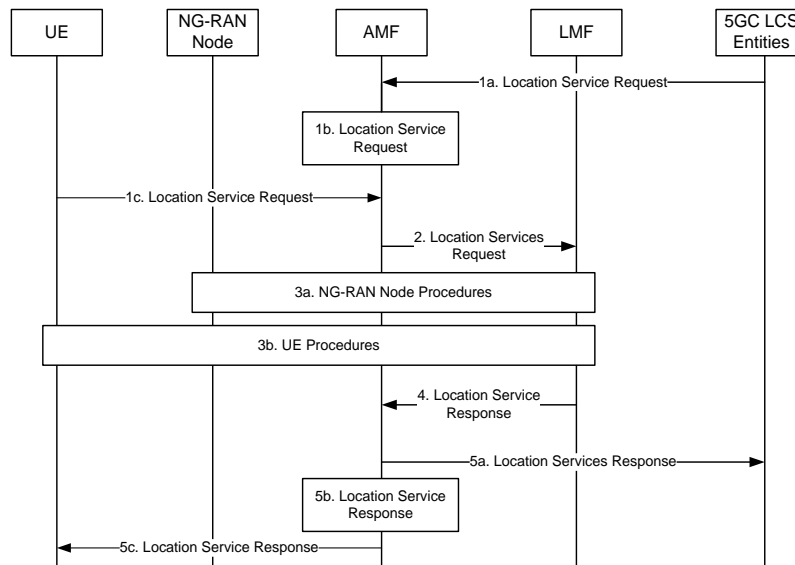


Figure 43: Location service support in 3GPP NR, [96].

In the following, we assume that each UE is equipped with GNSS capabilities, allowing it to estimate its location with a precision of a few meters considering commercial technologies. In principle, location-based algorithms would not require any adaptation to the current specifications. However, the estimated location is not made available by the UE directly to the NE in charge of computing the beamforming coefficients, but rather to the AMF and LMF. This might lead to a significant amount of overhead due to signalling to retrieve the UE locations, as they are not available in the RAN but only in the NGC also for privacy and security reasons. A possible adaptation to be (carefully) studied and eventually introduced is to **make the UE location available at RAN level** to reduce this overhead.

4.2.1.3 Procedures

Based on the overview of the role of the various NEs and the CSI/location reporting, we describe the high-level functional procedures that support user-centric beamforming.

DISTRIBUTED BEAMFORMING MANAGEMENT (DBFM)

With this solution, represented in Figure 39, all beamforming operations are implemented in the gNB-DU. Thus, the functional procedure is as follows:

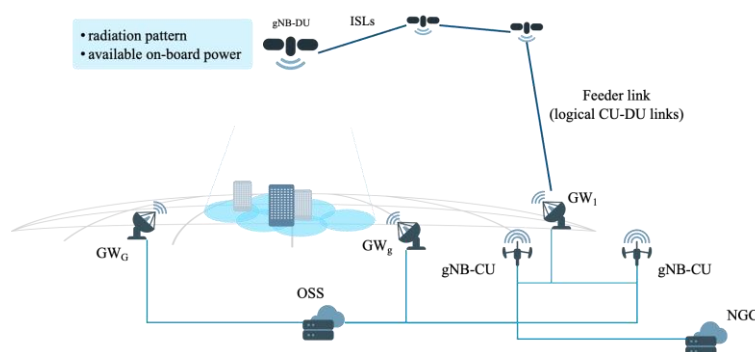


Figure 44: DBFM procedure - step 1.

1. Initially, it can be assumed that the entity in charge of computing the beamforming coefficients knows the radiation pattern at radiating element level and the total available power on-board the NTN node.
2. The UEs in visibility of the NTN node and requiring connectivity provide to the NTN node their location or CSI reports, the traffic request and type, and the type of terminal if possible.

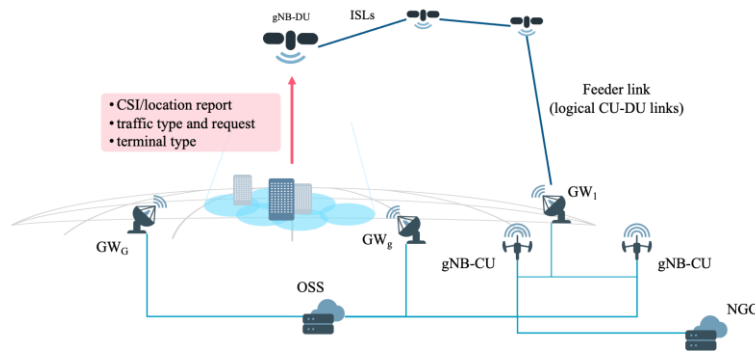


Figure 45: DBFM procedure - step 2.

3. For CSI-based solutions, the NTN node applies the RRM algorithm to compute the scheduling, the beamforming algorithm to compute the coefficients, and selects the best MCS per user. For location-based solutions, these operations can only be performed after the location of the UEs requesting a service has been retrieved from the LMF.

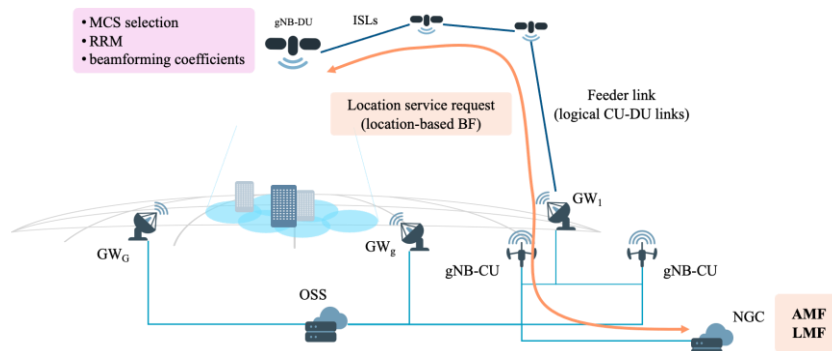


Figure 46: DBFM procedure - step 3.

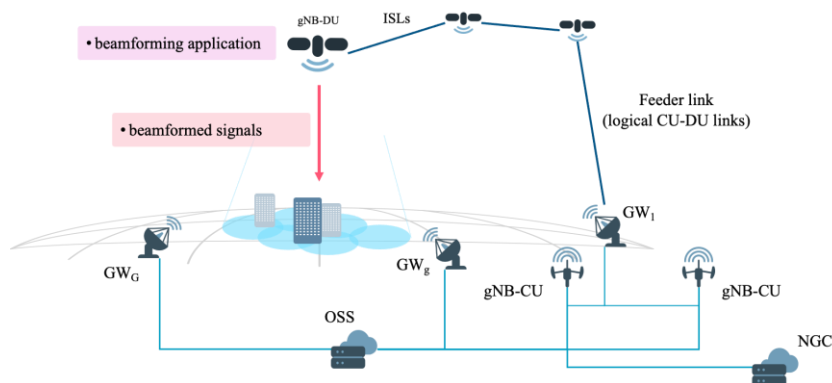


Figure 47: DBFM procedure - step 4.

- The NTN node applies the beamforming coefficients and sends the beamformed signals to the UEs to be served in each transmission time.

It shall be noticed that the DBFM approach is the most complex from the NTN node perspective, as all operations are implemented in the on-board gNB-DU. However, it is also the most efficient in terms of overhead, thanks to this centralisation.

Another relevant aspect to be highlighted is that, based on 3GPP specifications, all Packet Data Unit (PDU) sessions shall be managed and terminated in the gNB-CU. Thus, the DBFM architecture with split option 1 (*i.e.*, full gNB on-board) is already in line with this requirement. For split options 2, 3, and 4, even if from the beamforming management point of view everything can be done in the gNB-DU, still the connection to the gNB-CU is required to close the PDU sessions.

CENTRALISED BEAMFORMING MANAGEMENT ON-GROUND (CBFM-OG)

In this case, represented in Figure 40(a), the computation of the scheduling and the beamforming coefficients is in the on-ground gNB-CU. Thus:

- Initially, it can be assumed that the entity in charge of computing the beamforming coefficients knows the radiation pattern at radiating element level and the total available power on-board the NTN node.

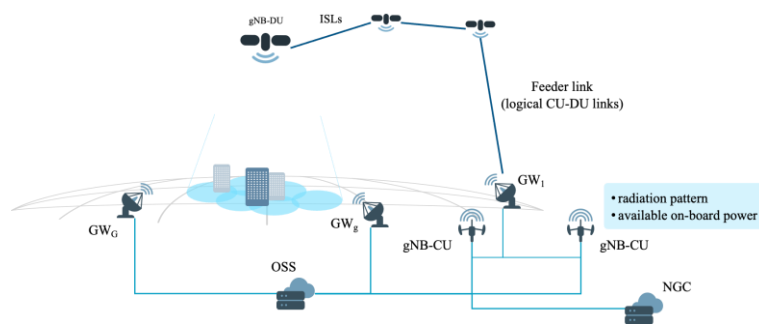


Figure 48: CBFM-OG procedure - step 1.

- The UEs in visibility of the NTN node and requiring connectivity provide to the gNB-CU their location or CSI reports, the traffic request and type, and the type of terminal if possible.

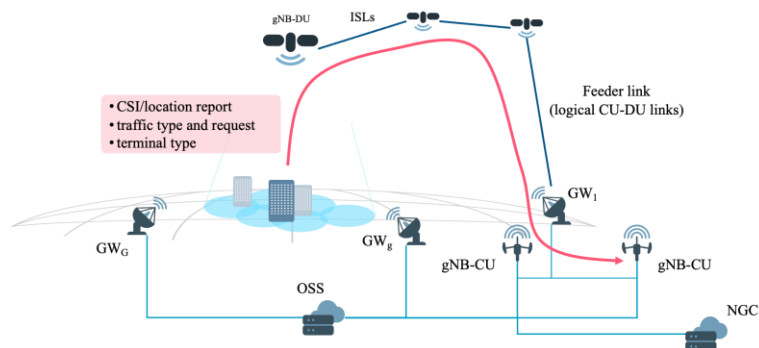


Figure 49: CBFM-OG procedure - step 2.

- For CSI-based solutions, the NTN node applies the RRM algorithm to compute the scheduling, the beamforming algorithm to compute the coefficients, and selects the best

MCS per user. For location-based solutions, these operations can only be performed after the location of the UEs requesting a service has been retrieved from the LMF as described in Section 4.2.1.2. The beamforming coefficients are then sent to the gNB-DU.

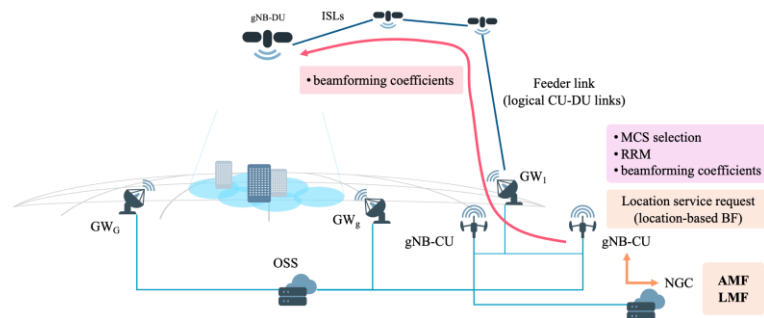


Figure 50: CBFM-OG procedure - step 3.

4. The NTN node applies the beamforming coefficients and sends the beamformed signals to the UEs to be served in each transmission time, as in the DBFM scenario in Figure 47.

It shall be noticed that the CBFM approach is significantly less complex from the NTN node perspective, as all operations apart the application of the coefficients are implemented in the on-board gNB-CU. However, it is also the less efficient in terms of overhead, due to the significant overhead introduced in steps 2 and 3.

CENTRALISED BEAMFORMING MANAGEMENT ON-BOARD (CBFM-OB)

This case is the companion of CBFM-OG, represented in Figure 40(b). Here, the computation of the scheduling and the beamforming coefficients is in the on-board gNB-CU. Thus:

1. Initially, it can be assumed that the entity in charge of computing the beamforming coefficients knows the radiation pattern at radiating element level and the total available power on-board the NTN node.

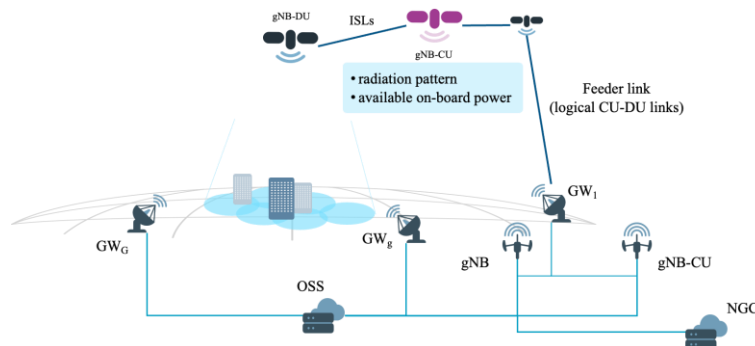


Figure 51: CBFM-OB procedure - step 1.

2. The UEs in visibility of the NTN node and requiring connectivity provide to the gNB-CU their location or CSI reports, the traffic request and type, and the type of terminal if possible.

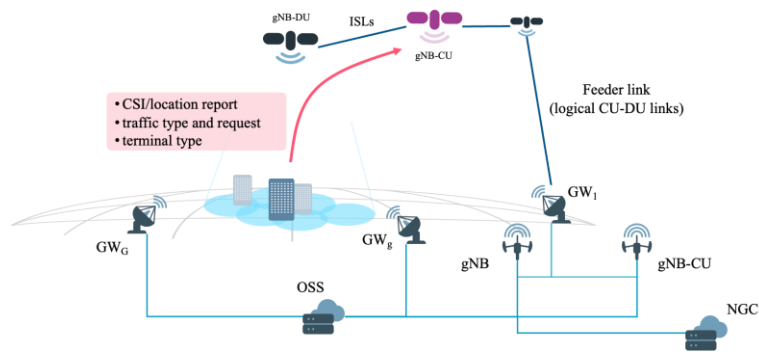


Figure 52: CBFM-OB procedure - step 2.

- For CSI-based solutions, the NTN node applies the RRM algorithm to compute the scheduling, the beamforming algorithm to compute the coefficients, and selects the best MCS per user. For location-based solutions, these operations can only be performed after the location of the UEs requesting a service has been retrieved from the LMF as described in Section 4.2.1.2. The beamforming coefficients are then sent to the gNB-DU.

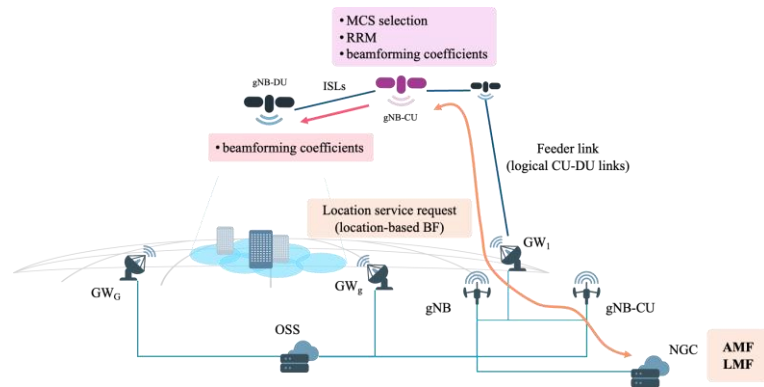


Figure 53: CBFM-OB procedure - step 3.

- The NTN node applies the beamforming coefficients and sends the beamformed signals to the UEs to be served in each transmission time, as in the DBFM scenario in Figure 47.

This solution has the same complexity as the CBFM-OG for the gNB-CU on-board an NTN node, but it requires a more complex constellation with advanced nodes embarking the gNB-CUs. This complexity provides the benefit of an extended flexibility in the global system management and an overhead almost as low as in the DBFM scenario. The only relevant information overhead is related to the location service request that shall flow to the NGC.

4.2.2 Aging interval

In Section 4.2.1, we provided a thorough discussion on the system procedures supporting user-centric beamforming, for both CSI-based and location-based techniques. In the former case, the UEs are assumed to be able to estimate the channel coefficient between them and each radiating element on-board; in the latter, UEs are equipped with GNSS capabilities and can estimate their location, which is assumed to be made available at the NE in charge of scheduling and computing the beamforming coefficients. In line with the functional procedures in Figure 45, Figure 49, and Figure 52, we can identify the *estimation time instant* in which the UEs estimate their CSI or locations and report them as t_E ; after an aging interval Δt , which depends on the specific architecture and category of beamforming algorithm, the transmission

can actually happen, *i.e.*, the *transmission time instant* is $t_T = \Delta t + t_E$, as shown in Figure 54. Clearly, during this aging interval, the NTN node and, perhaps, the UEs moved, which leads to a misalignment between the CSI/location used to compute the beamforming coefficients and the actual channel matrix encountered during the transmission. This ultimately leads to a performance loss in user-centric beamforming.

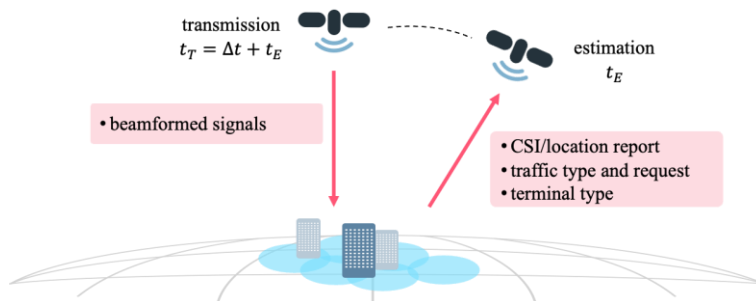


Figure 54: Aging interval and satellite position.

Table 23 shows the terms to be considered in the computation of the aging interval for the three identified architecture solutions. For location-based beamforming, two values are reported: i) *legacy* denotes the current possibilities with NR-NTN that include the interaction with the NGC; and ii) *advanced* denote the scenario in which the UEs' locations are provided to the NE computing the beamforming coefficients. In this table:

- τ_{proc} denotes the processing time to schedule the users and compute the beamforming coefficients;
- $\tau_{rep} \leq T_{rep}$ is the time elapsed since the last update of the ancillary information;
- $\tau_{NGC} = 2N_{hop}\tau_{ISL} + \tau_{feeder,DL} + \tau_{feeder,UL}$ is the time required to interact with the NGC, which includes twice the latency of N_{hop} ISLs and the uplink/downlink transmission on the feeder link;
- τ_{lsr} is the time required to complete the location service request with the AMF/LMF.

Table 23: Aging interval terms per user-centric beamforming architecture and algorithm.

Architecture	CSI-based Δt_{CSI}	Location-based legacy $\Delta t_{LOC}^{(leg)}$	Location-based advanced $\Delta t_{LOC}^{(adv)}$
DBFM	$\tau_{proc} + \tau_{rep}$	$\tau_{proc} + \tau_{rep} + \tau_{NGC} + \tau_{lsr}$	$\tau_{proc} + \tau_{rep}$
CBFM-OB	$\tau_{proc} + \tau_{rep} + 2\tau_{ISL}$	$\tau_{proc} + \tau_{rep} + \tau_{NGC} + \tau_{lsr}$	$\tau_{proc} + \tau_{rep} + 2\tau_{ISL}$
CBFM-OG	$\tau_{proc} + \tau_{rep} + \tau_{NGC}$	$\tau_{proc} + \tau_{rep} + \tau_{NGC} + \tau_{lsr}$	$\tau_{proc} + \tau_{rep} + \tau_{NGC}$

We can notice that the latency with location-based algorithms with legacy location reporting is independent of the architecture. In fact, in all cases the NGC is involved and, thus, the latency is the largest as it always involves all links between the NGC and the gNB-DU. For advanced location-based algorithms, the latency can be brought down to the values of the CSI-based solutions. At this point, it might be puzzling to grasp the motivation for location-based techniques, considering that the aging interval with advanced solutions can be equal to that of CSI-based algorithms in the best case. Actually, there are two significant advantages with location-based approaches: i) for fixed UEs, the location reporting can be performed more

sporadically reducing the overhead as the relative position compared to the NTN node can be updated based on the known NTN node position; and ii) while the location is estimated at t_E , the channel coefficients can be inferred from this value and the NTN node position at t_T , thus limiting the impact of aging on the beamforming performance compared to what can be done with CSI-based techniques. In addition, even with moving users, it was observed in past projects ([48], [54], [100]) and studies that the impact over short periods is almost negligible, as the largest contribution to the system dynamics is introduced by the NTN node movement on its orbit.

4.2.3 User-centric beamforming

In line with the framework defined in Section 2, we consider a DRA antenna equipped with $N_R = 512$ radiating elements providing connectivity to the users. The service area is defined according to the Earth-fixed beams principle, *i.e.*, it is fixed on-ground. It shall be noticed that, in the user-centric paradigm, no beam lattice is defined and the transmitted signals are digitally steered in the direction of each served user. The service area is defined as follows: i) its center is generally located at latitude and longitude (lat_S, lon_S) ; and ii) its extension is defined through the NTN node FoV, adjusted to guarantee a minimum elevation angle ε_S from altitude h_{sat} and assuming the Sub-Node Point (SNP) at (lat_S, lon_S) . For the numerical evaluation, we consider a complete pass of the NTN node over the service area, *i.e.*, as long as its ground track is contained within the service area boundary. Figure 55 shows an example of service area and ground track²; in this configuration, the geometric FoV (0° elevation) is 59.81° and the FoV considering $\varepsilon_S = 30^\circ$ (as per 3GPP specifications) is 48.46° .

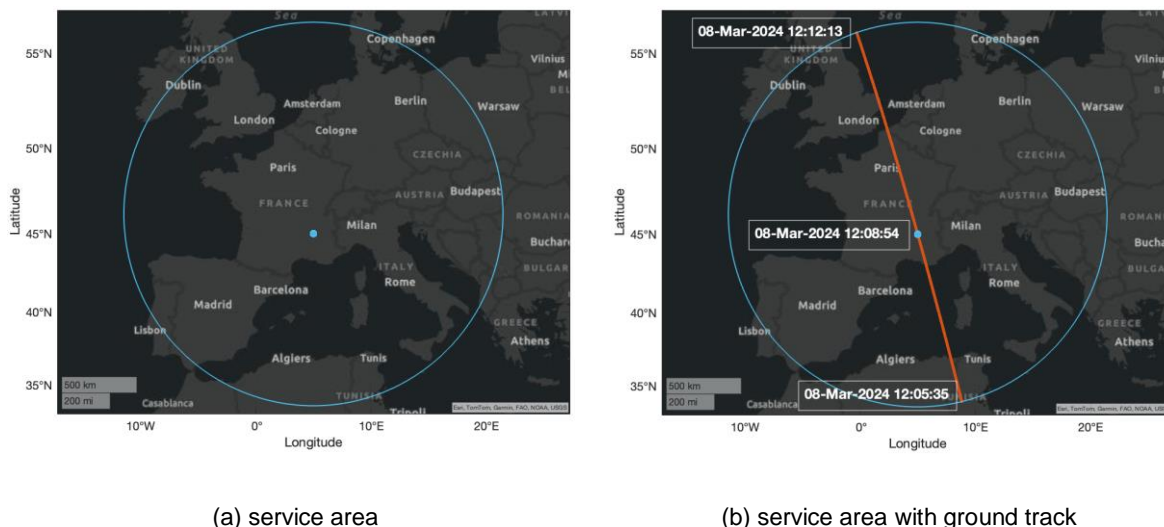


Figure 55: Service area and ground track for user-centric beamforming with $(lat_S = 45^\circ N, lon_S = 5^\circ E)$, $\varepsilon_S = 30^\circ$, $h_{sat} = 1000$ km.

As discussed in the previous sections, in the estimation time instant t_E the UEs estimate either their CSI vector (CSI-based beamforming) or their location (location-based beamforming). The channel coefficient at the generic time instant t between the i -th UE and the n -th on-board radiating element was defined in Section 2.4.1.4 and it is reported below for the sake of clarity:

² We are considering a satellite of the Polar orbit sub-constellation defined in D3.2, at 1000 km altitude with inclination 99° . The generality of the mathematical formulation or performance assessment in this document is not affected by this choice.

$$h_{i,n}^{(t)} = \frac{g_{i,n}^{(tx,t)} g_{i,n}^{(rx,t)}}{\frac{4\pi d_i^{(t)}}{\lambda} \sqrt{L_i^{(t)} \kappa B_i T_i}} e^{-j\frac{2\pi}{\lambda} d_i^{(t)}} \quad (47)$$

where we slightly modified the formulation to include in $L_i^{(t)} = L_i^{(sha,t)} + L_i^{(atm,t)} + L_i^{(sci,t)} + L_i^{(cl,t)}$ all stochastic losses, while leaving the free space loss as a separate term. For CSI-based techniques, the UEs directly estimate (47) as $\widehat{h}_{i,n}^{(t)}$ and report it to the NE computing the beamforming coefficients during the estimation phases. In location-based solutions, the UEs estimate their location and the NE derives the channel coefficients based on this information (either directly stored or from the LMF, as discussed in Section 4.2.1.3) and the current NTN node position on its orbit; notably, this approach excludes the stochastic terms in $L_i^{(t)}$ from the estimated CSI, as only geometry-related terms can be obtained, *i.e.*:

$$\widehat{h}_{i,n}^{(t)} = \frac{g_{i,n}^{(tx,t)} g_{i,n}^{(rx,t)}}{\frac{4\pi d_i^{(t)}}{\lambda} \sqrt{\kappa B_i T_i}} e^{-j\frac{2\pi}{\lambda} d_i^{(t)}} \quad (48)$$

It shall be noticed that, while the stochastic losses in $L_i^{(t)}$ are not considered in (48), for fixed users the channel coefficient can be estimated without any bias or error, when neglecting orbital perturbations and location estimation errors at the UE. In addition, as previously mentioned, even with moving users it was already observed in past analyses that the major impact on the performance of location-based solutions is still related to the NTN node movement. Thus, even if $L_i^{(t)}$ is not considered in computing the beamforming matrix, it can be expected that location-based algorithms outperform CSI-based solutions in LOS/NLOS channels, with a performance benefit that is larger for longer aging information intervals. In clear-sky conditions, $L_i^{(t)} = 0$ and, thus, no performance different is expected.

In the following, we denote as N_{slot} the number of transmission slots available during the serving time T_{serv} and as t_{slot} the time index of the transmission slot, *i.e.*, $t_{slot} = 1, \dots, N_{slot}$. Thus $T_{serv} = N_{slot} T_{slot}$, since T_{slot} was introduced in Section 4.2 to represent the duration of a transmission slot. During T_{serv} , there will be N_{sched} scheduling updates, each T_{sched} seconds, and N_{rep} estimation and reporting instants, each T_{rep} seconds, with $T_{rep} \ll T_{sched}$. For the sake of notation clarity, the following mathematical framework is introduced for a generic scheduling interval, *i.e.*, a time duration T_{sched} in which several estimation and transmission instants will occur; we generally denote as t_E the last estimation update and as t_T the current scheduled transmission slot.

We assume that N_{UE} users are uniformly distributed in the service area. Notably, at the generic estimation instant t_E , only a subset of them will be in the visibility of the NTN node, *i.e.*, with an elevation angle above a target ε_t . If we denote as $\varepsilon_i^{(t_E)}$ the elevation angle of the i -th user at t_E , the number of users that are in visibility in that instant and that can be scheduled by the RRM algorithm is given by:

$$N_{UE}^{(t_E)} = \left| \left\{ i: \varepsilon_i^{(t_E)} \geq \varepsilon_t, i = 1, \dots, N_{UE} \right\} \right| \quad (49)$$

An example of visible users depending on the NTN node position is shown in Figure 56. After the estimation phase, the NE computing the scheduling and beamforming coefficients has $N_{UE}^{(t_E)}$ estimated CSI vectors, with each N_R -dimensional complex vector representing the estimated/inferred CSI between the user and all the on-board radiating elements:

$$\widehat{\mathbf{h}}_{l,:}^{(t_E)} = \left[\widehat{h}_{l,1}^{(t_E)}, \dots, \widehat{h}_{l,n}^{(t_E)}, \dots, \widehat{h}_{l,N_R}^{(t_E)} \right], i = 1, \dots, N_{UE}^{(t_E)} \quad (50)$$

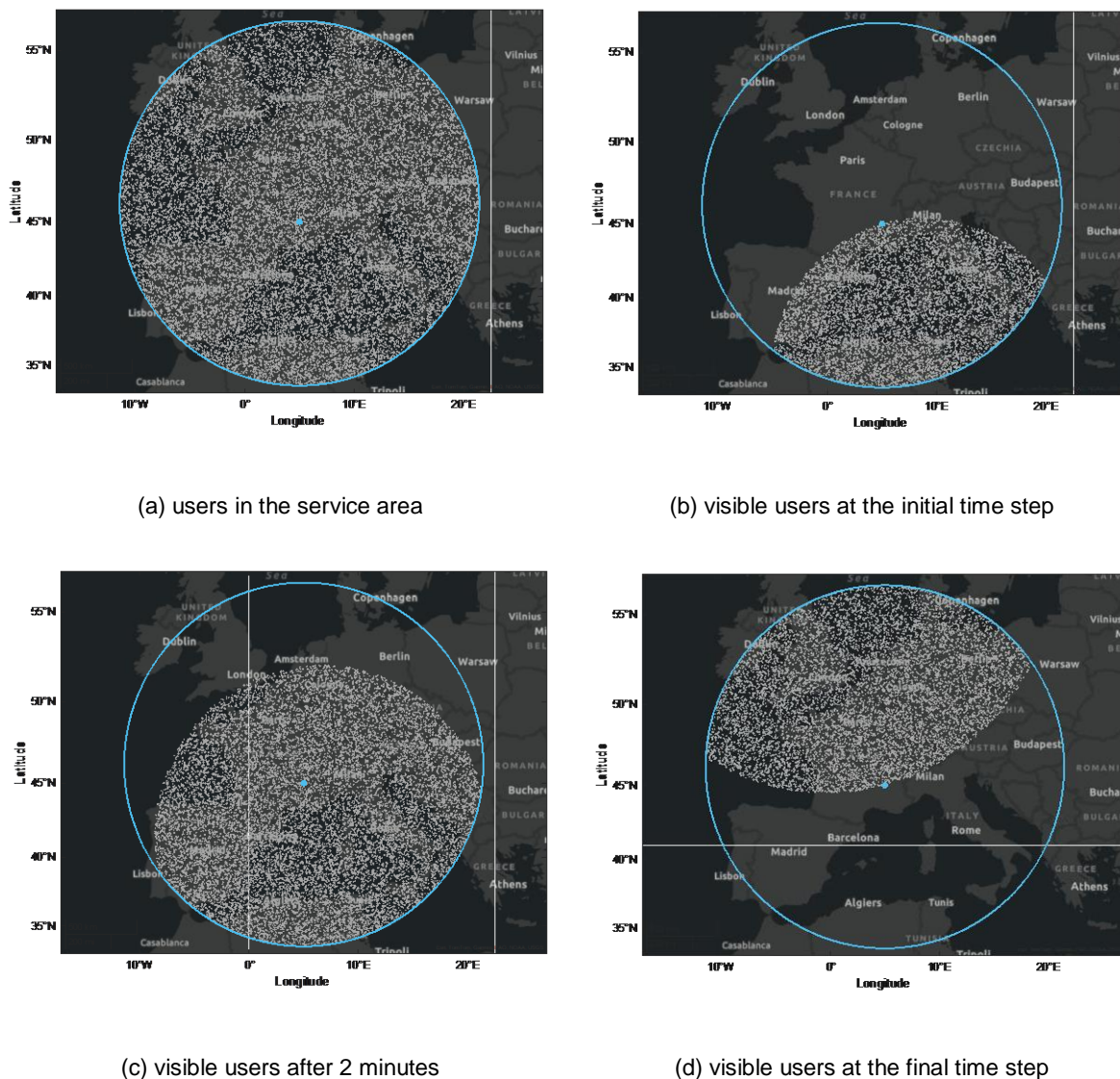


Figure 56: Example of visible users according to the NTN node position on its orbit.

The NE can then merge all the estimated CSI vectors in a $N_{UE}^{(t_E)} \times N_R$ complex channel matrix, in which each row contains the CSI vector of a visible user:

$$\mathbf{H}_{vis}^{(t_E)} = \left[\left(\widehat{\mathbf{h}}_{1,:}^{(t_E)} \right)^T, \dots, \left(\widehat{\mathbf{h}}_{l,:}^{(t_E)} \right)^T, \dots, \left(\widehat{\mathbf{h}}_{N_{UE}^{(t_E)},:}^{(t_E)} \right)^T \right]^T \quad (51)$$

While the specific algorithms will be introduced in Section 4.2.4, we can assume that the implemented RRM identifies the users to be served in each time slot for a given period of time T_{sched} . Denoting as $N_{slot}^{(sched)}$ the number of transmission slots are scheduled per T_{sched} , the RRM algorithm can be represented as a scheduling function $\mathcal{S}(\cdot)$ that samples $\mathbf{H}_{vis}^{(t_E)}$ for each time slot by selecting N_B rows each time. We denote as $\mathbf{H}_q^{(t_E)} = \mathcal{S} \left(\mathbf{H}_{vis}^{(t_E)} \right) \Big|_q$ the channel matrix

of the users scheduled for the generic q -th slot of the scheduling period, with $q = 1, \dots, N_{slot}^{(sched)}$. This matrix is used to compute the beamforming coefficients according to the selected user-centric algorithm. In particular, $\mathbf{H}_q^{(t_E)}$ is exploited to compute the $N_R \times N_B$ complex beamforming matrix according to the selected algorithm:

$$\mathbf{B}^{(t_E, q)} = \mathcal{B}(\mathbf{H}_q^{(t_E)}) \quad (52)$$

where $\mathcal{B}(\cdot)$ denotes the generic user-centric algorithm function of the input estimated channel matrix. Let us denote by $\mathbf{s}_q^{(t_E)} = [s_{1,q}^{(t_E)}, \dots, s_{N_B, q}^{(t_E)}]^T$ the N_B -dimensional vector of unit-variance symbols to be transmitted to the scheduled users in the generic q -th slot. These are linearly combined by the user-centric beamforming matrix such that all radiating elements transmit a complex-weighted superposition of all symbols, *i.e.*, the beamforming matrix is projecting the symbols from the N_B -dimensional user space to the N_R -dimensional feed space. The signal received at the generic k -th UE in the q -th time slot can be then written as:

$$y_{k,q}^{(t_E)} = \underbrace{\mathbf{h}_{k,:}^{(t_T)} \mathbf{b}_{:,k}^{(t_E, q)} s_{k,q}^{(t_E)}}_{\text{intended}} + \underbrace{\sum_{\substack{\ell=1 \\ \ell \neq k}}^{N_B} \mathbf{h}_{k,:}^{(t_T)} \mathbf{b}_{:, \ell}^{(t_E, q)} s_{\ell, q}^{(t_E)}}_{\text{interfering}} + z_{k,q}^{(t_E)} \quad (53)$$

where $z_{k,q}^{(t_E)}$ is a circularly symmetric Gaussian random variable (r.v.) with zero mean and unit variance, which is licit observing that the channel coefficients defined in (47)-(48) and Section 2.4.1.4 are normalised to the noise power. It shall be noticed that, in (52), the beamforming matrix is computed referring to the ancillary information obtained in the latest reporting period, while the channel encountered during the actual transmission is clearly different. More specifically, the larger the aging interval $t_T - t_E$, the less harmonised the beamforming matrix $\mathbf{B}^{(t_E, q)}$ will be to the actual channel conditions during the transmission, *i.e.*, to the $N_B \times N_R$ complex channel matrix $\mathbf{H}^{(t_T)} = \left[\left(\mathbf{h}_{1,:}^{(t_T)} \right)^T, \dots, \left(\mathbf{h}_{i,:}^{(t_T)} \right)^T, \dots, \left(\mathbf{h}_{N_B, :}^{(t_T)} \right)^T \right]^T$. Equation (53) can be easily extended to obtain the column vector of received symbols during the time slot:

$$\mathbf{y}_q^{(t_E)} = \mathbf{H}^{(t_T)} \mathbf{B}^{(t_E, q)} \mathbf{s}_q^{(t_E)} + \mathbf{z}_q^{(t_E)} \quad (54)$$

4.2.3.1 Key Performance Indicators

From the received symbols in (54), several Key Performance Indicators (KPIs) can be derived for each scheduled user starting from the following power transfer matrix:

$$\mathbf{A}^{(q)} = \left| \mathbf{H}^{(t_T)} \mathbf{B}^{(t_E, q)} \right|^2 \quad (55)$$

In this $N_B \times N_B$ matrix, the generic (i, j) -th element represents the power transmitted to the j -th user and received by the i -th user, normalised to the noise thermal power. Thus, all diagonal elements represent the intended received power, while all off-diagonal elements represent interfering power; in particular, all off-diagonal elements on a row represent the interference received by the i -th user due to the other $N_B - 1$ transmissions scheduled in the same time slot. Thus, for the generic k -th user, we can directly obtain:

- The Signal-to-Noise Ratio (SNR):

$$\text{SNR}_{k,q}^{(t_E, t_T)} = a_{k,k}^{(q)} \quad (56)$$

- The Interference-to-Noise Ratio (INR):

$$\text{INR}_{k,q}^{(t_E,t_T)} = \sum_{\substack{\ell=1 \\ \ell \neq k}}^{N_B} a_{k,\ell}^{(q)} \quad (57)$$

- The SINR:

$$\text{SINR}_{k,q}^{(t_E,t_T)} = \frac{\text{SNR}_{k,q}^{(t_E,t_T)}}{1 + \text{INR}_{k,q}^{(t_E,t_T)}} = \frac{\left\| \mathbf{h}_{k,:}^{(t_T)} \mathbf{b}_{:,k}^{(t_E,q)} \right\|^2}{1 + \sum_{\ell=1, \ell \neq k}^{N_B} \left\| \mathbf{h}_{k,:}^{(t_T)} \mathbf{b}_{:, \ell}^{(t_E,q)} \right\|^2} \quad (58)$$

From the above SINR, the rate achieved by the k -th user can be evaluated either from the Shannon bound formula or from the adopted MCS. In this framework, 3GPP TR 38.803, [97], reports that the spectral efficiency for system-level simulations can be obtained as follows:

$$\eta_{k,q}^{(t_E,t_T)} = \begin{cases} 0, & \text{SINR}_{k,q}^{(t_E,t_T)} < \text{SINR}_{\min} \\ \rho \cdot \log_2 \left(1 + \text{SINR}_{k,q}^{(t_E,t_T)} \right), & \text{SINR}_{\min} \leq \text{SINR}_{k,q}^{(t_E,t_T)} \leq \text{SINR}_{\max} \\ \rho \cdot \log_2 (1 + \text{SINR}_{\max}), & \text{SINR}_{k,q}^{(t_E,t_T)} > \text{SINR}_{\max} \end{cases} \quad (59)$$

where $\text{SINR}_{\min} = -10$ dB and $\text{SINR}_{\max} = 30$ dB are the minimum and maximum SINR of the MCS, respectively, and ρ is an attenuation factor representing the implementation losses. Since this factor is a multiplicative term outside the Shannon formula, we can assume $\rho = 1$ as a different value would simply act as scaling factor of all the results, without impacting the observations and the relationships among the various techniques and scenarios. It shall be noticed that the spectral efficiency computed in (59) represents an asymptotic value, *i.e.*, the spectral efficiency assuming that the generic k -th user was granted a resource in all the available time slots. To take into account the performance of the specific RRM algorithm, we also consider the experienced spectral efficiency per user, which is the sum of achieved spectral efficiencies weighted by the percentage of channel use. Let us denote by $\boldsymbol{\eta}_k$ the vector of spectral efficiencies achieved by the k -th user in the system in each allocated transmission slot, with $k = 1, \dots, N_{UE}$, and by $N_{slot,k}$ the number of transmission slots that the user received, *i.e.*, $\boldsymbol{\eta}_k$ is a $N_{slot,k}$ -dimensional vector. Then, the experienced spectral efficiency of the k -th user is given by:

$$\bar{\eta}_k = \sum_{p=1}^{N_{slot,k}} \frac{\eta_{k,p} T_{slot}}{T_{serv}} \quad (60)$$

Notably, this metric is significantly affected by the RRM and the users/traffic distributions. In addition to the above KPIs, we also consider:

- The asymptotic capacity:

$$C_{k,q}^{(t_E,t_T)} = B \eta_{k,q}^{(t_E,t_T)} \quad (61)$$

- The experienced capacity:

$$\bar{C}_k = B \bar{\eta}_k \quad (62)$$

- The percentage of unserved users, as the number of users for which the SINR is below the minimum allowed for the most robust 5G MCS SINR_{min} .

It is worthwhile highlighting that other metrics might be introduced in the prosecution of Task 4.2, depending on the specific system behaviours that might need to be better observed.

4.2.3.2 Beamforming algorithms

CSI-BASED

For CSI-based solutions, the channel matrix $\mathbf{H}_q^{(t_E)}$ is completely built based on the users' estimations. From the literature review previously discussed, the following digital techniques can be considered as of interest:

- **Zero Forcing (ZF):** The baseline implementation of the ZF algorithm is based on the inversion of the channel matrix $\mathbf{H}_q^{(t_E)}$. Notably, with this approach, the $(\mathbf{H}_q^{(t_E)})^H \mathbf{H}_q^{(t_E)}$ matrix is often ill-conditioned, *i.e.*, with a very large condition number, leading to a close-to-singular matrix. In these cases, the computation of the inverse matrix is prone to large numerical errors, resulting in a significant performance loss due to the inaccuracy of the matrix inversion; hence, to circumvent this issue, the following implementation of ZF is typically taken into account:

$$\mathbf{B}_{ZF}^{(t_E,q)} = \left((\mathbf{H}_q^{(t_E)})^H \mathbf{H}_q^{(t_E)} \right)^\dagger (\mathbf{H}_q^{(t_E)})^H \quad (63)$$

Where \dagger denotes the Moore-Penrose pseudo-inverse matrix. It is worth mentioning that the ZF scheme suffers from noise enhancement, therefore it may have poor performance in low SNR regime, since it does not take into account the noise power when implementing beamforming vectors.

- **Minimum Mean Square Error (MMSE):** the MMSE precoder, or regularized ZF (RZF), is designed to solve the MMSE problem. In particular:

$$\mathbf{B}_{MMSE}^{(t_E,q)} = \arg \min_{\mathbf{B}} \mathbb{E} \left\| \mathbf{H}_q^{(t_E)} \mathbf{B} \mathbf{s} + \mathbf{z} - \mathbf{s} \right\|^2 \quad (64)$$

$$\mathbf{W}_{MMSE} = \left(\mathbf{H}_q^{(t_E)} \right)^H \left(\mathbf{H}_q^{(t_E)} \left(\mathbf{H}_q^{(t_E)} \right)^H + \alpha \mathbf{I}_{N_B} \right)^{-1} \quad (65)$$

where α denotes the regularisation factor. Since the channel coefficients are normalised to the noise power, its optimal value is given by $\alpha = \frac{N_R}{P_{av}}$, where P_{av} is the total available transmission power on-board.

- **Signal-to-Leakage-plus-Noise Ratio (SLNR) BF:** In this scheme, the beamforming coefficients are calculated based on maximizing the SLNR for all the users in the service area. This standard results in a separated optimization issue that can be resolved using a closed analytical solution. The main goal is, for each user k , to maximize the intended signal power $\left\| \mathbf{h}_{k,:}^{(t_E)} \mathbf{b}_{:,k}^{(t_E,q)} \right\|^2$ and minimize the power leaked or interfered from such user to all other scheduled users, *i.e.*, $\sum_{i=1, i \neq k}^{N_B} \left\| \mathbf{h}_{i,:}^{(t_E)} \mathbf{b}_{:,k}^{(t_E,q)} \right\|^2$. Hence:

$$\text{SLNR}_{k,q}^{(t_E)} = \frac{\left\| \mathbf{h}_{k,:}^{(t_E)} \mathbf{b}_{:,k}^{(t_E,q)} \right\|^2}{\beta + \sum_{i=1, i \neq k}^{N_B} \left\| \mathbf{h}_{i,:}^{(t_E)} \mathbf{b}_{:,k}^{(t_E,q)} \right\|^2} \quad (66)$$

For the sake of simplicity, we can reformulate (63) as follows:

$$\text{SLNR}_{k,q}^{(t_E)} = \frac{\left\| \mathbf{h}_{k,:}^{(t_E)} \mathbf{b}_{:,k}^{(t_E,q)} \right\|^2}{\beta + \left\| \mathbf{z}_{:,k}^{(t_E,q)} \mathbf{b}_{:,k}^{(t_E,q)} \right\|^2} \quad (67)$$

Where:

$$\mathbf{z}_{:,k}^{(t_E,q)} = \left[\left(\mathbf{h}_{1,:}^{(t_E)} \right)^T, \dots, \left(\mathbf{h}_{k-1,:}^{(t_E)} \right)^T, \left(\mathbf{h}_{k+1,:}^{(t_E)} \right)^T, \dots, \left(\mathbf{h}_{N_B,:}^{(t_E)} \right)^T \right]^T \quad (68)$$

is a reduced channel matrix that does not include $\mathbf{h}_{k,:}^{(t_E)}$, where the vertical bar refers to a vertical concatenation, and $\beta = \frac{N_B}{P_t}$ indicates the SLNR regularization factor. The beamforming matrix targeted for the k -th user that maximizes its SLNR is given by:

$$\mathbf{b}_{:,k}^{(t_E,q,SLNR)} = \arg \max_{\mathbf{b}} \text{SLNR}_{k,q}^{(t_E)} = \arg \max_{\mathbf{b}} \frac{\left\| \mathbf{h}_{k,:}^{(t_E)} \mathbf{b}_{:,k}^{(t_E,q)} \right\|^2}{\beta + \left\| \mathbf{z}_{:,k}^{(t_E,q)} \mathbf{b}_{:,k}^{(t_E,q)} \right\|^2} \quad (69)$$

As discussed in the previously mentioned literature, we can obtain the optimal beamformer as a closed-form solution of the generalized eigenvalue problem. Such solution is given by:

$$\mathbf{b}_{:,k}^{(t_E,q,SLNR)} \propto \max \text{eigenvector} \left\{ \left(\beta \mathbf{I} + \left(\mathbf{z}_{:,k}^{(t_E,q)} \right)^H \mathbf{z}_{:,k}^{(t_E,q)} \right)^{-1} \left(\mathbf{h}_{k,:}^{(t_E)} \right)^H \mathbf{h}_{k,:}^{(t_E)} \right\} \quad (70)$$

in terms of the eigenvector corresponding to the largest eigenvalue of the matrix $\left(\beta \mathbf{I} + \left(\mathbf{z}_{:,k}^{(t_E,q)} \right)^H \mathbf{z}_{:,k}^{(t_E,q)} \right)^{-1} \left(\mathbf{h}_{k,:}^{(t_E)} \right)^H \mathbf{h}_{k,:}^{(t_E)}$, *i.e.*, λ_{max} . The column vector $\mathbf{b}_{:,k}^{(t_E,q,SLNR)}$ shall be selected according to (31), aiming to obtain the maximum SLNR value, *i.e.*, $\text{SLNR} = \lambda_{max}$.

LOCATION-BASED

With location-based solutions, the channel matrix $\mathbf{H}_q^{(t_E)}$ is built by deriving the geometry-related terms in the channel coefficient exploiting the knowledge of the users' locations and the NTN node ephemeris. From the literature review previously discussed, the following digital techniques can be considered as of interest:

- **Conventional Beamforming (CBF):** the beamforming weights are phase-only steering vectors to point the beam in the direction of the user. Let us denote as $\mathbf{p}_i^{(t_E)} = \left(u_i^{(t_E)}, v_i^{(t_E)} \right)$ the direction cosines of the i -th user's direction from the NTN node perspective at estimation time t_E . In addition, we denote as $g_E(u, v)$ the radiation pattern of each radiating element of the on-board antenna array. The value of the radiation pattern from the on-board antenna array in the i -th user's direction (at t_E) is thus computed as:

$$g^{(tx,t_E)}(u_i^{(t_E)}, v_i^{(t_E)}) = g_E(u_i^{(t_E)}, v_i^{(t_E)}) \sum_{n=1}^{N_R} e^{jk_0 \mathbf{r}_n \cdot \mathbf{p}_i^{(t_E)}} = g_E(u_i^{(t_E)}, v_i^{(t_E)}) \Phi(u_i^{(t_E)}, v_i^{(t_E)}) \quad (71)$$

where \mathbf{r}_n represents the position of the n -th radiating element in the antenna array, $k_0 = 2\pi/\lambda$ is the wave number, and $\Phi(u_i^{(t_E)}, v_i^{(t_E)}) = \sum_{n=1}^{N_R} e^{jk_0 \mathbf{r}_n \cdot \mathbf{p}_i^{(t_E)}}$ is the Array Factor (AF). With CBF, the weights are obtained by conjugating and normalising the AF:

$$\mathbf{b}_{:,k}^{(t_E,q,CBF)} = \frac{1}{\sqrt{N_R}} \sum_{n=1}^{N_R} e^{-jk_0 \mathbf{r}_n \cdot \mathbf{p}_i^{(t_E)}} = \frac{1}{\sqrt{N_R}} \Phi^*(u_i^{(t_E)}, v_i^{(t_E)}) \quad (72)$$

Since the weights are only made of complex exponentials with equal amplitude, this solution it is actually a full analogue scheme. CBF can be clearly considered as a location-based technique since the direction $(u_i^{(t_E)}, v_i^{(t_E)})$ is required.

- **Location-Based MMSE (LB-MMSE):** with this approach, the users' location report is exploited to compute the channel coefficients as in equation (48). Then, the MMSE beamformer is applied to this channel matrix, as in (65). The advantage of this solution is to keep the significant performance of the MMSE solution while exploiting location information rather than the CSI estimations.

Among the location-based solution, there are also variants that are based on a pre-defined beam lattice on-ground, such as MB and SS-MMSE. These solutions do not belong to the user-centric category, but they are worth to be mentioned as they represent a first step moving from beam-based to user-based beamforming. In fact, the beam lattice of these solution is typically over-dimensioned with respect to the number of radiating elements, *i.e.*, more beams than radiating elements are present. This is motivated by the need to properly sample the service area with very narrow beams. Then, either the users' location reports are exploited to associate them to the closest beam center or the users provide the index of the best serving beams; this ultimately allows to select the pre-computed beamforming vectors based on the users' scheduling. More details can be found in [54], [57].

4.2.3.3 Power distribution

In the generic beamforming matrix $\mathbf{B}^{(t_E,q)}$, we can observe that: i) the generic N_B -dimensional n -th row, with $n = 1, \dots, N_R$, defines the complex coefficients with which the N_B users' symbols are weighted before transmission from the n -th radiating element; and ii) the generic N_R -dimensional i -th column, with $i = 1, \dots, N_B$, defines the complex coefficients with which the k -th users' symbols are weighted and transmitted across the N_R radiating elements. Thus, the squared norm of the generic i -th column provides the power allocated to the i -th user, while the squared norm of the generic n -th row represents the power emitted by the n -th radiating element. Finally, the total emitted power can be computed through the Frobenius norm:

$$P_{TX} = \|\mathbf{B}^{(t_E,q)}\|_F^2 \quad (73)$$

Once one of the above-mentioned algorithms has been implemented, a fundamental step is that of a proper normalisation of the beamforming matrix. In fact, without normalisation, the following issues might arise: i) the total transmission power required by the beamforming algorithm can be larger than the total power available on-board, *i.e.*, $P_{TX} = \|\mathbf{B}^{(t_E,q)}\|_F^2 > P_{av}$, where P_{av} denotes the available power; and ii) the power emitted by a given radiating element

might be larger than the maximum allowed value, *i.e.*, $\|\mathbf{b}_{n,:}^{(t_E,q)}\|^2 > P_{av,el}$, with the risk of operating the on-board amplifiers in non-linear regime.

There is a vast literature on the most efficient power distribution strategy in beamforming scenarios (see [54] and [57], and the references therein). In general, there are three desirable properties for a power distribution strategy:

1. **Orthogonality preservation:** if the applied normalisation to distribute the power is a scalar, all of the beamforming columns are scaled by the same amount. This means that the power distribution strategy is not impacting the (quasi-)orthogonality among the beamformer columns provided by the selected algorithm. This aspect is fundamental, as the more orthogonal are the matrix columns, the lower the residual co-channel interference will be (*i.e.*, the larger the SINR).
2. **Maximum transmission power:** to exploit all of the available power on-board, the power distribution strategy shall be such that $\|\mathbf{B}^{(t_E,q)}\|_F^2 = P_{av}$.
3. **Maximum power per antenna:** to avoid that any of the radiating elements is required to emit more power than allowed, and also to keep the on-board amplifiers operating in the linear region, the power per radiating element shall be controlled. This control shall be such that each radiating element also emits all of the available power, to not negatively impact the link budget. Thus, the power distribution strategy shall be such that $\|\mathbf{b}_{n,:}^{(t_E,q)}\|^2 > P_{av,el}$ for all $n = 1, \dots, N_R$.

Unfortunately, it is not possible to satisfy all three properties at the same time. Thus, a trade-off among them is required and the best solution is strictly depending on the specific scenario, in terms of users/traffic distribution, transmission power, RRM, beamforming technique. In the literature, the most considered power distribution strategies are the following:

- **Sum Power Constraint (SPC)**

$$\mathbf{B}^{(t_E,q)} = \sqrt{\frac{P_{av}}{\text{tr}(\check{\mathbf{B}}^{(t_E,q)}(\check{\mathbf{B}}^{(t_E,q)})^H)}} \check{\mathbf{B}}^{(t_E,q)} \quad (74)$$

where as $\check{\mathbf{B}}^{(t_E,q)}$ represents the beamforming matrix obtained with one of the techniques discussed above prior to normalisation and $\mathbf{B}^{(t_E,q)}$ is its normalised version. This normalisation: i) guarantees that the overall power allocated by the precoding matrix is equal to that actually available, P_{av} ; and ii) preserves the orthogonality among the precoding matrix columns, *i.e.*, it does not degrade the optimal precoding solution obtained by perturbing the orthogonality. However, no control is introduced on the power allocated per radiating element.

- **Maximum Power Constraint (MPC)**

$$\mathbf{B}^{(t_E,q)} = \sqrt{\frac{P_{av}}{N_R \max_{n=1,\dots,N_R} \|\mathbf{b}_{n,:}^{(t_E,q)}\|^2}} \check{\mathbf{B}}^{(t_E,q)} \quad (75)$$

In this case, we guarantee that the overall power is upper bounded by P_{av} , while also ensuring that all the on-board radiating elements do not exceed the maximum power. As for the SPC approach, the orthogonality among the precoding matrix columns is

preserved. However, since only one radiating element is transmitting at maximum power, while the others are (significantly) limited in their emissions, this approach might lead to a degradation of the SNR and, in general, to a performance degradation in terms of the sum capacity.

- **Per Antenna Constraint (PAC)**

$$\mathbf{B}^{(t_E,q)} = \sqrt{\frac{P_{av}}{N_R}} \text{diag} \left(\frac{1}{\|\mathbf{b}_{1,:}^{(t_E,q)}\|}, \dots, \frac{1}{\|\mathbf{b}_{N_R,:}^{(t_E,q)}\|} \right) \check{\mathbf{B}}^{(t_E,q)} \quad (76)$$

It can be noticed that, with this approach, we let each radiating element transmit at an equal power level, while ensuring that the overall available power is not exceeded. However, since we are normalising each row of the beamforming matrix independently from each other, we introduce a performance degradation in terms of interference cancellation due to a perturbation in the orthogonality among the columns.

As demonstrated in the literature (e.g., [54] and the references therein), the optimal power distribution strategy is SPC, as it ensures that all the available power is transmitted while preserving the interference rejection properties of the beamformer. However, this solution does not limit the power per radiating element, which might lead to exceeding the maximum or to let the on-board amplifiers work in non-linear regions. Thus, MPC and PAC (or their variants) are usually those implemented. As discussed above, PAC disrupts the orthogonality in the beamformer columns and, thus, it is not recommended in scenarios with a large interference, e.g., when the generated beams are very close to each other and/or the transmission power is large.

4.2.4 Random RRM algorithms

In the following, we assume that all the uniformly distributed UEs in the service area are in a full buffer condition and that their traffic request is uniform. With a random scheduling approach, the scheduler does not take into account any traffic request from the users and the only requirement that is considered is that each user is served at least once during the NTN node propagation on its orbit. While this approach might seem simplistic, it allows to understand several trends and trade-offs related to the performance of user-centric beamforming algorithms and power distribution techniques in the considered system.

Algorithm 1 shows the benchmark Random Scheduling (RS) RRM. In a generic scheduling instant out of the N_{sched} available during the NTN node orbital movement, the RS algorithm provides the indexes of the users to be served in a subset of the total time slots. In particular, the total $N_B \times N_{slot}$ scheduling matrix is denoted as \mathbf{S} and, in the generic m -th scheduling instant, a $N_B \times N_{slot}^{(sched)}$ submatrix is defined, with $\mathbf{S} = [\mathbf{S}_1, \dots, \mathbf{S}_m, \dots, \mathbf{S}_{N_{sched}}]$. The algorithm takes as input the indexes of the users currently in the visibility of the NTN node (\mathbf{u}_{vis}) and two vectors that allow to keep track of the past allocations: i) a $N_{UE} \times 1$ allocation flag vector, \mathbf{f} , with $f_k = 1$ if the k -th user has already been granted a slot and 0 otherwise; and ii) a $N_{UE} \times 1$ allocation number vector, \mathbf{a} , with a_k representing the number of slots granted to the k -th user. Based on this input, the RS algorithm identifies the users that are in visibility and that have not yet been allocated ($\mathbf{u}_{vis}^{(0)} = \mathbf{f} \otimes \mathbf{u}_{vis}$, with \otimes representing the Kronecker product) and those already served at least once ($\mathbf{u}_{vis}^{(1)} = (\mathbf{f} + 1)_2 \otimes \mathbf{u}_{vis}$, where $(\mathbf{f} + 1)_2$ represents the modulo 2 sum). Then, for each time slot in the scheduling period, this algorithm selects a random permutation without repetition of the visible users not yet served, denoted by the function $\omega(\mathbf{x}, n)$ where \mathbf{x} is the input vector and n the number of its elements to be provided. If the cardinality of $\mathbf{u}_{vis}^{(0)}$ is less than the number of allocations per time slot N_B , the remaining

resources are assigned with another random permutation on the set of users that are in visibility and that were already served.

Algorithm 1: Random Scheduling algorithm.

Input	
	<ul style="list-style-type: none"> • Indexes of the visible users from the last report: \mathbf{u}_{vis} • $N_{UE} \times 1$ allocation flag vector \mathbf{f} • $N_{UE} \times 1$ allocation number vector \mathbf{a}
Output	
	<ul style="list-style-type: none"> • $N_B \times N_{slot}^{(sched)}$ scheduling matrix \mathbf{S}_m, $m = 1, \dots, N_{sched}$
For $i = 1, \dots, N_{slot}^{(sched)}$	
1	Identify the users without allocations: $\mathbf{u}_{vis}^{(0)} = \mathbf{f} \otimes \mathbf{u}_{vis}$ Identify the users with at least one allocation: $\mathbf{u}_{vis}^{(1)} = (\mathbf{f} + 1)_2 \otimes \mathbf{u}_{vis}$
	If $\text{Card}(\mathbf{u}_{vis}^{(0)}) \geq N_B$
	randomly select N_B indexes from $\mathbf{u}_{vis}^{(0)}$ and assign them to \mathbf{S}_m : $\mathbf{S}_m(i, :) = \omega(\mathbf{u}_{vis}^{(0)}, N_B)$
2	update the allocation flag vector \mathbf{f} : $\mathbf{f}_k = 1, \forall k \in \mathbf{S}_m(i, :)$
	update the allocation number vector \mathbf{a} : $\mathbf{a}_k = \mathbf{a}_k + 1, \forall k \in \mathbf{S}_m(i, :)$
	If $\text{Card}(\mathbf{u}_{vis}^{(0)}) < N_B$
	assign the available users to \mathbf{S}_m : $\mathbf{S}_m(i, 1: \text{Card}(\mathbf{u}_{vis}^{(0)})) = \mathbf{u}_{vis}^{(0)}$
3	randomly select $N_B - \text{Card}(\mathbf{u}_{vis}^{(0)})$ indexes from $\mathbf{u}_{vis}^{(1)}$ and assign them to \mathbf{S}_m : $\mathbf{S}_m(i, 1 + \text{Card}(\mathbf{u}_{vis}^{(0)}): N_B) = \omega(\mathbf{u}_{vis}^{(1)}, N_B - \text{Card}(\mathbf{u}_{vis}^{(0)}))$
	update the allocation flag vector \mathbf{f} : $\mathbf{f}_k = 1, \forall k \in \mathbf{S}_m(i, :)$
	update the allocation number vector \mathbf{a} : $\mathbf{a}_k = \mathbf{a}_k + 1, \forall k \in \mathbf{S}_m(i, :)$
End for	

One of the most detrimental factors in user-centric beamforming, or MIMO in general, is related to the channel matrix rank. In fact, when users that have similar CSI vectors are scheduled in the same time slot, the channel matrix to be inverted by the beamformer is ill-conditioned, with rows showing a non-negligible correlation. In the available literature, this has been demonstrated to always lead to a significant performance degradation.

Observing that, usually, users that are close to each other have very similar CSI vectors, we propose a slightly modified version of the RS RRM aimed at preventing the scheduling of such users in the same time slot. This algorithm, denoted as RS with Minimum Distance (RS-MD) is depicted in Algorithm 2. In this case, the algorithm takes two additional inputs: i) the radius r_{uv} in u-v coordinates of a hypothetic beam generated directly below the NTN node (as per 3GPP beam lattices described previously in this report); and ii) a scaling factor denoted as minimum distance coefficient, k_{dist} , used to adapt the minimum scheduling distance. The RS-MD algorithm still randomly selects users in each time slot; however, for each selected user,

the algorithm checks if its distance from those already identified is below $k_{dist}r_{uv}$; in this case, the user is discarded, and another one is randomly selected. Thus, this algorithm introduces a very high-level control on the distance among the users allocated to the same time slot. The objective is that of assessing the impact of this factor on the system performance for the future development of non-random RRM algorithms.

Algorithm 2: Random Scheduling with Minimum Distance algorithm.

Input	
	<ul style="list-style-type: none"> • Indexes of the visible users from the last report: \mathbf{u}_{vis} • $N_{UE} \times 1$ allocation flag vector \mathbf{f} • $N_{UE} \times 1$ allocation number vector \mathbf{a} • Minimum distance coefficient k_{dist} • Radius r_{uv}
Output	
	• $N_B \times N_{slot}^{(sched)}$ scheduling matrix \mathbf{S}_m , $m = 1, \dots, N_{sched}$
For $i = 1, \dots, N_{slot}^{(sched)}$	
1	Identify the users without allocations: $\mathbf{u}_{vis}^{(0)} = \mathbf{f} \otimes \mathbf{u}_{vis}$ Identify the users with at least one allocation: $\mathbf{u}_{vis}^{(1)} = (\mathbf{f} + \mathbf{1})_2 \otimes \mathbf{u}_{vis}$
2	Randomly select 1 index from $\mathbf{u}_{vis}^{(0)}$ and assign it to \mathbf{S}_m : $\mathbf{S}_m(i, 1) = \omega(\mathbf{u}_{vis}^{(0)}, 1)$ Initialise counter $\text{count} = 1$
	While $\text{count} < N_B$
	If $\text{Card}(\mathbf{u}_{vis}^{(0)}) > 1$
3	randomly select 1 index from $\mathbf{u}_{vis}^{(0)}$: $x = \omega(\mathbf{u}_{vis}^{(0)}, 1)$ compute the distance between the selected user and those already scheduled: $\mathbf{d} = \text{dist}(x, \mathbf{S}_m(i, 1:\text{count}))$ if $d_k < k_{dist}r_{uv}$, assign the user: $\text{count} = \text{count} + 1$ $\mathbf{S}_m(i, \text{count}) = x$ else discard user x from $\mathbf{u}_{vis}^{(0)}$ for the current time slot
4	If $\text{Card}(\mathbf{u}_{vis}^{(0)}) = 0$ randomly select $N_B - \text{count}$ index from $\mathbf{u}_{vis}^{(1)}$ and assign them to \mathbf{S}_m : $\mathbf{S}_m = \omega(\mathbf{u}_{vis}^{(1)}, N_B - \text{count})$ $\text{count} = \text{count} + N_B - \text{count}$
End while	
5	update the allocation flag vector \mathbf{f} : $f_k = 1, \forall k \in \mathbf{S}_m(i, :)$ update the allocation number vector \mathbf{a} : $a_k = a_k + 1, \forall k \in \mathbf{S}_m(i, :)$
End for	

Figure 57 shows the Cumulative Distribution Function of the minimum intra-slot distance, *i.e.*, the minimum distance computed between all users scheduled in the same time slot, with RS (equal to RS-MD with $k_{dist} = 0$) and RS-MD with $k_{dist} = 1, 2, \dots, 7$. In the considered system configuration, detailed in Section 4.3, $r_{uv} = 0.0316$, which corresponds to a hypothetical beam below the NTN node with Half Power Beam Width (HPBW) 3.6243° and 3 dB angle 1.8122° . The elbow of the Cumulative Distribution Functions (CDFs) with RS-MD is located at the corresponding threshold distance $k_{dist}r_{uv}$; when in a scheduling slot it is not possible to find another unserved user guaranteeing the minimum distance requirement, the algorithm drops this condition and schedules a random user. Thus, with lower thresholds, the vast majority of the scheduling slots are composed by N_B users with a distance larger than $k_{dist}r_{uv}$. When the threshold is increased, the probability of finding users satisfying the minimum distance decreases (which justifies the increase in the percentage of slots below the threshold), while the minimum distance in slots that satisfy the condition is clearly increased. As previously mentioned, this algorithm is relatively simple, yet effective to understand the impact of intra-slot distances on the beamforming performance.

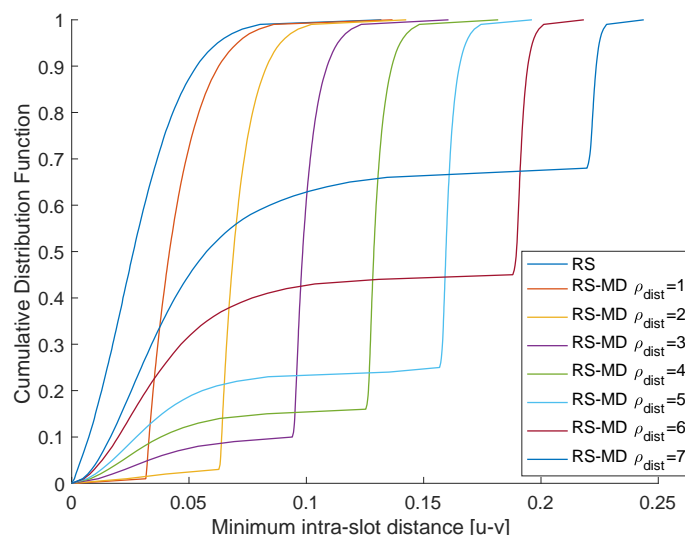
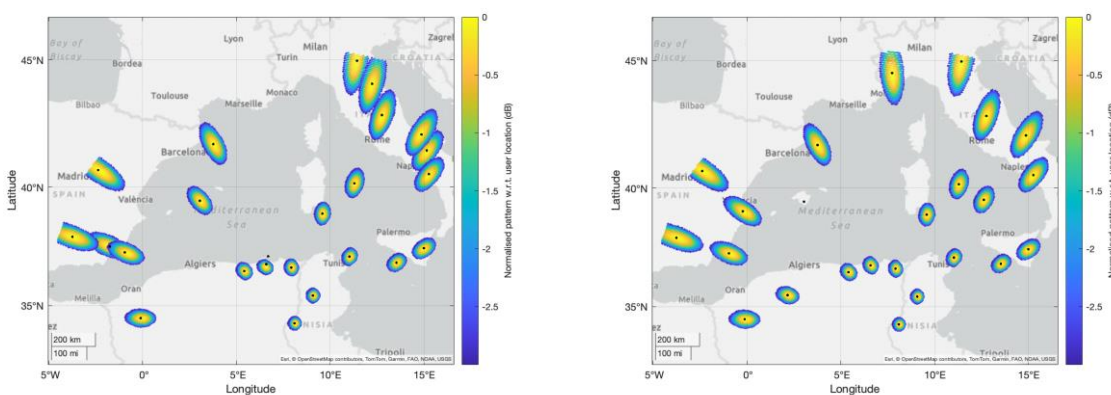


Figure 57: Minimum intra-slot distance with RS and RS-MD, $k_{dist} = 1, 2, \dots, 7$, $r_{uv} = 0.0316$.



(a) $k_{dist} = 0$

(b) $k_{dist} = 2$

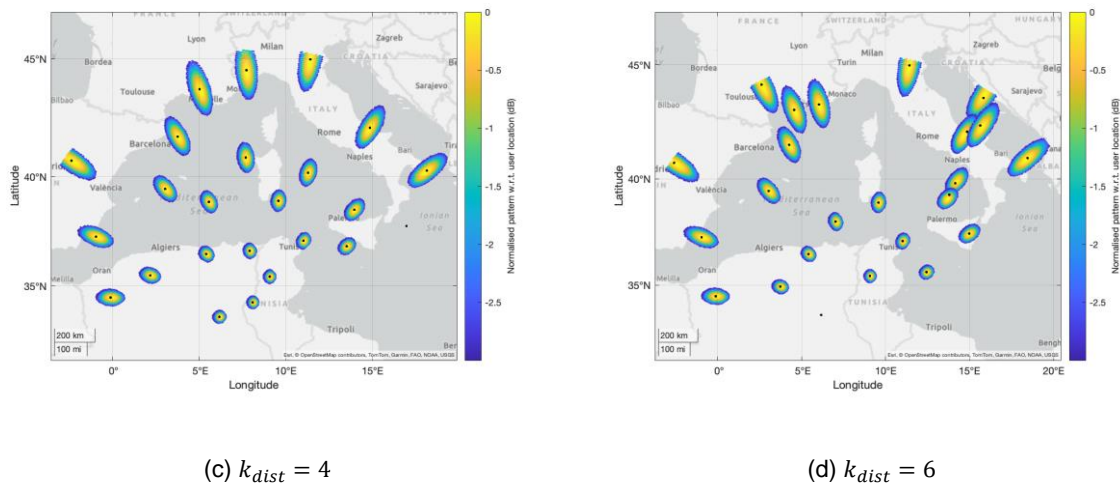


Figure 58: RS-MD scheduling example with different minimum distance coefficients.

Figure 58 shows an example of scheduling with RS/RS-MD for a varying minimum distance coefficient. It can be noticed that, as long as there are users sufficiently distant from each other, the algorithm indeed is able to increase the intra-slot distance. When the coefficient is too large, the probability of not finding an optimal separation increases and some users might be below the required threshold. This is in line with the trends represented in Figure 57.

4.3 PERFORMANCE ASSESSMENT: STANDALONE NODE

4.3.1 Simulation parameters

Table 24 summarises the simulation parameters for the system-level assessment. Users are considered fixed for this initial assessment. The user density is relatively limited mainly due to the computational complexity of the required analyses, as $N_{UE} \times N_R$ matrices are often involved in the user-centric beamforming assessment. However, it shall also be noticed that we are considering: i) a single polarisation out of the two available on-board the NTN node; ii) a single NTN node of a large constellation composed of two orbit shells (see D3.2); and iii) a single Satellite Network Operator (SNO). When considering a full global system, with multiple satellites and operators, even this limited density would increase to a realistic number of total served users. In addition, the users are uniformly distributed in the service area on both land and sea areas; in future developments of this work, to be presented in D4.6, most of the users will be located on land areas and with non-uniform distributions (*i.e.*, with cold and hot spots). This will be particularly relevant after discussing the initial results. Thus, the user density values reported here are considered sufficient to understand the first performance trends and trade-offs. With the current service area dimension and user densities, we have approximately: 5100 UEs (10^{-3} UE/km²), 10300 UEs ($2 \cdot 10^{-3}$ UE/km²), and 20500 UEs ($4 \cdot 10^{-3}$ UE/km²).

With respect to the SCS, we consider 120 kHz, which is one of the admitted values for 3GPP NTN. In this case, the user bandwidth is obtained by considering 12 sub-carriers per PRB, with 132 PRBs. Thus, the total bandwidth is given by $B = 12 \cdot 132 \cdot 120,000$ Hz = 190.08 MHz. In FR2, Very Small Aperture Terminals (VSAT) are considered as per 3GPP TR 38.821.

Table 24: Parameters for system-level simulations with a single NTN node.

Parameter	Value	Comments
Sub-Carrier Spacing (SCS)	120 kHz	In this case, 132 PRBs are available
Operating Frequency Range	FR2 (Ka-band)	See 3GPP TR 38.821
Carrier frequency	20 GHz	See 3GPP TR 38.821
User bandwidth B	190.08 MHz	$132 \cdot 120 \cdot 12$ kHz
User density	$10^{-3}, 2 \cdot 10^{-3}, 4 \cdot 10^{-3}$ UE/km ²	
Number of radiating elements N_R	512	See Section 2.3.1
Power per radiating element $P_{av,el}$	65 mW	See Section 2.3.1
Total power on-board P_{av}	15.2218 dBW	$10 \log_{10}(0.0065 \cdot 512)$
Minimum distance coefficient ρ_{dist}	0 (RM) 1, ..., 7 (RM-MD)	See Section 4.2.4
Minimum user elevation angle ε_t	30°	See Section 4.2.3
Service area elevation angle ε_s	30°	See Section 4.2.3
Channel type	clear-sky, LOS	See Section 2.4.1.4 and 3GPP TR 38.811
Scheduling periodicity T_{sched}	2 s	See Section 4.2.1
Reporting periodicity T_{rep}	80 ms	See Section 4.2.1
Transmission time slot T_{slot}	10 ms	See Section 4.2.1
NTN node altitude	1000 km	See Section 2.1
Service area center	(45°N, 5°E)	See Section 4.2.3
UE terminal	VSAT	See Section 2.3.2 and 3GPP TR 38.821

4.3.2 Numerical results

The numerical results are provided and discussed in terms of the KPIs introduced in Section 4.2.3.1, *i.e.*, asymptotic spectral efficiency and capacity, and experienced spectral efficiency and capacity (*i.e.*, with channel use). We provide the results with the MMSE (CSI-based), LB-MMSE (location-based), and CBF (location-based) algorithms described in Section 4.2.3.2; for each of them, all power distribution approaches are considered (as per Section 4.2.3.3). The CSI/location reports provided by the users are assumed to be ideal, *i.e.*, without estimation errors. However, with the parameters listed in Table 24, we do have ancillary information aging due to the satellite movement. As the RS/RS-MD do not take into account the users' report to define the scheduled slots (random RRM), the aging interval can be as large as $T_{rep} = 80$ ms.

The considered architecture is DBFM, as it is in line with the 5G-STARDUST assumptions on the on-board capabilities. For location-based algorithms, we assume the advanced location service, *i.e.*, the latitude and longitude information on the users is available in the NTN node. As extensively discussed in this document, this approach will require adaptations to the current 3GPP NTN specifications (as the CSI-based solution, related to the estimation of the channel coefficients at radiating element level).

4.3.2.1 Clear-sky

Figure 59 provides the average asymptotic spectral efficiency, $\mathbb{E}_{k,q} \left\{ \eta_{k,q}^{(t_E, t_T)} \right\}$, and the average asymptotic capacity, $\mathbb{E}_{k,q} \left\{ C_{k,q}^{(t_E, t_T)} \right\}$, computed as reported in Section 4.2.3.1 and averaged over all Monte Carlo iterations, users, and transmission time slots. The values were obtained with a user density of 10^{-3} . Figure 60 and Figure 61 show the results obtained with $2 \cdot 10^{-3}$, $4 \cdot 10^{-3}$ users per km², respectively. The following trends can be observed:

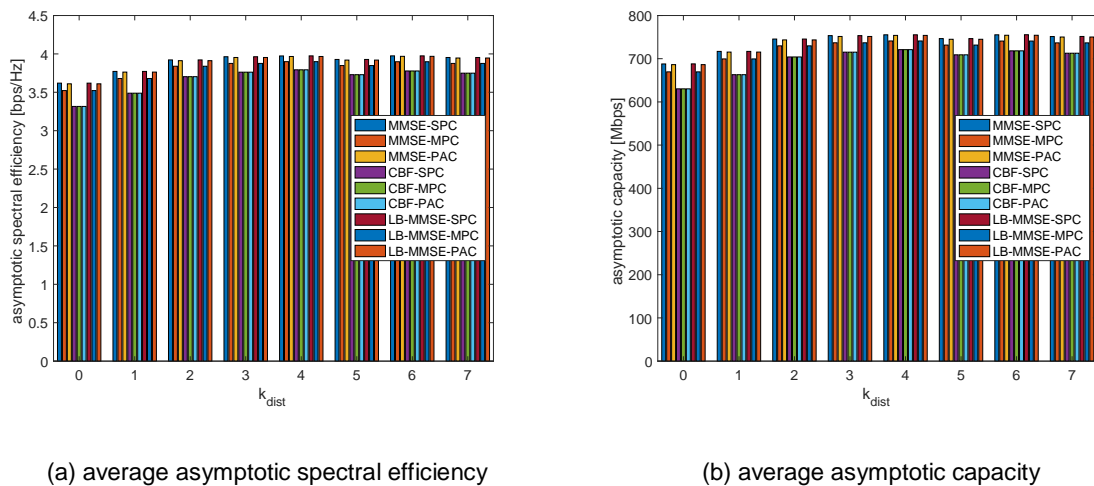


Figure 59: Asymptotic spectral efficiency and capacity with 10^{-3} UEs/km² in clear-sky conditions.

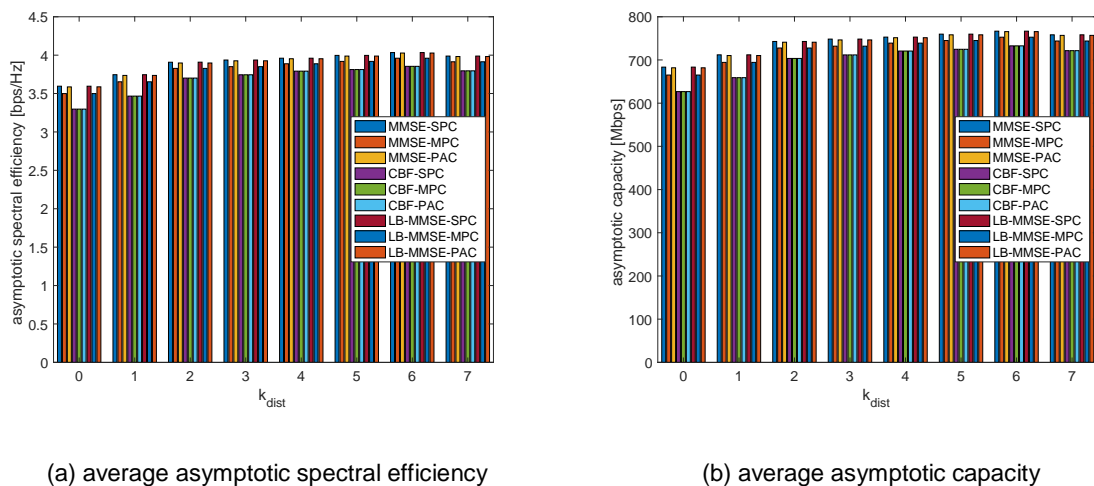


Figure 60: Asymptotic spectral efficiency and capacity with $2 \cdot 10^{-3}$ UEs/km² in clear-sky conditions.

- The asymptotic performance is not impacted at all by the users' density when random scheduling solutions are implemented. This shall not be surprising, as the impact of the users' density is usually evident when considering the channel use, *i.e.*, the amount of resources that the users are granted, and non-random RRM.
- The performance is increasing for increasing values of the minimum distance coefficient up to approximately $k_{dist} = 3$ with 10^{-3} users per km² and $k_{dist} = 5$ with $2 \cdot 10^{-3}$ and $4 \cdot 10^{-3}$ users per km², then they are almost constant. The RS-MD algorithm, when a user is too close to those already scheduled in a time slot, tries to find another user farther away. The probability of having close users, and users available farther away, increases for increasing user densities, and this motivates this trend on the asymptotic performance.
- For all densities and minimum distance coefficients, the best beamforming algorithms are the MMSE and LB-MMSE, as expected. However, compared to other studies (*e.g.*, [45], [48], [54]), the advantage with respect to CBF is relatively limited (approximately 10% of

the asymptotic spectral efficiency). As already discussed in the previous sections, we are considering an extremely large service area (basically covering Europe) and only 24 users served per time slot; consequently, the average SIR in each scheduled slot is already limited by design, with users that are relatively far away from each other. This is even more impactful with larger k_{dist} values, of course, and the gain of MMSE/LB-MMSE compared to CBF is more limited. Finally, it shall be noticed that MMSE and LB-MMSE have the same performance. With ideal CSI/location estimation, in fact, since there is no additional loss in the channel coefficients, both user-centric beamformers have the same estimated channel matrix and the same performance (also due to the fact that the scheduler is not depending on the specific algorithm).

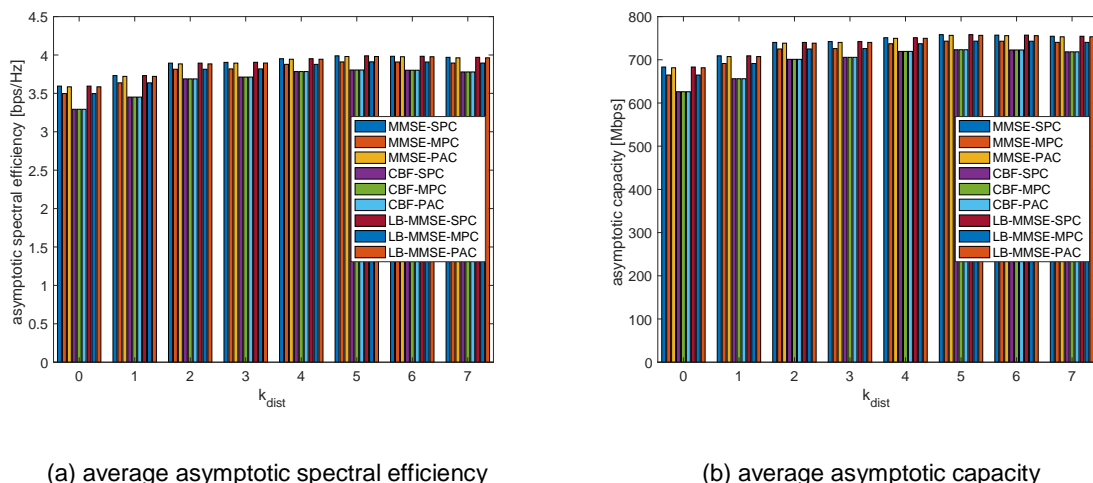


Figure 61: Asymptotic spectral efficiency and capacity with $4 \cdot 10^{-3}$ UEs/km² in clear-sky conditions.

- The best option for the power distribution is the SPC, as expected. However, the PAC distribution provides a performance which is almost identical to that one, despite its disruptive impact on the orthogonality of the beamformer columns. MPC solutions show the worst performance among the three. This is again motivated by the interference limited by design; in fact, a solution that exploits the entire available power (PAC) while not preserving the orthogonality (as MPC) shows a better performance. As such, PAC seems the best option for the power distribution, as it provides a performance close to the best theoretical one while ensuring that the power requirements are met.

Figure 62 shows the average experienced capacity, $\mathbb{E}_k\{\bar{C}_k\}$, when considering the channel use percentage, *i.e.*, the number of allocations and rate/capacity per allocation per user, with 10^{-3} and $2 \cdot 10^{-3}$ UE/km². These two densities are already sufficient to show a critical behaviour. While the trends in terms of beamforming algorithm and power distributions are almost the same of the asymptotic capacity, we can observe a significant reduction of the capacity for increasing densities. This is motivated, in line with equations (60) and (62), by the lower amount of allocations per user that can be granted when more users must be served. To substantiate this system behaviour, Figure 63 to Figure 65 show the CDF of the number of allocations per user. The CDF of the allocations with $4 \cdot 10^{-3}$ UE/km² shown in Figure 65 is provided to indicate that a further reduction in the experienced performance is expected also in this case, probably with a factor 2.

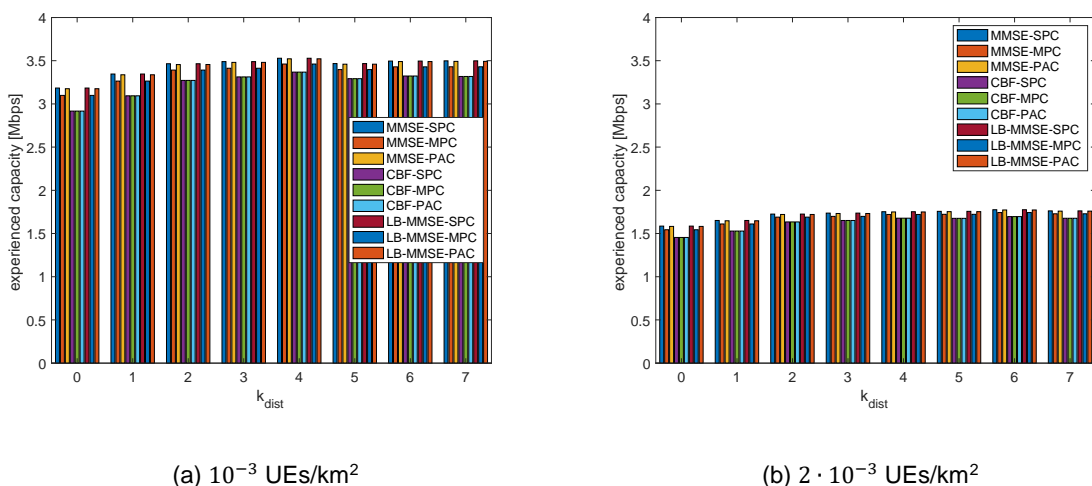


Figure 62: Average experienced capacity in clear-sky conditions.

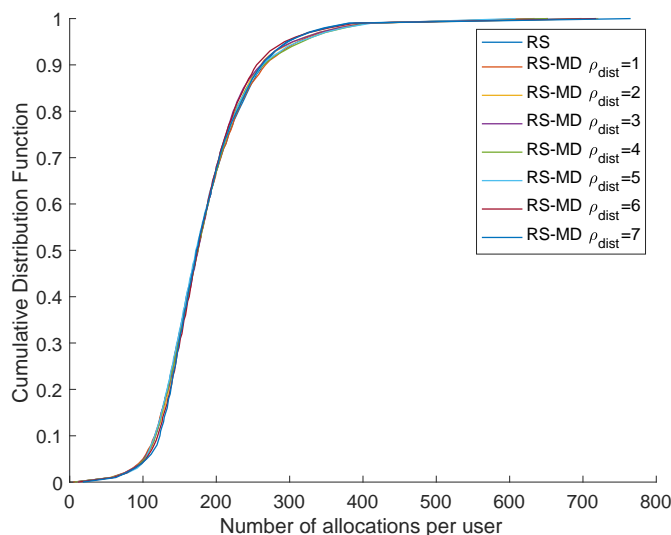


Figure 63: CDF of the number of allocations per user, with 10^{-3} UEs/km² in clear-sky conditions.

This initial assessment of user-centric beamforming already highlights the significant impact of the users density and their distribution in the service area on the performance of random scheduling solutions. In fact, these are directly linked to the number of allocations per user and the minimum distance among them, which are the main performance drivers.

With respect to the limited experienced capacity that can be achieved, it shall be noticed that the considered system has a single NTN node serving an area approximately covering Europe, with at most 24 user-centric beams per time slot. The orbital period in which the satellite is providing service to the area (represented in Figure 55) is approximately 400 seconds, *i.e.*, 6 minutes and 40 seconds. Clearly, in these conditions, having thousands of users leads to a scenario with each user being served for a very limited amount of time. This has a detrimental impact on the performance. For instance, let us focus on a user that obtained a sum-rate equal to $\sum_{p=1}^{N_{slot,k}} \eta_{k,p} = 581$ bps/Hz over $N_{slot,k} = 160$ allocations (approximately 3.6 bps/Hz, which is relatively good). The total serving time of the NTN node considered in the assessment is

$T_{serv} = 398.15$ seconds. With $T_{slot} = 10$ ms, equation (60) leads to an experienced spectral efficiency $\bar{\eta}_k = \sum_{p=1}^{N_{slot,k}} \frac{\eta_{k,p} T_{slot}}{T_{serv}} = 581 \frac{10^{-2}}{398.15} \cong 0.0146$ bps/Hz and, thus, $\bar{C}_k \cong 2.77$ Mbps of experienced capacity over 190.08 MHz, in line with the results discussed above.

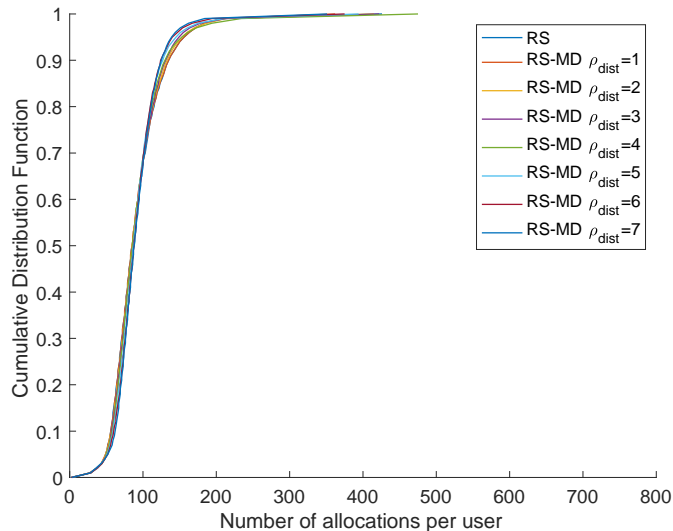


Figure 64: CDF of the number of allocations per user, with $2 \cdot 10^{-3}$ UEs/km² in clear-sky conditions.

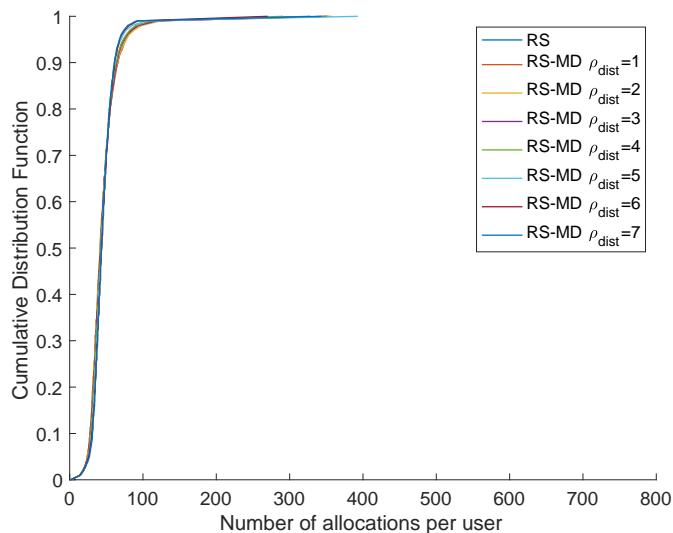


Figure 65: CDF of the number of allocations per user, with $4 \cdot 10^{-3}$ UEs/km² in clear-sky conditions.

Even when considering, as in this document, a single NTN node with a single polarisation, out of the two polarisations from a large NTN constellation, this suggests that user-centric beamforming solutions might be more beneficial to provide large capacities to hot-spot zones distributed over the service area, rather than to the entire visible service area. This would have a two-fold impact: i) increase the number of allocations per user, leading to a larger experienced performance; and ii) increase the co-channel interference, leading to larger benefits in exploiting MMSE solutions.

Based on the above observations, one of the most relevant evolutions of the analyses on user-centric beamforming will be that of properly modelling non-uniform user distributions, as preliminarily discussed in Section 4.4.2. In addition, also the assumption of uniform traffic distributions is a bit simplistic; its non-uniform behaviour will be in part implicitly considered through non-uniform user distributions, but also through the proper modelling of different traffic requests per user.

Despite the assumptions considered here, the analysis discussed above allowed to identify the factor that contribute the most to the performance and the relationship among the user-centric beamforming algorithms and their power distribution solutions, in particular observing the asymptotic performance.

4.3.2.2 Line-Of-Sight

For LOS channels (see Section 2.4 for their characterisation), we consider a sub-urban propagation environment. Figure 66 to Figure 68 show the asymptotic performance, and, compared to the clear-sky conditions discussed above, we can notice that:

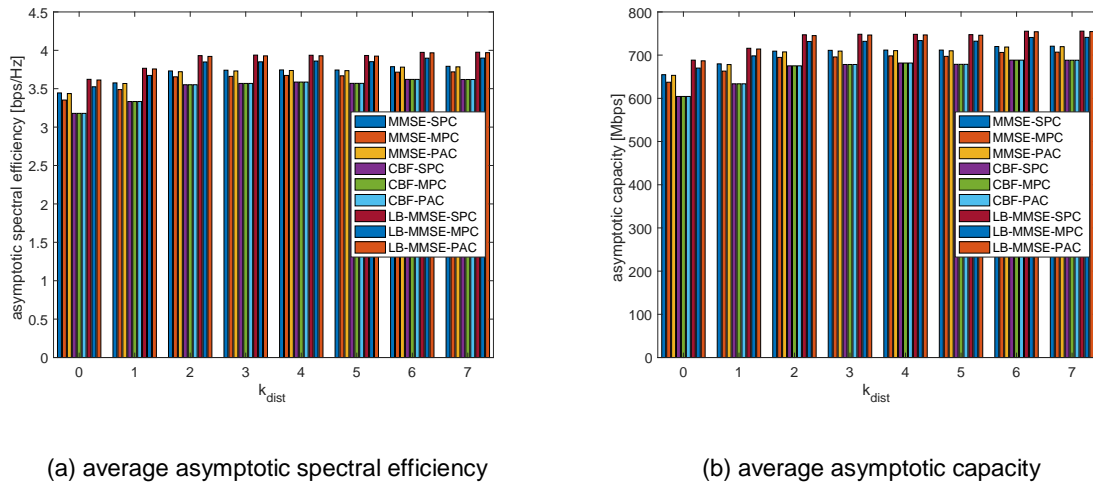
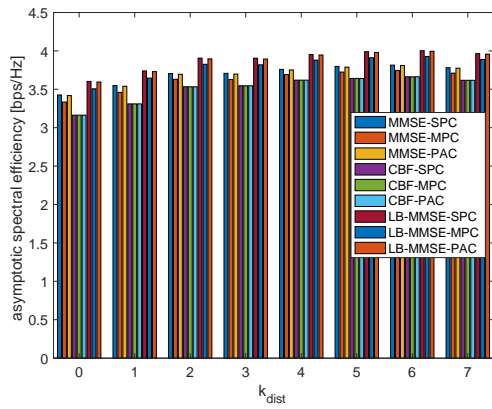
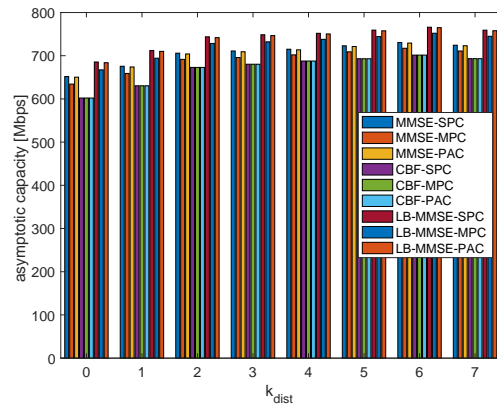


Figure 66: Asymptotic spectral efficiency and capacity with 10^{-3} UEs/km² in Line-Of-Sight sub-urban conditions.

- The performance of the LB-MMSE algorithm is better than the MMSE (CSI-based). This is motivated by the presence of the additional losses. In fact, with MMSE the users estimate all the terms in each channel coefficient and report it to the NTN node, while with LB-MMSE only the geometry terms are considered. When the actual transmission occurs, the introduction of uncorrelated stochastic terms between the estimation and transmission time instants affects the alignment of the MMSE beamforming matrix to the channel conditions, with a performance loss. This behaviour is negligible with CFB and LB-MMSE, showing that, with uncorrelated additional losses, it is better to not consider them in the channel coefficients rather than having wrong estimates.
- The general trends discussed above related to the minimum distance coefficient, power distributions, and user density still hold.

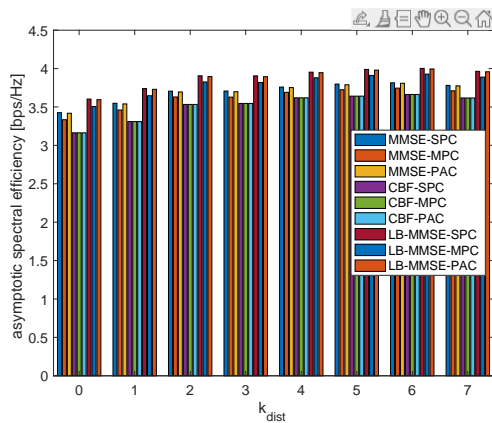


(a) average asymptotic spectral efficiency

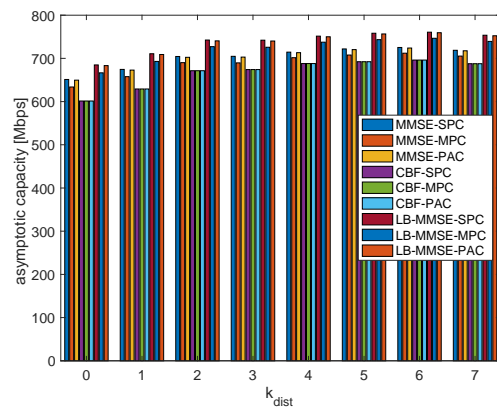


(b) average asymptotic capacity

Figure 67: Asymptotic spectral efficiency and capacity with $2 \cdot 10^{-3}$ UEs/km² in Line-Of-Sight sub-urban conditions.



(a) average asymptotic spectral efficiency



(b) average asymptotic capacity

Figure 68: Asymptotic spectral efficiency and capacity with $4 \cdot 10^{-3}$ UEs/km² in Line-Of-Sight sub-urban conditions.

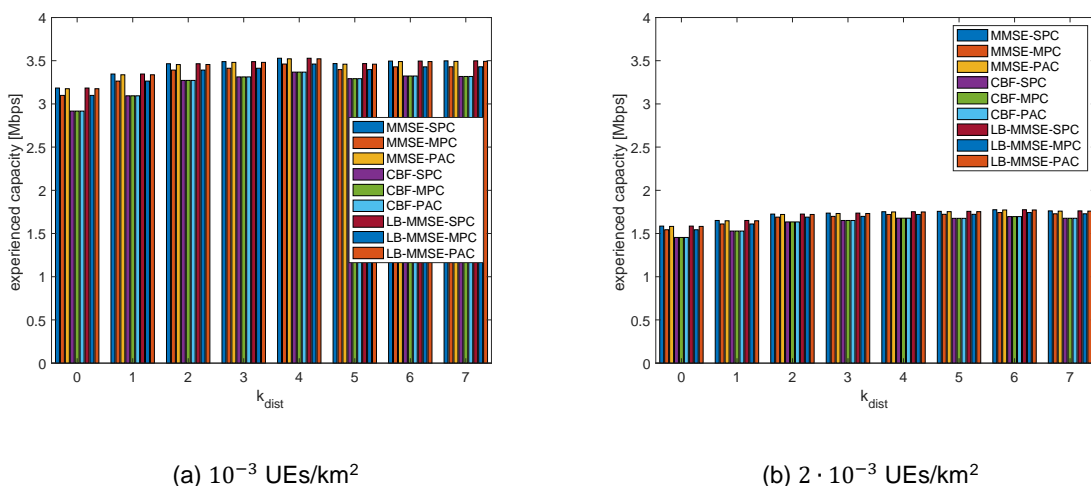
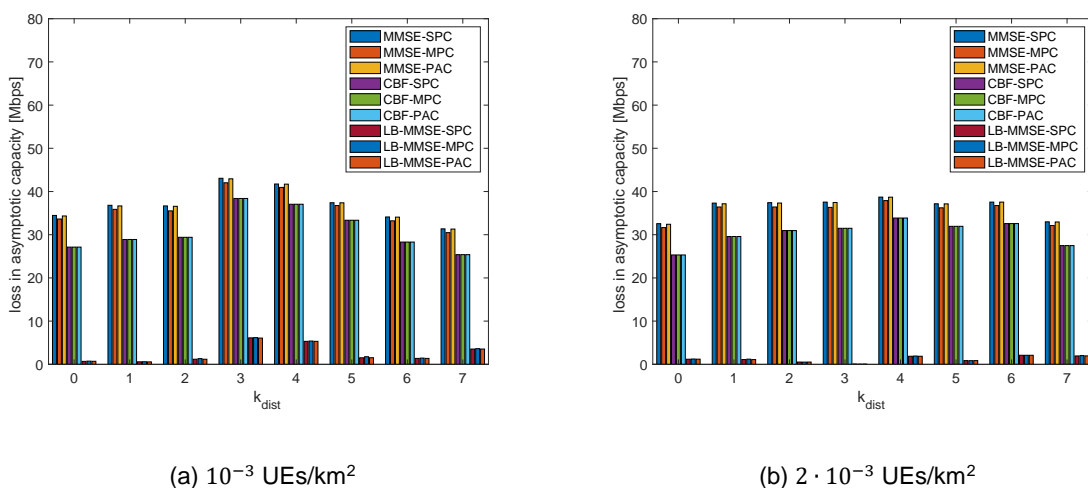
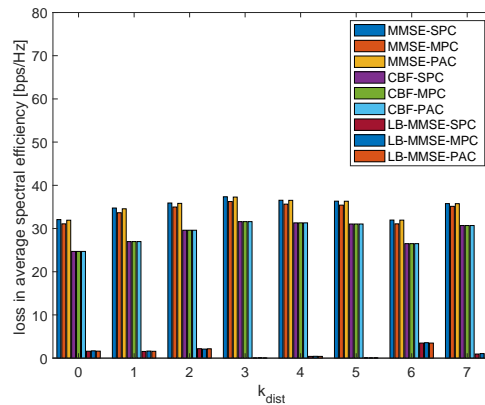


Figure 69: Average experienced capacity in Line-of-Sight sub-urban conditions.

Figure 69 show the performance with channel use, in line with the observations reported for the clear-sky channel.

To further highlight the larger impact of stochastic terms on the performance of CSI-based MMSE algorithms, Figure 70 shows the loss in the asymptotic capacity when comparing clear-sky with LOS channel conditions. It can be noticed that, apart from very low user densities, the loss is relatively stable. Location-based algorithms always provide a reduced loss compared to CSI-based MMSE. Moreover, LB-MMSE, which takes into account the channel coefficients without additional losses, performs significantly better from this perspective compared to CBF, which is a beam-steering approach.





(c) $4 \cdot 10^{-3}$ UEs/km²

Figure 70: Loss in the asymptotic capacity in Line-Of-Sight sub-urban compared to clear-sky.

4.4 OVERVIEW OF THE NEXT ACTIVITIES

The performance of user-centric beamforming algorithms has been preliminarily evaluated under several initial assumptions to identify the most important factors impacting the system performance. This analysis indeed pointed out the paths that shall be further developed in the prosecution of the studies in Task 4.2. Below, we provide a high-level overview of the next steps in the assessment of user-centric beamforming. In particular, the above system model will be extended along two main directions: i) the design and implementation of non-random RRM algorithms; and ii) the definition of proper models for non-uniform users and traffic distributions. In addition, the analyses will also consider the non-ideal estimation of the required ancillary information (CSI or location) and the potential movement of the users. Finally, the performance of the proposed beamforming and RRM algorithms will be compared to legacy beam-based solutions, such as Multi-Beam (MB) and Spatially Sampled MMSE (SS-MMSE) proposed in the literature.

It shall be noticed that the models and proposals reported below will be subject to a thorough assessment in terms of feasibility and representativeness and, as such, they might be adjusted/discarded/complemented during the next studies in Task 4.2.

4.4.1 Non-random RRM

Below, we provide a detailed description of some RRM algorithms introduced in the literature review in Section 4.1.2, which are considered to provide interesting baseline solutions to be elaborated (re-designed or only adjusted) for the prosecution of Task 4.2. It shall be noticed that other non-random RRM solutions can also be defined in the next activities.

4.4.1.1 Heuristic RRM (H-RRM) algorithm

The H-RRM algorithm proposed in [57] exploits information on the users' location and the known pre-defined beam pattern to pre-compute the SINR variations related to different scheduling assignments with a limited computational complexity. This RRM is thus beam-based, and not user-centric, and it is applied to GSO systems; however, the good performance and its computationally efficient implementation make this solution a solid baseline to be taken into account for the non-random RRM design. Moreover, it shall be noticed that this algorithm

is designed to operate with an MB beamforming algorithm and, thus, the applicability to the identified user-centric beamforming solutions shall also be assessed.

The H-RRM algorithm identifies the beams to be illuminated by defining the optimal colouring scheme, in which each colour represents a time frame and the users having the same colour are served by means of the MB algorithm. The Air Interface is the DVB-S2X; however, it can be expected that the framing structure will impact the performance due to a different numerology, but not in terms of applicability to NR-NTN framing.

Let us focus on a Superframe (SF) with duration T_{SF} , in which N_{FR} frames having duration T_{FR} are present. The algorithm defines the users' scheduling with a time frame resolution, *i.e.*, each frame corresponds to a colour. Each frame is then further divided into N_{SL} slots having duration T_{SL} . To each slot, the RRM assigns a specific Modulation and Coding scheme (ModCod) defined by the DVB-S2X Adaptive Coding and Modulation (ACM) tables. ModCods inside each frame, the RRM algorithm allows different users of the same beam to be served based on their SINR. In each slot, N_{SY} symbols are transmitted with baud rate $R_s = \frac{1}{T_s}$. In this context, the following relations hold:

$$T_{SL} = N_{SY}T_s, T_{FR} = N_{SL}T_{SL}, T_{SF} = N_{FR}T_{FR} \quad (77)$$

For the s -th slot in the f -th frame, the number of transmitted bits is given by:

$$N_b^{SL}(s, f) = N_{SY} \eta_{ACM}(s, f) \quad (78)$$

where $\eta_{ACM}(s, f)$ is the spectral efficiency corresponding to the ModCod selected for the s -th slot in the f -th frame. The total number of bits transmitted in the frame is thus:

$$N_b^{FR}(f) = N_{SY} \sum_{s=1}^{N_{SL}} \eta_{ACM}(s, f) \quad (79)$$

With respect to the SF, the total number of transmitted bits is:

$$N_b^{SF} = N_{SY} \sum_{f=1}^{N_{FR}} \sum_{s=1}^{N_{SL}} \eta_{ACM}(s, f) \quad (80)$$

Thus, the corresponding SF average bit rate is computed as follows:

$$R_b^{SF} = \frac{N_b^{SF}}{T_{SF}} = \frac{N_{SY}}{T_{SF}} \sum_{f=1}^{N_{FR}} \sum_{s=1}^{N_{SL}} \eta_{ACM}(s, f) \quad (81)$$

It is worth highlighting that, in the proposed H-RRM approach, it is not required to adapt the super-frame format to the actual traffic distribution. This simplifies the beam-hopping functioning and the associated signalling implementation.

Denoting by N_{UE} the number of users, let us define the $N_{UE} \times N_{UE}$ generalised co-channel matrix \mathbf{X} , in which a unit entry at position (i, j) identifies the assignment of the same radio resource to the i -th and j -th users. This matrix is symmetric with unit diagonal elements. In addition, let us denote as \mathbf{A} the $N_{UE} \times N_{UE}$ generalised power transfer matrix computed as in (55), for all the considered users. Then, we can define a co-channel power transfer matrix \mathbf{A}_{CC} :

$$\mathbf{A}_{CC} = \mathbf{X} \odot \mathbf{A} \quad (82)$$

In the framework of this algorithm, the power transfer matrix can be computed since the system is based on a pre-defined beam lattice. Thus, exploiting the information on the user location, all quantities discussed below can be pre-computed.

The INR and SINR of the i -th user computed in Section 4.2.3.1 can thus be formulated as:

$$\text{INR}_i = \sum_{\substack{j=1 \\ j \neq i}}^N x_{i,j} a_{i,j} \quad (83)$$

$$\text{SINR}_i = \frac{a_{i,i}}{1 + \sum_{\substack{j=1 \\ j \neq i}}^N x_{i,j} a_{i,j}} = \frac{\text{SNR}_i}{1 + \text{INR}_i} \quad (84)$$

By defining the $N_{UE} \times N_C$ binary colouring matrix \mathbf{C} , with N_C being the number of colours, and considering that the i -th user shall be assigned to one colour only, the rows of \mathbf{C} must satisfy the following condition:

$$\sum_{k=1}^{N_C} c_{i,k} = 1, \forall i \quad (85)$$

Moreover:

$$\sum_{i=1}^{N_{UE}} \sum_{k=1}^{N_C} c_{i,k} = N_{UE} \quad (86)$$

The channel matrix \mathbf{X} can be obtained as the matrix product of \mathbf{C} with its transpose:

$$\mathbf{X} = \mathbf{C} \mathbf{C}^T \quad (87)$$

The main target of the H-RRM algorithm is to assign colours to the users aiming at reducing the mutual co-channel interference. Thus, from the power transfer matrix \mathbf{A} we can focus on the off-diagonal elements only, as the diagonal ones denote the intended power. This leads to the introduction of \mathbf{Q} as the interference matrix:

$$\mathbf{Q} = \mathbf{S} - \text{diag}\{\text{diag}(\mathbf{A})\} \quad (88)$$

in which all diagonal entries are null by definition and non-diagonal elements are equal to $a_{i,j}$. The sum co-channel interference, evaluated as the total INR, can be assumed as a figure of merit of the overall performance and it satisfies the following definition:

$$\text{INR}_T = \sum_{i=1}^{N_{UE}} \text{INR}_i = \sum_{i=1}^{N_{UE}} \sum_{j=1}^{N_{UE}} x_{i,j} c_{i,j} \quad (89)$$

The above sum co-channel interference can be written as:

$$\text{INR}_T = \mathbf{1}^T (\mathbf{Q} \odot \mathbf{X}) \mathbf{1} = \text{tr}(\mathbf{C}^T \mathbf{Q} \mathbf{C}) = [\text{vec}(\mathbf{C})]^T (\mathbf{I} \otimes \mathbf{Q}) \text{vec}(\mathbf{C}) \quad (90)$$

where the N_{UE} -dimensional vector $\mathbf{1}$ has all unit entries, $\text{vec}(\mathbf{C})$ is the vectorization of the matrix \mathbf{C} into a column vector and \otimes indicates the Kronecker product. Equation (90) can be written as a Mixed Integer Quadratic Programming (MIQP) problem of the form:

$$\begin{aligned} & \text{minimise } [\text{vec}(\mathbf{C})]^T (\mathbf{I} \otimes \mathbf{Q}) \text{vec}(\mathbf{C}) \\ & \text{subject to } \sum_{k=1}^{N_C} c_{i,k} = 1, \forall i \\ & c_{i,k} \in \{0,1\}, \forall i, \forall k \end{aligned}$$

To solve this problem, an efficient heuristic approach has been proposed in [57] for a beam colouring problem. In particular, an auxiliary $N_{UE} \times N_C$ co-channel interference matrix is $\mathbf{V} = \mathbf{Q}\mathbf{C}$ is introduced. The generic element $v_{i,k}$ represents the aggregated co-channel interference on the i -th user due to the k -th interfering co-channel user and it can be written as the product between the i -th row of \mathbf{Q} with the k -th column of \mathbf{C} :

$$v_{i,k} = \mathbf{q}_{i,:} \cdot \mathbf{c}_{:,k} \quad (91)$$

Algorithm 3: H-RRM algorithm.

Input

- Power transfer matrix: \mathbf{A}
- Number of colours: N_C
- Number of users: N_{UE}

Output

- Colouring matrix: \mathbf{C}

Initialisation

$$\mathbf{Q} = \mathbf{S}$$

$$q_{i,i} = 0$$

$$c_{i,k} = 0$$

$$f_i = 0$$

Find the user with the worst single-entry interference: $i^{(1)} = \underset{i}{\text{argmax}} \left[\underset{k}{\text{argmax}} q_{i,k} \right]$

Colour 1 to the first user: $k^{(1)} = 1$

Assign colour $k^{(1)}$ to user $i^{(1)}$: $c_{i^{(1)},k^{(1)}} = 1$

Update the user flag: $f_{i^{(1)}} = 1$

While $\sum_{i=1}^{N_{UE}} f_i \neq N_{UE}$

1 Evaluate $\mathbf{A}^{(n)} = \mathbf{Q}\mathbf{C}^{(n)}$

Find the user with the worst aggregated interference:

2
$$i^{(n)} = \underset{i, f_i=0}{\text{argmax}} \left[\underset{k}{\text{argmax}} a_{i,k} \right]$$

Find the colour with the least aggregated interference:

3
$$k^{(n)} = \underset{k}{\text{argmin}} a_{i^{(n)},k}$$

4 Assign colour $k^{(n)}$ to user $i^{(n)}$:

$$c_{i^{(n)},k^{(n)}} = 1$$

5 Remove the user from the list:

$$f_{i^{(n)}} = 1$$

End while

To understand how the algorithm works, let us assume that, at the n -th iteration of the RRM algorithm, a number of users has been assigned to a colour such that the temporary colouring matrix $\mathbf{C}^{(n)}$ satisfies the condition $\sum_{k=1}^{N_C} c_{i,k}^{(n)} = 1$ if the i -th user has been assigned a colour and 0 otherwise. For all non-assigned users, $\mathbf{A}^{(n)} = \mathbf{Q}\mathbf{C}^{(n)}$ allows to select the row with the worst interference and, within it, the least interfering colour. Thus, this algorithm is **prioritising the assignments for the most interfered users, by selecting the least interfering colour**.

Algorithm 3 shows the pseudo-code of the H-RRM algorithm. It can be noticed that the first user is assigned to colour 1, as it is clearly the user showing the highest interference from any other user. In the implementation of the algorithm, it shall be noticed that $\mathbf{A}^{(n)} = \mathbf{Q}\mathbf{C}^{(n)}$ shall be computed only for the non-assigned users. Thus, a user flag f_i is used to dynamically optimise the size of the matrices to the smallest possible dimension, to ease the computational complexity.

The H-RRM algorithm provides a good performance for both uniform and non-uniform traffic distributions. However, its applicability to the 5G-STARUST analyses shall be properly evaluated. In fact, in our system, the NTN node is on a LEO orbit, which means that not all of the users are visible for the entire period in which the scheduling shall be optimised. Rather, it shall be applied only to visible users, also taking into account the time for which these users will remain visible, which can be estimated based on their location and the satellite ephemeris. In addition, the H-RRM algorithm operates in a beam-based system, while in 5G-STARUST user-centric beamforming is considered. These aspects will be discussed in the prosecution of Task 4.2.

4.4.1.2 Graph-based RRM (G-RRM)

Building on the graph-based algorithms introduced in the literature review in Section 4.1.2, the scheduling problem can be formulated as a clustering problem. Let us denote by \mathcal{U} the set of all users, then the scheduler shall allocate each user to one or more clusters $\{C_1, \dots, C_p\}$ with $C_p \subseteq \mathcal{U}$ and $\cup_{p=1}^P C_p = \mathcal{U}$, *i.e.*, each user is allocated to at least one cluster. We denote as $K_p = |C_p|$ the cardinality of the p -th cluster, *i.e.*, the number of co-channel users in the p -th cluster. For each time slot, the RRM selects a cluster to be scheduled, which results in a complex cluster channel matrix \mathbf{H}_p . Then, as extensively discussed in the previous sections, the beamforming algorithm provides the coefficients for the transmission in the identified time slot.

Let us denote as $\mathcal{G}(\mathcal{V}, \mathcal{E})$ an undirected and unweighted graph with vertex \mathcal{V} and edges \mathcal{E} . A *clique* \mathcal{Q} of $\mathcal{G}(\mathcal{V}, \mathcal{E})$ is a subset of vertices, *i.e.*, $\mathcal{Q} \subseteq \mathcal{V}$, such that every two distinct vertices are adjacent. This means that the clique \mathcal{Q} is a complete sub-graph of $\mathcal{G}(\mathcal{V}, \mathcal{E})$. In our context, the set of vertices \mathcal{V} coincides with the set of users \mathcal{U} and the set of edges is built based on a dissimilarity measure that depends on the type of ancillary information available at the transmitter. In particular:

- CSI-based: the Channel coefficient of Correlation (CoC) is computed as

$$|\Psi|_{i,j} = \frac{\left| \mathbf{h}_{i,:}^{(t_E)} \left(\mathbf{h}_{j,:}^{(t_E)} \right)^H \right|}{\left\| \mathbf{h}_{i,:}^{(t_E)} \right\| \left\| \mathbf{h}_{j,:}^{(t_E)} \right\|} \in [0,1] \quad (92)$$

The set of edges is then completely determined by an adjacency matrix Θ , where $\theta_{i,j} = 1$ if $|\Psi|_{i,j} \leq \delta_C$ and 0 otherwise and δ_C denotes a properly designed threshold. If $\theta_{i,j} = 0$, the i -th and j -th user are denoted as co-linear and, thus, no edge is constructed between

them. On the contrary, when the $\theta_{i,j} = 1$ the i -th and j -th user are considered orthogonal, which means that they can be scheduled together and an edge can be constructed.

Algorithm 4: G-RRM algorithm.

Input	
•	Adjacency matrix Θ associated to the graph $\mathcal{G}(\mathcal{V}, \mathcal{E})$
Output	
•	Cluster sets $\{\mathcal{C}_1, \dots, \mathcal{C}_P\}$ and cluster weights $\gamma_p, p = 1, \dots, P$
Initialisation	
	$p = 1$
	$\mathcal{V} = \mathcal{U}$
While $\mathcal{V} \neq \emptyset$	
1	Compute the maximum clique: $\mathcal{Q}_{max} = \text{MaxCliqueDyn}(\mathcal{G})$
	Define the cluster:
2	$\mathcal{C}_p = \mathcal{Q}_{max}$
	$K_p = \mathcal{C}_p $
3	Remove all edges associated with the vertices \mathcal{Q}_{max}
4	Update the set of users to be served:
	$\mathcal{V} = \mathcal{V} - \mathcal{Q}_{max}$
5	Update the graph $\mathcal{G}(\mathcal{V}, \mathcal{E})$ and increase the cluster counter:
	$p = p + 1$
End while	
For $p = 1, \dots, P$	
	Compute the cluster weights:
6	$\gamma_p = \frac{K_p}{\sum_{p=1}^P K_p}$
End for	

- Location-based: given the users' latitude and longitude coordinates, the great circle distance between them is given by

$$|\Gamma|_{i,j} = 2R_E \sin^{-1} \sqrt{\varphi_{i,j}}$$

$$\varphi_{i,j} = \sin^2 \left(\frac{\text{lat}_j - \text{lat}_i}{2} \right) + \cos \text{lat}_j \cos \text{lat}_i \sin^2 \left(\frac{\text{lon}_j - \text{lon}_i}{2} \right) \quad (93)$$

The adjacency matrix can be constructed again by comparing the values obtained in (93) with a given threshold, δ_D . In this case, the interpretation is however different: if $\theta_{i,j} = 0$, the two users are too close and, thus, their directions are considered to be not optimally separated through beamforming, while with $\theta_{i,j} = 1$ the users are sufficiently separated and an edge can be constructed.

The thresholds δ_C, δ_D define an upper-bound of the dimension of a clique, *i.e.*, to the optimal number of users that can be efficiently scheduled together. A maximum clique $\mathcal{Q}_{max} \subseteq \mathcal{V}$ is a clique such that no other clique can be defined with more vertices. The proposed G-RRM implements a greedy iterative search aims at minimising the total number of clusters, P , given

the optimised threshold values. This is achieved by: i) maximising the dimension of each cluster by iteratively finding the maximum clique of the updated graph; and ii) generating disjoint sets of scheduled users, which also provides a minimisation of the number of clusters.

The G-RRM algorithm is shown in Algorithm 4. The cluster weights computed at the last step of the algorithm are introduced to adapt the duration of the time slot to the number of users scheduled per cluster. This is introduced in order to have a fair-proportional scheduler. The function $\text{MaxCliqueDyn}(G)$ computing the maximum clique is an efficient branch-and-bound algorithm defined in [95].

4.4.2 User and traffic distribution

With respect to the users' distribution, a first step will be that of taking into account land and maritime UEs. Figure 71 shows an example of such deployment with a uniform user distribution on land with density $2 \cdot 10^{-3}$ and 1%, 2%, 5%, and 10% of the land density on sea. These values are merely used for this example and the possibility to consider larger user distributions or different proportions between land and sea users will be evaluated.

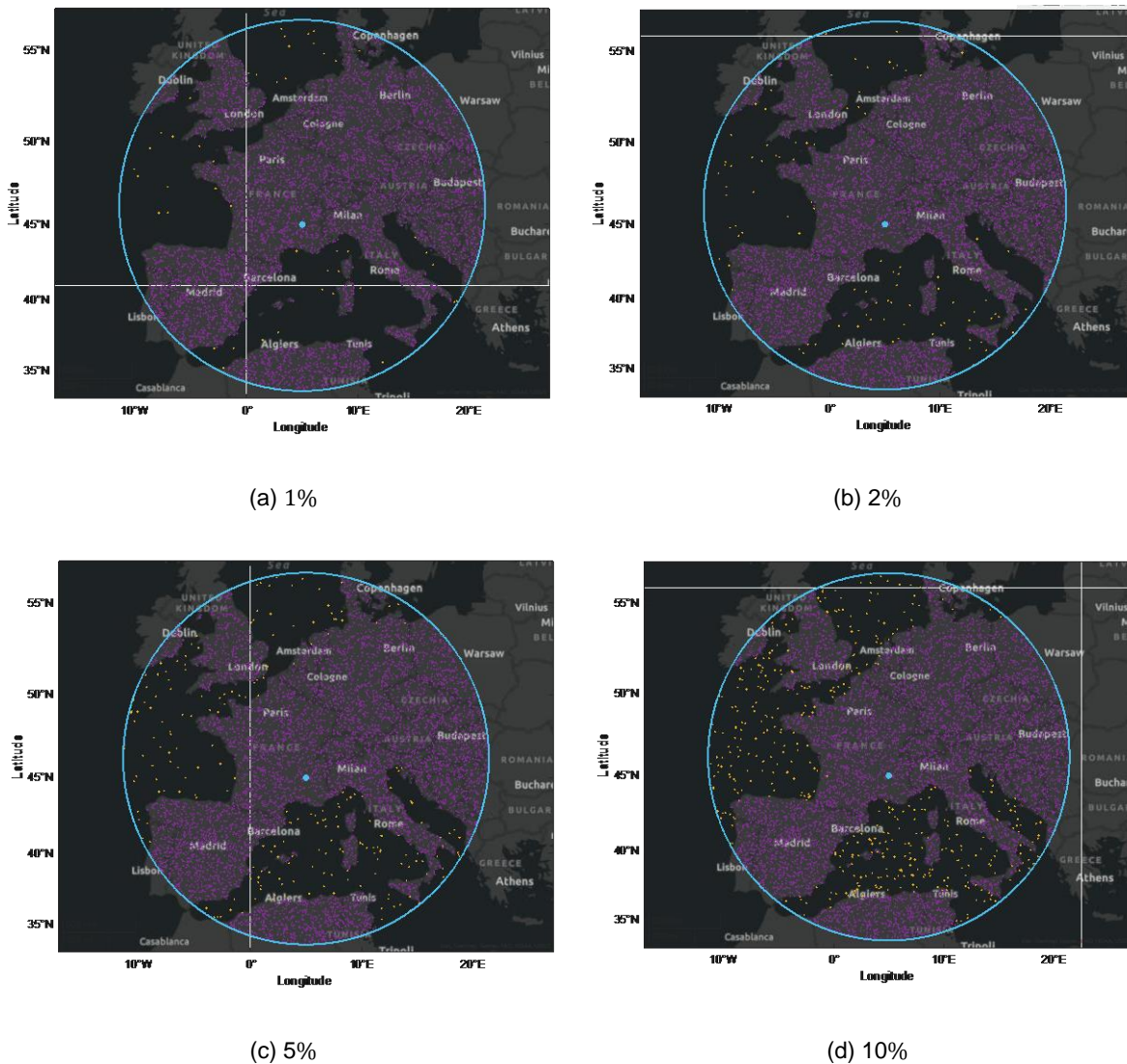


Figure 71: Example of separate uniform UEs' distributions on land and sea.

A second step in properly modelling the geographical location of the user extends the above model by introducing a non-uniform distribution. To this aim, the datasets described in D4.1 will be reviewed and their applicability to model non-uniform users' distributions will be evaluated. Also, other open-source databases can be considered. For instance, population information can be obtained from the Global Human Settlement Layer (GHSL) by the Joint Research Centre (JRC) of the European Commission (EC), [98]. This dataset contains a geographical raster of the estimated population count in different periods and spatial resolutions. Such information might also be used to extrapolate statistical models from the available data, to then have stochastic non-uniform user distributions in the service area, [99]. Figure 72 shows an example of population database obtained from the GHSL.

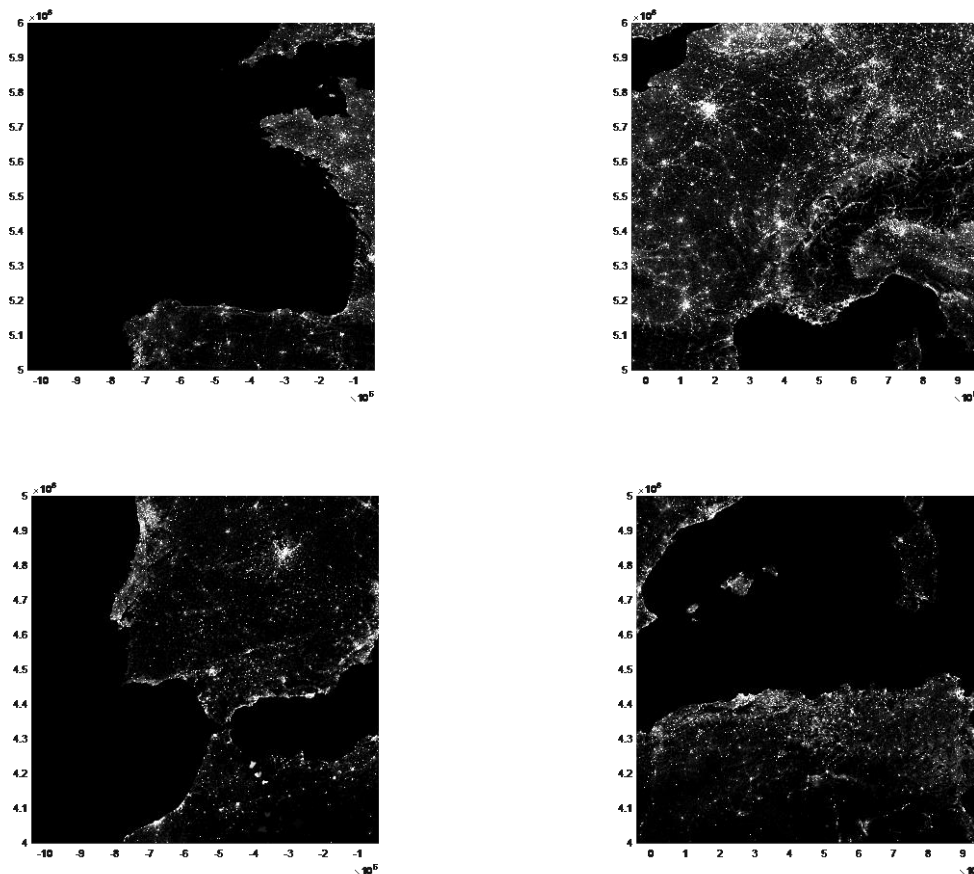


Figure 72: Example of population database from the GHSL of the EC JRC, [98].

With respect to the traffic distribution, as for the users, the first solution will be that of evaluating the applicability and generality of the datasets provided in D4.1, either directly or as inputs to obtain more general stochastic models. Moreover, in the literature, non-uniform models have been recently considered. In [57], a truncated bi-dimensional Gaussian distribution model is implemented, while the studies in [98] exploit the above-mentioned JRC EC database. These solutions will be reviewed, and their applicability discussed, during Task 4.2 activities.

In addition to the above database-oriented approaches, also simpler, yet effective for the purpose of user-centric beamforming, mathematical models might be considered. For instance, let us assume that N_{HS} traffic hot-spots are uniformly distributed in the service land area. In each hot-spot center, the traffic is maximum and equal to C_{max} , while the traffic request follows an exponentially decaying function with exponential decay constant λ_C . At a pre-defined

distance from the hot-spot center, r_{HS} , the traffic is truncated to a minimum value C_{min} . Based on these considerations, the traffic at a given distance d from the hot-spot center is:

$$C(d) = C_{max} e^{-\lambda_C d \frac{r_{thr}}{r_{HS}}} \quad (94)$$

where r_{thr} is a scaling factor equal to the distance at which the baseline exponentially decaying function $C_{max} e^{-\lambda_C d}$ equals C_{min} . When multiple hot-spots are present, the traffic for each user is taken as the maximum value, *i.e.*: $C_i = \max_{q=1, \dots, N_{HS}} C_q(d_{i,q})$, where $d_{i,q}$ is the distance of the i -th user from the q -th hot-spot center and $C_q(d_{i,q})$ the corresponding capacity according to (94).

Clearly, other mathematical models are possible and can be evaluated during the execution of the project. An example with the exponential decaying model is depicted in Figure 73 for different hot-spot radius values. It shall be noticed that this model can also be implemented super-imposing different uniformly distributed hot-spots, *i.e.*, hot-spot distributions with different coefficients, minimum/maximum capacity, and/or radius. The definition of the model parameters ($N_{HS}, r_{HS}, \lambda_C, C_{min}, C_{max}$) can also be performed by exploiting D4.1 databases.

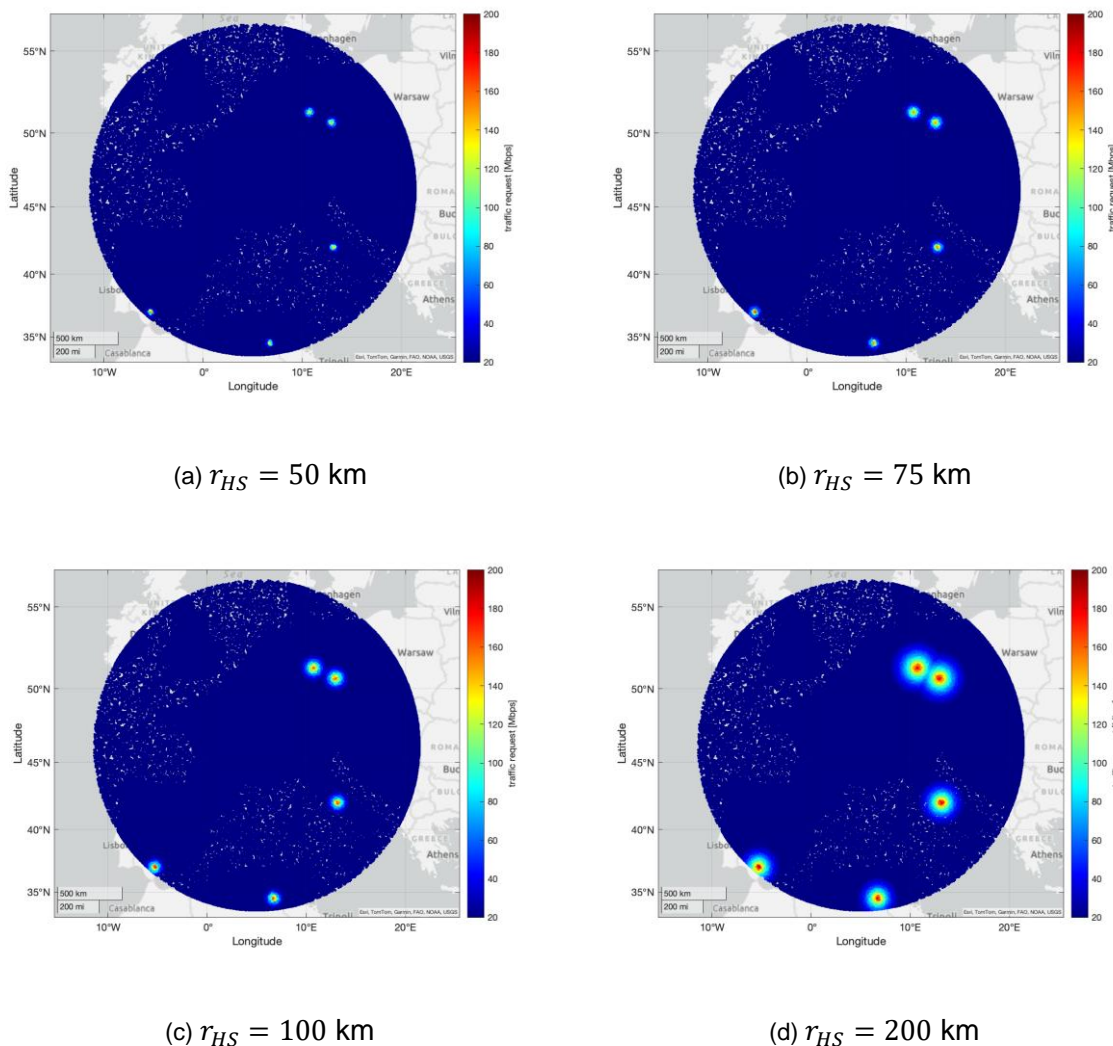


Figure 73: Example of exponentially decaying traffic model, $N_{HS} = 5$, $C_{min} = 20$ Mbps, $C_{max} = 200$ Mbps, $\lambda_C = 0.5, 1$ UE/km².

4.4.3 Users' movement

An effective model of the users' movement, if required for the performance assessment, was reported in the EC SPACE-29-TC-2020 project DYNASAT³ and reported in Deliverable D3.5, [100]. For the sake of completeness, we describe the model below.

Table 25: Receiver speed characteristics, [101].

Receiver scenario	Receiver speed v_{UE} [km/h]	Receiver type
Fixed	0	VSAT, handheld
Pedestrian	3	handheld
Public Safety A	100	Handheld
Public Safety B	250	VSAT
Vehicular	250	VSAT
Aircraft	1000	VSAT

3GPP TS 22.261 provides the maximum speed values for several categories of users, reported in Table 25, [101]. According to the proposed model, each user is assumed to be moving in a random direction distributed as a uniform random variable $\mathcal{U}(0,360^\circ)$ with respect to the z-axis in an Earth-Centered Earth-Fixed (ECEF) reference system (*i.e.*, the North Pole direction). Let us denote by ψ_i such random direction and by v_i the speed of the generic i -th user in [km/h]. During a time slot with duration T_{slot} seconds, the user moves from the location $\mathbf{p}_{i,t-1} = (\text{lat}_{i,t-1}, \text{lon}_{i,t-1})$ at instant $t - 1$ to a new location $\mathbf{p}_{i,t} = (\text{lat}_{i,t}, \text{lon}_{i,t})$. The Earth central angle between these two locations on the Earth's surface can be computed as:

$$\delta_i^{(t,t-1)} = \frac{180 T_{slot} v_i}{\pi 3.6 R_E} \quad (95)$$

Let us denote as $\mathbf{p}_{i,t-1}^{(ECEF)}$ and $\mathbf{p}_{i,t}^{(ECEF)}$ the starting and final positions of the i -th user in ECEF coordinates, *i.e.*:

$$\begin{aligned} \mathbf{p}_{i,t-1}^{(ECEF)} &= \begin{bmatrix} \cos \text{lat}_{i,t-1} \cos \text{lon}_{i,t-1} \\ \cos \text{lat}_{i,t-1} \sin \text{lon}_{i,t-1} \\ \sin \text{lat}_{i,t-1} \end{bmatrix} \\ \mathbf{p}_{i,t}^{(ECEF)} &= \begin{bmatrix} \cos \text{lat}_{i,t} \cos \text{lon}_{i,t} \\ \cos \text{lat}_{i,t} \sin \text{lon}_{i,t} \\ \sin \text{lat}_{i,t} \end{bmatrix} \end{aligned} \quad (96)$$

It can be shown that:

$$\mathbf{p}_{i,t}^{(ECEF)} = \begin{bmatrix} -\sin \delta_i^{(t,t-1)} (\sin \text{lat}_{i,t} \cos \text{lon}_{i,t-1} \cos \psi_i + \sin \text{lon}_{i,t-1} \sin \psi_i) + \cos \delta_i^{(t,t-1)} \cos \text{lat}_{i,t} \cos \text{lon}_{i,t-1} \\ -\sin \delta_i^{(t,t-1)} (\sin \text{lat}_{i,t} \sin \text{lon}_{i,t-1} \cos \psi_i - \cos \text{lon}_{i,t-1} \sin \psi_i) + \cos \delta_i^{(t,t-1)} \cos \text{lat}_{i,t} \sin \text{lon}_{i,t-1} \\ \sin \delta_i^{(t,t-1)} \cos \text{lat}_{i,t} \cos \psi_i + \cos \delta_i^{(t,t-1)} \sin \text{lat}_{i,t} \end{bmatrix} \quad (97)$$

From (97), it is straightforward to obtain $\mathbf{p}_{i,t} = (\text{lat}_{i,t}, \text{lon}_{i,t})$:

³ The model was defined and implemented by the University of Bologna, coordinator of the DYNASAT project, which is one of the CNIT Research Unit collaborating in 5G-STARUST.

$$\begin{aligned} \text{lat}_{i,t} &= \sin^{-1} p_{i,t}^{(ECEF,z)} \\ \text{lon}_{i,t} &= \text{atan2} \left(p_{i,t}^{(ECEF,y)}, p_{i,t}^{(ECEF,x)} \right) \end{aligned} \quad (98)$$

Figure 74 shows an example of users' movement according to the proposed model.

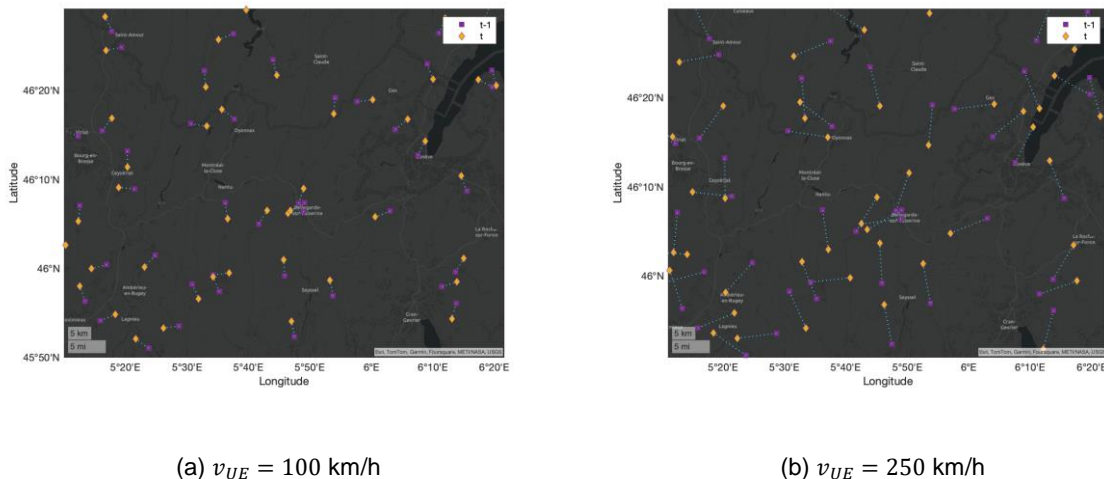


Figure 74: Example of users' movement over 2 minutes.

4.4.4 Non-ideal estimation of the ancillary information

When considering a non-ideal estimation of the ancillary information required by user-centric beamforming and RRM algorithms, two paths are possible. The first is to implement the CSI estimation procedure or a GNSS estimation procedure in each UE; however, the overall complexity would be extremely increased, as each UE shall implement these procedures, and also the signals and signalling to support them shall be included. In addition, the estimation procedures would be not entirely based on 3GPP specifications, *i.e.*, consolidated technical solutions, as the proposed algorithms require adaptations to them, as extensively discussed in this document. Considering that the intent is that of assessing the performance of the proposed algorithms with non-ideal estimations, the introduction of mathematical models is deemed to be the best option.

For location-based algorithms, the users' movement model described in the previous section can be again exploited. In fact, let us denote as Δd_{err} the maximum GNSS positioning error. The positioning error at the i -th UE can be modelled as a uniform r.v. $d_{err,i} \sim \mathcal{U}(-\Delta d_{err}, \Delta d_{err})$. From (95), this corresponds to an Earth central angle between the exact location and the estimated one given by:

$$\delta_i^{(err)} = \frac{180}{\pi} \frac{d_{err,i}}{R_E} \quad (99)$$

Then, the coordinates of the estimated location can be computed according to (96)-(98).

For CSI-based algorithms, two models can be considered, both allowing a relatively simple control on the amount of error that is introduced on the exact coefficients:

- Let us assume that the UEs implement a Data Aided (DA) estimation algorithm, that in the estimation time instant t_E operates by exploiting ℓ_{DA} known symbols and with an

estimation SNR given by $\text{SNR}_{i,n}^{(CSI,t_E)}$ for the n -th radiating element. The Cramer-Rao Bound (CRB) of the estimation on the amplitude and phase is given by:

$$\sigma_{A,i,n}^2 = \frac{1}{\ell_{DA} \text{SNR}_{i,n}^{(CSI,t_E)}} \quad (100)$$

$$\sigma_{P,i,n}^2 = \frac{1}{2\ell_{DA} \text{SNR}_{i,n}^{(CSI,t_E)}} \quad (101)$$

We can assume that the error on the amplitude and phase estimation of coefficient $h_{i,n}^{(t_E)}$ are modelled as: i) $|e_{i,n}^{(t_E)}| \sim \mathcal{N}\left(0, |h_{i,n}^{(t_E)}|^2 \sigma_{A,i,n}^2\right)$, where the amplitude of the channel coefficient is required since the CRB provides a normalised variance of the estimation error; and ii) $\arg\left(e_{i,n}^{(t_E)}\right) \sim \mathcal{N}\left(0, \sigma_{P,i,n}^2\right)$.

We assume that the CSI estimation error is equal a percentage of the amplitude and phase of the exact coefficient, χ_{CSI} , *i.e.*: i) $|e_{i,n}^{(t_E)}| = \chi_{CSI} |h_{i,n}^{(t_E)}|$; and ii) $\arg\left(e_{i,n}^{(t_E)}\right) = \chi_{CSI} \arg\left(h_{i,n}^{(t_E)}\right)$. It is also possible to implement two different error percentages for the amplitude and phase of the coefficient, *i.e.*, $\chi_{CSI,a}$ and $\chi_{CSI,p}$.

Other models or solutions might be considered during the execution of the project and presented in the next iteration of this deliverable.

5 FLEXIBLE AND UNIFIED AIR INTERFACE

5.1 WAVEFORM DESIGN

Below, we provide a description of the current 5G/5G-Advanced waveform, CP-OFDM, and the most relevant candidate for future 6G communications, Orthogonal Time Frequency Space (OTFS) modulation.

5.1.1 OFDM-based

The baseline waveform CP-OFDM of the NR standard is considered, with reference to the PDSCH. Due to an extended numerology, this modulation format ensures large flexibility and adaptability. The frame structure is designed to provide flexibility in the choice of subcarrier spacing, FFT size, subframe duration, and CP length.

The subframe duration for a reference numerology with subcarrier spacing ($15 \cdot 2^n$) kHz is ($1/2^n$) ms, with $n = 0, 1, \dots, 5$, i.e., from 15 kHz to up to 480 kHz subcarrier spacings. The PRB is defined as 12 subcarriers. With respect to the modulation schemes, QPSK, 16QAM, 64QAM, and 256QAM are supported for both the downlink. Flexible LDPC codes are implemented as channel coding schemes for the user plane.

In [5], the NR features that requires some adaptations to support operation via satellite are discussed. In the following, we report the ones that refer to the data channels, and that involve the physical layer protocols.

- Regarding the propagation channel, the synchronization of the receiver at both UE and gNB level can be improved by modifying the reference signals in the physical signals to take into account the Doppler and possibly some specific multipath channel model. This was partially mentioned also in the previous Sections.
- The CP can be adapted to compensate for the delay spread and the jitter. The sub-carrier spacing may be extended with greater values to accommodate larger Doppler.
- Considering the frequency plan, the carrier numbering could be reviewed to support the targeted spectrum (S band, Ka band) and the pairing between UL/DL bands with specific band separation. The carrier bandwidth could be extended up to a maximum of 800 MHz. Alternatively, carrier aggregation method can be used to provide equivalent throughput while enabling a greater flexibility of carrier allocation between the cells while respecting frequency reuse constraints.
- With regards to the power limited link budget, the operation point of the power amplifier at satellite or at the UE shall be set as close as possible to saturation. This can be achieved by using extended multicarrier modulation and coding schemes especially characterized by low PAPR, by adopting PAPR reduction and nonlinear distortion mitigation techniques or by operating the high power amplifier with the minimum output back-off. It is also recommended to provide modulation and coding schemes able to work at very low signal-to-noise ratio.
- The propagation delays are significantly longer than in terrestrial networks, therefore the HARQ scheme would create unacceptable jitter. Adaptation can be required for the UL slot aggregation.

- The selection of the Modulation and Coding scheme as part of the AMC procedure based on the CQI can be more challenging since the propagation delay creates a larger response time and hence requires a margin to compensate for the possible outdated CQI. The AMC procedure could be modified with potential signalling extension.

5.1.2 OTFS

OTFS modulation is very effective for linear and time variant channels. In addition, this modulation format is very promising for applications of joint communication and sensing, where the same signal used to communicate with a receiver is also used to estimate parameters of interest related to this receiver, such as speed and distance. OTFS modulation is based on the idea to transmit the symbols in the Doppler-delay domain.

Data symbols $\{x[k, l]\}$, for $k = 0, \dots, N - 1$ and $l = 0, \dots, M - 1$, belonging to a finite alphabet (e.g., some QAM or PSK constellation), are arranged into an $N \times M$ two-dimensional grid in the Doppler-delay domain. These symbols are assumed to be spaced by $1/NT$ in the Doppler domain and $1/M\Delta f$ in the delay domain. The grid is thus $\Gamma = \{(k/NT, l/M\Delta f)\}$ for $k = 0, \dots, N - 1$ and $l = 0, \dots, M - 1$. The values of T and Δf are usually selected in such a way $\max_p\{\tau_p\} < T$ and $\max_p\{v_p\} < \Delta f$, where $\{\tau_p\}$ and $\{v_p\}$ are the delay and the Doppler of the channel. The symbols are then converted from the Doppler-delay domain to the time-frequency domain. As illustrated by Figure 6, which shows equivalent descriptions of an LTV channel, this conversion requires a Fourier transform with respect to the delay and an inverse transform with respect to the Doppler. The discrete transforms will be clearly employed. In the literature, this two-dimensional transform is called inverse symplectic finite Fourier transform (ISFFT). As said, it is nothing else than an inverse discrete Fourier transform with respect to the Doppler and a discrete Fourier transform with respect to the delay and converts the block of symbols $\{x[k, l]\}$ of dimension $N \times M$ into a block of symbols $\{X[n, m]\}$, of the same dimension, defined as:

$$X[n, m] = \sum_{k=0}^{N-1} \sum_{l=0}^{M-1} x[k, l] e^{j2\pi(\frac{nk}{N} - \frac{ml}{M})} \quad (102)$$

for $n = 0, \dots, N - 1$ and $m = 0, \dots, M - 1$. Then, the continuous-time transmitted signal $s(t)$ is generated as:

$$ss(t) = \sum_{n=0}^{N-1} \sum_{m=0}^{M-1} X[n, m] p_{tx}(t - nT) e^{j2\pi m\Delta f(t - nT)} \quad (103)$$

i.e., symbol $X[n, m]$ is transmitted at time n and over subcarrier m , and $p_{tx}(t)$ is a generic transmit shaping pulse. The transform that generates the modulated signal $s(t)$ from symbols $\{X[n, m]\}$ is usually called Heisenberg transform in the OTFS literature.

By properly selecting the shaping pulse and the values of T and Δf , (99) can represent any of the multicarrier modulation formats available in the literature. As an example, when $\Delta f = 1/T$ and $p_{tx}(t)$ is a rectangular pulse of duration T , (99) is a classical OFDM modulation with properly precoded information symbols. In this case, the cyclic prefix is not required. In fact, as we will see, despite in the name of OTFS there is still the term “orthogonal”, under realistic channel conditions there is no chance to have orthogonality, even when a cyclic prefix is adopted. For this reason, a guard interval of some symbols in the time domain is usually inserted to avoid interblock interference only.

The received signal is

$$r(t) = \sum_{p=0}^{P-1} a_p s(t - \tau_p) e^{j2\pi\nu_p t} + w(t) \quad (104)$$

having also taken into account the presence of additive white Gaussian noise (AWGN) $w(t)$. At the receiver side, without loss of generality, we will assume to use a bank of filters matched to the pulses $\{p_{rx}(t)e^{j2\pi m\Delta f t}\}_{m=0}^{M-1}$. The signals at the output of this bank of matched filters are sampled at the discrete times $t = nT$, $n = 0, \dots, N - 1$, obtaining the samples $\{Y[n, m]\}$. In the OTFS literature, the filtering of the received signal with the bank of matched filters plus sampling is usually called Wigner transform. The symplectic finite Fourier transform (SFFT) is then used to come back to the samples in the Doppler-delay domain $\{y[k, l]\}$, for $k = 0, \dots, N - 1$ and $l = 0, \dots, M - 1$:

$$y[k, l] = \frac{1}{NM} \sum_{n=0}^{N-1} \sum_{m=0}^{M-1} Y[n, m] e^{j2\pi(-\frac{nk}{N} + \frac{ml}{M})} \quad (105)$$

The block diagram of an OTFS system is shown in Figure 75. As said, the inner dashed block can be a classical multicarrier system. Information symbols are simply formatted in $N \times M$ two-dimensional frames that are precoded through the ISFFT at the transmitter and properly post-processed at the receiver through the SFFT. The interpretation of the OTFS modulation as a classical OFDM modulation with properly precoded information symbols and post-processing at the receiver as a main advantage. In fact, in this case a classical OFDM transceiver can be reused. Since OFDM is widely used in wireless standards, the transition to OTFS is very easy.

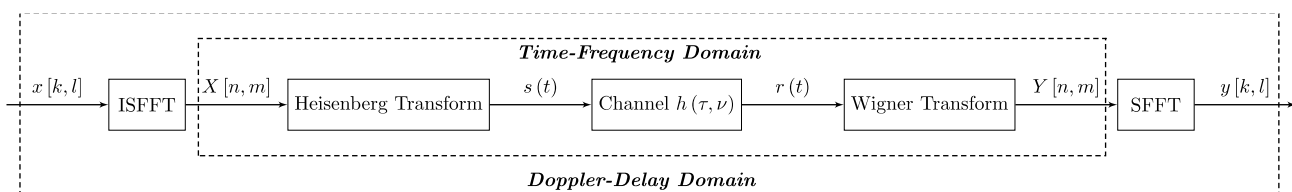


Figure 75: Block diagram of an OTFS system.

Let us now discuss the effect of the channel on the transmitted symbols. We will assume that $p_{rx}(t) = p_{tx}(t)$, $\Delta f = 1/T$, and that $p_{tx}(t)$ is a rectangular pulse of duration T . Under these assumptions, the noise samples affecting the useful signal in both samples $\{Y[n, m]\}$ and $\{y[k, l]\}$ are white. In other words, the SFFT does not color the noise. In the following, these noise samples will be omitted for the sake of notational simplicity. Under the assumption of absence of interblock interference, sample $Y[n, m]$ can be expressed as

$$Y[n, m] = \sum_{n'=0}^{N-1} \sum_{m'=0}^{M-1} X[n', m'] H[n, m, n', m'] \quad (106)$$

where $H[n, m, n', m']$ is the time-frequency domain channel. Since $X[n, m]$ is generated via ISFFT, the received signal in the Doppler-delay domain is obtained by the application of the SFFT

$$y[k, l] = \frac{1}{NM} \sum_{n=0}^{N-1} \sum_{m=0}^{M-1} Y[n, m] e^{j2\pi(-\frac{nk}{N} + \frac{ml}{M})} = \sum_{k', l'} x[k', l'] h[k, l, k', l'] \quad (107)$$

where $h[k, l, k', l']$ is the ISI coefficient of the Doppler-delay pair $[k', l']$ seen by the sample $[k, l]$. The input-output equation above highlights that we have a linear system with

two-dimensional ISI. It can be organized in matrix form. Writing the $N \times M$ matrices of transmitted symbols and received samples as NM -dimensional column vectors (stacking the columns of the corresponding matrices on top of each other), we obtain the block-wise input output relation in the form:

$$\mathbf{y} = \mathbf{\Psi}\mathbf{x} + \mathbf{w} \tag{108}$$

where $\mathbf{\Psi}$ is the $NM \times NM$ channel matrix.

The effect of the channel on the transmitted symbols is described in the following. Let us first assume that $P = 1$. In this case, $\gamma(v, \tau) = a_1 \delta(v - v_1) \delta(\tau - \tau_1)$ and every symbol is shifted by the same quantity proportional to the Doppler-delay pair (v_1, τ_1) associated to the scatterer. When v_1 and τ_1 are multiple of the grid spacings in the Doppler-delay domain ($1/NT$ in the Doppler domain and $1/M\Delta f$ in the delay domain), there is a simple shift. Otherwise, there is also a leakage of energy in the adjacent positions, as illustrated by Figure 76. When $P > 1$, we have P different shifts. It is thus clear that we can have orthogonality only when $P = 1$. In this case, a symbol-by-symbol detector can be employed. In a more realistic case orthogonality is hardly obtained and more sophisticated detectors must be employed, also taking interference into account.

For the performance evaluation of the scenario at hand, the OTFS parameters will be selected in order to be compliant with the NR numerology.

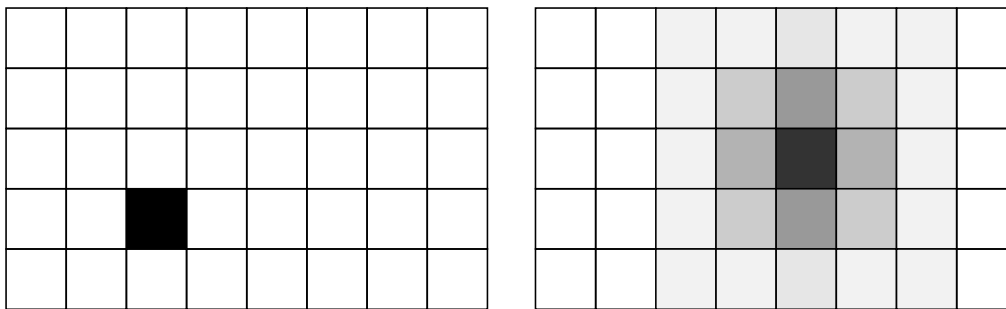


Figure 76: Effect of the channel with $\gamma(v, \tau) = a_1 \delta(v - v_1) \delta(\tau - \tau_1)$ on the generic transmitted symbol. The original position of the symbol is shown on the left. The position of the same symbol after the channel is shown on the right. The shift has to be understood as a circular shift.

5.1.3 Performance assessment

Based on the results of Section 4.3, link-level performance results were carried out following a first simplified approach. System-level simulations provided SNR, INR and SINR values given a set of scenarios in different conditions, but, in any case, concerning snapshots of the satellite passage over a predefined region, where in each snapshot 24 users are served (snapshot and time slots are used interchangeably in this document although it can be slightly misleading as time slots are also the smallest time grouping of OFDM symbols in NR glossary).

The first link-level simulation scenario was then based on these results, taking into account the SINR values, therefore by considering the interference due to the users served at the same time as AWGN, which is, however, a good approximation especially for OFDM signalling. Then, the actual Doppler effects induced by the satellite-user links were also accounted for, in order to measure the impact of such impairment on the detection algorithms. The signal parameters were obviously the same employed in the system-level simulations and are summarised in Table 26, were only the relevant parameters were reported.

Table 26: Parameters for link-level simulations

Parameter	Value	Comments
Sub-Carrier Spacing (SCS)	120 kHz	In this case, 132 PRBs are available
Operating Frequency Range	FR2 (Ka-band)	See 3GPP TR 38.821
Carrier frequency	20 GHz	See 3GPP TR 38.821
Resource blocks	132	
DMRS/PRTS	1096/198	Out of 1584x14 data symbols per slot
User bandwidth B	190.08 MHz	$132 \cdot 120 \cdot 12$ kHz
User density	$5 \cdot 10^{-3}$ UE/km ²	
Channel type	clear-sky	See Section 2.4.1.4 and 3GPP TR 38.811
Transmission snapshot (time slot) T_{slot}	1 s	See Section 4.2.1

5.1.4 Doppler effects

Given the selection of users to be served, each of them experiences a different value of Doppler shift due to its position with respect to satellite position and orbit. Figure 77 shows the distribution of the Doppler shifts across the whole satellite passage for all served users, and, as it can be noticed, the probability density is almost uniform between ± 375 kHz, provided the carrier frequency of 20 GHz.

The remarkable frequency offset due to the Doppler shift is usually estimated during the initial access by a proper algorithm included in the SSB synchronization procedure, nevertheless a residual offset should be considered also during the downlink data transmission.

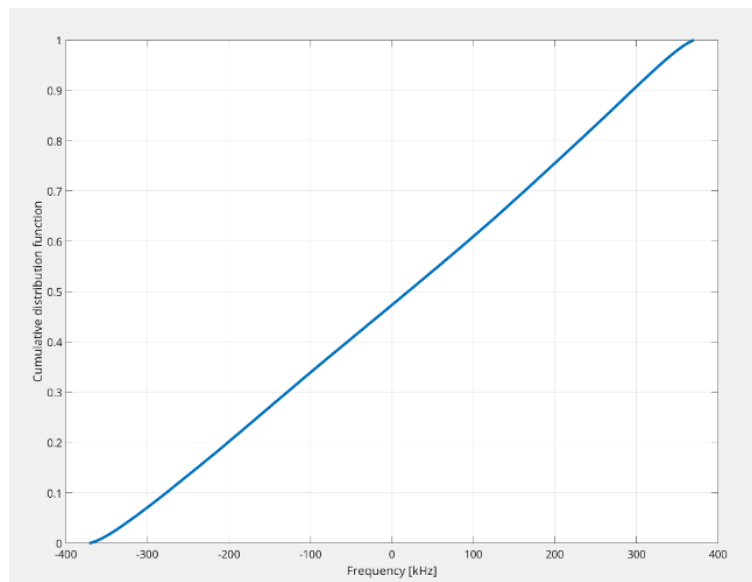


Figure 77: CDF of experienced Doppler shifts.

We chose to set a 1% residual offset due to inaccurate estimation or variation in the transition between synchronization and data transmission.

5.1.5 Waveform and simulation parameters

Once the amount of residual frequency offset was set, a proper configuration of DM-RS and phase tracking reference signal (PTRS) was determined. Some specific short simulations were

carried to find the best trade-off between overhead and performance, and the resulting OFDM slot time-frequency grid is represented in Figure 78.

It should be noticed that the pilot symbols configuration is slot-based, and each slot includes 14 OFDM symbols. Then, the global overhead, given the $1584 \times 14 = 22176$ data resource elements and the sum of 1096 DMRS and 198 PTRS resource elements, is 6.2%.

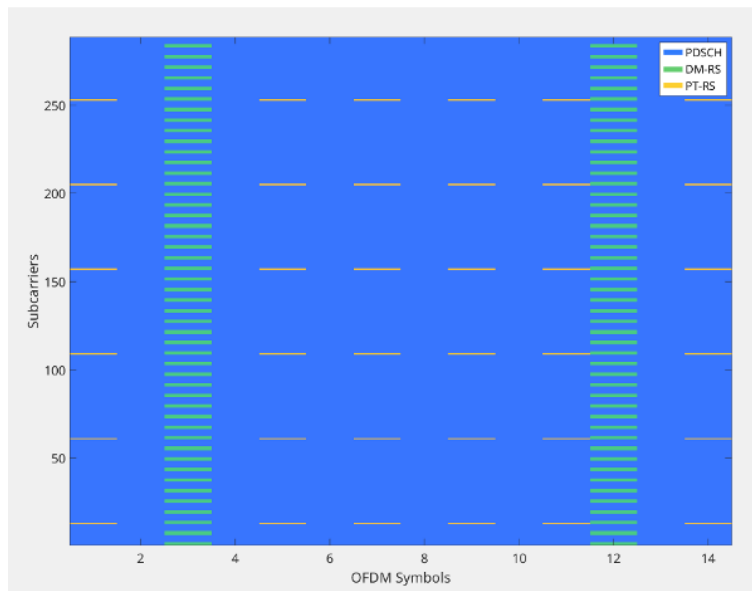


Figure 78: OFDM time-frequency grid.

As concerns other relevant waveform parameters, the FFT size for the chosen number of resource blocks is 2048 points, and the corresponding sample rate is 245.750 MHz. Given the SCS of 120 kHz, the slots per frame are 80, and one frame was simulated per user per snapshot.

5.1.6 Pragmatic capacity

5G New Radio exploits CSI feedback to select the proper configuration of the PDSCH, in terms of coding, modulation, MIMO precoding, etc. The feedback is provided by measurements performed by the user on the signal received by the gNB, mainly by exploiting the CSI-RS. In the present simulation approach, we avoided the implementation of such complex feedback mechanism, which is left for the forthcoming advancement, and thus we chose to adopt as a performance indicator the pragmatic capacity, namely the (symbol-by-symbol) mutual information of the virtual channel with input constellation symbols (with uniform probability) and output provided by the soft-output of the receiver detector, therefore separating the performance of the detector by the decoding. In this way it is possible to evaluate the performance of a few actual modulations (*i.e.*, QPSK, 16QAM, 64QAM) without resorting to any specific code rate. This approach is also particularly suitable for standard NR detectors, as they usually do not employ turbo detection/decoding.

By transmitting a sequence of length K of symbols $\{x_k\}$ from a given constellation \mathcal{C} , and receiving the corresponding noisy and impaired sequence of symbols $\{\hat{x}_k\}$, the pragmatic capacity can be computed by Monte Carlo simulations as

$$I_{PC} = \log_2 |\mathcal{C}| - \frac{1}{N} \sum_{k \in K} P(x_k, \hat{x}_k) \log_2 \frac{1}{P(x_k | \hat{x}_k)} \quad (109)$$

where the set K already accounts for the pilot symbols, therefore directly including the overhead in the computation. The soft-outputs are nothing but the processed received samples after the MMSE detector, hence they read

$$\hat{x}_k = \frac{H_{k,k}^*}{|H_{k,k}|^2 + \sigma^2} y_k \quad (110)$$

where $H_{k,k}$ refers to the discrete time-frequency matrix channel impulse response entry corresponding to k^{th} input and k^{th} output, σ^2 is the noise variance and y_k represent the received samples at the user side.

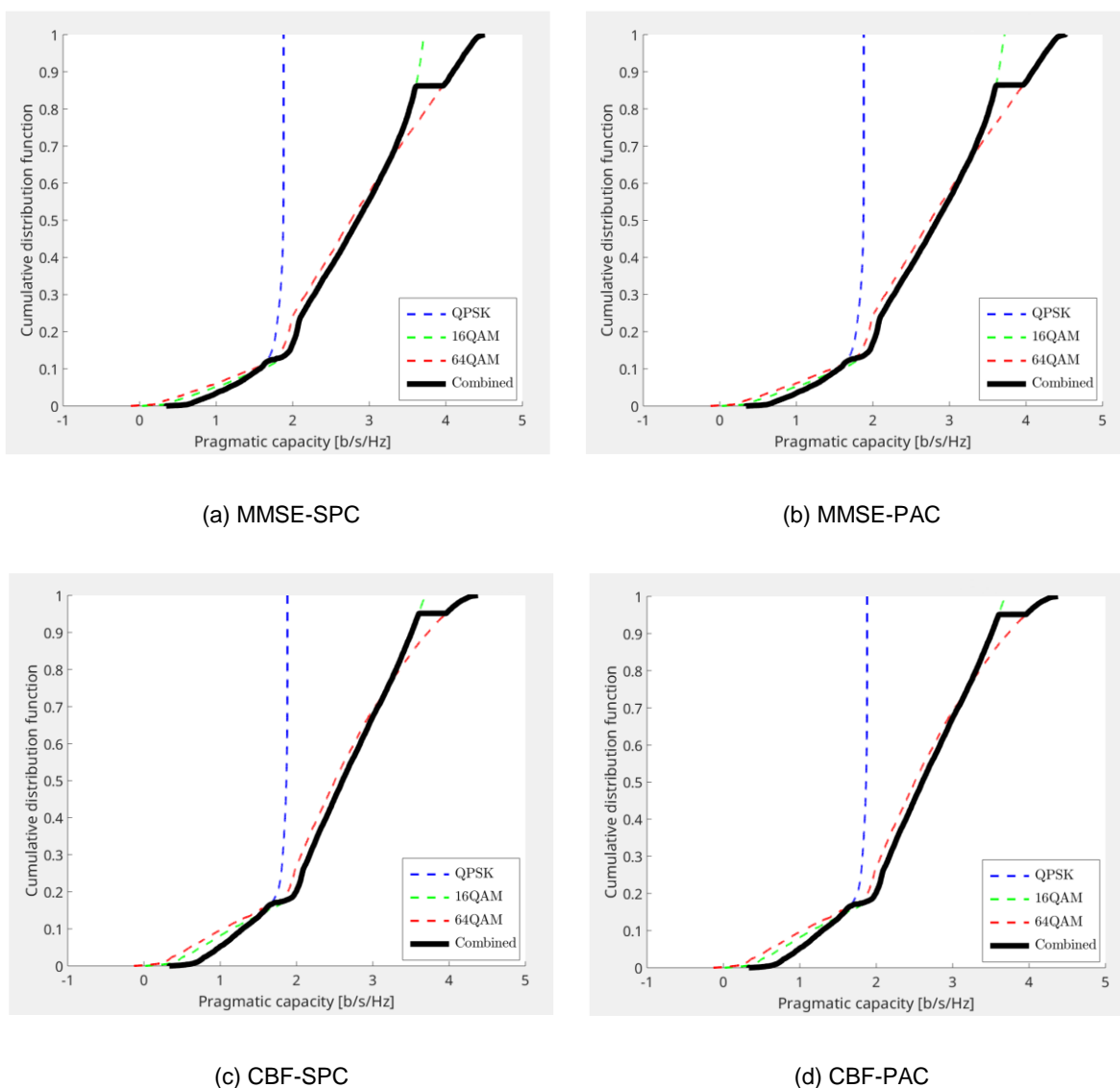


Figure 79: CDF of the pragmatic capacity with user-centric beamforming.

Figure 79 shows the pragmatic capacity CDF for the case of MMSE and CBF algorithms with SPC and PAC normalisations. Three curves are represented, corresponding to QPSK, 16QAM and 64QAM, all computed from the SINR derived with the system-level simulator described in Section 4. The overall distribution, named “Combined” in figure, was just obtained as the

maximum value among the mentioned three, but arbitrarily keeping the lowest one when the difference between them is below 10%, since it is reasonable to keep the complexity as low as possible if the gain is small. This approach, in any case, has a negligible impact on the overall performance (below 1%).

Final results on the mean values of the pragmatic capacity and throughput are reported in Table 27. Compared to the results reported in the previous section, here there is no distinction among the different values of the minimum distance. Then, an average throughput value per user is computed as if the same users were served across the whole satellite passage. More sophisticated computations accounting for the actual users visibility time will be possible in the next simulations.

Table 27: Results of link-level simulations

BF ALGORITHM	KPI	Value
MMSE-PAC	Mean overall pragmatic capacity	2.700 b/s/Hz
	Mean throughput per user	513.220 MHz
MMSE-SPC	Mean overall pragmatic capacity	2.705 b/s/Hz
	Mean throughput per user	514.170 MHz
CBF-PAC	Mean overall pragmatic capacity	2.502 b/s/Hz
	Mean throughput per user	475.580 MHz
CBF-SPC	Mean overall pragmatic capacity	2.531 b/s/Hz
	Mean throughput per user	481.092 MHz

5.2 NEXT DEVELOPMENTS

Given the provided assessment of link-level performance in a simplified scenario, the next steps will be to implement a simulator able to actually transmit and receive NR signals from the satellite to each served users, in order to measure the impact of the real inter-channel interference, without resorting to the Gaussian approximation. Moreover, by including the CQI report as feedback from the users to the satellite, it will be possible to select the proper modulation and coding according to the channel state information, in this way enabling the actual detection and decoding of the transmitted bit sequences, and therefore the computation of bit and packet error rates (BER/PER).

Then, the same results will be derived for the OTFS modulation with comparable sets of parameters, first, again, in terms of pragmatic capacity, and then in terms of BER/PER.

6 CONCLUSIONS

In this deliverable, we investigated many aspects related to the 3GPP NR-NTN standard, also including the waveform, and user-centric beamforming technologies as outcomes of Tasks 4.1 “Flexible and unified Air Interface” and Task 4.2 “User-Centric and Digital Beamforming Solutions,” respectively. In particular, the enhancements that are needed in the 3GPP NTN to support the architecture defined in WP3 have been addressed together with the design of user-centric beamforming and RRM algorithms.

After the definition of the common framework (antenna and channel models, payload, orbits, etc.), the elements of the air interface that might require adaptations have been identified, focusing on the Initial Access procedure, i.e., moving the UE from RRC_IDLE to RRC_CONNECTED state. In this context, the following topics have been addressed: i) compensation schemes; ii) mapping between cells and beams; iii) SSB multiplexing and detection; iv) SI scheduling; v) polarisation management; and vi) PRACH detection.

Two Doppler compensation schemes have been described. The first is referred to as UE compensation, which is the basic configuration described in 3GPP. An additional mechanism is to pre- and post-compensate at the satellite the Doppler on the DL and UL with respect to the beam centre; then, the user is only affected by the differential Doppler between the true coordinates and the centre of the beam reducing by an order of magnitude the frequency misalignment. The impact of these compensation mechanisms has been evaluated in DL and UL synchronization stages. The assessment revealed that for DL synchronization, the application of satellite compensation reduces the frequency uncertainty. As for the UL, the mobility of the terminal is the most detrimental effect. To support the airway scenario in which the terminal is mounted on a plane, the UE shall exploit the knowledge of the plane velocity to reduce the frequency offset. Alternatively, the RAR shall provide CFO corrections to reduce the frequency misalignment. The last observation is that the robustness of the preamble format needs to be enhanced to support GNSS-free operation during the network attachment.

With respect to the beam lattice, the preferred option in the project is to have a fixed grid on Earth. This is interesting from a system point of view, as a stationary user that is inside the FoV of the satellite will be served by the same beam in the visibility period. Based on the beam shapes and the grids, different options have been compared. The first one, is the scheme proposed by 3GPP, which consists of defining a hexagonal grid on the u-v plane. The main issue is that this solution does not produce a uniform grid on Earth. One possibility is to deploy a homogenous grid according to the footprint radius at Nadir. The consequence is that the FoV is divided into a large number of beams and, thus, large overlapping will be experienced at the edge due to the beam deformation. The alternative is to synthesize uniform beam shapes. This is achieved by taking as a reference the largest beam at the edge and widening the rest. Remarkably, in this case the number of beams in the FoV is substantially reduced. The most interesting conclusion is that a large number of beams preserves the EIRP but requires more resources in terms of time slots and hops, to sweep the coverage area. By deploying uniform beams, the resources needed to sweep the area are decreased. However, this comes at the cost of reducing the EIRP due to the widening. Essentially, the system is not using all the available power in all the amplifiers. An appealing solution is to bridge the gap between these two extreme cases, which would require to analyse in more detail the widening algorithm in the final version of this document, D4.6.

For what concerns the cell mapping, three options have been discussed: i) number of cells higher than the number of beams, which entails discontinuous transmission and is not supported by the standard; ii) deploying as many cells as active beams, with handover as its main drawback; and iii) deploy a single cell, with the challenge of the implementation of a single scheduler for the whole coverage area. The initial assessment reveals that having a single cell

offers more degrees of freedom to schedule the users. However, there are other implementation aspects that must be further analysed. The detailed comparison will be performed in D4.6.

With respect to user-centric beamforming, an extensive overview and discussion on the possible architectures to implement Multiple Input Multiple Output (MIMO) solutions is provided. The first step in this analysis is related to the identification of the protocol stack layers in which the requested operations are performed: i) scheduling and computation of the beamforming coefficients in the high Medium Access Control (MAC) layer; and ii) application of the beamforming coefficients in the low Physical layer (PHY). Based on these considerations, the various functional split options provided by 3GPP are mapped onto three different beamforming management architectures: DBFM, CBFM-OG, and CBFM-OB. For all the architecture options introduced above, the various Network Elements (NE) are described in terms of the required operations and the high-level functional procedures are provided. These procedures provide a description of the process and flow of information to support user-centric beamforming techniques that are either based on Channel State Information (CSI) or on the location estimates provided by the UEs. This analysis pointed out two potential modifications required in the 3GPP specifications:

- CSI-based beamforming: support the estimation of channel coefficients at radiating element level. A proposed solution to this aim consists in exploiting the available CSI-RS operating at beam level to estimate the channel between the NTN node and the UE; then, the known antenna array configuration and radiation pattern can be exploited to complement this information.
- Location-based: make the location information available at RAN level and not only in the AMF/LMF. Notably, this modification shall also take into account privacy aspects.

The initial performance assessment, with random scheduling, allowed to identify the major performance trends and trade-offs. The numerical assessment revealed that, over a very large service area (basically covering Europe) and with only 24 user-centric beams per time slot, the asymptotic capacity is in line with the expectations (600-800 Mbps), while the experienced capacity (*i.e.*, including the percentage of channel use per user) is particularly low. This is due to the very limited amount of time allocated to the transmission of each user (a few seconds in the best case). This analysis points out the direction for the next analyses to be performed in Task 4.2, *i.e.*, consider non-uniform users and traffic distributions. For these, various models and options are introduced in the document and will be discussed in the next steps. Scenarios with hot-spot areas where users are concentrated will allow to truly assess the benefit of user-centric beamforming as: i) the users in the hot-spot areas will be served for larger periods of time, increasing the experienced capacity; and ii) increasing the co-channel interference will boost the performance benefit of algorithms based on MMSE beamforming or its variants. In these scenarios, the importance of RRM algorithms will be central. Thus, non-random RRM solutions will be designed, starting from two solutions (Heuristic RRM, H-RRM, and Graph-based RRM, G-RRM) proposed in this document.

Finally, a link-level performance assessment was performed assuming Gaussian interference and taking as input the SINR produced by the system-level simulator as an initial evaluation. The performance is in line with the system-level, also showing a performance loss due to the transmission of modulated signals and the introduction of Doppler shift and signalling overhead. The next steps for link-level evaluations will include the implementation of a software simulator that actually transmits and receives NR signals without resorting to the simplified assumptions based on Gaussian interference. In addition, also the inclusion of CQI reports will allow to implement ACM schemes. Finally, the OTFS waveform will be considered.

7 REFERENCES

- [1]. 5G-STAR DUST, D3.1, "System Requirements Analysis and Specifications," July 2023.
- [2]. 5G-STAR DUST, D3.2, "End-to-end ground and space integrated architecture," February 2024.
- [3]. ETSI TR 103 886, Draft document, SESSCN(22)000025, October 2022. Available: <https://portal.etsi.org/Contribution.aspx?MeetingId=44694>.
- [4]. 3GPP TR 38.821, "Solutions for NR to support non-terrestrial networks (NTN) (Release 16)," April 2023.
- [5]. 3GPP TR 38.811, "Study on New Radio (NR) to support non-terrestrial networks (Release 15)," Oct. 2020.
- [6]. ITU-R P.676-13, "Attenuation by atmospheric gases and related effects," 2022.
- [7]. ITU-R P.835-6, "Reference standard atmospheres," 2017.
- [8]. 3GPP TR 38.901, "Study on channel model for frequencies from 0.5 to 100 GHz (Release 17)," Jan. 2024.
- [9]. L. You, K. -X. Li, X. G. J. Wang, X. -G. Xia and B. Ottersten, "Massive MIMO Transmission for LEO Satellite Communications," IEEE Journal on Selected Areas in Communications, vol. 38, no. 8, pp. 1851-1865, Aug. 2020.
- [10]. I. Ali, N. Al-Dhahir and J. E. Hershey, "Doppler characterization for LEO satellites," IEEE Transactions on Communications, vol. 46, no. 3, pp. 309-313, Marvh 1998.
- [11]. 3GPP TS 38.331, "NR; Radio Resource Control (RRC) protocol specification (Release 17)," September 2023.
- [12]. 3GPP TR 38.804, "Study on New Radio Access Technology; Radio Interface Protocol Aspects (Release 14)," March 2017.
- [13]. 3GPP TS 38.300, "NR; NR and NG-RAN Overall Description; Stage 2 (Release 16)," September 2020.
- [14]. 3GPP TS 38.212, "NR; Multiplexing and channel coding (Release 18)," September 2023.
- [15]. 3GPP TS 38.213, "NR; Physical layer procedures for control (Release 18)," September 2023.
- [16]. 3GPP TS 38.304, "NR; User Equipment (UE) procedures in Idle mode and RRC Inactive state (Release 17)," September 2023.
- [17]. A. Vanelli-Coralli, N. Chuberre, G. Masini, A. Guidotti and M. E. Jaafari, "5G Non-Terrestrial Networks: Technologies, Standards, and System Design," to be published by Wiley-IEEE Press, January 2024.
- [18]. 3GPP TS 38.214, "NR; Physical layer procedures for data (Release 18)," September 2023.
- [19]. 3GPP TSG-RAN WG2 Meeting #108, R2-1916351, Thales, "[108#06][NTN] Earth fixed vs. Earth moving cells in NTN LEO (Thales)," November 2019.
- [20]. G. C. Brown, J. C. Kerce and M. A. Mitchell, "Extreme Beam Broadening using Phase Only Pattern Synthesis," Fourth IEEE Workshop on Sensor Array and Multichannel Processing, 2006., Waltham, MA, USA, 2006, pp. 36-39, doi: 10.1109/SAM.2006.1706079.

- [21]. S. O. Petersson and M. A. Girnyk, "Energy-Efficient Design of Broad Beams for Massive MIMO Systems," in *IEEE Transactions on Vehicular Technology*, vol. 71, no. 11, pp. 11772-11785, Nov. 2022, doi: 10.1109/TVT.2022.3192245.
- [22]. 3GPP TS 38.211, "NR; Physical channels and modulation (Release 18)," December 2023.
- [23]. P. Nayeri, F. Yang and A. Z. Elsherbeni, "Single-feed multi-beam reflectarray antennas," 2010 IEEE Antennas and Propagation Society International Symposium, Toronto, ON, Canada, 2010, pp. 1-4, doi: 10.1109/APS.2010.5562104.
- [24]. V. R. Chandrika, J. Chen, L. Lampe, G. Vos and S. Dost, "SPIN: Synchronization Signal-Based Positioning Algorithm for IoT Nonterrestrial Networks," in *IEEE Internet of Things Journal*, vol. 10, no. 23, pp. 20846-20867, 1 Dec.1, 2023, doi: 10.1109/JIOT.2023.3283989
- [25]. J. Zhu, Y. Sun and M. Peng, "Timing Advance Estimation in Low Earth Orbit Satellite Networks," in *IEEE Transactions on Vehicular Technology*, vol. 73, no. 3, pp. 4366-4382, March 2024, doi: 10.1109/TVT.2023.3325328.
- [26]. J. J. van de Beek, M. Sandell and P. O. Borjesson, "ML estimation of time and frequency offset in OFDM systems," in *IEEE Transactions on Signal Processing*, vol. 45, no. 7, pp. 1800-1805, July 1997, doi: 10.1109/78.599949.
- [27]. Saarnisaari H, de Lima C., "Application of 5G new radio for satellite links with low peak-to-average power ratios," *Int J Satell Commun Network*. 2021; 39: 445–454. <https://doi.org/10.1002/sat.1378>
- [28]. W. Wang, Y. Tong, L. Li, A. -A. Lu, L. You and X. Gao, "Near Optimal Timing and Frequency Offset Estimation for 5G Integrated LEO Satellite Communication System," in *IEEE Access*, vol. 7, pp. 113298-113310, 2019, doi: 10.1109/ACCESS.2019.2935038.
- [29]. 3GPP TS 38.101-1, "NR; User Equipment (UE) radio transmission and reception; Part 1: Range 1 Standalone (Release 18)," Dec. 2023.
- [30]. 3GPP TR 38.854, "NR support for high speed train scenario in frequency range 2 (FR2) (Release 18)," Aug. 2023.
- [31]. L. Zhen, H. Qin, B. Song, R. Ding, X. Du and M. Guizani, "Random Access Preamble Design and Detection for Mobile Satellite Communication Systems," in *IEEE Journal on Selected Areas in Communications*, vol. 36, no. 2, pp. 280-291, Feb. 2018, doi: 10.1109/JSAC.2018.2804138.
- [32]. M. Caus and A. I. Pérez-Neira, "FBMC-Based Random Access Signal Design and Detection for LEO Base Stations," in *IEEE Transactions on Wireless Communications*, vol. 22, no. 3, pp. 2156-2170, March 2023, doi: 10.1109/TWC.2022.3209898.
- [33]. V. Icolari, A. Guidotti, D. Tarchi and A. Vanelli-Coralli, "An interference estimation technique for Satellite cognitive radio systems," 2015 IEEE International Conference on Communications (ICC), London, UK, 2015, pp. 892-897, doi: 10.1109/ICC.2015.7248435.
- [34]. Chatzinotas, S., Evans, B., Guidotti, A., Icolari, V., Lagunas, E., Maleki, S., Sharma, S. K., Tarchi, D., Thompson, P., and Vanelli-Coralli, A. (2017) Cognitive approaches to enhance spectrum availability for satellite systems. *Int. J. Satell. Commun. Network.*, 35: 407–442. doi: 10.1002/sat.1197.
- [35]. H. Kokkinen, A. Piemontese, L. Kulacz, F. Arnal and C. Amatetti, "Coverage and interference in co-channel spectrum sharing between terrestrial and satellite networks," 2023 IEEE Aerospace Conference, Big Sky, MT, USA, 2023, pp. 1-9, doi: 10.1109/AERO55745.2023.10115567.
- [36]. G. Caire, M. Debbah, L. Cottatellucci, R. De Gaudenzi, R. Rinaldo, R. Mueller, G. Gallinaro, "Perspectives of adopting interference mitigation techniques in the context of broadband

- multimedia satellite systems," ICSSC 2005, 23rd AIAA International Communications Satellite Systems Conference, 2005.
- [37]. P.-D. Arapoglou, K. Liolis, M. Bertinelli, A. Panagopoulos, P. Cottis and R. De Gaudenzi, "MIMO over Satellite: A Review," in *IEEE Communications Surveys & Tutorials*, vol. 13, no. 1, pp. 27-51, First Quarter 2011, doi: 10.1109/SURV.2011.033110.00072.
- [38]. N. Zorba, M. Realp and A. I. Perez-Neira, "An improved partial CSIT random beamforming for multibeam satellite systems," 2008 10th International Workshop on Signal Processing for Space Communications, Rhodes, Greece, 2008, pp. 1-8, doi: 10.1109/SPSC.2008.4686703.
- [39]. Arapoglou, P.-D., Ginesi, A., Cioni, S., Erl, S., Clazzer, F., Andrenacci, S., and Vanelli-Coralli, A. (2016) DVB-S2X-enabled precoding for high throughput satellite systems. *Int. J. Satell. Commun. Network.*, 34: 439–455. doi: 10.1002/sat.1122.
- [40]. Dimitrios Christopoulos, Pantelis-Daniel Arapoglou and Symeon Chatzinotas. "Linear Precoding in Multibeam SatComs: Practical Constraints," AIAA 2013-5716. 31st AIAA International Communications Satellite Systems Conference. October 2013.
- [41]. G. Zheng, S. Chatzinotas and B. Ottersten, "Generic Optimization of Linear Precoding in Multibeam Satellite Systems," in *IEEE Transactions on Wireless Communications*, vol. 11, no. 6, pp. 2308-2320, June 2012, doi: 10.1109/TWC.2012.040412.111629.
- [42]. Dimitrios Christopoulos, Symeon Chatzinotas, Giorgio Taricco, Miguel Angel Vázquez, Ana Pérez-Neira, Pantelis-Daniel Arapoglou, Alberto Ginesi, "Chapter 3 - Multibeam joint precoding: frame-based design," Editor(s): Symeon Chatzinotas, Björn Ottersten, Riccardo De Gaudenzi, *Cooperative and Cognitive Satellite Systems*, Academic Press, 2015, Pages 83-118, ISBN 9780127999487, <https://doi.org/10.1016/B978-0-12-799948-7.00003-7>.
- [43]. S. Chatzinotas, G. Zheng and B. Ottersten, "Joint Precoding with Flexible Power Constraints in Multibeam Satellite Systems," 2011 IEEE Global Telecommunications Conference - GLOBECOM 2011, Houston, TX, USA, 2011, pp. 1-5, doi: 10.1109/GLOCOM.2011.6134087.
- [44]. V. Joroughi, M. R. B. Shankar, S. Maleki, S. Chatzinotas, J. Grotz and B. Ottersten, "On-Board Precoding in a Multiple Gateway Multibeam Satellite System," 2018 IEEE 88th Vehicular Technology Conference (VTC-Fall), Chicago, IL, USA, 2018, pp. 1-5, doi: 10.1109/VTCTFall.2018.8690982.
- [45]. A. Guidotti and A. Vanelli-Coralli, "Design Trade-Off Analysis of Precoding Multi-Beam Satellite Communication Systems," 2021 IEEE Aerospace Conference (50100), Big Sky, MT, USA, 2021, pp. 1-12, doi: 10.1109/AERO50100.2021.9438169.
- [46]. P. J. Honnaiah, E. Lagunas, N. Maturo and S. Chatzinotas, "Demand-Aware Beam Design and User Scheduling for Precoded Multibeam GEO Satellite Systems," WSA 2021; 25th International ITG Workshop on Smart Antennas, French Riviera, France, 2021, pp. 1-6.
- [47]. F. Ortiz, E. Lagunas and S. Chatzinotas, "Unsupervised Learning for User Scheduling in Multibeam Precoded GEO Satellite Systems," 2022 Joint European Conference on Networks and Communications & 6G Summit (EuCNC/6G Summit), Grenoble, France, 2022, pp. 190-195, doi: 10.1109/EuCNC/6GSummit54941.2022.9815569.
- [48]. A. Guidotti, C. Amatetti, F. Arnal, B. Chamailard and A. Vanelli-Coralli, "Location-assisted precoding in 5G LEO systems: architectures and performances," 2022 Joint European Conference on Networks and Communications & 6G Summit (EuCNC/6G Summit), Grenoble, France, 2022, pp. 154-159, doi: 10.1109/EuCNC/6GSummit54941.2022.9815611.
- [49]. D. Tuzi, T. Delamotte and A. Knopp, "Beamforming performance of satellite swarm-based antenna arrays for 6G direct-to-cell connectivity," WSA & SCC 2023; 26th International ITG Workshop on

- Smart Antennas and 13th Conference on Systems, Communications, and Coding, Braunschweig, Germany, 2023, pp. 1-6.
- [50]. D. Tuzi, T. Delamotte and A. Knopp, "Satellite Swarm-Based Antenna Arrays for 6G Direct-to-Cell Connectivity," in *IEEE Access*, vol. 11, pp. 36907-36928, 2023, doi: 10.1109/ACCESS.2023.3257102.
- [51]. M. Y. Abdelsadek, G. K. Kurt and H. Yanikomeroğlu, "Distributed Massive MIMO for LEO Satellite Networks," in *IEEE Open Journal of the Communications Society*, vol. 3, pp. 2162-2177, 2022, doi: 10.1109/OJCOMS.2022.3219419.
- [52]. Y. Omid, Z. M. Bakhsh, F. Kayhan, Y. Ma and R. Tafazolli, "Space MIMO: Direct Unmodified Handheld to Multi-Satellite Communication," *GLOBECOM 2023 - 2023 IEEE Global Communications Conference*, Kuala Lumpur, Malaysia, 2023, pp. 1447-1452, doi: 10.1109/GLOBECOM54140.2023.10437580.
- [53]. F. Riera-Palou, G. Femenias, M. Caus, M. Shaat and A. I. Pérez-Neira, "Scalable Cell-Free Massive MIMO Networks With LEO Satellite Support," in *IEEE Access*, vol. 10, pp. 37557-37571, 2022, doi: 10.1109/ACCESS.2022.3164097.
- [54]. A. Guidotti, A. Vanelli-Coralli and C. Amatetti, "Federated Cell-Free MIMO in Non-Terrestrial Networks: Architectures and Performance," in *IEEE Transactions on Aerospace and Electronic Systems*, doi: 10.1109/TAES.2024.3362769.
- [55]. A. Guidotti, C. Sacchi and A. Vanelli-Coralli, "Feeder Link Precoding for Future Broadcasting Services," in *IEEE Transactions on Aerospace and Electronic Systems*, vol. 58, no. 4, pp. 3126-3146, Aug. 2022, doi: 10.1109/TAES.2022.3144243.
- [56]. Dakkak MR, Riviello DG, Guidotti A, Vanelli-Coralli A. Evaluation of multi-user multiple-input multiple-output digital beamforming algorithms in B5G/6G low Earth orbit satellite systems. *Int J Satell Commun Network*. 2023; 1-17. doi:10.1002/sat.1493
- [57]. P. Angeletti and R. De Gaudenzi, "A Pragmatic Approach to Massive MIMO for Broadband Communication Satellites," in *IEEE Access*, vol. 8, pp. 132212-132236, 2020, doi: 10.1109/ACCESS.2020.3009850.
- [58]. M. Á. Vázquez, X. Artiga and A. I. Pérez-Neira, "Closed-Form Multicast Precoding for Satellite Flexible Payloads," *2021 29th European Signal Processing Conference (EUSIPCO)*, Dublin, Ireland, 2021, pp. 910-914, doi: 10.23919/EUSIPCO54536.2021.9616268.
- [59]. Z. Lin et al., "SLNR-Based Secure Energy Efficient Beamforming in Multibeam Satellite Systems," in *IEEE Transactions on Aerospace and Electronic Systems*, vol. 59, no. 2, pp. 2085-2088, April 2023, doi: 10.1109/TAES.2022.3190238
- [60]. V. Jorroughi, M. Á. Vázquez and A. I. Pérez-Neira, "Generalized Multicast Multibeam Precoding for Satellite Communications," in *IEEE Transactions on Wireless Communications*, vol. 16, no. 2, pp. 952-966, Feb. 2017, doi: 10.1109/TWC.2016.2635139.
- [61]. Y. C. B. Silva and A. Klein, "Linear Transmit Beamforming Techniques for the Multigroup Multicast Scenario," in *IEEE Transactions on Vehicular Technology*, vol. 58, no. 8, pp. 4353-4367, Oct. 2009, doi: 10.1109/TVT.2009.2021603.
- [62]. G. Interdonato, H. Q. Ngo and E. G. Larsson, "Enhanced Normalized Conjugate Beamforming for Cell-Free Massive MIMO," in *IEEE Transactions on Communications*, vol. 69, no. 5, pp. 2863-2877, May 2021, doi: 10.1109/TCOMM.2021.3055522.
- [63]. M. A. Albreem, A. H. A. Habbash, A. M. Abu-Hudrouss and S. S. Ikki, "Overview of Precoding Techniques for Massive MIMO," in *IEEE Access*, vol. 9, pp. 60764-60801, 2021, doi: 10.1109/ACCESS.2021.3073325.

- [64]. M Rabih Dakkak, Daniel Gaetano Riviello, Alessandro Guidotti, Alessandro Vanelli-Coralli, "Assessment of Beamforming Algorithms with Subarrayed Planar Arrays for B5G/6G LEO Non-Terrestrial Networks," European Wireless 2023; 28th European Wireless Conference, 2023.
- [65]. Y. Aslan, J. Puskely, A. Roederer and A. Yarovoy, "Active Multiport Subarrays for 5G Communications," 2019 IEEE-APS Topical Conference on Antennas and Propagation in Wireless Communications (APWC), Granada, Spain, 2019, pp. 298-303, doi: 10.1109/APWC.2019.8870449.
- [66]. Palacios Joan, González-Prelcic Nuria, Mosquera Carlos, Shimizu Takayuki, Wang Chang-Heng, "A Hybrid Beamforming Design for Massive MIMO LEO Satellite Communications," *Frontiers in Space Technologies*, vol.2, 2021, doi: 10.3389/frspt.2021.696464.
- [67]. J. P. Choi and V. W. S. Chan, "Optimum power and beam allocation based on traffic demands and channel conditions over satellite downlinks," in *IEEE Transactions on Wireless Communications*, vol. 4, no. 6, pp. 2983-2993, Nov. 2005, doi: 10.1109/TWC.2005.858365.
- [68]. J. P. Choi and V. W. S. Chan, "Resource management for advanced transmission antenna satellites," in *IEEE Transactions on Wireless Communications*, vol. 8, no. 3, pp. 1308-1321, March 2009, doi: 10.1109/TWC.2009.071131.
- [69]. M. A. V. Castro and G. S. Granados, "Cross-layer packet scheduler design of a multibeam broadband satellite system with adaptive coding and modulation," *IEEE Trans. Wireless Commun.*, vol. 6, no. 1, pp. 248-258, Jan. 2007.
- [70]. J. Leiand, M. A. Vazquez-Castro, "Joint power and carrier allocation for the multibeam satellite downlink with individual SINR constraints," in *Proc. IEEE Int. Conf. Commun.*, Cape Town, South Africa, May 2010, pp. 1-5.
- [71]. J. Anzalchi, A. Couchman, P. Gabellini, G. Gallinaro, L. D'Agostina, N. Alagha, and P. Angeletti, "Beam hopping in multi-beam broadband satellite systems: System simulation and performance comparison with non-hopped systems," in *Proc. 5th Adv. Satell. Multimedia Syst. Conf. 11th Signal Process. Space Commun. Workshop*, Cagliari, Italy, Sep. 2010, pp. 248-654.
- [72]. J. Lizarraga, P. Angeletti, N. Alagha, and M. Aloisio, "Flexibility performance in advanced Ka-band multibeam satellites," in *Proc. IEEE Int. Vac. Electron. Conf.*, Monterey, QC, USA, Apr. 2014, pp. 45-46.
- [73]. X. Alberti, J. M. Cebrian, A. Del Bianco, Z. Katona, J. Lei, M. A. Vazquez-Castro, A. Zanus, L. Gilbert, and N. Alagha, "System capacity optimization in time and frequency for multibeam multimedia satellite systems," in *Proc. 5th Adv. Satell. Multimedia Syst. Conf.*, 11th Signal Process. Space Commun. Workshop, Cagliari, Italy, Sep. 2010, pp. 226-233.
- [74]. J. Lei and M. A. Vazquez-Castro, "Multibeam satellite frequency/time duality study and capacity optimization," *J. Commun. Netw.*, vol. 13, no. 5, pp. 472-480, Oct. 2011.
- [75]. U. Park, H. W. Kim, D. S. Oh, and B. J. Ku, "Flexible bandwidth allocation scheme based on traffic demands and channel conditions for multi-beam satellite systems," in *Proc. IEEE Veh. Technol. Conf. (VTC Fall)*, Sep. 2012, pp. 1-5.
- [76]. B. G. Evans, P. T. Thompson, and A. Kyrgiazos, "Irregular beam sizes and non-uniform bandwidth allocation in HTS," in *Proc. 31st AIAA Int. Commun. Satell. Syst. Conf.*, Oct. 2013, pp. 1-7.
- [77]. H. Wang, A. Liu, X. Pan, and J. Li, "Optimization of power allocation for a multibeam satellite communication system with interbeam interference," *J. Appl. Math.*, vol. 2014, Nov. 2014, Art. no. 469437, doi: 10.1155/2014/469437.

- [78]. S. Dimitrov, S. Erl, B. Barth, S. Jaeckel, A. Kyrgiazos, and B. G. Evans, "Radio resource management techniques for high throughput satellite communication systems," in Proc. Eur. Conf. Netw. Commun. (EuCNC), Paris, France, Jun. 2015, pp. 175–179.
- [79]. A. I. Aravanis, M. R. S. Bhavani, P. D. Arapoglou, G. Danoy, P. G. Cottis, and B. Ottersten, "Power allocation in multibeam satellite systems: A two-stage multi-objective optimization," IEEE Trans. Wireless Commun., vol. 14, no. 6, pp. 3171–3182, Jun. 2015.
- [80]. T. Qi and Y. Wang, "Energy-efficient power allocation over multibeam satellite downlinks with imperfect CSI," in Proc. IEEE WCSP, Nanjing, China, Oct. 2015, pp. 1–5.
- [81]. E. Castañeda, A. Silva, A. Gameiro, and M. Kountouris, "An overview on resource allocation techniques for multi-user MIMO systems," IEEE Commun. Surveys Tuts., vol. 19, no. 1, pp. 239–284, 1st Quart., 2017.
- [82]. A. Guidotti and A. Vanelli-Coralli, "Geographical scheduling for multi-cast precoding in multi-beam satellite systems," in Proc. 9th Adv. Satell. Multimedia Syst. Conf., 15th Signal Process. Space Commun. Workshop (ASMS/SPSC), Berlin, Germany, Sep. 2018, pp. 10–12.
- [83]. A. Ginesi, P. D. Arapoglu, and E. Re, "Interference-resilient flexible techniques for payload allocation resource allocation in broadband satellites," International Patent WO 2017 2 11 430 A1, Dec. 14, 2017.
- [84]. G. Cocco, T. de Cola, M. Angelone, Z. Katona, and S. Erl, "Radio resource management optimization of flexible satellite payloads for DVB-S2 systems," IEEE Trans. Broadcast., vol. 64, no. 2, pp. 266–280, Jun. 2018.
- [85]. R. Zhang, Y. Ruan, Y. Li, and C. Liu, "Interference-aware radio resource management for cognitive high-throughput satellite systems," Sensors, vol. 20, no. 1, p. 197, Dec. 2019, doi: 10.3390/s20010197.
- [86]. T. Ramirez and C. Mosquera, "Resource management in the multi-beam NOMA-based satellite downlink," in Proc. IEEE Int. Conf. Acoust., Speech Signal Process. (ICASSP), Barcelona, Spain, May 2020, pp. 1–6.
- [87]. S. Kisseleff, E. Lagunas, T. S. Abdu, S. Chatzinotas, and B. Ottersten, "Radio resource management techniques for multibeam satellite systems," IEEE Commun. Lett., vol. 25, no. 8, pp. 2448–2452, Aug. 2021.
- [88]. H. Chen and C. Qi, "User Grouping for Sum-Rate Maximization in Multiuser Multibeam Satellite Communications," ICC 2019 - 2019 IEEE International Conference on Communications (ICC), 2019, pp. 1-6, doi: 10.1109/ICC.2019.8761875.
- [89]. X. Yi and E. K. S. Au, "User Scheduling for Heterogeneous Multiuser MIMO Systems: A Subspace Viewpoint," in IEEE Transactions on Vehicular Technology, vol. 60, no. 8, pp. 4004-4013, Oct. 2011, doi: 10.1109/TVT.2011.2165976.
- [90]. K. Storek and A. Knopp, "Fair User Grouping for Multibeam Satellites with MU-MIMO Precoding", GLOBECOM 2017 - 2017 IEEE Global Communications Conference, 2017, pp. 1-7, doi: 10.1109/GLOCOM.2017.8255098.
- [91]. X. Yi and E. K. S. Au, "User Scheduling for Heterogeneous Multiuser MIMO Systems: A Subspace Viewpoint," in IEEE Transactions on Vehicular Technology, vol. 60, no. 8, pp. 4004-4013, Oct. 2011, doi: 10.1109/TVT.2011.2165976.
- [92]. D. G. Riviello, B. Ahmad, A. Guidotti and A. Vanelli-Coralli, "Joint Graph-based User Scheduling and Beamforming in LEO-MIMO Satellite Communication Systems," 2022 11th Advanced Satellite Multimedia Systems Conference and the 17th Signal Processing for Space Communications

- Workshop (ASMS/SPSC), Graz, Austria, 2022, pp. 1-8, doi: 10.1109/ASMS/SPSC55670.2022.9914723.
- [93]. B. Ahmad, D. G. Riviello, A. Guidotti and A. Vanelli-Coralli, "Graph-Based User Scheduling Algorithms for LEO-MIMO Non-Terrestrial Networks," 2023 Joint European Conference on Networks and Communications & 6G Summit (EuCNC/6G Summit), Gothenburg, Sweden, 2023, pp. 270-275, doi: 10.1109/EuCNC/6GSummit58263.2023.10188287.
- [94]. B. Ahmad, D. G. Riviello, A. Guidotti and A. Vanelli-Coralli, "Improved Graph-Based User Scheduling For Sum-Rate Maximization in LEO-NTN Systems," 2023 IEEE International Conference on Acoustics, Speech, and Signal Processing Workshops (ICASSPW), Rhodes Island, Greece, 2023, pp. 1-5, doi: 10.1109/ICASSPW59220.2023.10193499.
- [95]. Konc, Janez and Dušanka Janežič. "An improved branch and bound algorithm for the maximum clique problem", MATCH - Communications in Mathematical and in Computer Chemistry, vol. 58, no. 3, pp. 569-590, 2007.
- [96]. 3GPP TS 38.305, "NG Radio Access Network (NG-RAN); Stage 2 functional specification of User Equipment (UE) positioning in NG-RAN," 2024.
- [97]. "Study on new radio access technology: Radio frequency (RF) and co-existence aspects," in 3GPP TR 38.803 V14.3.0.
- [98]. Schiavina, Marcello; Freire, Sergio; MacManus, Kytt, "GHS-POP R2022A - GHS population grid multitemporal (1975-2030)," European Commission, Joint Research Centre (JRC), 2024.
- [99]. B. De Filippo, B. Ahmad, D. G. Riviello, A. Guidotti, A. Vanelli-Coralli, "Non-Uniform User Distribution in Non-Terrestrial Networks with Application to User Scheduling," submitted to IEEE MeditCom, April 2024.
- [100]. EC SPACE-29-TEC-2020 Project DYNASAT (Dynamic spectrum sharing and bandwidth-efficient techniques for high-throughput MIMO Satellite systems), "D3.5: Bandwidth Efficient Techniques evaluation (version 2)," 2022.
- [101]. 3GPP TS 22.261, "Service requirements for the 5G system," September 2023.
- [102]. 3GPP TS 38.101-1, "User Equipment (UE) radio transmission and reception," September 2020.
- [103]. 3GPP TS 38.104, "Base Station (BS) radio transmission and reception," September 2023.
- [104]. M. Ichikawa, T. Hara, M. Saito, M. Okada and H. Yamamoto, "Evaluation of BER degradation due to phase nonlinearity of SSPA on MC-CDMA signals," 2005 IEEE International Conference on Personal Wireless Communications, 2005. ICPWC 2005., New Delhi, India, 2005, pp. 533-536, doi: 10.1109/ICPWC.2005.1431404.
- [105]. M. Odroma, S. Meza and Y. Lei, "New modified Saleh models for memoryless nonlinear power amplifier behavioural modelling," IEEE Communications Letters, vol. 13, no. 6, p. 399-401, 2009.
- [106]. L. Wang and C. Tellambura, "A simplified clipping and filtering technique for PAR reduction in OFDM systems," IEEE Signal Processing Letters, vol. 12, no. 6, pp. 453-456, June 2005.
- [107]. "Digital Video Broadcasting (DVB), Second generation framing structure, channel coding and modulation systems for Broadcasting, Interactive Services, News Gathering and other broadband satellite applications, Part II: S2-Extensions (DVB-S)," in ETSI EN 302 307-2.